Lehrstuhl für Elektrische Energiespeichertechnik
Fakultät für Elektrotechnik und Informationstechnik
Technische Universität München

Enhancing the Performance of Lithium-Ion Cells via New Active Materials and Improved Electrode and Cell Design

Ludwig Kraft, M.Sc.

Vollständiger Abdruck der von der Fakultät für Elektrotechnik und Informationstechnik der Technischen Universität München zur Erlangung des akademischen Grades eines

Doktor-Ingenieurs (Dr.-Ing.)

genehmigten Dissertation.

Vorsitzender:		Prof. Dr.-Ing. Martin Buss
Prüfer der Dissertation:	1.	Prof. Dr.-Ing. Andreas Jossen
	2.	Prof. Dr. Hubert A. Gasteiger

Die Dissertation wurde am 09.06.2021 bei der Technischen Universität München eingereicht und durch die Fakultät für Elektrotechnik und Informationstechnik am 31.08.2021 angenommen.

Abstract

The rising worldwide demand for electric vehicles with sufficient driving ranges and fast charging capabilities requires sophisticated energy storage systems that meet the specific safety requirements and have an adequate lifespan. Currently, lithium-ion batteries comprising a liquid electrolyte are the predominant technology for electric vehicles. The driving range and the fast charging capability of an electric vehicle are defined by the energy and the power of the lithium-ion battery, respectively. It is therefore necessary to consider both the energy content and the power capability when improving the performance of lithium-ion batteries.

In this thesis, performance enhancements of single lithium-ion cells via new active materials and an improved electrode and cell design are investigated. The characteristic cell properties such as the capacity and the voltage level are mostly defined by the active materials of the anode and the cathode. A higher energy of a lithium-ion cell is significantly correlated to active materials with an increased specific capacity and a lower anode or higher cathode potential.

In the first part of this work, a high capacitive lithium- and manganese-rich lithium nickel cobalt manganese oxide (LMR-NCM) is evaluated and compared against an established lithium nickel cobalt aluminum oxide (NCA) cathode active material in multilayer lithium-ion pouch cells; graphite anodes are used for both cell systems. While the specific capacity of the LMR-NCM/graphite cells is ≈30% higher compared to the NCA/graphite cells, their energy density on the cell level is only ≈11% higher due to lower mean discharge voltages. The arising overpotentials and the pronounced voltage hysteresis of the LMR-NCM result in an energy inefficiency that causes a strong temperature increase of the cells, which cannot be neglected during operation.

In the second part of this work, the rate capability of lithium-ion cells is increased via an altered electrode morphology. Graphite anodes are laser-structured in order to create hole-like structures that serve as enhanced transport pathways for the lithium-ions. Experiments on coin cells comprising NCM cathodes and either unstructured or structured graphite anodes show, that the discharge capacity of the cells with the laser-structured anodes is boosted in a certain C-rate window by around 15%. Both the location of the C-rate window and the maximum benefit in capacity retention depend on different electrode properties and can be predicted by electrochemical models. Simulation studies of lithium-ion cells comprising laser-structured graphite anodes reveal, that reduced lithium-ion concentration gradients in the liquid electrolyte cause the improved rate capability for discharge and charge operations.

Kurzfassung

Die weltweit steigende Nachfrage an Elektrofahrzeugen mit einer akzeptablen Reichweite und Schnellladefähigkeit verlangt die Entwicklung von ausgeklügelten Energiespeichersystemen, die die speziellen Sicherheitsanforderungen erfüllen und eine ausreichende Lebensdauer aufweisen. Heutzutage werden in Elektrofahrzeugen fast ausschließlich Lithium-Ionen-Batterien mit einem flüssigen Elektrolyt eingesetzt. Die Reichweite eines Elektrofahrzeugs wird dabei vom Energieinhalt der Batterie bestimmt, die Schnellladefähigkeit hingegen von der Leistungsfähigkeit der Batterie. Aus diesem Grund müssen bei der Weiterentwicklung von Lithium-Ionen-Batterien sowohl der Energieinhalt als auch die Leistungsfähigkeit miteinbezogen werden.

Im Rahmen dieser Arbeit werden Verbesserungsmöglichkeiten von einzelnen Lithium-Ionen-Zellen durch neue Aktivmaterialien und durch ein angepasstes Elektroden- und Zelldesign untersucht. Die charakteristischen Zelleigenschaften, dazu zählen die Kapazität und die Spannungslage der Zelle, werden dabei maßgeblich von den Aktivmaterialien der Anode und Kathode beeinflusst. Eine Steigerung der Energie einer Lithium-Ionen-Zelle wird sowohl durch Aktivmaterialien mit einer höheren spezifischen Kapazität, als auch durch Anodenaktivmaterialien mit einem niedrigeren Potenzial oder Kathodenaktivmaterialien mit einem höheren Potenzial erreicht.

Im ersten Teil dieser Arbeit wird ein hochkapazitives Lithium- und Mangan-reiches Lithium-Nickel-Cobalt-Mangan-Oxid (LMR-NCM) untersucht und dabei mit einem etablierten Lithium-Nickel-Cobalt-Aluminium-Oxid (NCA) Kathodenaktivmaterial in mehrlagigen Pouchzellen verglichen; für beide Zellsysteme werden Graphitanoden verwendet. Verglichen mit den NCA/Graphit-Zellen liegt die spezifische Kapazität der LMR-NCM/Graphit-Zellen um ≈30% höher. Die Energiedichte auf Zellebene ist ≈11% höher, da die LMR-NCM/Graphit-Zellen niedrigere mittlere Entladespannungen aufweisen. Die auftretenden Überspannungen und die ausgeprägte Spannungshysterese des LMR-NCM Kathodenmaterials sorgen für eine Energieineffizienz, die zu einer starken Temperaturerhöhung der Zellen führt und beim späteren Einsatz nicht vernachlässigt werden kann.

Im zweiten Teil der Arbeit wird die Ratenfähigkeit von Lithium-Ionen-Zellen durch eine angepasste Elektrodenmorphologie gesteigert. Dafür werden mit einem Laser lochartige Strukturen in Graphitanoden eingebracht, um somit die Transportwege der Lithium-Ionen zu verbessern. Experimente an Knopfzellen mit NCM Kathoden und unstrukturierten oder strukturierten Graphitanoden zeigen, dass die Entladeratenfähigkeit der Zellen mit den strukturierten Anoden in einem definierten Strombereich um bis zu 15% gesteigert werden kann. Der genaue Strombereich und die maximale Verbesserung hängen von verschiedenen Faktoren ab und können mithilfe von elektrochemischen Modellen analysiert werden. Mit Simulationsstudien von Lithium-Ionen-Zellen mit strukturierten Graphitanoden wird nachgewiesen, dass hauptsächlich die verringerten Lithium-Ionen-Konzentrationsgradienten im flüssigen Elektrolyt für die verbesserte Lade- und Entladeratenfähigkeit verantwortlich sind.

Contents

Abbreviations

AAM . . . . . anode active material

AB . . . . . acetylene black

CAM . . . . . cathode active material

CB . . . . . carbon black

CMC . . . . . carboxymethyl cellulose

DEC . . . . . diethyl carbonate

DMC . . . . . dimethyl carbonate

DOF . . . . . degree of freedom

EC . . . . . ethylene carbonate

ECM . . . . . equivalent circuit model

EMC . . . . . ethyl methyl carbonate

EU . . . . . European Union

EV . . . . . electric vehicle

FCEV . . . . . fuel cell electric vehicle

FEC . . . . . fluoroethylene carbonate

FIB . . . . . focused ion beam

HEV . . . . . hybrid electric vehicle

LCO . . . . . lithium cobalt oxide

LFP . . . . . lithium iron phosphate

LIB . . . . . lithium-ion battery

LMO . . . . . lithium manganese oxide

LMR-NCM . . . lithium- and manganese-rich NCM

LNMO . . . . . lithium nickel manganese oxide

LTO . . . . . lithium titanate

MuDiMod . . . . multidimensional model

NCA . . . . . lithium nickel cobalt aluminum oxide

NCM . . . . . lithium nickel cobalt manganese oxide

NMC . . . . . see NCM

NMP N-Methyl-2-pyrrolidone

NT . . . . . Newman-Tiedemann model

p2D . . . . . pseudo two-dimensional model

p4D . . . . . pseudo four-dimensional model

PC . . . . . propylene carbonate

PCM . . . . . phase change material

PE . . . . . polyethylene

PHEV . . . . . plug-in hybrid electric vehicle

PP . . . . . polypropylene

PSD . . . . . particle size distribution

PVDF . . . . . polyvinylidene fluoride

RVE . . . . . representative volume element

SBR . . . . . styrene-butadiene rubber

SEI . . . . . solid electrolyte interphase

SEM . . . . . scanning electron microscopy

SHE . . . . . standard hydrogen electrode

Si-C . . . . . silicon-graphite

SOC . . . . . state of charge

SOH . . . . . state of health

SPI . . . . . solid permeable interphase

SPM . . . . . single particle model

Symbols

c_l . . . . . lithium-ion concentration in the liquid phase in $\mathrm{mol\,m^{-3}}$

c_p . . . . . specific heat capacity in $\mathrm{J\,kg^{-1}\,K^{-1}}$

c_s . . . . . lithium-ion concentration in the solid phase in $\mathrm{mol\,m^{-3}}$

$c_\mathrm{s,max}$ . . . . . maximum lithium-ion concentration in the solid phase in $\mathrm{mol\,m^{-3}}$

D_l . . . . . diffusion coefficient in the electrolyte in $\mathrm{m^2\,s^{-1}}$

D_s . . . . . diffusion coefficient in the active material in $\mathrm{m^2\,s^{-1}}$

E_eq . . . . . thermodynamic equilibrium potential in V

F . . . . . Faraday constant, $96\,485\,\mathrm{C\,mol^{-1}}$

$f_\pm$ . . . . . mean activity coefficient

h . . . . . convective heat transfer coefficient in $\mathrm{W\,m^{-2}\,K^{-1}}$

i_0 . . . . . exchange current density in $\mathrm{A\,m^{-2}}$

i_app . . . . . applied current density in $\mathrm{A\,m^{-2}}$

i_l . . . . . current density in the liquid phase in $\mathrm{A\,m^{-2}}$

i_s . . . . . current density in the solid phase in $\mathrm{A\,m^{-2}}$

j_n . . . . . pore wall flux density in $\mathrm{mol\,m^{-2}\,s^{-1}}$

k . . . . . thermal conductivity in $\mathrm{W\,m^{-1}\,K^{-1}}$

$k_\mathrm{a/c}$ . . . . . anodic/cathodic reaction rate constant in $\mathrm{m\,s^{-1}}$

L . . . . . total thickness of the cell stack in m

l . . . . . length/thickness in m

l_dir . . . . . direct path length in m

l_eff . . . . . effective path length in m

l_neg . . . . . thickness of the negative electrode domain in m

l_pos . . . . . thickness of the positive electrode domain in m

l_sep . . . . . thickness of the separator domain in m

N_l . . . . . flux density in the liquid phase in $\mathrm{mol\,m^{-2}\,s^{-1}}$

N_M . . . . . MacMullin number

N_s . . . . . flux density in the solid phase in $\mathrm{mol\,m^{-2}\,s^{-1}}$

q_cond . . . . . heat flux density from conductive heat transport in $\mathrm{W\,m^{-2}}$

q_conv . . . . . heat flux density from convective heat transport in $\mathrm{W\,m^{-2}}$

q_rad . . . . . heat flux density from radiative heat transport in $\mathrm{W\,m^{-2}}$

q_vol . . . . . volumetric heat generation in $\mathrm{W\,m^{-3}}$

R . . . . . universal gas constant, $8.314\,\mathrm{J\,mol^{-1}\,K^{-1}}$

r_p . . . . . particle radius in m

T . . . . . absolute temperature in K

t . . . . . time in s

t_+^0 . . . . . transference number of lithium-ions

T_∞ . . . . . ambient temperature in K

T_surf . . . . . surface temperature in K

$\alpha_\mathrm{a/c}$ . . . . . anodic/cathodic charge transfer coefficient

α_Brugg . . . . . Bruggeman exponent

ε_rad . . . . . emissivity

ε_l . . . . . porosity of the electrode/separator

ε_na . . . . . volume fraction of non-active material

ε_s . . . . . volume fraction of the solid active material

η . . . . . overpotential in V

κ . . . . . electrolyte conductivity in $\mathrm{S\,m^{-1}}$

ϕ_l . . . . . potential in the liquid phase in V

ϕ_s . . . . . potential in the solid phase in V

ρ . . . . . density in $\mathrm{kg\,m^{-3}}$

σ . . . . . solid phase conductivity in $\mathrm{S\,m^{-1}}$

σ_SB . . . . . Stefan-Boltzmann constant, $5.67 \cdot 10^{-8}\,\mathrm{W\,m^{-2}\,K^{-4}}$

τ . . . . . tortuosity

1 Introduction

Currently, lithium-ion batteries (LIBs) are the preferred electrical energy storage solution for a variety of mobile and stationary applications. Ever since their market introduction by Sony in 1991 [1], LIBs have been gaining more and more popularity and are widely used for consumer electronics, power tools, electric bikes, and electric vehicles (EVs), and furthermore for home and grid storage systems [2, 3], as depicted in Fig. 1.1. The importance of LIBs in our everyday lives was emphasized by the Nobel Prize in Chemistry 2019, which was awarded to John B. Goodenough, M. Stanley Whittingham, and Akira Yoshino for their contributions to the development of LIBs [4]. Especially the increasing energy density of LIBs together with decreasing costs allow their use in a multitude of applications [5, 6]. While Sony's first generation LIB from 1991 had an energy density of 80 $\mathrm{Wh\,kg^{-1}}$ (200 $\mathrm{Wh\,l^{-1}}$) [1], the latest commercially available cylindric LIBs reach around 270 $\mathrm{Wh\,kg^{-1}}$ (800 $\mathrm{Wh\,l^{-1}}$) on the cell level [7–9]. In addition, the cell prices have dropped from around 460 $\mathrm{USD\,kWh^{-1}}$ in 2013 to 100 $\mathrm{USD\,kWh^{-1}}$ in 2020, allowing an even broader field of application [9].

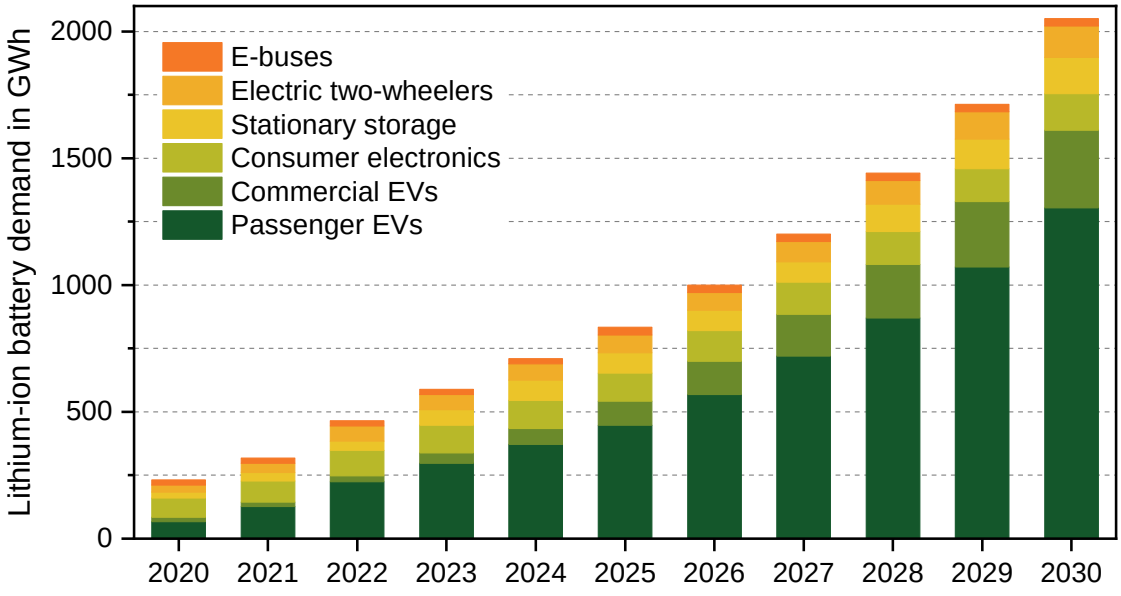

Figure 1.1: Projections of the worldwide annual lithium-ion battery demand (figure derived from BloombergNEF 2020 Electrical Vehicle Outlook [10]).

The worldwide demand for LIBs is rapidly growing and is projected to reach around 2000 GWh per year in 2030, as seen in Fig. 1.1. Today, EVs already account for the highest demand in annual LIB production capacity [11–13]. Due to the consumer demand for EVs with affordable costs and a satisfactory driving range, LIBs with a liquid electrolyte are the predominant technology used for electromobility [2]. While there is a small share of fuel cell electric vehicles (FCEVs), the use of hydrogen as an energy source is rather suited for vehicles that require larger driving ranges [14, 15], such as trucks

and heavy duty vehicles, but also for aircraft [16]. On the other hand, solid state technologies using lithium-metal anodes and a solid electrolyte and so-called post-LIBs, e.g., lithium-air, lithium-sulfur and also sodium-ion batteries, are still under ongoing development; they face various challenges and cannot yet provide the required energy density, rate capability, and long-term cycling stability that is needed for use in EVs [15, 17, 18].

Propelled by the growing EV market, the LIB manufacturing capacity is likewise rapidly growing. An estimation of the production capacity of the Top 10 lithium-ion battery manufacturers in 2028 is shown in Fig. 1.2. However, these projections are volatile as more and more companies are entering the market and make announcements of new LIB gigafactories. Recently, Volkswagen announced on their "Power Day" on March 15, 2021, that six gigafactories with a total production capacity of 240 GWh per year are to be established by 2030 – together with partners like Northvolt – to secure the supply of battery cells for their EVs [19]. A worldwide increasing LIB manufacturing capacity creates a competition between cell manufacturers and an economy of scale, driving down costs for batteries [12].

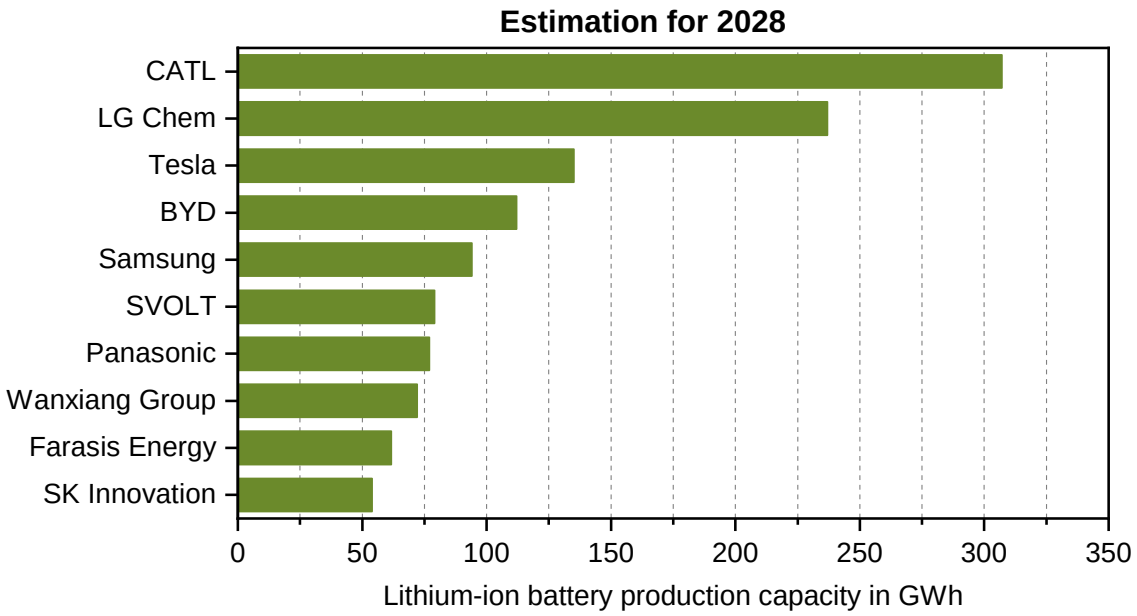

Figure 1.2: Estimation of the production capacity of the Top 10 lithium-ion battery manufacturers in 2028 (data from Benchmark Mineral Intelligence [20]).

The trend towards electromobility is further driven by political requirements, as seen in the European Union (EU) CO_2 targets for the transportation sector in order to reduce emissions of new passenger cars [21]. The fleet-wide average target for 2015 was $130\,g_{CO_2}\,km^{-1}$, which was reportedly reached already two years before [22]. As of 2021, this target is reduced to $95\,g_{CO_2}\,km^{-1}$, and car manufacturers must pay penalties if their fleet emissions exceed the targeted value [22]. To further reduce CO_2 emissions, additional regulations for newly registered passenger cars were stated: based on the 2021 values of $95\,g_{CO_2}\,km^{-1}$, a reduction of 15% from 2025 onwards and 37.5% from 2030 onwards was defined [23]. The CO_2 emissions of most cars with an internal combustion engine are higher than the set values, so in order to avoid penalty payments, automobile manufacturers have to increase their share of EVs, plug-in hybrid electric vehicles (PHEVs), hybrid electric vehicles (HEVs), or hydrogen powered FCEVs [15, 24]. Some countries even announced to ban the registration of new cars that are purely powered by an internal combustion engine within the next decade. Norway is leading the trend

towards electromobility in Europe and wants to prohibit the registration of gasoline and diesel cars by 2025 [12]. With almost 12 million new passenger car registrations in 2020 in Europe, the average market-wide share of electrified vehicles (EVs, PHEVs, HEVs, and FCEVs) was around 11% [25].

As the number of EVs will most certainly increase in the upcoming years, the demand for LIBs with an adequate energy density and power capability will likewise be affected. A significant amount of research focuses on the development of new cell systems and active materials with a higher capacity. However, the electrode and cell design also plays an important role to fulfill the requirements of specific applications. While applications such as mobile phones and tablets rely on high energy LIBs, applications like power tools require high power LIBs. EVs are a prominent example of a combination of both types: on the one hand, an EV battery should have a high energy density in order to reach sufficient driving ranges, on the other hand, the battery needs an adequate power capability, which is necessary for fast charging.

Within the scope of this thesis, performance enhancements of state-of-the-art LIBs are investigated. The capacity and the energy of a LIB can not only be boosted with new active materials, but also with an improved electrode and cell design. As illustrated in Fig. 1.3, these points are addressed in this thesis, which is structured into the following three main parts:

- Starting with the fundamentals of LIBs in Chapter 2, their working principle, their specific electrode and cell components, and the design of battery systems including the thermal management are presented. Subsequently, a general overview of LIB models is given, followed by the description of the electrochemical pseudo two-dimensional model (p2D), the modeling of structured electrodes, and the 3D thermal model, as these model types were used within the scope of this work.
- In Chapter 3, approaches to increase the capacity and energy of a LIB with new active materials are presented including the effects that must be considered when projecting the performance from laboratory cells to larger cell formats. For this evaluation, a cathode active material that offers a comparatively high specific capacity, but is still subject of current research, is benchmarked against an established cathode active material in multilayer lithium-ion pouch cells. Besides the rate capability and the long-term stability, a special focus lies on the efficiency and the corresponding thermal behavior of the cells with the high capacitive active material.
- In Chapter 4, the rate capability of LIBs is enhanced via a specific electrode design: The morphology of graphite anodes is altered with a laser-structuring process in order to allow an improved lithium-ion transport in the liquid electrolyte. This anode structuring process is beneficial for the cell performance for both charge and discharge operations, but only in a limited C-rate window. The investigation of the performance enhancement and of the underlying limiting mechanisms are supported by different modeling approaches and simulations studies.

Finally, in Chapter 5, the main findings of this work are concluded and a brief outlook of future work is given.

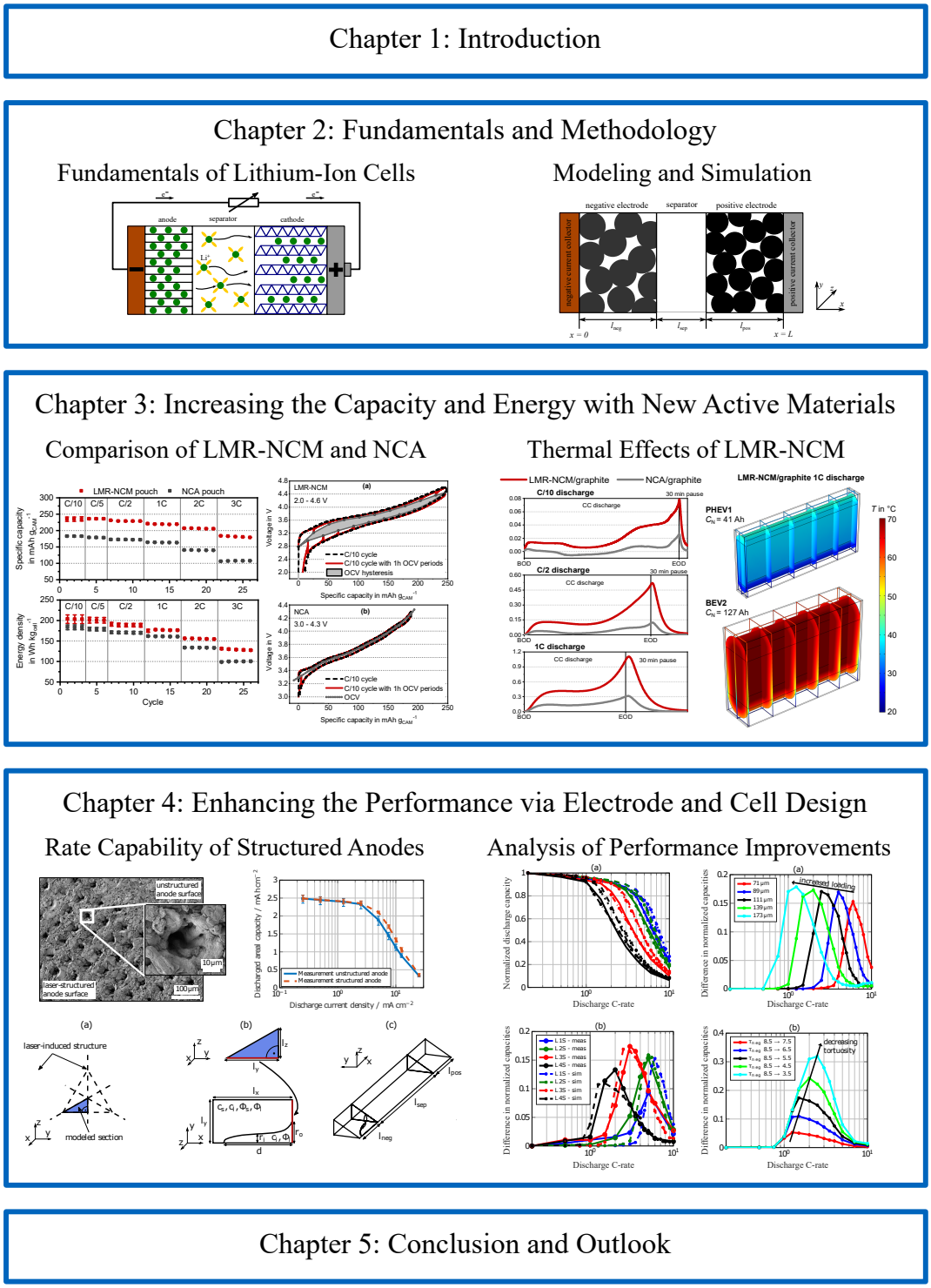

Figure 1.3: Structure and outline of this thesis.

2 Fundamentals and Methodology

The word lithium originates from the greek word *lithos*, which means stone, and was discovered by the Swedish chemist Johan August Arfwedson in 1817 [26]. The element lithium (Li) belongs to the alkali metals and is the lightest of all metals. Furthermore, lithium has an extremely low potential of $-3.04\,\mathrm{V}$ vs. standard hydrogen electrode (SHE) and a high specific capacity of $3860\,\mathrm{mAh\,g^{-1}}$ and is therefore an attractive anode material for batteries [27, 28]. Lithium metal anodes have been used in primary lithium cells for a few decades, but pose problems for rechargeable lithium metal batteries with ongoing cycling due to dendrite formation, which can cause severe safety issues [27, 29]. This dendrite growth associated with lithium metal anodes is not only present in lithium metal batteries with a liquid electrolyte, but also in cells with a solid state electrolyte [17, 30]. For this reason, intercalation electrodes for both anode and cathode are predominantly used in state-of-the-art rechargeable LIBs. The studies in this work are based on LIBs with two intercalation electrodes and a liquid electrolyte, which will be further specified and explained in the following sections.

2.1 Fundamentals of Lithium-Ion Cells

A LIB consists of two electrodes, an anode and a cathode, a separator that guarantees electrical insulation between the two electrodes, and an electrolyte that enables lithium-ion transport. Common LIBs incorporate two porous intercalation or alloying electrodes and a porous separator, which are soaked with liquid electrolyte. A schematic illustration of the working principle of a LIB during discharge is displayed in Fig. 2.1.

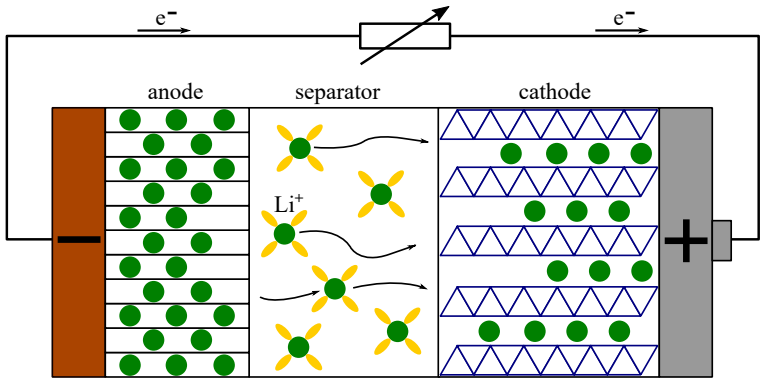

Figure 2.1: Schematic working principle of a lithium-ion battery consisting of anode, separator, and cathode domain during discharge (derived from Ref. [31]).

In general, the terms anode and cathode define the discharge of a LIB. If the cell is fully charged, the lithium-ion inventory is stored in the negative electrode (anode) and the positive electrode (cathode) is delithiated. Note that the electrodes must neither be completely lithiated nor completely delithiated, this is only related to the amount of lithium-ions that are continuously cycled between both electrodes.

During discharge, an oxidation takes place at the anode and lithium-ions deintercalate from the host lattice into the liquid electrolyte and move through the separator towards the positive electrode. At the cathode, a reduction takes place and the lithium-ions intercalate into the host lattice of the positive electrode. The participating electrons from the oxidation move through an exterior electrical circuit from the anode to the cathode and take part in the reduction. During charge, the described processes reverse, i.e., the oxidation/deintercalation takes place at the cathode and the lithium-ions and the electrons move towards the anode where the reduction/intercalation takes place.

2.1.1 Review of Common Cathode and Anode Active Materials

There is a variety of different cathode active materials (CAMs) and anode active materials (AAMs) that are used for LIBs; a general overview of common active materials is displayed in Fig. 2.2. The range of the specific capacity as well as the average discharge potential vs. Li/Li^+ are indicated by the colored area for each material. Table 2.1 summarizes the presented active materials in terms of specific capacity and average discharge potential as well as advantages and disadvantages. Note that both in Fig. 2.2 and Table 2.1 only approximate material properties are given, as these properties strongly depend on several factors, e.g., the voltage window in which the cells are cycled, the current rate, the operating temperature, and possible performance modifications of the material.

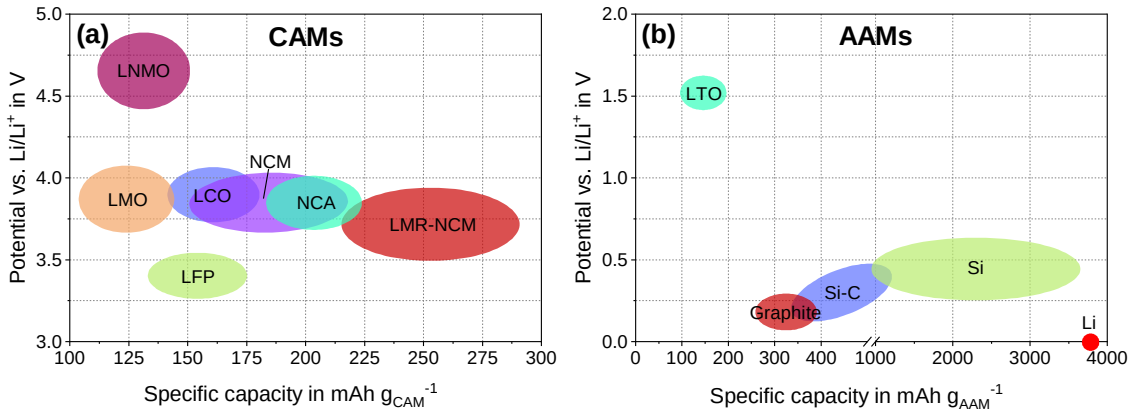

Figure 2.2: Overview of common (a) cathode active materials (CAMs) and (b) anode active materials (AAMs) with regard to their approximate discharge potentials vs. Li/Li^+ and specific capacities (derived from Ref. [31–35]).

Cathode active materials There is a vast number of different CAMs, however, most CAMs that are used in LIBs for commercially available products are layered transition metal oxides [32, 37]. A selection of conventional CAMs is shown in Fig. 2.2a. Besides the layered oxides, there are also spinel oxides, polyanionic compounds, to which lithium iron phosphate (LFP) belongs, and conversion cathodes [32, 33, 37]. CAMs can further be classified with regard to their crystal structure: layered, spinel, and olivine [31, 33].

Layered transition metal oxides include lithium cobalt oxide (LCO) ($LiCoO_2$), lithium nickel cobalt manganese oxide (NCM) ($LiNi_xCo_yMn_zO_2$, also referred to as NMC), and lithium nickel cobalt aluminum oxide (NCA) ($LiNi_xCo_yAl_zO_2$). The subscripts x, y, and z indicate the stoichiometry of the material with $x + y + z = 1$. In 1991, LCO was first commercialized by Sony as CAM for rechargeable

Table 2.1: Overview of cathode and anode active materials with regard to their reversible/practical specific capacity, average de-/lithiation potential vs. Li/Li^+, and advantages and disadvantages (data taken from Ref. [2, 32–36]).

AM	Specific capacity in $mAh\,g^{-1}$	Average potential vs. Li/Li^+ in V	Advantages	Disadvantages
CAM				
LCO	150	3.9	In common use, good cycle life, good energy	Moderate charged state thermal stability
NCM-111	160	3.7	Very good combination of energy, power, cycle life, and thermal stability	Patent issues
NCM-622	170	3.7		
NCM-811	200	3.7		
NCA	200	3.7	Very good energy, good power capability, good cycle life	Moderate charged state thermal stability
LMR-NCM	250	3.6	Very good energy, cost-efficient	Voltage hysteresis, voltage fading, moderate cycle life
LMO	110	4.1	Very good thermal stability, cost-efficient, very good power capability	Moderate cycle life, lower energy
LNMO	140	4.7	Good energy, cost-efficient	Electrolyte instability, moderate cycle life
LFP	165	3.45	Very good thermal stability and cycle life, good power capability cost-efficient	Lower energy, special preparation conditions
AAM				
Graphite	360	0.1	In common use, good cycle life	Lithium-plating during fast charging
LTO	150	1.55	Very good cycle life and thermal stability	Lower energy
Si	3579	0.4	Very good energy, cost-efficient	High volume changes, moderate cycle life
Li	3860	0	Very good energy	High reactivity, moderate cycle life

AM - active material, CAM - cathode active material, AAM - anode active material

LIBs and is still used in portable electronic devices [2, 31, 36]. LCO is an established material that has a long cycle life, but comes at a high cost due to the high share of cobalt [2, 35]. NCM is a widely-used material with a good energy density, power capability, and cycle life and is used for LIBs in various applications, ranging from portable electronic devices and power tools to EVs [2, 38]. In Fig. 2.2a, NCM-111 ($LiNi_{1/3}Co_{1/3}Mn_{1/3}O_2$) with around 160 mAh g^{-1} is on the left-hand side of the indicated purple area for NCMs, whereas the nickel-rich NCM-811 ($LiNi_{0.8}Co_{0.1}Mn_{0.1}O_2$) with around 200 mAh g^{-1} is at the right-hand side [32, 34, 36]. Another nickel-rich material with a comparably good energy density, power capability, and cycle life is NCA, reportedly used by Panasonic and Tesla for their EVs [38, 39], but also used for premium electronic applications [2].

Lithium- and manganese-rich NCM (LMR-NCM) is a layered transition metal oxide-based CAM that offers a higher specific capacity with around 250 mAh g^{-1} but is not yet commercialized [2, 40–43]. The price of the commodity manganese is an order of magnitude lower than that of nickel, and by comparing the stoichiometry of a manganese-rich LMR-NCM (e.g., $Li_{1.14}[Ni_{0.26}Co_{0.14}Mn_{0.60}]_{0.86}O_2$) to a nickel-rich NCA (e.g., $LiNi_{0.81}Co_{0.15}Al_{0.04}O_2$), up to 34% can be saved in raw material costs [44]. LMR-NCM faces some challenges that have to be addressed, such as a pronounced voltage hysteresis, voltage fading, and gassing, but the comparably lower material costs and high specific capacity render it to be a promising material for future LIBs [39, 42, 45, 46]. A detailed assessment of LMR-NCM in coin cells as well as large-format multilayer pouch cells is given in Chapter 3 [44, 47, 48].

All of the previously stated CAMs contain cobalt, a scarce and toxic material, which has a relatively high price. Therefore, the share of cobalt in layered transition metal oxides is becoming more and more reduced, e.g., from NCM-111 to NCM-811, or even completely eliminated [49–53]. There is also a cobalt-free alternative for LMR-NCM [54].

The spinel lithium manganese oxide (LMO) ($LiMn_2O_4$) has a very good thermal stability and power capability and is cost-efficient, but has a low specific capacity (≈110 mAh g^{-1}) and an only moderate cycle life [2]. It is especially used in high power applications, but also in some EVs, often in combination with layered oxides [32, 38, 39]. The high-voltage spinel lithium nickel manganese oxide (LNMO) ($LiNi_{0.5}Mn_{1.5}O_4$) has a very high voltage of ≈4.7 V vs. Li/Li^+, but a low specific capacity (≈140 mAh g^{-1}) [31, 32, 35]. Moreover, most electrolytes are instable at such high voltages resulting in an electrolyte decomposition and a low cycle life [31, 35, 37].

LFP ($LiFePO_4$) has an olivine structure, a very good thermal stability, a long cycle life, and is cost-efficient [2, 33, 35, 37]. Disadvantages are the comparatively low specific capacity (≈165 mAh g^{-1}) and low discharge voltage (≈3.45 V), resulting in a low energy density [31]. Because of the long cycle life, LFP is suited for stationary energy storage applications, for which the energy density is not as important as for EVs [2, 3, 55, 56]. Despite the poor electronic conductivity of LFP, which can be enhanced with a carbon surface coating of the active material particles [31, 37], LFP is used in high power applications and also in some EVs [2, 38].

Anode active materials In comparison to the grand variety in CAMs, the number of the most common AAMs is rather manageable, an overview is displayed in Fig. 2.2b. AAMs can be classified into intercalation materials, such as graphite and lithium titanate (LTO), alloying-type materials, e.g., silicon and silicon-oxides, and conversion materials [31, 33, 35].

The most prominent intercalation anode material is graphite with a theoretical specific capacity of 372 mAh g^{-1} [35, 57, 58]. The specific capacity of graphite is low in comparison to other AAMs, but

still higher than that of most CAMs. To date, graphite-based anode materials can be found in most commercial LIBs in all different kinds of applications [58]. Graphite anodes were commercialized more than 20 years ago and come with a long cycle stability [33, 35]. The reversibility of the lithium-ion intercalation and deintercalation is strongly influenced by the solid electrolyte interphase (SEI), a passivation layer on the surface of the graphite particles that is formed from electrolyte decomposition products, mainly within the first few cycles of a cell containing graphite anodes [57, 58]. The SEI is permeable to lithium-ions, but prevents an ongoing reductive electrolyte decomposition as well as a detrimental solvent co-intercalation [57, 58].

Another common intercalation anode material is LTO ($Li_4Ti_5O_{12}$) with a rather low specific capacity of $175\,mAh\,g^{-1}$ and a relatively high potential of $1.55\,V$ vs. Li/Li^+ [31, 33, 35]. Despite the low capacity and energy density of the material, LTO exhibits a very good thermal stability, high rate capability, and a high cycle life [33, 35], and was even used in a few EVs [2, 38]. The high cycle life arises from the low volume changes of only 0.2% during lithiation and delithiation; LTO is therefore considered a "zero strain" material, whereas graphite anodes in comparison exhibit volume changes up to 10% for full lithiation [31, 33, 58, 59]. An additional safety feature is the high potential of LTO vs. Li/Li^+, which avoids lithium-plating during charging. Moreover, the potential of LTO lies within the electrochemical stability window of common liquid electrolytes, largely avoiding an SEI formation [31, 33].

Silicon (Si) and silicon-oxides (SiO_x) belong to the alloying-type materials. If fully utilized, pristine silicon offers a very high specific capacity of $3579\,mAh\,g^{-1}$ that is accompanied by large volume changes up to 300% [31, 33, 35, 60]. With ongoing cycling, these volume changes lead to mechanical and chemical degradation and a deteriorating cycle life [31]. However, if only ≈30% (≈$1000\,mAh\,g^{-1}$) of the available capacity of silicon is used, the volume expansion can be reduced to around 100% and the cycle life thereby increased [60]. This partial usage of the available capacity is indicated by the wide green area representing silicon in Fig. 2.2b. Another approach is the addition of silicon or silicon-oxides to graphite anodes (silicon-graphite (Si-C) in Fig. 2.2b) to boost the specific capacity of pristine graphite while keeping the volume change at an acceptable level [58, 61, 62]. Such Si-C anodes are already used in commercially available cells [7, 63, 64] and are also reportedly used by Tesla in their latest EVs [38, 39].

Finally, pure lithium anodes offer the highest theoretical capacity of $3860\,mAh\,g^{-1}$, and in combination with the low electrochemical potential ($0\,V$ vs. Li/Li^+, $-3.04\,V$ vs. SHE), a very high energy density [35, 65, 66]. Disadvantages are an infinite volume change, the high reactivity of lithium metal, and lithium dendrite formation, which can cause safety-critical short circuits [35, 67]. In order to achieve a maximized energy density without excess lithium on the anode side, there are so-called "anode-free" lithium metal batteries, where the lithium from the cathode is deposited on the anode during the first charge [68–70].

2.1.2 Electrode and Single Cell Design

The active materials of the cathode and the anode are the most important parts of an electrode as they define the capacity and energy. But there are further passive components, which are necessary for a working LIB. In the following, the components for an electrode as well as common electrolytes and separators are described and a classification of different cell formats is given.

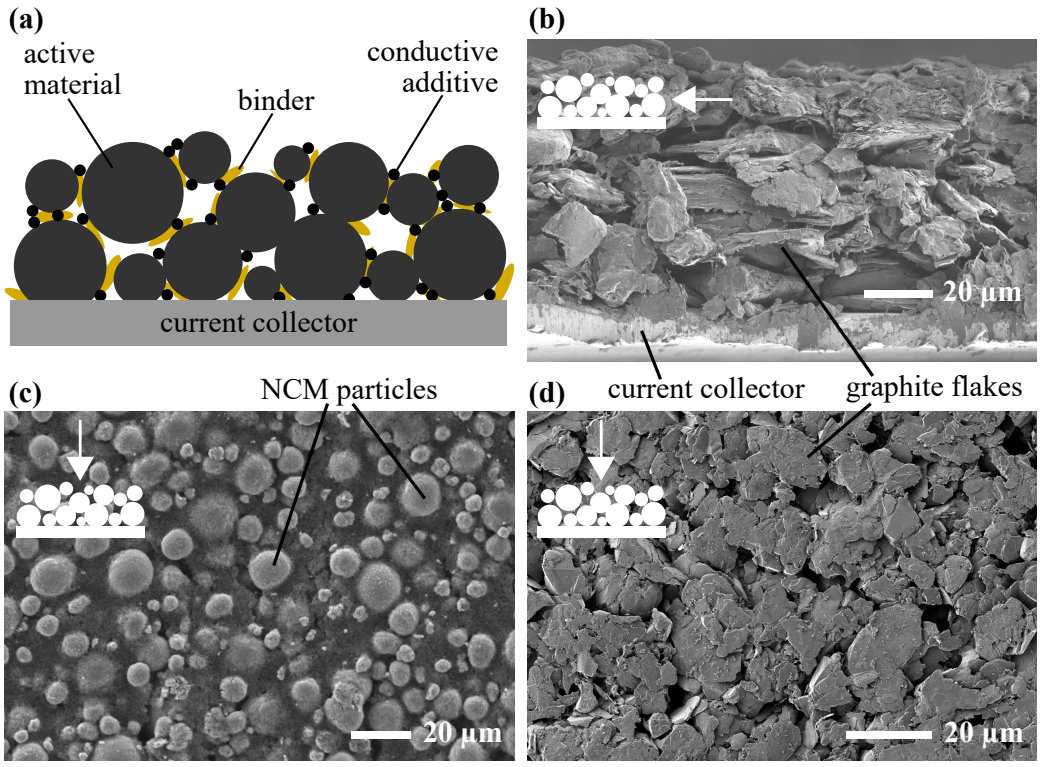

Figure 2.3: (a) Schematic illustration of the electrode components. SEM images of (b) a side view of a graphite electrode with flake-like particles and a copper current collector on the bottom, (c) a top view of an NCM-111 electrode with spherical particles, and (d) a top view of a graphite electrode with flake-like particles.

Electrodes A LIB electrode consists of a composite coated on a substrate foil, which serves as a current collector during operation. The composite consists of an active material, a binder to ensure mechanical stability, and optional additives, e.g., to enhance the electronic conductivity of the electrode or to maintain the integrity of the porous electrode structure. A schematic illustration of the electrode components is shown in Fig. 2.3a, and exemplary scanning electron microscopy (SEM) images of graphite and NCM-111 electrodes are given in Fig. 2.3b-d.

The current collectors have to be electrochemically stable in the potential operation window of the corresponding electrode, which is about 0–2 V (vs. Li/Li^+) for the anode and 3–5 V (vs. Li/Li^+) for the cathode [71, 72]. Owing to the electrochemical stability at lower potentials, copper is commonly employed as the current collector for the anode while aluminum is stable at higher potentials and therefore employed as the current collector for the cathode [73, 74]. At a temperature of 25 °C, copper has an electronic conductivity of $58.4 \cdot 10^6\,\mathrm{S\,m^{-1}}$, and aluminum has an electronic conductivity of $36.9 \cdot 10^6\,\mathrm{S\,m^{-1}}$ [26]. In order to reach a similar electric resistance, the aluminum current collectors for the positive electrode are thicker than the copper current collectors for the negative electrode.

During electrode production, different liquids, e.g., N-Methyl-2-pyrrolidone (NMP) or water, are used in the mixing process for the slurry preparation before the coating is cast onto the substrate foil, subsequently dried, and then calendered to the desired thickness and porosity. Polyvinylidene fluoride (PVDF) is a conventional binder that is used for NMP based anodes and cathodes [46, 47, 75–80]. For water based graphite anodes, styrene-butadiene rubber (SBR) and carboxymethyl cellulose (CMC) binders are often used [47, 79, 81]. As the binder has to ensure mechanical stability of the electrode

during continuous cycling and thereby prevent detrimental aging mechanisms, its role is even more important for active materials with a high volume expansion such as Si-C or pure silicon [60, 62, 82].

For graphite anodes, carbonaceous conductivity enhancers can be applied in small amounts in order to adjust the electronic and the thermal conductivity; besides enhancing the conductivity, carbonaceous additives also serve as active material for the negative electrode [31]. While graphite has a high electronic conductivity, the electronic conductivity of most cathode materials is rather low [83, 84]. Therefore, conductive additives such as carbon black (CB) or acetylene black (AB) are generally utilized to boost the electronic conductivity of cathodes [46, 47, 75, 76, 78–80, 84].

Electrolyte The electrolyte is vital for the performance, safety, and lifetime of a LIB, as it has to keep its stability when exposed to the low potentials on the anode as well as the high potentials on the cathode [85, 86]. In general, a liquid electrolyte has to provide a charge transfer with ions as the charge carrier and consists of a solute, i.e., a salt that is dissolved in a solvent [87]. For LIBs, there are only a few examined lithium salts (e.g., $LiBF_4$, $LiAsF_6$, $LiClO_4$, LiBOB) with the most prominent salt being $LiPF_6$, which is commonly used in a combination with a nonaqueous organic solvent [86, 87]. In contrast to the few lithium salts, there is a variety of solvents with diverse properties. An ideal solvent should be able to dissolve lithium salts to sufficient concentration, should have an adequate thermal stability, low viscosity, and low reactivity with other cell components, and should be nontoxic as well as economical [87]. Usually, a composition of different solvents is employed to meet the cell-specific requirements. Established electrolyte solvents are carbonates, such as ethylene carbonate (EC), propylene carbonate (PC), ethyl methyl carbonate (EMC), diethyl carbonate (DEC), dimethyl carbonate (DMC), and fluoroethylene carbonate (FEC) [85, 87, 88].

Because of the electrochemical potential window, the electrolyte is constantly exposed to a reduction on the anode. By the formation of a passivation layer on the surface of the anode, the so-called SEI, further electrolyte reduction is prevented [89, 90]. The SEI formation mainly takes place in the first charge of a LIB, but it is growing with ongoing cycling [89, 91, 92]. On the cathode, the electrolyte is exposed to high potentials and oxidation, and a surface passivation layer, called solid permeable interphase (SPI), is formed on the cathode [86]. Both passivation layers should be permeable to lithium-ions but block electron transport, thereby preventing further electrolyte degradation [86, 89]. There is a multiplicity of different electrolyte additives to improve the stability of the passivation layers and thus prevent electrolyte and cell aging [90]. Other electrolyte additives increase ionic conductivity for a better cell performance or improve the thermal stability for safety reasons [86, 93].

Besides common liquid electrolytes as described above, there are also solid polymer and gel polymer electrolytes [87, 94, 95], ionic liquids [93, 96–98], as well as solid electrolytes [99–102]. Most of these electrolyte technologies have been investigated for several decades but still face challenges for a widespread use in LIBs, e.g., an adequate ionic conductivity at room temperature, mechanical stability, the formation of a stable SEI, or a stable contact at the electrode interphases.

Therefore, liquid electrolyte systems remain the technology of choice for state-of-the-art LIBs. With all the various electrolyte systems for LIBs, the interactions and stability together with the electrode materials are of utmost importance and dictate the specific electrolyte characteristics in the end [87].

Separator LIBs comprising liquid electrolytes make the usage of a separator indispensable in order to allow a lithium-ion flow, but prevent physical contact and safety-critical short circuits between both

electrodes [103, 104]. Ideally, the ionic resistance of a separator should be zero, while the electronic resistance should be infinite; practically, the electronic conductivity of polymers is in the order of magnitude of 10^{12}–$10^{14}\,\Omega\,\mathrm{cm}$ [103]. The ionic conductivity on the other hand, is defined by the liquid electrolyte and the porous structure of the separator, represented by its porosity (around 40–60%) and tortuosity (≈2.5–7) [105, 106]. While separators used to have thicknesses of 20–30 µm [103–106], state-of-the-art separators for high energy LIBs are as thin as 7–10 µm [64]. Besides the stated characteristics, the thermal stability plays a crucial role, as a shrinking or melting of the separator at elevated temperatures could cause short circuits and safety-critical states [104, 107]. In fact, certain separator designs can mitigate and even prevent a thermal runaway [103].

There are different types of separators, namely, porous membranes, nonwoven mats, and multilayers consisting of these types [103, 104]. Porous membranes made of polyolefin such as polypropylene (PP) or polyethylene (PE) are most commonly used in LIBs [103, 105]. Besides monolayer separators consisting of one material, there are also bilayer (e.g., PP/PE) and trilayer separators (e.g., PP/PE/PP) [103–105]. This concept provides a shutdown mechanism at elevated temperatures, as PE has a thermal shutdown temperature of 120–150 °C (PP ≈160 °C), which is lower than the onset temperature of a thermal runaway: in case of a cell temperature increase above 120 °C, the PE layer would melt to a nonporous film and thereby block the lithium-ion flow and increase the electrical resistance, while the PP layers still keep their mechanical integrity and separate both electrodes [103–105]. Another possibility to enhance the thermal safety characteristics of separators with a low thermal stability are ceramic coatings, as ceramics possess an excellent thermal stability [103, 107].

Cell formats Since there are many diverse applications that use batteries as their energy source, there is also a multitude of different LIB cell designs and sizes [48, 108, 109]. The main cell formats for LIBs can be categorized into prismatic, pouch, and cylindric, as depicted in Fig. 2.4 on the left side. The electrode stack – also called jelly roll for wound electrodes – consists of double-sided anodes and cathodes with separators in between and is adapted to the desired cell format via stacking or winding, as seen in Fig. 2.4 on the right side. As there is no counter electrode for the outer layer(s) of each cell format, a single-sided anode is often employed at these positions. Pouch cells use stacked electrodes, cylindrical cells use wound electrodes, and prismatic cells use either stacked electrodes or flat wound electrodes [110–112].

Prismatic cells use a hard case, e.g., made of an aluminum alloy, that ensures a mechanical stability of the cell [113, 114]. Large prismatic cells are usually designed for a specific application like EVs [38, 39]; several automotive cell formats are for instance defined in the standard DIN 91252 [115]. Prismatic cell cases (thickness ≈0.7 mm [114]) add extra weight and volume to the cell, but have a good mechanical stability and enable an integration of various safety devices, such as vents and fuses [116], and sensors, e.g., reference electrodes and temperature sensors [117].

Pouch cells are a special kind of prismatic cell: instead of a hard case surrounding the cell, the electrode stack is packed into a flexible pouch foil. The pouch foil is usually made of an aluminum foil, which is laminated with plastics on both sides to guarantee an electrical insulation and an electrochemical stability against the inner cell components such as the electrodes and the liquid electrolyte [118]. The thicknesses of pouch foils range from around 68–158 µm (e.g., pouch foils AvALL68 - AvALL158, Avocet Precision Metals, UK) and thereby save weight and volume in contrast to a hard case but forfeit mechanical stability. The flexibility in the pouch cell design allows an integration in many different applications ranging from thin consumer cells for mobile phones, tablets, and laptops to large

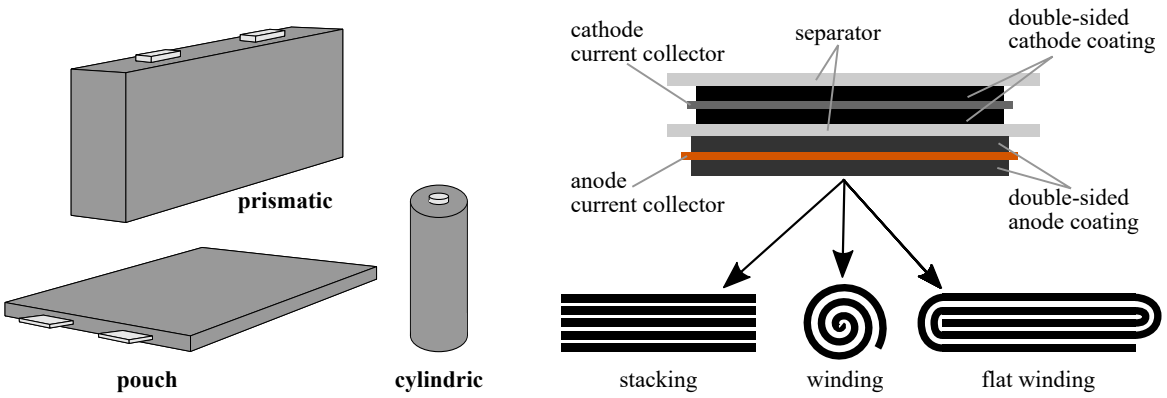

Figure 2.4: Left: Cell formats for LIBs. Right: Schematic electrode stack consisting of double-sided anodes and cathodes with separators in between. Stacking the layers is used for pouch cells, winding for cylindric cells, and flat winding or stacking for prismatic cells (derived from Ref. [48]).

pouch cells for EVs [38, 39].

Cylindric cells use a hard case – also called can – that incorporates the spirally wound jelly roll. The can is typically made of stainless steel and has a thickness of about 0.17–0.25 mm [119–121]. Because of the standardized, robust design of cylindric cells including several safety features and affordable costs, they are produced in billions worldwide and used in many different applications such as power and garden tools and stationary energy storage systems [7, 122, 123]. While the majority of car manufacturers use prismatic or pouch cells, Tesla incorporates cylindric cells into their EVs [38, 39]. The 18650 format (18 mm diameter, 65 mm height) used to be the most popular format for cylindric cells, but is replaced by larger formats like the 21700 [123]. By changing the format from 18650 to 21700, the energy content per cell is enhanced by ≈50% [123] and in addition, manufacturing costs can be decreased [38, 39]. Reportedly, Tesla introduced the even larger 46800 cell format to further increase the energy density and power output [124]. However, with larger cell formats, inhomogeneities regarding temperature and current distribution within the cell increase and must be carefully considered [48, 109, 124].

Cell design Starting with the specific design of a single cell, there are certain guidelines to construct a high power or a high energy cell, or a cell that lies somewhere in between. Thereby, the electrode geometry plays a crucial role: The energy of a cell with a given format is defined by the share of active materials with regard to all the remaining passive components, so with a higher share of active materials, the energy content increases. This can be realized via thicker and less porous electrode coatings. However, with thicker and less porous electrode coatings, the power capability of the cell drastically decreases, mostly ascribed to lithium-ion transport limitations in the liquid electrolyte [125–128]. This major tradeoff between energy density and power capability has to be considered in the cell design process.

A comparison of two commercially available cylindric cells is depicted in Fig. 2.5, where the LG 18650-HB2 (NCM-532/graphite) and Samsung INR21700-48G (NCA/Si-C) represent a high power and a high energy cell, respectively [64]. Distinct differences between these two cells can be identified in the specifications: With 20C, the LG 18650-HB2 offers ten times the maximum continuous discharge rate in comparison to 2C for the Samsung INR21700-48G, but only half the energy density though. The factors of the cell design that influence these characteristics will be explained in the following.

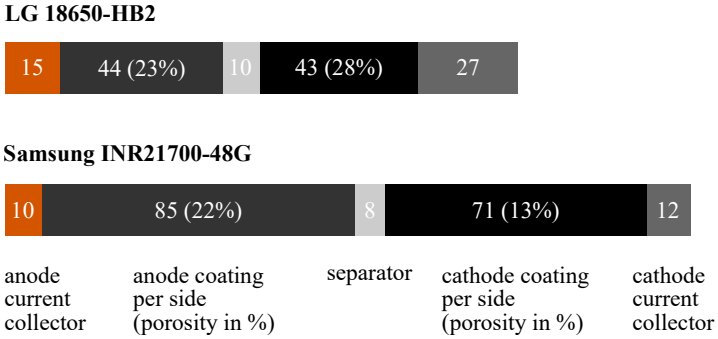

Specifications	HB2	48G
Capacity in Ah	1.5	4.8
Discharge rate (max.)	20C	2C
Energy density in Wh kg^{-1}	131	263
Power density in kW kg^{-1}	2.6	0.5

Figure 2.5: Comparison of two cylindric cells representing a high power (LG 18650-HB2) and a high energy design (Samsung INR21700-48G). Left: layer thicknesses in µm of a schematic electrode stack. The corresponding electrode porosities are calculated values. Right: rated capacity, maximum continuous discharge rate, energy density on the cell level, and power density on the cell level. Note that in this case, the power density was calculated based on the nominal average discharge voltage at a low current multiplied by the maximum continuous discharge current (data taken from Ref. [64]).

Further examples for cylindric high energy cells that are commercially available and offer an energy density on the cell level of about 260 Wh kg^{-1} are the LG INR18650-MJ1 and the Samsung INR21700-50E [7, 63]. Generally, such high energy cells either use a nickel-rich NCA (Samsung INR21700-48G, Samsung INR21700-50E) or a nickel-rich NCM (LG INR18650-MJ1) as cathode active material and a Si-C as anode active material [7, 63, 64]. The cathode porosities of high energy cells are often below 20%; the porosity of the Samsung INR21700-48G cathode was calculated to be only 13% [64]. The anode porosites of high energy cells however are higher than 20%, most likely to prevent detrimental lithium-plating during charging operations, which would compromise the cycle life of the cell. Sturm et al. [63] analyzed the LG INR18650-MJ1 cell and reported anode coating thicknesses of 87 µm with a porosity of 22% and cathode thicknesses of 66 µm with a porosity of 17%. On the other hand, the LG 18650-HB2 (NCM-532/graphite) with an energy density of ≈130 Wh kg^{-1} is rather considered a high power cell [64]. The coating thickness of both electrodes of the LG 18650-HB2 cell is much thinner (≈43–44 µm) and their porosities are reportedly higher (23–28%) [64]. Quinn et al. [123] investigated several cylindric cells and came to the conclusion that the energy density on the cell level is a function of the anode coating thickness. The cathode coating thickness is thereby defined via the balancing of both electrodes, i.e., the areal capacity ratio of negative/positive electrode, also called N/P ratio.

Besides the electrode geometry, the electrode composition can also be adapted for the desired purpose. A reduction of the share of binder and further additives results in an increased active material share and consequently a higher energy. However, the binder ensures mechanical stability over prolonged cycling, meaning a binder reduction may compromise the long-term stability [84]. A reduction of conductive additives reduces the rate capability, which is especially important for the design of cells for high power applications. Zheng et al. [84] investigated the physical and electrochemical properties of an NCA electrode with different shares of PVDF binder and AB as conductive additive and stated the following main findings: Too little binder results in a poor physical connection between the active material particles and in a decrease of the electronic conductivity and of the electrochemical performance of the electrode. On the other hand, too much binder results in a decreased ionic conductivity of the electrode, as the binder has ion-blocking properties. In addition, too much binder results in an increased electrode tortuosity, which in turn decreases the electrochemical performance [129, 130]. Based on their

experiments, they concluded that a composition with a PVDF/AB ratio of 5:3 would be optimal for their NCA electrode [84]. In the end, the exact proportions of each electrode material must be carefully considered, as their amount and interplay define the electrode characteristics.

The energy density on the cell level can also be increased via a reduction of the current collector thicknesses. High power cells use thicker current collectors (15–30 µm) than high energy cells (10–15 µm), to minimize the electric resistance and the corresponding ohmic losses during operation [64, 131]. The electric resistance of the current collectors and the resulting ohmic heating losses are especially important for cells with a high capacity and therefore large electrode areas [132]. Moreover, as the current collectors are made of metals, they have a huge impact on the thermal conductivity of the electrode stack, which is $\approx 0.9\,\mathrm{W\,m^{-1}\,K^{-1}}$ in the through-plane direction and $\approx 27\,\mathrm{W\,m^{-1}\,K^{-1}}$ in the in-plane direction [133]. The thermal performance of the cell should thus be included in the overall design process. For instance, tab cooling concepts take advantage of the high in-plane thermal conductivity and therefore benefit from thicker current collectors [131, 134, 135].

Besides the thickness of the current collectors, the corresponding tab design likewise influences the current density and temperature distribution along the electrodes, which is especially important for cells with large electrode areas [132, 136–139]. While high energy cells that are designed for low currents might get along with only one tab for each electrode, a higher number of tabs, wider tabs, or a better tab placement reduce local inhomogeneities arising from non-uniform current density and temperature distributions [63, 109, 131]. These inhomogeneities increase for thicker cells like the cylindric 26650 format [109], which is why the 46800 cell format proposed by Tesla relies on a continuous tab design – also called tabless – to gain more uniform current density distributions and to reduce temperature gradients within the core with the aid of an adequate cooling system [124].

Finally, thinner separators – and thereby less electrolyte – also increase the energy density on the cell level, which is why state-of-the-art separators for high energy LIBs are as thin as 7–10 µm [64]. However, there is a tradeoff between separator thickness and safety, as thinner separators may have an adverse effect on the mechanical strength and safety characteristics of the cell [104].

To summarize, the design of a cell is quite a complex process, with many tradeoffs between a high energy density and a high power density and most applications demand specific cell properties, which must be considered during the cell design process. Moreover, requirements on the thermal behavior and safety of the application likewise have an impact on the cell design and an optimization only towards high energy densities is not always reasonable.

Electrode structuring The energy content of a LIB can be boosted with thicker electrodes that have a low porosity, which simultaneously reduces the power capability [126, 127]. For higher loads, transport limitations, which are caused by lithium-ion concentration gradients in the liquid electrolyte, are a major contributor to the overall cell polarization and thereby define the power capability [127]. A modification of the electrode structure of both LIB anodes [140–143] and cathodes [144–149] can help to counteract these limitations by providing enhanced transport pathways for the lithium-ions. There are various fabrication processes to influence the structure of the electrode, e.g., co-extrusion [144, 145, 147], freeze casting [148], magnetic particle alignment [150], and laser-structuring [141, 143, 146, 149].

Co-extrusion techniques are applied during the coating process, where an additional material is used besides the electrode slurry to shape the desired structures. This additional material is then removed during a subsequent heating process, as for instance described by Cobb and Blanco [145] for co-extruded

LCO cathodes. Delattre et al. [148] specified a similar structuring approach, the freeze casting of NCA cathodes: this shaping technique uses a water-based particle suspension that undergoes a directional freezing of ice crystals, which generate an anisotropic electrode structure after removing the ice via sublimation.

The active material particle shape is a crucial factor for the electrode tortuosity. Ebner et al. [151] investigated different active materials with regard to their distinct particle shape and the influence on the resulting tortuosity anisotropy. For their study, a spherical NCM-111, a triaxial LCO, and a platelet-shaped graphite were chosen. The spherical NCM particles caused comparatively low isotropic tortuosities. The non-spherical LCO particles resulted in higher anisotropic tortuosities with lower tortuosity values in the in-plane direction and higher values in the through-plane direction of the electrode. This tortuosity anisotropy was even more pronounced for the flake-like graphite particles. During electrode coating and calendering, the particles tend to align parallel to the current collector, which results in highly tortuous pathways in the through-plane direction of the electrode [106, 151, 152].

To overcome the undesired alignment of graphite particles during electrode production, Billaud et al. [150] proposed a magnetic alignment technique: by coating the non-magnetic graphite particles with superparamagnetic iron oxide nanoparticles, the graphite particles can be vertically aligned on the current collectors with an external magnetic field during electrode fabrication. With this technique, the through-plane tortuosity of the graphite electrodes was decreased by a factor of four [150].

Laser-structuring methods apply pulsed laser irradiation to ablate the electrode composite and create macro channels or pores in cathodes [146, 149] or anodes [76, 80, 153]. Laser processing techniques are already successfully implemented in battery production lines, as seen in the laser cutting of electrodes or laser welding of tabs and current collectors, and are therefore a promising technology for electrode structure modifications [154]. The influence of laser-structured graphite anodes on the performance of LIBs is described in detail in Chapter 4.

2.1.3 Batteries on System Level

In the previous section, a general overview of electrode and cell compositions for LIBs was given. While some LIBs are not built for a particular application and can be purchased separately on the market, such as various 18650 or 21700 cylindric cells, others are specifically designed for their later integration into an application, e.g., prismatic cells for EVs. The use case of the application then defines the characteristics of the LIB: Is a high power cell needed that can sustain high currents for a short period of time, or rather a high energy cell that can deliver a low current for a long period of time? Furthermore, most applications use multiple single cells that are connected in series or in parallel and integrated into modules. These modules in turn can be integrated into even larger units, like battery packs or racks, and are usually combined with a thermal management system to keep their temperatures within a safe operational range. A schematic illustration of an integration of prismatic, pouch, and cylindric cells into modules and packs is depicted in Fig. 2.6.

Energy density considerations There are some smaller applications that only use one single cell as their energy source, e.g., mobile phones and tablets. Larger applications however, such as stationary energy storage systems and EVs, demand a higher power or energy, which cannot be delivered by a single cell. Therefore, multiple single cells are integrated into larger units, namely modules and packs.

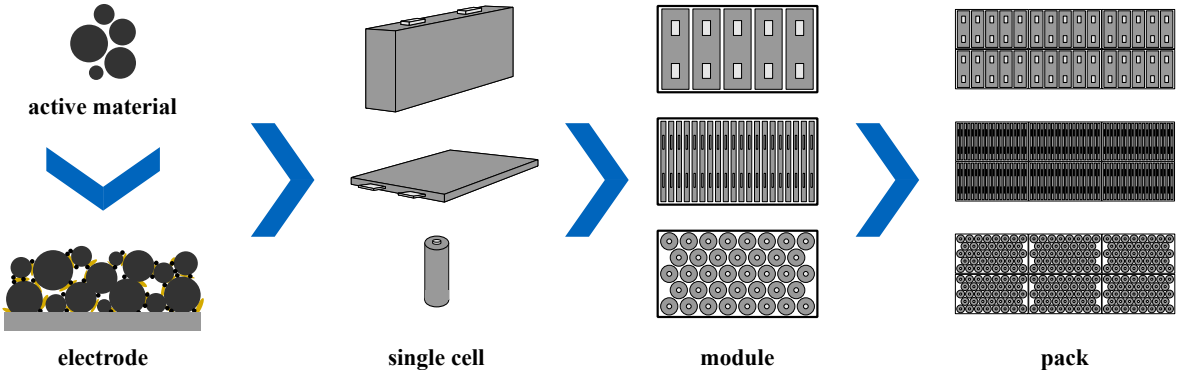

Figure 2.6: Exemplary overview of the process chain, from the active material and electrode level to the integration of single prismatic, pouch, and cylindric cells into standardized modules and packs.

With each step of integrating a smaller unit into a larger unit, passive components are added, and both the gravimetric and volumetric energy densities at the higher integration level are further reduced [31, 32, 112].

On the material level, the energy density is solely defined by the active material, i.e., the specific capacity and potential, as displayed in Fig. 2.2. For a state-of-the-art nickel-rich NCM or NCA, by assuming a specific capacity of 200 $\mathrm{mAh\,g^{-1}}$ at a potential of 3.75 V vs. $\mathrm{Li/Li^+}$, the energy density on the material level is around 750 $\mathrm{Wh\,kg^{-1}}$ [32]. For this calculation of the energy density, $\mathrm{Li/Li^+}$ is used as a reference, but the additional weight of the counter/reference electrode is not considered. Higher energy densities on the material level can be achieved by enhancing the specific capacity and/or the potential of active materials, which is often the focus of current research [31, 35].

During electrode production, inactive materials such as the current collectors, the binder, and conductive additives are added, which reduces the energy density on the electrode level [122]. A reduction of the share of these passive components corresponds to the design of a high energy cell, which was explained in the previous section. On the cell level, the energy density is drastically reduced, as a counter electrode and further inactive components are necessary, e.g., the separator, the electrolyte, and the current collector tabs, while other factors such as electrode overhang areas, safety devices, and the housing must also be considered [32, 122]. Furthermore, the electrodes are stacked or wound to fit into the desired cell format, compare Fig. 2.4, which leaves voids as the inner volume cannot be fully utilized. Energy densities of the latest commercially available cylindric cells using a nickel-rich CAM reach 270 $\mathrm{Wh\,kg^{-1}}$ (800 $\mathrm{Wh\,l^{-1}}$) on the cell level [7–9], which is about one third of the gravimetric energy density of 750 $\mathrm{Wh\,kg^{-1}}$ for the CAM on the material level.

On the module level, single cells are connected in series and parallel in order to increase the voltage and the capacity of the module, respectively. Thereby, the cell format plays a decisive role for packing single cells into a module: prismatic and pouch cells achieve a higher packing efficiency than cylindric cells [122], as can be seen in Fig. 2.6. An inefficient packing as well as passive components such as connectors between the single cells and the housing of the module result in a further reduction of the energy density. This also applies for an integration of single modules into battery packs, as additional packing material, wiring, and the cooling system have to be incorporated [32, 112]. On the pack level, energy densities of 90–180 $\mathrm{Wh\,kg^{-1}}$ (250–400 $\mathrm{Wh\,l^{-1}}$) are currently achieved [31].

While the voltage of a single module is usually kept below 60 V because of safety reasons during the production and assembly process, battery packs for EVs have a typical voltage between 200–400 V [32, 122, 155]. Some EVs like the Porsche Taycan even use 800 V systems in order to increase the power for both discharge and charge operations [156–158]. The energy content of battery packs of smaller EVs (e.g., BMW i3, Mitsubishi i-MIEV, Nissan Leaf) is somewhere between 16–35 kWh resulting in driving ranges of around 100–200 km, while larger EVs such as the Tesla Model S and Model 3 use battery packs with 60–100 kWh to achieve driving ranges of 300–600 km [2, 39]. In order to enhance the energy density of the final battery pack, optimizations on each level from the active material up to the battery pack must be taken into consideration.

Thermal management systems A thermal management system is usually incorporated into applications that use multiple LIB modules or a LIB pack to control and adjust the temperature of the single cells [159]. With an active cooling system, safety-critical cell temperatures above 80 °C can be avoided, as they can lead to hazardous states and even a thermal runaway in the worst case [160]. Reportedly, Nissan dispensed with an active cooling system in some EV Leaf models, which caused overheating problems during driving and charging operations especially at higher outside temperatures. As a consequence, the available power during driving or charging had to be drastically reduced [131, 161].

Besides the safety aspects, LIBs are very temperature-sensitive with regard to their performance and aging characteristics [132, 159, 162]. At a higher operating temperature, the transport properties and the reaction kinetics are enhanced, resulting in a decreased internal cell resistance and an improved charge and discharge performance [163–166]. At low temperatures on the contrary, the internal resistances increase and the intercalation kinetics are slowed, which is why charging with a high current should be avoided, as detrimental lithium-plating on the surface of graphite anodes is likely to occur [167–169]. Lithium-plating is especially critical for charging at a low temperature with high currents to a high state of charge (SOC), for example during fast charging operations of high energy density LIBs in an EV [170, 171]. To avoid poor performance including lithium-plating at sub-zero temperatures, the thermal management system of an EV should be able to heat the LIBs to normal operation temperatures [172]. Yang et al. [173] even proposed to heat the cells to 60 °C during fast charging operations to enhance the kinetics and the transport and thereby prevent lithium-plating.

Although the performance of LIBs is enhanced at higher operating temperatures, this also increases deleterious side reactions, which is why during normal charge and discharge operations, the temperature of most LIBs should be kept around room temperature to reduce the cycle aging and prolong the lifetime of the battery [174, 175]. The calendar aging, however, is kept minimal if LIBs are stored at low temperatures and at medium to low SOCs [176, 177]. Optimized thermal management strategies can thus prolong the battery lifetime and reduce the respective life cycle costs [178].

For all the stated reasons, a thermal management system including an active cooling is often indispensable to guarantee a safe operation of LIBs under different operating conditions and to adjust the temperature via cooling or heating if necessary. There are different cooling approaches with advantages and disadvantages that are in general specifically designed for each application. In the following, the three cooling strategies convective cooling, tab cooling, and base plate cooling will be explained, and an overview is displayed in Fig. 2.7.

A convective heat transfer can be differentiated into natural or free convection and forced convection. In a forced convective cooling system, e.g., by using a fan or a pump, a coolant directly flows over

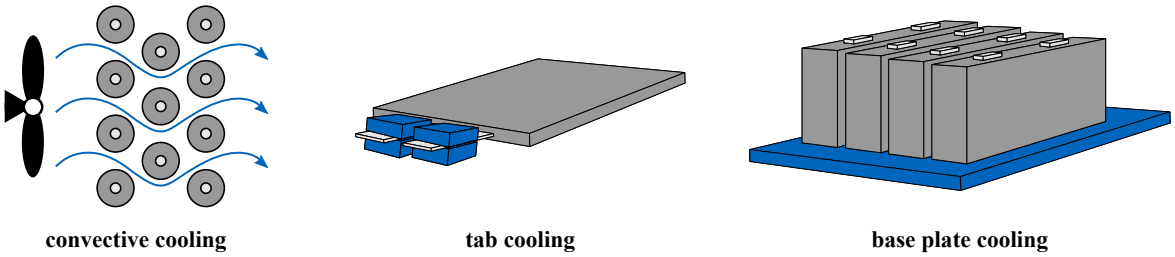

Figure 2.7: Overview of different cooling strategies: convective cooling with air of cylindric cells, tab cooling of a pouch cell, and base plate cooling of prismatic cells.

the surface of the cell in order to dissipate the heat, as indicated in Fig. 2.7. There are various coolants such as air, water, glycol, and oil [179, 180]. Feng et al. [181] classified the convective heat transfer coefficients with 5–25 $\mathrm{W\,m^{-2}\,K^{-1}}$ for a natural convection in air, meaning that there is no active cooling and the cell is only passively cooled, 15–250 $\mathrm{W\,m^{-2}\,K^{-1}}$ for a forced convection in air, and 300–1000 $\mathrm{W\,m^{-2}\,K^{-1}}$ for water surrounding the cell. The heat transfer coefficients show, that convective air cooling has its limits with regard to the maximum heat dissipation, and higher values can be achieved with liquids. On the other hand, air cooling systems have a simple design and low costs, while a liquid cooling is rather complex to implement in battery systems, as leakages and an electrical contact to the battery tabs must be prevented [180, 182].

Passive and active air cooling is often used for stationary energy storage systems [183], and can also be used for EVs (including HEVs and PHEVs), though, it is inefficient for high charge/discharge rates and causes temperature inhomogeneities within the cells [179, 182, 184]. Hunt et al. [185] experimentally compared the effects of surface cooling and tab cooling on the performance and degradation of lithium-ion pouch cells and found that the temperature inhomogeneities of the surface cooled cells lead to an accelerated aging, whereas tab cooling could extend the lifetime of a battery pack by as much as three times.

As depicted in Fig. 2.7, tab cooling takes advantage of the high thermal conductivity of the metallic current collectors and uses the cell tabs as heat sinks. Copper and aluminum current collectors have a thermal conductivity of around 398 $\mathrm{W\,m^{-1}\,K^{-1}}$ and 238 $\mathrm{W\,m^{-1}\,K^{-1}}$, respectively, whereas the thermal conductivity of the remaining cell components (separator, anode coating, cathode coating, electrolyte) is comparatively low and within the range 0.3–1.6 $\mathrm{W\,m^{-1}\,K^{-1}}$ [48, 186]. By utilizing the current collectors for the heat transport, the thermal gradients within the cell are reduced and the local current densities and SOCs are more evenly distributed [186]. This also implicates that thicker tabs and current collectors affect the tab cooling efficiency and that the layout of the thermal management system should go hand in hand with the cell design. Hales et al. [135] stated, that increasing the tab thickness of pouch cells by 34% results in an enhancement of the tab cooling performance of 20%. However, tab cooling has its limitations and strongly depends upon the cell design parameters; experimental studies confirmed that tab cooling of large-format pouch cells faces problems to remove sufficient heat, and surface cooled cells showed a superior aging behavior and thus a longer cycle life [187].

In the right illustration in Fig. 2.7, a schematic base plate cooling of four prismatic cells is shown, where a cooling plate is attached to the bottom of the cells. The temperature of the cooling plate can be adjusted via the coolant that flows through channels within the plate [188, 189]. This kind of cooling is often used for automotive battery modules and packs as in the Porsche Taycan [158]. The cooling

plate must not necessarily be attached to the bottom of the cells. There are other concepts that use thinner cooling plates mounted between the large lateral areas of prismatic and pouch cells [162, 180, 190–192]. Such cooling concepts have a higher complexity, but can have a better cooling performance and lower the temperature gradients within the cells [192]. For a liquid cooling of modules and battery packs consisting of cylindric cells, there are different concepts based on cooling plates and channels attached on the top and bottom, but also in between the cells [193, 194]. The battery packs of Tesla's EV models consist of several thousand of cylindric cells and cooling tubes are integrated in between these cells [195].

A passive cooling system of LIBs can also be realized via phase change materials (PCMs) surrounding the cells [196–198]. PCMs take advantage of the latent heat of phase change in order to keep the temperature of LIBs in an optimum range and to obtain a homogeneous temperature distribution [192, 198]. While PCMs have the capability of absorbing a large amount of heat at the same temperature in a phase change process with little or no energy consumption, there remain challenges regarding a continuous heat load after completion of the phase change process, and also regarding the low thermal conductivity of the material, leakages, volume changes, as well as inhomogeneities in repeated melting and solidifying processes [162]. Whereas some passive cooling systems rely exclusively on PCMs, there are concepts that utilize a combination of PCMs and an active cooling system [199, 200].

2.2 Modeling and Simulation of Lithium-Ion Cells

Modeling is an essential tool to better understand, predict, and optimize LIBs [201]. With the width of applications that rely on LIBs, including a variety of application-specific use-cases, the diversity of models is extensive. An overview of battery models that are relevant for the scope of this thesis is given in the following section, with a focus on the electrochemical pseudo two-dimensional model and the 3D thermal model, as these were also used in the publications specified in Chapter 3 and 4.

2.2.1 Review of Empirical and Mechanistic Modeling Approaches

There is a multitude of different models for LIBs, some of which are displayed in Fig. 2.8. Depending on the intended use of the model, there is always a tradeoff between model complexity and computational speed, ranging from mechanistic electrochemical 3D models to empirical equivalent circuit models (ECMs) [201–205].

Electrochemical 3D models usually represent a small section of the battery because of the high computational demand [206–209]. Fully resolved 3D models rely on a reconstruction of their highly complex 3D electrode geometry, e.g., obtained with X-ray tomography [210–213] or a focused ion beam (FIB) combined with SEM [212, 214–216], and an elaborate post-processing of the recorded raw data. Mass transport phenomena in the solid phase of the electrodes and the liquid electrolyte as well as kinetics at the electrode/electrolyte interfaces are solved. The high complexity comes with a low computational speed, and the parameterization effort of 3D models also has to be considered. With a higher number of parameters, which can either be measured or taken from literature, errors and discrepancies of the modeling results are more likely.

A widely used electrochemical model for LIBs that does not rely on reconstructed 3D data is the p2D model, which was published in the early 1990s by Doyle, Fuller, and Newman including a code

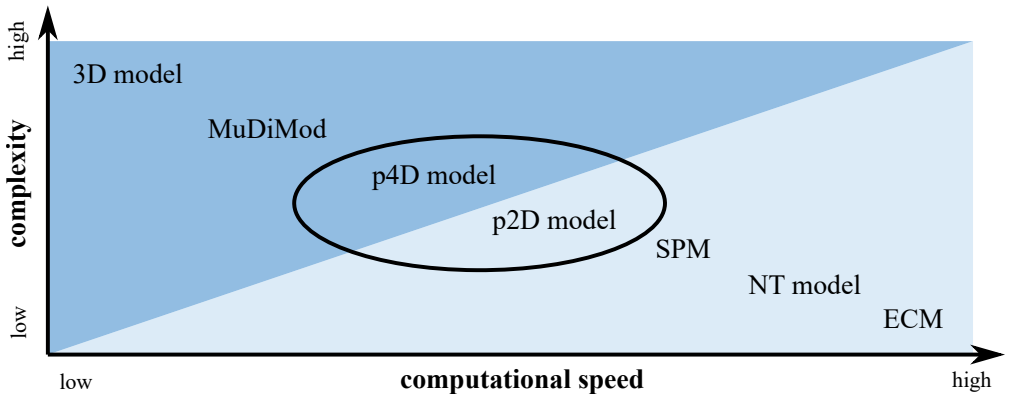

Figure 2.8: Classification of selected LIB models with regard to their complexity and computational speed. The encircled p2D and p4D models were used within the scope of this thesis.

framework written in Fortran [217–219]. The fundamentals of the theory behind the p2D model even date back to the 1960s, when Newman and Tobias published a set of equations to describe current distributions in porous electrodes [220]. The p2D model generally consists of a 1D representation of the electrode stack and a pseudo dimension for the active material particles. It is based on a system of equations that describes mass and charge transport phenomena in the active material particles of both intercalation electrodes and the liquid electrolyte as well as kinetics at the particle/electrolyte interfaces. The particle domain of p2D models is not fully resolved, making its computational speed much faster in comparison to 3D models. A detailed description of the p2D model including the governing equations is given in Chapter 2.2.2, and a specific use case is given in Chapter 4.2 [76].

In a standard p2D model, the electrode stack of a cell is described only in one geometrical dimension. However, especially with larger cells and higher loads, spatial inhomogeneities, e.g., regarding the current density distribution along the electrodes influenced by the tab design and thermal imbalances, cannot be neglected [137–139, 221]. These spatial inhomogeneities can be considered in adapted multidimensional models (MuDiMods), in which 2D current collectors are implemented and multiple p2D models are connected in parallel in between the two current collectors [108, 109, 137, 139, 222, 223].

The pseudo four-dimensional model (p4D) used in this work [80] is an application-specific adaption of the p2D model and described in Chapter 4.1. Because of an altered electrode geometry, the electrode and separator domains are represented by a homogenized 3D geometry with an additional pseudo dimension for the active material particles.

Single particle models (SPMs) homogenize and simplify electrodes as one single spherical intercalation particle assuming a uniform current distribution along the thickness of the electrode [224–226]. Spatial inhomogeneities within an electrode are completely neglected. The SPM describes mass transport within the solid particle and reaction kinetics on its surface. Mass transport in the liquid electrolyte is only considered in some adapted SPMs that are better suited for higher charge/discharge rates [227, 228].

The Newman-Tiedemann model (NT) – named after John Newman and William Tiedemann – is a semi-empirical model, which considers potential and current distributions in large-format cells with planar electrodes and was originally utilized to find an optimal placement for reference electrodes with regard to the tab locations [229]. This modeling approach is based on a linearized cell polarization and

an electrochemically representative resistance between the current collector foils, which describes the electrochemical behavior of the electrode stack. Extended NT models can be used, e.g., to describe temperature inhomogeneities [221] or to optimize the current collector and tab design [230] of large-format pouch cells.

ECMs are empirical models that describe the cell behavior with the aid of electrical circuit elements. Because of their simplicity and very fast computational speed, ECMs are commonly used for a multitude of applications [231–235]. A very simple form of an ECM consists of a serial connection of an SOC-dependent voltage source and an internal ohmic resistance. Multiple resistor-capacitor elements can be connected in series to represent the dynamic cell behavior with different time constants [236].

2.2.2 Model Structure of the Electrochemical p2D Model

The p2D model is based on the theory of porous electrodes and concentrated solutions, allowing an adequate representation of the cell via its main reaction direction perpendicular to the electrode layers [217–219]. This 1D model includes a pseudo representation of the active material particle domain and is therefore called p2D. The active material particles are considered as ideal spherical particles of the same size. The solving process of the p2D model incorporates a differential algebraic equation system, where the local concentrations c_l and c_s as well as the local potentials ϕ_l and ϕ_s in the liquid and solid phase are the relevant variables in the underlying equations. A schematic representation of the model is displayed in Fig. 2.9.

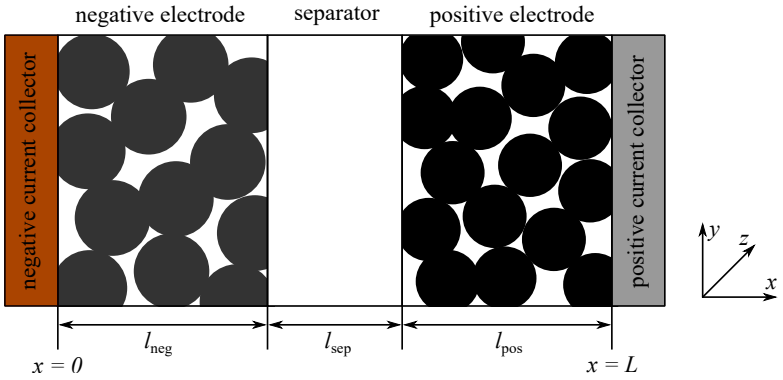

Figure 2.9: Schematic representation of the p2D model with its three domains negative electrode, separator, and positive electrode (derived from Ref. [218]).

The p2D model only represents the x-direction perpendicular to the current collectors and assumes that gradients along the y- and z-direction are negligible. This assumption is valid for a homogeneous cell setup, e.g., for small-scale laboratory cells [202]. The pseudo dimension is represented via the r-direction along the radius r_p of the active material particles. At each mesh point within the electrode domains, a radial diffusion within a single particle is calculated. This solid diffusion equation is solved for each particle independently and an equalization of solid phase concentrations between two particles is only possible via the liquid phase. In the basic p2D model for a cell with two intercalation electrodes, there are three domains in the model, the negative electrode, the separator, and the positive electrode with their respective thicknesses l_neg, l_sep, and l_pos adding up to the total thickness L:

$$L = l_\mathrm{neg} + l_\mathrm{sep} + l_\mathrm{pos} \tag{2.1}$$

The current collectors on both sides are typically neglected due to the their high electrical conductivity and the resulting low electrical potential drops. Each representative volume element (RVE) in the model can be split into its volume fractions for the solid active material ε_s, the porosity filled with liquid electrolyte ε_l, and non-active materials ε_na as described in Chapter 2.1.2:

$$\varepsilon_\mathrm{s} + \varepsilon_\mathrm{l} + \varepsilon_\mathrm{na} = 1 \tag{2.2}$$

The separator domain is only defined via its porosity ε_l and the non-active share, as no active material is incorporated. The pores of both electrodes and the separator are filled with liquid electrolyte, which is non-conducting for electrons but enables a mass and charge transport of lithium-ions between the electrodes. The liquid electrolyte consists of a solvent, which can be a mixture of various components, and a solute. In most cases a binary electrolyte is considered, i.e., the conducting salt dissociates into one sort of anions and one sort of cations, for example:

$$\mathrm{LiPF_6} \longrightarrow \mathrm{Li^+} + \mathrm{PF_6}^- \tag{2.3}$$

A concentration gradient ∇c_l of any species – charged or neutral – in the electrolyte results in a diffusive flux:

$$N_\mathrm{l,diff} = -D_\mathrm{l} \nabla c_\mathrm{l} \tag{2.4}$$

Particles diffuse from areas with high concentration to areas with lower concentration and the diffusion coefficient D_l describes how fast this balancing process takes place. In order to account for a transport in porous media, the diffusion coefficient D_l is replaced by the effective diffusion coefficient $D_\mathrm{l,eff}$ according to Equation 2.27. In general, the ∇ operator (transpose) is defined as:

$$\nabla = \left(\frac{\partial}{\partial x}, \frac{\partial}{\partial y}, \frac{\partial}{\partial z} \right)^\mathrm{T} \tag{2.5}$$

In the p2D model, when only gradients in the x-direction are considered, the ∇ operator is defined as:

$$\nabla = \frac{\partial}{\partial x} \tag{2.6}$$

If a charged species – in this case lithium-ions – is brought into an electric field, a migrative flux needs to be considered:

$$N_\mathrm{l,mig} = \frac{i_\mathrm{l} t_+^0}{\mathrm{F}} \tag{2.7}$$

, where i_l is the current density, t_+^0 the transference number of lithium-ions within the electrolyte, and F the Faraday constant. The current density in the liquid phase i_l can be expressed as:

$$i_\mathrm{l} = -\kappa \nabla \phi_\mathrm{l} + \frac{2\kappa \mathrm{R} T}{\mathrm{F}} \left(1 + \frac{\partial \ln f_\pm}{\partial \ln c_\mathrm{l}} \right) (1 - t_+^0) \nabla \ln c_\mathrm{l} \tag{2.8}$$

, where κ is the electrolyte conductivity, R the universal gas constant, T the temperature, and $f_\pm$ the mean activity coefficient. Analogous to the correction of the diffusion coefficient, the electrolyte conductivity κ is replaced by the effective electrolyte conductivity κ_eff according to Equation 2.28 to account for a transport in porous media. The first term of Equation 2.8 is based on Ohm's law,

the second term is a correction term that has to be considered in concentrated solutions because of interactions between anions, cations, and the solvent. The total lithium-ion flux N_l in the electrolyte is a superposition of the diffusive and the migrative flux:

$$N_\mathrm{l} = N_\mathrm{l,diff} + N_\mathrm{l,mig} \tag{2.9}$$

The p2D model meets a mass and charge conservation, meaning that the amount of particles in the liquid electrolyte and intercalated in the active material has to stay in balance and that the charge transported via electrons and ions is consistent. In the liquid electrolyte, the mass balance is calculated with:

$$\varepsilon_\mathrm{l}\frac{\partial c_\mathrm{l}}{\partial t} = -\nabla N_\mathrm{l} + \frac{3\varepsilon_\mathrm{s}}{r_\mathrm{p}} j_\mathrm{n} \tag{2.10}$$

The left side of the equation describes the change of lithium-ion concentration in a RVE over time t and is applied in the liquid electrolyte in the pores of the electrodes or the separator and therefore scaled with the porosity ε_l. The right side is the sum of the change in lithium-ion flux and the reaction term. In the separator domain, there is no active material and no reaction takes place, therefore the reaction term is left out in the mass balance. In the electrodes, the reaction term describes the production or consumption of lithium-ions on the surface of the active material particles with a radius r_p. Because of the 1D model representation, the fraction $3\varepsilon_\mathrm{s}/r_\mathrm{p}$ is necessary to reference the pore wall flux density j_n from the spherical particle surface to the spherical particle volume. The pore wall flux density j_n is defined via the Butler-Volmer equation:

$$j_\mathrm{n} = \frac{i_0}{\mathrm{F}}\left(e^{\frac{\alpha_\mathrm{a}\mathrm{F}}{\mathrm{R}T}\eta} - e^{-\frac{\alpha_\mathrm{c}\mathrm{F}}{\mathrm{R}T}\eta}\right) \tag{2.11}$$

with the charge transfer coefficients $\alpha_\mathrm{a/c}$, the exchange current density i_0

$$i_0 = \mathrm{F} k_\mathrm{c}^{\alpha_\mathrm{a}} k_\mathrm{a}^{\alpha_\mathrm{c}} (c_\mathrm{s,max} - c_\mathrm{s})^{\alpha_\mathrm{a}} c_\mathrm{s}^{\alpha_\mathrm{c}} \left(\frac{c_\mathrm{l}}{c_\mathrm{l,ref}}\right)^{\alpha_\mathrm{a}} \tag{2.12}$$

and the overpotential η

$$\eta = \phi_\mathrm{s} - \phi_\mathrm{l} - E_\mathrm{eq} \tag{2.13}$$

The exchange current density i_0 is calculated with the anodic and cathodic reaction rate constants $k_\mathrm{a/c}$, and the solid and liquid lithium-ion concentrations on the particle surface. The concentration $c_\mathrm{s,max}$ describes the maximum amount of lithium-ions that can be intercalated into the active material. The symmetry of the reaction that is generally assumed, sets the charge transfer coefficients to $\alpha_\mathrm{a} = \alpha_\mathrm{c} = 0.5$. The reference lithium-ion concentration $c_\mathrm{l,ref}$ is usually set to $1\,\mathrm{mol\,m^{-3}}$ to get a consistent unit for the expression. The overpotential η – sometimes also referred to as surface overpotential [217] – represents the potential drop on the particle surface based on the thermodynamic equilibrium potential E_eq of the active material.

In the solid phase of the active material, the mass balance expressed in spherical coordinates is:

$$\frac{\partial c_\mathrm{s}}{\partial t} = -\nabla N_\mathrm{s} = D_\mathrm{s}\left(\frac{\partial^2 c_\mathrm{s}}{\partial r^2} + \frac{2}{r}\frac{\partial c_\mathrm{s}}{\partial r}\right) \tag{2.14}$$

, where the flux density in the solid phase N_s represents a mass transport via diffusion with the

diffusion coefficient in the active material D_s. The spherical particles of the solid phase are described via their radius r_p and the corresponding pseudo dimension r with radially symmetric lithium-ion concentrations. On the particle surface at $r = r_\mathrm{p}$, the mass transport stays consistent with the pore wall flux density j_n that is given by the Butler-Volmer equation and describes the intercalation or deintercalation of lithium-ions.

$$-D_\mathrm{s} \frac{\partial c_\mathrm{s}}{\partial r}\bigg|_{r=r_\mathrm{p}} = j_\mathrm{n} \tag{2.15}$$

The concentrations within the particles are considered radially symmetrical:

$$\frac{\partial c_\mathrm{s}}{\partial r}\bigg|_{r=0} = 0 \tag{2.16}$$

The current density in the solid phase i_s is defined via Ohm's law and the solid phase conductivity σ:

$$i_\mathrm{s} = -\sigma \nabla \phi_\mathrm{s} \tag{2.17}$$

The applied current density i_app is the sum of the solid phase current density i_s and the liquid phase current density i_l:

$$i_\mathrm{app} = i_\mathrm{s} + i_\mathrm{l} \tag{2.18}$$

In order to maintain a conservation of charge, a change in i_s effects a change in i_l:

$$\nabla i_\mathrm{s} = -\nabla i_\mathrm{l} \tag{2.19}$$

In the separator domain, there is no active material and thus no reaction and the liquid phase current density i_l has to stay constant:

$$\nabla i_\mathrm{l} = 0 \tag{2.20}$$

In addition to the boundary conditions regarding the solid phase lithium-ion concentration in the particle's r-dimension, there are further boundary conditions for the concentrations and potentials at the domain boundaries in the x-direction. Lithium-ions cannot leave the system, therefore, at its very left ($x = 0$) and right boundary ($x = L$), the lithium-ion concentration gradient ∇c_l and the resulting flux density N_l must be zero:

$$\nabla c_\mathrm{l}|_{x=0 \ \& \ x=L} = 0 \tag{2.21}$$

At the same boundaries, the potential gradient $\nabla \phi_\mathrm{l}$ and the resulting liquid phase current density i_l must be zero:

$$\nabla \phi_\mathrm{l}|_{x=0 \ \& \ x=L} = 0 \tag{2.22}$$

The solid phase potential gradient $\nabla \phi_\mathrm{s}$ at the boundaries is defined via the applied current density i_app (with $i_\mathrm{l} = 0$) and the electronic conductivity σ:

$$\nabla \phi_\mathrm{s}|_{x=0 \ \& \ x=L} = -\frac{i_\mathrm{app}}{\sigma} \tag{2.23}$$

At the boundaries of the separator domain, there is only an ionic current density as the separator is electronically insulating:

$$\nabla\phi_\mathrm{s}|_{x=l_\mathrm{neg}\ \&\ x=l_\mathrm{neg}+l_\mathrm{sep}} = 0 \tag{2.24}$$

The solid phase potential ϕ_s at the left boundary is typically set to zero:

$$\phi_\mathrm{s}|_{x=0} = 0 \tag{2.25}$$

When particles move through porous electrodes and separators they must take detours and their transport path length is prolonged. To adequately incorporate prolonged path lengths in 1D models, a correction factor for the electrolyte properties D_l and κ is introduced. Prolonged transport path lengths can be described by the tortuosity τ, which correlates the effective path length l_eff to the direct path length l_dir [106]:

$$\tau = \frac{l_\mathrm{eff}}{l_\mathrm{dir}} \tag{2.26}$$

The effective path length in a porous structure depends on its porosity ε_l. A decrease in electrode porosity leads to an increase of the effective path length and the respective tortuosity. Many electrochemical models use the Bruggeman exponent $\alpha_\mathrm{Brugg} = 1.5$ for a correction of the electrolyte properties [237–240]. However, the Bruggeman exponent of 1.5 was originally calculated for materials with ideal spherical particles of identical size [241] and therefore just gives a lower limit for the resulting tortuosity. As an example, NCM particles are spherical and thus their tortuosity τ is very close to the Bruggeman correction, but natural graphite is platelet-shaped and shows an anisotropic tortuosity that can be much higher than the Bruggeman correlation [151]. Furthermore, most active materials do not consist of particles of exactly the same size and there is a particle size distribution (PSD), which influences the alignment of the particles and thereby the tortuosity and the overall cell performance [242–246]. A transport parameter correction is not only needed for the porous electrodes, but also for the porous separators, most of which have higher tortuosity values than the ones calculated with the ideal Bruggeman correction [106, 247]. For all these reasons, a better way to express the correction of the electrolyte properties is directly via the porosity ε_l and tortuosity τ of electrodes and separators, as these parameters can be experimentally determined [106, 129, 151]:

$$D_\mathrm{l,eff} = \varepsilon_\mathrm{l}^{\alpha_\mathrm{Brugg}} D_\mathrm{l} = \frac{\varepsilon_\mathrm{l}}{\tau} D_\mathrm{l} = \frac{D_\mathrm{l}}{N_\mathrm{M}} \tag{2.27}$$

$$\kappa_\mathrm{eff} = \varepsilon_\mathrm{l}^{\alpha_\mathrm{Brugg}} \kappa = \frac{\varepsilon_\mathrm{l}}{\tau} \kappa = \frac{\kappa}{N_\mathrm{M}} \tag{2.28}$$

The ratio of τ and ε_l is also defined as the MacMullin number N_M [248]:

$$N_\mathrm{M} = \frac{\tau}{\varepsilon_\mathrm{l}} \tag{2.29}$$

2.2.3 Modeling of Structured Electrodes

The modeling approaches that were used in this thesis to describe and analyze LIBs with structured electrodes are based on the set of equations as specified in the preceding Chapter 2.2.2.

In order to investigate the gradients arising from structured electrodes not only in the x-direction perpendicular to the cell layers, but also in the in-plane y- and z-directions, a p4D model including a representative electrode structure was developed [76]. This p4D model, which is described in detail in Chapter 4.1, consists of three main domains: anode, separator, and cathode. As the graphite anodes were laser-structured, the geometry of the anode was complemented by a domain for the 3D hole structure. While the anode domain incorporates the solid and liquid volume fractions $\varepsilon_{\mathrm{s,neg}}$ and $\varepsilon_{\mathrm{l,neg}}$, the hole structure domain is solely filled with liquid electrolyte, hence $\varepsilon_{\mathrm{l,hole}} = 1$. Furthermore, an anisotropic tortuosity ($\tau_{\mathrm{x}} = 8$, $\tau_{\mathrm{y}} = \tau_{\mathrm{z}} = 2.5$) that is typical for flake-like graphite particles was implemented in the remaining anode domain [151]. The geometries of the separator and the cathode were not altered, and both domains were parameterized with an isotropic tortuosity.

In a second modeling approach, as described in Chapter 4.2, a standard p2D model was adapted to adequately represent the performance changes of LIBs comprised of structured electrodes [80]. Within a p2D model, the structured electrodes cannot be directly implemented via the electrode geometry. However, the structuring process reduces the overall through-plane tortuosity of the electrode. So a tortuosity reduction of the structured electrode results in an improved rate capability of the representative lithium-ion cell. In Fig. 2.10, the simulation results of the discharge rate capability enhancements by decreasing the anode tortuosity τ_{neg} are shown. Both the anode and the cathode of the simulated cell had a thickness of 116 µm and a porosity of 35% [80]. A reduction of the anode tortuosity from 8.5 down to 3.5, e.g., by aligning the graphite particles, would increase the available capacity at a discharge rate of 2.5C by more than 30%. For comparison, Billaud et al. [150] were able to reduce the through-plane tortuosity of their electrodes with flake-like graphite particles by magnetic alignment from 14 down to 3.8.

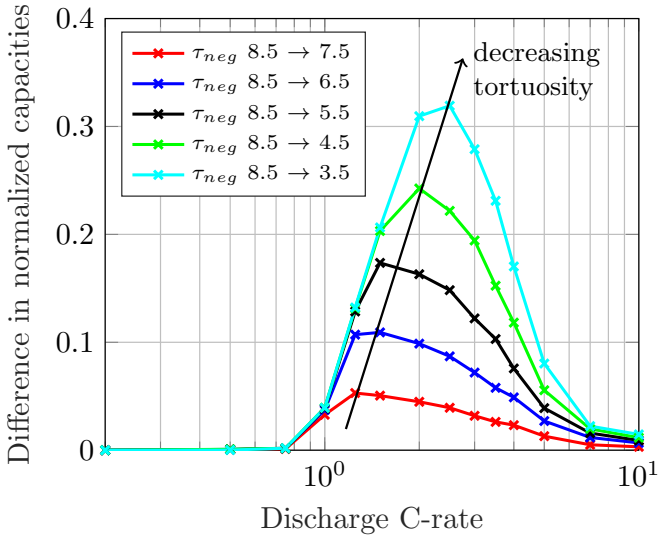

Figure 2.10: Simulated difference in normalized discharge rate capability of lithium-ion cells with decreasing anode tortuosity (taken from Ref. [80]).

2.2.4 Model Structure of the 3D Thermal Model

The temperature has a significant impact on the performance and lifetime of LIBs, and with the aid of thermal models, various cooling strategies for LIBs can be analyzed and optimized. There are thermal models of the cell itself, which are often coupled with electrochemical models [109, 114, 137, 221, 222, 249–252], but also thermal models that describe the whole battery pack including the corresponding cooling system [179, 182, 189, 193].

In general, there are three underlying heat transport mechanisms that are implemented in thermal models: heat conduction, convection, and radiation [253]. The conductive heat flux density q_{cond} describes a heat transport at a cross-section area within solids, provoked by a temperature difference ΔT along a transport length l [253]:

$$q_{\mathrm{cond}} = k\frac{\Delta T}{l} \tag{2.30}$$

The thermal conductivity k can be anisotropic for some materials or composite materials, e.g., for an electrode stack of a lithium-ion cell [133]. The convective heat flux density q_{conv} describes a heat transport between a solid object that is surrounded by a fluid. The convection is driven by a temperature difference between the surface temperature of the object T_{surf} and the ambient temperature T_{∞} and expressed with the convective heat transfer coefficient h [253]:

$$q_{\mathrm{conv}} = h(T_{\mathrm{surf}} - T_{\infty}) \tag{2.31}$$

The radiative heat flux density q_{rad} describes a heat transport from the surface of an object to the ambience. It is defined with the emissivity $\varepsilon_{\mathrm{rad}}$ of the object's surface and the Stefan-Boltzmann constant σ_{SB} [253]:

$$q_{\mathrm{rad}} = \varepsilon_{\mathrm{rad}}\sigma_{\mathrm{SB}}(T_{\mathrm{surf}}^4 - T_{\infty}^4) \tag{2.32}$$

In 3D thermal models, similar to the mass balance for the p2D model, the temperature change over time within a RVE can be calculated with the general energy balance [132, 249]

$$\rho c_{\mathrm{p}}\frac{\partial T}{\partial t} = \nabla(k\nabla T) + q_{\mathrm{vol}} \tag{2.33}$$

, with the density ρ, the specific heat capacity c_{p}, the thermal conductivity k, and the volumetric heat generation q_{vol}. The volumetric heat generation q_{vol} describes the irreversible heat due to ohmic, charge transfer, and mass transport losses as well as the reversible heat due to entropy [254]. In the 3D thermal model, the ∇ operator (transpose) is defined as:

$$\nabla = \left(\frac{\partial}{\partial x}, \frac{\partial}{\partial y}, \frac{\partial}{\partial z}\right)^{\mathrm{T}} \tag{2.34}$$

The boundary conditions of a thermal model depend on the specific use case. Regarding LIBs, heat conduction takes place via the electric connectors to the battery, an attached cooling plate, or just the adjacent housing of the application. Convection takes place if the cell is not completely encased and, e.g., air surrounds parts of the cell surface.

3 Increasing the Capacity and Energy of Lithium-Ion Cells with New Active Materials

An overview of common cathode and anode active materials for LIBs was presented in Chapter 2.1.1. Both, the capacity and the energy of a LIB are essentially determined by the chosen active material combination. However, a higher cell capacity must not always result in a higher energy, as the average voltage levels of the active materials also play a crucial role.

Within this chapter, the performance of LIBs comprising the cathode active material LMR-NCM is investigated. LMR-NCM is a CAM, which offers a higher specific capacity in comparison to a state-of-the-art nickel-rich NCA or NCM-811 [31, 32, 35]. As a proper assessment of the energy density on the cell level cannot be conducted with small-scale laboratory cells, in the first part of this chapter, an evaluation of large-format multilayer LMR-NCM/graphite and NCA/graphite pouch cells is presented [44, 47]. Also, self-heating effects at high C-rates as well as aging effects are only feasible in larger cell formats [44]. In the second part of this chapter, the implications of the heat generation caused by arising overpotentials and the pronounced voltage hysteresis of cells containing LMR-NCM are further analyzed with calorimetric measurements and 3D thermal model simulations [48].

3.1 Comparative Evaluation of LMR-NCM and NCA Cathode Active Materials

Two CAMs, a LMR-NCM with a reversible capacity of around 250 $\mathrm{mAh\,g^{-1}}$ and an established NCA with around 200 $\mathrm{mAh\,g^{-1}}$ were comparatively evaluated in large-format multilayer pouch cells with graphite anodes for either CAM. Both, the LMR-NCM/graphite and the NCA/graphite pouch cells were designed to reach a reversible capacity of ≈5.5 Ah at a 1C discharge rate. The conducted research on these cells was split into two publications: Part I - Production, Electrode Characterization, and Formation [47] & Part II - Rate Capability, Long-Term Stability, and Thermal Behavior [44].

In Part I of this study [47], the cell design, the production, the electrode characterization, and the formation of the pouch cells are described in detail. The main findings include the different processing behavior of the two CAMs during the cell production, as cathode porosities of 30–35% were difficult to achieve by calendering the LMR-NCM electrodes. Moreover, the substantially increased gassing of LMR-NCM/graphite pouch cells necessitated an adapted formation procedure, which was carried out at a higher temperature and included two degassing steps.

In this section, Part II of this study, titled *Comparative Evaluation of LMR-NCM and NCA Cathode Active Materials in Multilayer Lithium-Ion Pouch Cells: Part II. Rate Capability, Long-Term Stability, and Thermal Behavior* [44] is presented. Parts of the article were presented at the *Batterieforum Deutschland 2020* in Berlin in January 2020.

For the comparative evaluation, a rate capability test and a long-term cycling study were conducted

in order to thoroughly assess the specific capacities and energy densities achieved on the cell level. Distinct differences between the two pouch cell types were the wider voltage window of the LMR-NCM/graphite cells (2.0–4.6 V) and the pronounced voltage hysteresis of LMR-NCM between charge and discharge. In comparison, the NCA/graphite cells were cycled between 3.0–4.3 V and showed almost no voltage hysteresis. For low discharge currents, the specific capacity related to the CAM mass was around 30% higher for the LMR-NCM/graphite pouch cells (235 $\mathrm{mAh\,g_{CAM}^{-1}}$) compared to the NCA/graphite cells (180 $\mathrm{mAh\,g_{CAM}^{-1}}$). However, because of the LMR-NCM voltage hysteresis and the lower mean discharge voltage of the LMR-NCM/graphite cells, the energy density on the cell level was only ≈11% higher.

In the long-term cycling study, the aging behavior was evaluated with a continuous C/2 cycling and checkup cycles at regular intervals. The checkups assessed the remaining capacity with a C/10 cycle as well as the internal resistance with a pulse test and a 1C cycle. Initially, the LMR-NCM/graphite cells showed a better performance but exhibited a faster degradation of both the specific capacity and the energy density. The overall cycle life of the LMR-NCM/graphite pouch cells was limited to only 250 cycles due to a rupture of the pouch foil caused by the strong gassing. The cells were projected to reach 80% of their initial specific capacity after approximately 350 cycles. The 80% state of health (SOH) criterion of their initial energy density was reached after already 230 cycles, caused by a faster voltage fading. In contrast, the NCA/graphite cells reached their 80% SOH criteria of the specific capacity after 980 cycles and of the energy density after 710 cycles. The checkup cycles were carried out every 25 C/2 cycles and assessed the remaining capacity of the cells with a C/10 charge/discharge cycle and the internal resistance with a 10 s discharge pulse at an SOC of approximately 40%. The pulse test showed that the resistances of both cell types rose equally by ≈40% between the 50^{th} and the 250^{th} cycle and that the overall capacity decay was not dominated by increasing cell resistances but was rather caused by a loss of cyclable lithium.

Author contribution The pouch cells were built by the battery production team of David Schreiner and Florian Günter. Ludwig Kraft conducted the pouch cell measurements, the data was interpreted by Ludwig Kraft and Tanja Zünd. Tanja Zünd and Rebecca Wilhelm built the coin cells, conducted the coin cell measurements and provided the data for comparison. The results of the experiments were analyzed and interpreted by Ludwig Kraft and Tanja Zünd. The manuscript was written by Ludwig Kraft and Tanja Zünd and edited by the co-authors. All authors discussed the data and commented on the results.

Comparative Evaluation of LMR-NCM and NCA Cathode Active Materials in Multilayer Lithium-Ion Pouch Cells: Part II. Rate Capability, Long-Term Stability, and Thermal Behavior

Ludwig Kraft, Tanja Zünd, David Schreiner, Rebecca Wilhelm, Florian J. Günter, Gunther Reinhart, Hubert A. Gasteiger, Andreas Jossen

Journal of The Electrochemical Society 168 (2), p. 020537, 2021

Permanent weblink:
http://dx.doi.org/10.1149/1945-7111/abe5e6

Journal of The Electrochemical Society, 2021 **168** 020537

Comparative Evaluation of LMR-NCM and NCA Cathode Active Materials in Multilayer Lithium-Ion Pouch Cells: Part II. Rate Capability, Long-Term Stability, and Thermal Behavior

Ludwig Kraft,[1,=,*,z] Tanja Zünd,[2,=,*] David Schreiner,[3] Rebecca Wilhelm,[2,*] Florian J. Günter,[3] Gunther Reinhart,[3] Hubert A. Gasteiger,[2,] and Andreas Jossen[1]**

[1]*Institute for Electrical Energy Storage Technology, Technical University of Munich, D-80333 Munich, Germany*
[2]*Chair of Technical Electrochemistry, Technical University of Munich, D-85748 Garching, Germany*
[3]*Institute for Machine Tools and Industrial Management, Technical University of Munich, D-85748 Garching, Germany*

A lithium- and manganese-rich layered transition metal oxide-based cathode active material (LMR-NCM) with a reversible capacity of 250 mAh g^{-1} vs graphite is compared to an established NCA/graphite combination in multilayer lithium-ion pouch cells with a capacity of 5.5 Ah at a 1C discharge rate. The production of the cells, the electrode characterization as well as the formation is described in Part I of this study. In Part II, the two cell types are evaluated for their rate capability and their long-term stability. The specific capacity of the LMR-NCM pouch cells is ≈30% higher in comparison to the NCA pouch cells. However, due to the lower mean discharge voltage of LMR-NCM, the energy density on the cell level is only 11% higher. At higher discharge currents, a pronounced heat generation of the LMR-NCM pouch cells was observed, which is ascribed to the LMR-NCM voltage hysteresis and is only detectable in large-format cells. The cycling stability of the LMR-NCM cells is somewhat inferior due to their faster capacity and voltage fading, likely also related to electrolyte oxidation. This results in a lower energy density on the cell level after 210 cycles compared to the NCA pouch cells.

 [DOI: 10.1149/1945-7111/abe5e6]

Manuscript submitted January 14, 2021; revised manuscript received February 11, 2021. Published February 23, 2021.

The demand for lithium-ion batteries with a higher capacity and energy density is rising, especially driven by mobile applications like electric vehicles (EVs).[1–4] As a consequence, the specific capacity of the active materials must increase. State-of-the-art cathode active materials (CAMs) are lithium-nickel-cobalt-manganese-oxides (NCMs) or lithium-nickel-cobalt-aluminum-oxides (NCAs). The capacity of NCMs can be increased by a higher Ni content, e.g., from NCM-111 with 150 mAh g^{-1} up to 200 mAh g^{-1} for NCM-811 for comparable upper cutoff voltages.[1,2,5] The Ni-rich NCA materials exhibit a similar specific capacity of around 200 mAh g^{-1}.[6,7] A promising not yet commercialized CAM that offers a higher capacity is Li- and Mn-rich NCM (LMR-NCM) with a reversible capacity of around 250 mAh g^{-1}.[8–12]

Material costs account for 45%–75% of the total manufacturing costs on the cell level, and the CAMs have the biggest share of the material costs with 39%–54%.[13–16] This makes Mn-rich materials more cost effective compared to Ni-rich materials. In February 2021, the price of the commodity Ni (21 USD kg^{-1} [17]) was an order of magnitude higher than that of Mn (2 USD kg^{-1} [18]). While currently used NCA and NCM CAMs still contain Co, ongoing research aims toward reducing or eliminating Co.[19–21] Similarly, it has also been shown that Co can be eliminated from LMR-NCM CAMs.[22] Based on the stoichiometry of the two CAMs that are investigated in our work, up to 34% can be saved in raw material costs comparing a LMR-NCM ($Li_{1.14}[Ni_{0.26}Co_{0.14}Mn_{0.60}]_{0.86}O_2$) to an NCA ($LiNi_{0.81}Co_{0.15}Al_{0.04}O_2$) with commodity prices of Co (45 USD kg^{-1} [23]), Li (10 USD kg^{-1} [24]), and Al (2 USD kg^{-1} [25]). Therefore, the high specific capacity combined with the lower material costs render LMR-NCM to a promising CAM for future lithium-ion batteries.[4,11,26,27]

There is a wide variety of lithium-ion cells exhibiting different cell formats, designs, and materials. Reported energy densities of various cells and cell formats range from 83 Wh kg^{-1} for high power cells to 267 Wh kg^{-1} for high energy cells.[28–31] The energy density on the cell level can be enhanced by thicker and less porous electrodes, by electrode compositions with a higher active material share, or by the use of active materials with a higher specific capacity, while reducing the share of passive parts like separators, current collectors, tab connectors, or the housing.[1,32] Up-to-date, high energy cells that reach >250 Wh kg^{-1} often use a Ni-rich CAM, either NCM-811 or NCA, and a graphite anode that contains a small amount of silicon.[29–31,33] Ding et al.[30] reported energy densities of cylindrical cells used by Tesla in EVs of 236 Wh kg^{-1} for an NCA/graphite cell and 260 Wh kg^{-1} for an NCA/silicon-graphite cell.

In this work, a LMR-NCM material is evaluated and compared to a commercially available NCA material that serves as a benchmark. Based on our scale-up experiments with laboratory-scale coin cells with LMR-NCM, this CAM was used to design multilayer pouch cells, which were produced on the pilot scale production line at the Technical University of Munich,[34] as described in Part I of this study.[35] To appropriately assess the performance of the LMR-NCM pouch cells, NCA pouch cells with the same electrode and cell configuration were produced on the same line. The cells were standardized by adjusting the loading of the electrode sheets, delivering an areal capacity of 2.3 mAh cm^{-2} or a total capacity of 5.5 Ah at a 1C discharge rate. For both cell types, graphite was used as anode material. For simplicity, the LMR-NCM/graphite and NCA/graphite pouch cells will further on be referred to as LMR-NCM and NCA pouch cells, respectively.

The production of the cells, the electrode characterization, as well as their formation is described in Part I of this study.[35] In Part II, the characteristics of both cell types were evaluated by discharge rate capability tests and by an aging study, in which we compare their capacity, mean discharge voltage, and energy density fading, their internal resistance buildup, as well as their self-heating at high discharge rates. While previous publications on LMR-NCM were carried out with small-scale laboratory cells (e.g., coin cells), stating energy densities up to 1000 Wh kg^{-1} at the material level,[11,12,26] to the best of our knowledge, there is no published research on large-format LMR-NCM cells that would allow a rigorous assessment of the energy densities achieved on the cell level. Especially the evaluation of self-heating effects at high C-rates and gassing effects during formation and extended aging is only feasible with large-format cells, so that the here presented study with large-format multilayer pouch cells will provide new insights with regards to these aspects.

[=]These authors contributed equally to this work.
[*]Electrochemical Society Student Member.
[**]Electrochemical Society Fellow.
[z]E-mail: ludwig.kraft@tum.de

Experimental

The large-format multilayer pouch cells were produced on the semi-automatic manufacturing pilot line at the Technical University of Munich.[34] To compare the performance of the two CAMs, both pouch cell types were designed to have a similar areal capacity of 2.3 mAh cm^{-2} at a 1C discharge, amounting to a total capacity of around 5.5 Ah at 1C. A target capacity of 5.5 Ah at 1C results in an energy of 17.6 Wh for the LMR-NCM and 19.8 Wh for the NCA pouch cells (based on averaged discharge voltages at 1C of 3.2 V for the LMR-NCM and 3.6 V for the NCA cells). The here used multilayer pouch cell design was based on small-scale laboratory coin cell measurements that were conducted in Part I of this study.[35] Details on the electrode production as well as the pouch cell assembly and formation are also provided in Part I of this study.[35]

Electrode specifications.—In this study, a LMR-NCM CAM with a stoichiometry of $Li_{1.14}[Ni_{0.26}Co_{0.14}Mn_{0.60}]_{0.86}O_2$ (BASF, Germany), which can as well be written as 0.33 $Li_2MnO_3 \cdot 0.67$ $LiNi_{0.38}Co_{0.21}Mn_{0.41}O_2$ and was also investigated by Teufl et al.,[36] and an NCA with a stoichiometry of $LiNi_{0.81}Co_{0.15}Al_{0.04}O_2$ (BASF, Germany) were used. The cathodes consisted of 92.5 wt% CAM (LMR-NCM or NCA), 4 wt% conductive carbon (Super-C65, Timcal, Switzerland), 3.5 wt% polyvinylidene-fluoride binder (PVdF, Solef 5130, Solvay, Belgium), and were coated double-sided on a 15 μm aluminum substrate foil (1055 A, Korff, Switzerland). The CAM loading was set to 11.7 mg cm^{-2} (≡2.9 mAh cm^{-2} at C/10, based on a nominal capacity of 250 mAh g_{CAM}^{-1}) and 13.0 mg cm^{-2} (≡2.6 mAh cm^{-2} at C/10, based on a nominal capacity of 200 mAh g_{CAM}^{-1}) for the LMR-NCM and NCA electrode sheets, respectively. The nominal capacities of both CAMs relate to LMR-NCM/Li cells in a voltage range of 2.0–4.7 V (250 mAh g_{CAM}^{-1}) and NCA/Li cells in a voltage range of 3.0–4.5 V (200 mAh g_{CAM}^{-1}), and were used for the calculation of the nominal cell capacities as stated in Table I. The cathodes were calendered to an electrode coating porosity of 42%.

The anodes consisted of 97 wt% graphite (SGL Carbon, Germany), 1.5 wt% carboxymethyl cellulose binder (CMC Sunrose MAC200, NPI, Japan), 1.5 wt% styrene-butadiene rubber binder (SBR, Zeon, Japan), and were coated on a 11 μm copper substrate foil (Cu-PHC, hard rolled blank, with a nominal thickness of 12 μm Schlenk, Germany). The graphite electrode loadings were set to 9.5 mg cm^{-2} (≡3.4 mAh cm^{-2} at C/10, based on a nominal capacity of 355 mAh $g_{graphite}^{-1}$) for LMR-NCM and 10.2 mg cm^{-2} (≡3.6 mAh cm^{-2} at C/10, based on a nominal capacity of 355 mAh $g_{graphite}^{-1}$) for NCA based pouch cells. The anodes were calendered to an electrode coating porosity of 30%. The resulting areal capacity ratios of negative/positive electrode (N/P ratio) were 1.17 for the LMR-NCM and 1.38 for the NCA pouch cells.

Pouch cell assembly.—Both cell types contained 16 double-coated cathodes and 17 double-coated anodes. The electrodes were alternately stacked with a z-folded monolayer polypropylene (PP) separator (Celgard 2500, France) with a thickness of 25 μm. An FEC:DEC based electrolyte (1 M $LiPF_6$ in a 12:64:24 (by volume) mixture of FEC:DEC:co-solvent and 2 wt% of a proprietary additive, BASF, Germany) was used for the LMR-NCM cells, while an EC:DEC based electrolyte (1 M $LiPF_6$ in a 3:7 (by weight) mixture of EC:DEC and 2 wt% vinylene carbonate (VC), BASF, Germany) was used for the NCA cells. The proprietary additive improves full-cell cycle stability and has a similar effect as the one described in Ref. 37.

The individual cell specifications are listed in Table I. The CAM mass was determined by weighing the electrode sheets before the assembling process, while the finally determined mass of the cell after the electrolyte filling, the degassing after formation, and the final cell sealing process includes the current collectors, the welded-on tabs, and the pouch foil. For comparison of the cells, the specific capacity used in the later studies was related to the CAM mass. The gravimetric energy density, however, was related to the total pouch cell mass. On account of an error in the production process, the loading of the graphite anodes for the NCA pouch cells was slightly too high, resulting in an N/P ratio of 1.38 instead of the originally intended N/P ratio of 1.2. Assuming a N/P ratio of 1.17 for the NCA pouch cells (as is the case with the LMR-NCM cells), the total cell mass would be reduced by ≈4.4 g (due to a reduced anode loading by 1.6 mg cm^{-2} with an active material ratio of 97 wt% and a total anode area of 2687 cm^2), resulting in 4% higher gravimetric energy density values. Nevertheless, the stated gravimetric energy densities were calculated with the actual cell mass of the NCA pouch cells. For the evaluation of the volumetric energy density, a volume of ≈51.6 cm^3 for the LMR-NCM and ≈49.7 cm^3 for the NCA pouch cells was used (based on the cell thicknesses and the length and width of the deep-drawn pocket of the pouch bag). Unless stated otherwise, the term energy density refers to the gravimetric energy density. Based on a nominal reversible capacity at C/10 of 250 mAh g^{-1} for LMR-NCM and 200 mAh g^{-1} for NCA, the nominal cell capacity was calculated according to the CAM mass. In all later measurements, the C-rates for the charging and discharging procedures were referred to the nominal cell capacity at C/10 of each cell, as stated in Table I. For a detailed overview of the production and formation process of the LMR-NCM pouch cells, the reader is referred to Part I of this study.[35]

Coin cell specifications.—As a reference, experiments with both the LMR-NCM and the NCA cathodes with graphite anodes were also conducted with laboratory 2032-type coin cells. Cathodes with 14 mm diameter and anodes with 15 mm diameter were punched out from a single side coated part of the electrodes used for the pouch cells as described above, i.e., with the same areal capacities as specified above. The electrodes were dried in a glass oven (Büchi, Switzerland) under dynamic vacuum at 120 °C for 12 h. The coin cells were assembled in an argon filled glove box (O_2, H_2O < 0.1 ppm, MBraun, Germany) with a separator of 17 mm in diameter and 50 μL of electrolyte. The separator and the electrolyte for the corresponding CAMs were the same for the coin and pouch cells.

Electrochemical measurements.— *Cell formation and mounting.*— A formation procedure with a first constant current (CC) C/15 cycle including degassing steps, followed by two CC C/10 cycles was carried out. The LMR-NCM cells were charged to 4.7 V in their first formation cycle to activate the material;[10] in all subsequent cycles, the upper cutoff voltage was set to 4.6 V. A more detailed description of the formation procedure is given in Part I of this study.[35] The LMR-NCM

Table I. Specifications of the LMR-NCM/graphite and NCA/graphite pouch cells with an identical CAM-based areal capacity of ≈2.3 mAh cm^{-2} at 1C. Note that the here used pouch cells represent a subset of the pouch cells presented in Part I of this study.[35]

Cell type	Number of cells	CAM[a)] mass	Cell mass[b)]	Nominal cell capacity[c)]
LMR-NCM	5	27.64 ± 0.32 g	111.6 ± 1.6 g	6.91 ± 0.08 Ah
NCA	6	31.34 ± 0.41 g	115.8 ± 2.0 g	6.27 ± 0.08 Ah

a) CAM—cathode active material. b) Determined by weighing the cells after formation, degassing, and final sealing of the cells. c) Based on the nominal specific CAM capacity at C/10 (LMR-NCM: 250 mAh g^{-1}, NCA: 200 mAh g^{-1}).

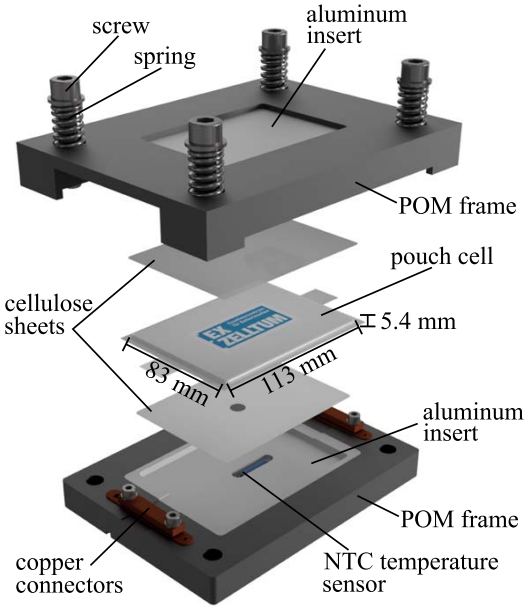

Figure 1. Schematic CAD drawing of the cell holder including the pouch cell. The 5.4 mm thickness of the depicted pouch cell represents a mean value of the thicknesses of the LMR-NCM (5.5 mm) and NCA (5.3 mm) cells.

cells were cycled between 2.0 V and 4.6 V and the NCA cells between 3.0 V and 4.3 V. Note that all C-rates are referenced to the nominal specific CAM capacity of 250 mAh g^{-1} for LMR-NCM cells and of 200 mAh g^{-1} for NCA cells.

The pouch cells were mounted in custom-built cell holders as depicted in Fig. 1. Both the bottom and top part of the cell holder consisted of a thermoplastic polyoxymethylene (POM) frame with an aluminum insert. Via the screw/spring combination a pressure of 0.2 MPa was applied to the pouch cells. Cellulose sheets (Pacopads 5500, Pacothane Technologies, USA) were put between the cell and the aluminum inserts to obtain a homogeneous compressive force across the active area. An integrated negative temperature coefficient (NTC) temperature sensor was attached to measure the temperature on the surface of the pouch cells with a precision of ±1 K. All pouch cell measurements were performed with an XCTS battery test system (BaSyTec, Germany) in a controlled climate chamber (WT3-600/40-S, Weiss Umwelttechnik, Germany) at 25 °C. The coin cells were cycled with a Maccor battery tester (series 4000, USA) in a controlled climate chamber (Binder, Germany) at 25 °C. A detailed overview of all measurement procedures is listed in Table II, the tests were consecutively performed in the stated order for each of the cells.

Initial C/10 cycle and open circuit voltage curve.—After formation, the cells were charged and discharged with a CC C/10 cycle. In a subsequent CC C/10 cycle, a pause of 1 h was included after each hour, which sums up to ten 1 h pauses during the charge and ten 1 h pauses during the discharge. While pausing, the relaxation of the open circuit voltage (OCV) was measured.

Discharge rate capability test.—Next, the discharge rate capability test was carried out with CC discharging with C/10, C/5, and C/2. The preceding charging C-rate was set to the discharging C-rate. The CC charging phase was followed by a constant voltage (CV) phase until a cutoff current of C/20 was reached. For two cells of each cell type, an extended discharge rate capability test was carried out with also 1C, 2C, and 3C discharge rates, whereby the charging current in the CC phase was limited to C/2 (with a CV phase terminated at C/20) for each discharge rate. The specific capacity was related to the mass of the corresponding CAM, whereas the energy density was related to the total cell mass as stated in Table I. The values for each cycle were averaged over all cells of the corresponding cell type and plotted with the corresponding standard deviation. If the measurement procedure only consisted of two samples, their mean value was plotted with the minimum and maximum value, indicated by the error bars.

Aging study.—In the final aging test, the cells were repeatedly cycled with a C/2 CCCV charge (with a cutoff current of C/20) and a C/2 CC discharge. Every 25 cycles, a checkup procedure was carried out. In the checkup procedure, the cells were initially charged with C/10 to a voltage of 3.7 V, which corresponds to a state-of-charge (SOC) of approximately 40% for both cell types, followed by a 1 h resting period at OCV. Then the cell resistance was determined with the direct current internal resistance (DCIR) method by applying a C/2 CC discharge pulse for 10 s and measuring the cell voltage. The resistance is calculated by Ohm's law and the total voltage drop and referenced to the cathode area (73.73 cm^2 per layer). After the DCIR test, the cells were first discharged with C/10 to their lower cutoff voltage, and then, the cell capacity was assessed by a full C/10 charge/discharge cycle. Only the four cells (2x LMR-NCM, 2x NCA) that were stressed with the extended rate capability test were additionally discharged with three 1C CC cycles in each checkup.

Results and Discussion

The comparative evaluation of the performance of the large-format multilayer LMR-NCM and NCA pouch cells is divided into two parts: the rate capability behavior, and the aging behavior of the cells in the long-term cycling study.

Rate capability behavior.—The results of the discharge rate capability test, depicting the C-rate dependence of the specific CAM capacity, the charge averaged mean cell discharge voltage, and the gravimetric cell energy density are displayed in Fig. 2; the corresponding values normalized to those at C/10 are stated in Table III.

For low C-rates, i.e., C/10 and C/5, the discharge capacity stayed almost constant for both materials, and the LMR-NCM cells delivered around 30% higher specific capacities. With increasing rates, less capacity can be discharged from the cells, especially for the high C-rates of 2C and 3C. At a 2C discharge, only 88% can be discharged from the LMR-NCM cells and 77% from the NCA cells, when referenced to their capacity at C/10. At a 3C discharge, the LMR-NCM cells delivered 77%, while the NCA cells dropped to 59%. Previous studies with NCA[38,39] and LMR-NCM[10,40,41] showed that the capacity loss at high C-rates is largely due to the poor charge transfer kinetics and/or the slow solid-state diffusion at low SOC. However, it is noteworthy that the capacity loss with increasing C-rate was much more pronounced for LMR-NCM/lithium coin cells that were investigated in Part I of this study[35]: at the same loading (≈12 mg cm^{-2}) and cathode porosity (≈42%), the capacity at 3C was only ≈120 mAh g_{CAM}^{-1} (see Fig. 2 in Ref. 35), compared to the ≈180 mAh g_{CAM}^{-1} obtained here for the LMR-NCM/graphite pouch cells (red symbols in Fig. 2a). As will be shown later, this was most likely linked to the strong cell temperature rise of the LMR-NCM pouch cells at high C-rates.

The mean discharge voltage at C/10 shown in Fig. 2b of the LMR-NCM cells was at 3.5 V, while it was at 3.7 V for the NCA cells. At a 3C rate, the mean discharge voltage of the LMR-NCM cells decreased by ≈660 mV, which was more than double compared to the ≈310 mV drop of the NCA cells, revealing the strong rate dependency of the LMR-NCM CAM.

The gravimetric energy density of the pouch cells, displayed in Fig. 2c, is a product of the discharge capacity and the mean discharge voltage, referenced to the total mass of the pouch cells.

Table II. Sequence of the measurement procedures applied to the LMR-NCM/graphite and NCA/graphite pouch and coin cells.

Cycling procedure	Cycles	Charge	Stop condition	Discharge	Stop condition
C/10 cycle	1	CC @ C/10	$U \geqslant U_{max}$	CC @ C/10	$U \leqslant U_{min}$
C/10 relax cycle (initial OCV curve)	1	CC @ C/10	$t \geqslant 1$ h or $U \geqslant U_{max}$	CC @ C/10	$t \geqslant 1$ h or $U \leqslant U_{min}$
		Pause	$t \geqslant 1$ h	Pause	$t \geqslant 1$ h
Rate capability test	3	CC @ C/10	$U \geqslant U_{max}$	CC @ C/10	$U \leqslant U_{min}$
		CV @ U_{max}	$I \leqslant$ C/20		
	3	CC @ C/5	$U \geqslant U_{max}$	CC @ C/5	$U \leqslant U_{min}$
		CV @ U_{max}	$I \leqslant$ C/20		
	5	CC @ C/2	$U \geqslant U_{max}$	CC @ C/2	$U \leqslant U_{min}$
		CV @ U_{max}	$I \leqslant$ C/20		
Extended rate capability test[a)]	5	CC @ C/2	$U \geqslant U_{max}$	CC @ 1C	$U \leqslant U_{min}$
		CV @ U_{max}	$I \leqslant$ C/20		
	5	CC @ C/2	$U \geqslant U_{max}$	CC @ 2C	$U \leqslant U_{min}$
		CV @ U_{max}	$I \leqslant$ C/20		
	5	CC @ C/2	$U \geqslant U_{max}$	CC @ 3C	$U \leqslant U_{min}$
		CV @ U_{max}	$I \leqslant$ C/20		
Aging cycles	25	CC @ C/2	$U \geqslant U_{max}$	CC @ C/2	$U \leqslant U_{min}$
		CV @ U_{max}	$I \leqslant$ C/20		
Checkup procedure	**Cycles**	**Procedure**		**Stop condition**	
Initialization	1	CC charge @ C/10		$U \geqslant U_{pulse}$	
		Pause		$t \geqslant 1$ h	
Pulse Test	1	CC discharge @ C/2		$t \geqslant 10$ s	
C/10 cycle	1	CC discharge @ C/10		$U \leqslant U_{min}$	
		CC charge @ C/10		$U \geqslant U_{max}$	
		CC discharge @ C/10		$U \leqslant U_{min}$	
1C cycle[a)]	3	CC charge @ C/2		$U \geqslant U_{max}$	
		CV charge @ U_{max}		$I \leqslant$ C/20	
		CC discharge @ 1C		$U \leqslant U_{min}$	

Before the first stated C/10 cycle, the cells underwent a formation procedure consisting of one C/15 and two C/10 cycles. The C-rates refer to the nominal cell capacities listed in Table I. All measurements were performed at an ambient temperature of 25 °C. CC—constant current, CV—constant voltage. LMR-NCM: $U_{max} = 4.6$ V, $U_{min} = 2.0$ V, $U_{pulse} = 3.7$ V. NCA: $U_{max} = 4.3$ V, $U_{min} = 3.0$ V, $U_{pulse} = 3.7$ V.a) Two cells each were discharged with the extended rate capability test and the 1C checkup cycles.

At low discharge rates the energy density was around 200 Wh kg^{-1} (≈433 Wh l^{-1}) for the LMR-NCM and 180 Wh kg^{-1} (≈419 Wh l^{-1}) for the NCA pouch cells. In contrast to the 30% increase in specific capacity, the benefit in gravimetric energy density was only 11%. An adjusted N/P ratio of 1.17 for the NCA pouch cells (rather than the here used N/P ratio of 1.38) would result in 4% higher energy densities, reducing the energy density advantage of the LMR-NCM cells to 7%. One reason for the lower gain in energy density compared to the gain in capacity of the LMR-NCM cells was their lower mean discharge voltage. Nevertheless, in this study, the LMR-NCM pouch cells maintained a higher energy density of ≈11% compared to the NCA pouch cells for C-rates up to 1C; this advantage became even more pronounced at higher rates of 2C (+16%) and 3C (+29%), which, as described later, is related to the substantial LMR-NCM cell temperature rise.

Both pouch cell types described in this work were not designed for a specific application or optimized with regards to their energy density. High energy cells use thinner current collectors and separators as well as lower electrode porosities, which requires less electrolyte.[29,33] All these measures save weight and volume and thereby increase the gravimetric and volumetric energy density on the cell level. Based on the cylindrical cells for EVs reported by Ding et al.[30] with 236 Wh kg^{-1} (NCA/graphite) and 260 Wh kg^{-1} (NCA/silicon-graphite), by switching the CAM from NCA to LMR-NCM and assuming a gravimetric energy density increase of 7% compared to the properly balanced NCA/graphite or NCA/silicon-graphite cells, 253 Wh kg^{-1} (LMR-NCM/graphite) and 278 Wh kg^{-1} (LMR-NCM/silicon-graphite) could be reached.

The performance of the laboratory coin cells served as a comparison for the large-format multilayer pouch cells. As already mentioned above with regards to the discharge rate capability test, the LMR-NCM/graphite coin cells (as well as the LMR-NCM/lithium coin cells measured in Part I[35]) showed a specific capacity that was ≈34% lower than that of the corresponding pouch cells for a 3C discharge (see Fig. 3a). In contrast, the specific capacity of the NCA laboratory coin cells was in good agreement for all C-rates with the NCA pouch cells (see solid gray squares and open gray triangles in Fig. 3a). Just for clarification, for the 2C and 3C discharge in Fig. 3a, the open gray triangles indicating the specific capacity of the NCA coin cells are superposed by the open red triangles for the LMR-NCA coin cells.

While the coin cells can be considered isothermal at an ambient temperature of 25 °C during operation due to their low energy content and high thermal mass, this is not the case for large-format pouch cells. The maximum temperature of the pouch cells was reached at the end of each discharge and is depicted in Fig. 3b. As described in the experimental section, the temperature was measured on the surface of the pouch cells within the cell holder (see Fig. 1). The cell holder, consisting partly of aluminum and the thermoplastic POM, influenced the heat dissipation of the cells. As there were no

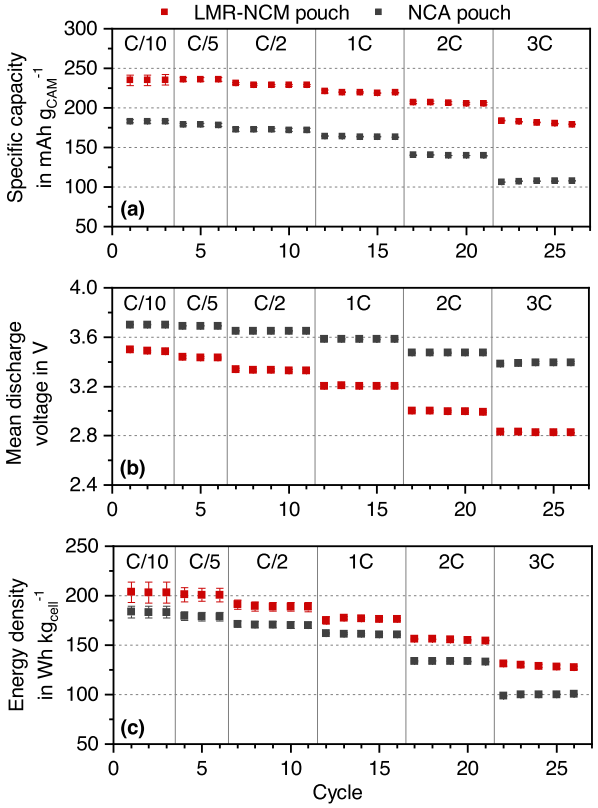

Figure 2. Discharge rate capability of the LMR-NCM and NCA pouch cells (as specified in Table I), depicting the C-rate dependence of (a) the specific capacity related to the CAM mass, (b) the mean cell discharge voltage, and (c) the energy density with respect to the total mass of the cell. The cells were discharged with a CC procedure at an ambient temperature of 25 °C in the voltage windows 4.6–2.0 V for LMR-NCM and 4.3–3.0 V for NCA, respectively (see Table II). The error bars for the rates of C/10, C/5, and C/2 represent the standard deviation between 5 LMR-NCM and 6 NCA cells; for the rates of 1C, 2C, and 3C, the error bars mark the minimum/maximum values of 2 cells of each type.

rest periods at the end of discharge during the rate capability test, the cells could not cool down to the 25 °C ambient temperature of the climate chamber and had an initial temperature of around 27.5 °C at the beginning of the rate capability test (see Fig. 3b). The temperature of the LMR-NCM cells strongly increased with increasing C-rates, reaching a temperature of 53 °C for the 3C discharge, while the NCA cells only reached 33 °C.

Figure 3c displays the round-trip energy efficiencies of both the LMR-NCM and NCA pouch and coin cells. The generated heat in a cell can be correlated to the energy that is irreversibly lost between charge and discharge. After formation, this energy inefficiency is mainly caused by a voltage hysteresis between charge and discharge and therefore pronounced in LMR-NCM cells.[42] During the 3C discharge (following a C/2 CCCV charge, see Table II), the energy loss of the LMR-NCM pouch cells was above 6 Wh (corresponding to an energy efficiency of ≈70%), while the NCA pouch cells only lost around 2 Wh (corresponding to an energy efficiency of ≈85%). Table IV lists the mean charge (E_{CH}) and discharge (E_{DCH}) energies of the LMR-NCM and NCA pouch cells vs discharge rate (DCH C-rate) as well as the resulting round-trip energy efficiencies (η), defined as

$$\eta = \frac{E_{DCH}}{E_{CH}} \cdot 100\% \quad [1]$$

It also lists the overall dissipated energy per cycle (ΔE_{tot})

$$\Delta E_{tot} = E_{CH} - E_{DCH} \quad [2]$$

Meister et al.[42] classified different anode and cathode materials according to their round-trip energy efficiency for a 1C charge/discharge cycle at an ambient temperature of 20 °C. In their study, graphite had a round-trip energy efficiency of ≈94%, their LMR-NCM ($0.5\ Li_2MnO_3 \cdot 0.5\ LiNi_{0.4}Mn_{0.4}Co_{0.2}O_2$) had a round-trip energy efficiency of ≈85%, while NCA was not investigated. Their LMR-NCM/graphite combination would result in a round-trip energy efficiency of ≈80%. This round-trip energy efficiency at a 1C rate reflects the results for the LMR-NCM/graphite pouch cells obtained in our study (≈81% at 1C). Note that these values were measured at an ambient temperature of 20 °C, while our measurements were performed at an ambient temperature of 25 °C.

To further evaluate the difference in round-trip energy efficiency of both cell types, the charge and discharge voltage profiles of each cell type have to be closer examined. The total energy loss related to voltage hysteresis can be split into a resistive part ΔE_R, due to cell polarization during operation, and into a current-independent part ΔE_{OCV}, originating from the intrinsic active material voltage hysteresis that is particularly pronounced for LMR-NCMs.[26,42]

$$\Delta E_{tot} = \Delta E_R + \Delta E_{OCV} \quad [3]$$

The additional energy that is lost due to parasitic side reactions was neglected in our estimation of the energy losses, as they are minor for the high coulombic efficiencies >99.9% for both cell types in our study. The reversible heat (entropy) during a full charge/discharge cycle is considered close to zero (under the assumption that no net entropy can be generated in a reversibly cyclable cell) and therefore insignificant for the total energy loss.

For the evaluation of the energy losses, a C/10 charge/discharge cycle with and without intermittent 1 h OCV rest periods was carried out. The LMR-NCM pouch cells were cycled in a voltage range of 2.0–4.6 V and the NCA pouch cells in a voltage range of 3.0–4.3 V, the results are displayed in Fig. 4. Clearly visible is the pronounced hysteresis of the voltage profile of the LMR-NCM cells. When OCV rest periods are added to the C/10 cycling, represented by the red lines, the purely resistive part is omitted. The cell voltage is allowed

Table III. Specific CAM capacity, mean cell discharge voltage, and gravimetric cell-level energy density of the LMR-NCM and NCA pouch cells. The values for the C-rates were referenced to their mean C/10 value and the corresponding standard deviation, based on the data shown in Fig. 2.

	Cell type	C/5	C/2	1C	2C	3C
Specific capacity	LMR-NCM	100.4 ± 2.9 %	97.6 ± 2.8 %	93.5 ± 2.7 %	87.8 ± 2.5 %	77.3 ± 2.2 %
	NCA	97.9 ± 1.1 %	94.4 ± 1.1 %	89.6 ± 1.0 %	76.7 ± 0.9 %	58.8 ± 0.7 %
Mean dis. voltage	LMR-NCM	98.5 ± 0.2 %	95.5 ± 0.2 %	91.8 ± 0.2 %	85.9 ± 0.2 %	81.1 ± 0.2 %
	NCA	99.7 ± 0.1 %	98.6 ± 0.1 %	96.8 ± 0.1 %	93.9 ± 0.1 %	91.6 ± 0.1 %
Energy density	LMR-NCM	99.1 ± 5.1 %	93.3 ± 4.8 %	87.0 ± 4.5 %	76.7 ± 4.0 %	63.7 ± 3.3 %
	NCA	97.7 ± 3.2 %	93.1 ± 3.0 %	88.0 ± 2.8 %	73.0 ± 2.4 %	54.6 ± 1.8 %

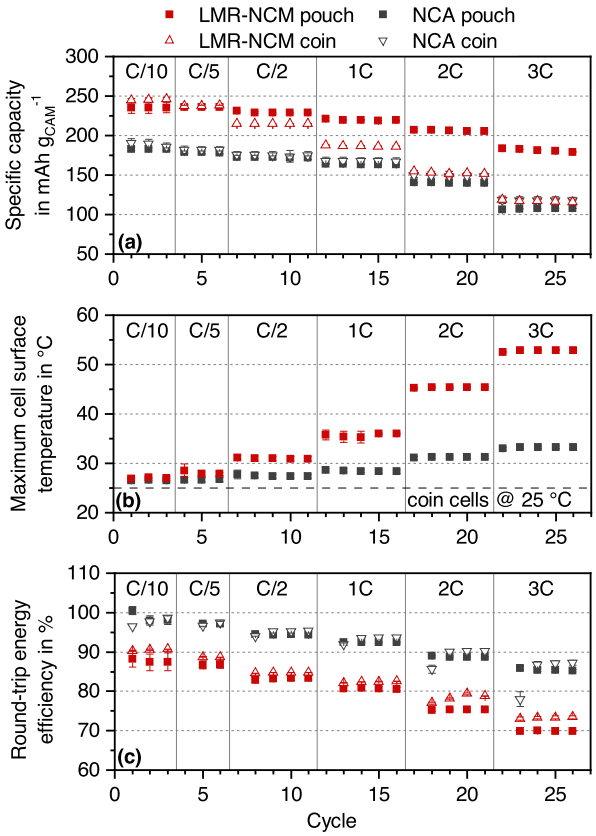

Figure 3. (a) Specific capacity related to the CAM mass of the LMR-NCM and NCA pouch cells in comparison to the laboratory coin cell measurements (all with graphite anodes), (b) maximum temperature measured on the surface of the pouch cells within the cell holder, and (c) round-trip energy efficiency calculated from the ratio of charge and discharge energy in a given cycle (note that the first cycle for each new C-rate setting is omitted). The pouch cell data correspond to those depicted in Fig. 2. The error bars for the coin cell measurements (barely visible) represent the standard deviation between 3 individual coin cells of each type.

to relax and the tips of the red curve mark the OCV profile after 1 h rest periods. A connection of these tips leave the gray shaded area that indicates the energy lost due to the LMR-NCM material hysteresis. The voltage profile of the NCA cells showed a minor hysteresis, which almost vanished completely when OCV rest periods were added to the cycling procedure. For this reason, the gray area in Fig. 4b is quasi not visible and appears as the dotted gray line. Via integration of the C/10 charge/discharge cycle, the energy loss ΔE_{tot} can be derived.[26]

$$\Delta E_{tot} = \oint I\ V\ dt \qquad [4]$$

Here, I and V refer to the cell current and voltage, respectively. An integration of the gray shaded areas in Fig. 4 yields ΔE_{OCV}. ΔE_R is then calculated using Eq. 3 and ΔE_{tot} determined from the black dashed lines in Fig. 4, using Eq. 4. The results are listed in Table V. These energy values, obtained by integration of the voltage curve of a single pouch cell of each type, are in good agreement with the measured C/10 round-trip efficiencies during the rate capability test, as stated in Table IV (87.5% ± 2.2% for the LMR-NCM and 98.1% ± 1.1% for the NCA pouch cells).

The total energy ΔE_{tot} that was lost over one C/10 charge/discharge cycle was substantially less for the NCA pouch cell, accounting for 2.3% of the charge energy E_{CH}. In contrast, the LMR-NCM cell lost 13.5% of the charge energy. More than a third of the total losses in the LMR-NCM cells at C/10 could be attributed to the intrinsic LMR-NCM material OCV hysteresis, whereas the ratio $\Delta E_{OCV}/\Delta E_{tot}$ was only 7% for the NCA cells. The NCA voltage hysteresis was almost only generated by overpotential contributions (ΔE_R).

The energy lost due to the OCV hysteresis of the LMR-NCM pouch cells caused the pronounced temperature rise visible in Fig. 3b. For lower discharge currents, there was enough time to dissipate the excess heat to the cell holders and the ambient air. If the same energy is released in a short time period, it cannot dissipate fast enough, resulting in an increasing cell temperature. The OCV voltage hysteresis of LMR-NCM and the resulting energy inefficiency are major drawbacks for commercialization and are thus in the focus of current research.[26] Regarding the discharge capacities and the round-trip energy efficiencies in the rate capability test, LMR-NCM is rather suited for high energy than high power applications.

Cycling behavior.—In the aging study (see Figs. 5 and 6), the large-format LMR-NCM and NCA pouch cells were evaluated with regards to their cycling behavior, using diagnostic checkups every 25 cycles. The dashed lines in Figs. 5a and 5c mark the 80% state-of-health (SOH) thresholds for the specific capacity and energy density, referenced to 80% of the initial capacity and cell energy density during the C/2 discharge in the rate capability test (i.e., 80% of the values in cycle 7 shown in Figs. 2a and 2c). With ongoing cycling, both the LMR-NCM and the NCA cells showed a gradual decline in their specific capacity.

Table IV. Mean round-trip energy efficiencies η of the LMR-NCM and NCA pouch cells (data shown in Figs. 2 and 3), listed here for the third cycle of each discharge C-rate. The details of the discharge rate capability test are given in Table II.

Type	DCH C-rate	E_{CH}	E_{DCH}	ΔE_{tot}	η
LMR-NCM	C/10	26.6 Wh	23.3 Wh	3.33 Wh	87.5% ± 2.2%
	C/5	26.2 Wh	22.7 Wh	3.46 Wh	86.8% ± 1.0%
	C/2	25.5 Wh	21.2 Wh	4.31 Wh	83.1% ± 0.6%
	1C	24.2 Wh	19.5 Wh	4.64 Wh	80.8% ± 0.5%
	2C	22.7 Wh	17.1 Wh	5.62 Wh	75.3% ± 0.3%
	3C	20.3 Wh	14.2 Wh	6.10 Wh	70.0% ± 0.1%
NCA	C/10	21.9 Wh	21.5 Wh	0.42 Wh	98.1% ± 1.1%
	C/5	21.4 Wh	20.8 Wh	0.62 Wh	97.1% ± 0.7%
	C/2	20.9 Wh	19.8 Wh	1.17 Wh	94.4% ± 0.4%
	1C	20.0 Wh	18.5 Wh	1.51 Wh	92.4% ± 0.2%
	2C	17.3 Wh	15.3 Wh	1.94 Wh	88.7% ± 0.3%
	3C	13.5 Wh	11.5 Wh	1.96 Wh	85.4% ± 0.3%

CH—charge, DCH—discharge, tot—total.

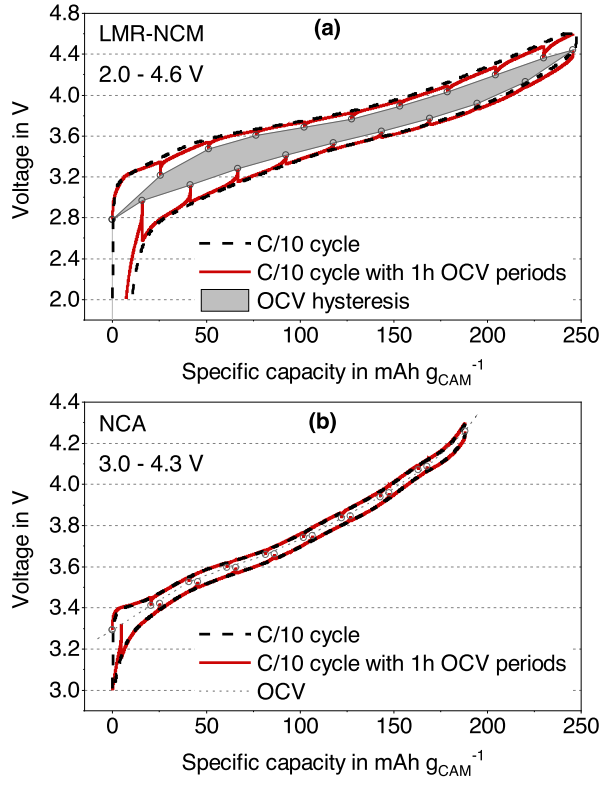

Figure 4. C/10 cycle procedures with and without 1 h OCV rest periods (see Table II) of an (a) LMR-NCM (2.0–4.6 V) and a (b) NCA (3.0–4.3 V) pouch cell at an ambient temperature of 25 °C.

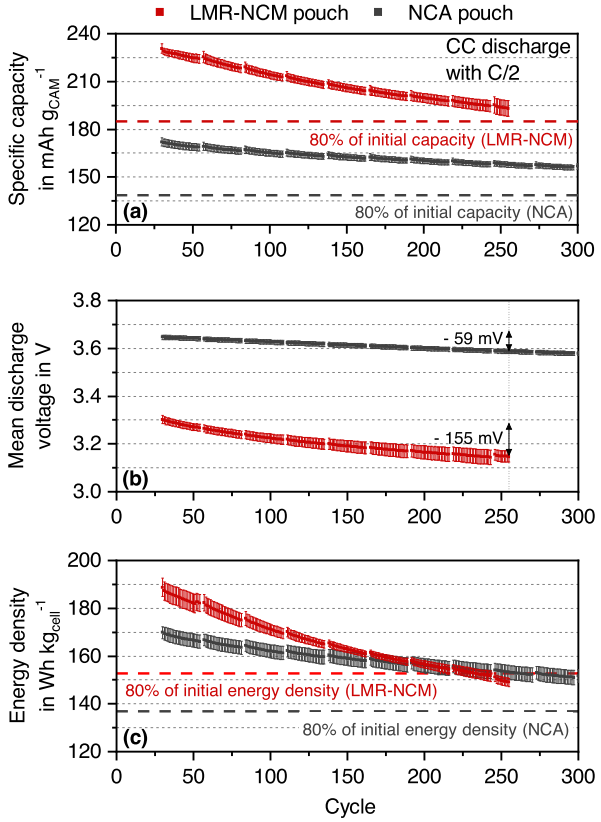

Figure 5. Cycle stability of the LMR-NCM and NCA pouch cells with regards to their (a) specific capacity related to the CAM mass, (b) mean cell discharge voltage, and (c) energy density related to the total mass of the cell. The cells were charged and discharged with a C/2 CC procedure including a CV phase at the end of charge at an ambient temperature of 25 °C in the voltage windows 2.0–4.6 V for LMR-NCM and 3.0–4.3 V for NCA, respectively (see Table II). Shown are the average values from 6 LMR-NCM and 5 NCA pouch cells, with error bars representing the standard deviation. The 80% initial capacity and energy density values marked by the dashed horizontal lines are referenced to the respective values in cycle 7 shown in Figs. 2a and 2c.

After approximately 250 cycles, too much gas was generated in the LMR-NCM pouch cells, which caused a rupture of the pouch foil. The strong gassing of the LMR-NCM cells likely derives from two effects: i) the oxidative decomposition of the electrolyte due to its reaction with released lattice oxygen at the very high degrees of delithiation of the LMR-NCM at 100% SOC[43]; ii) the gradual thermal decomposition of FEC,[44] which is particularly problematic for electrolytes with high FEC content. While we did not determine the gas composition, the literature suggests the evolution of mostly CO_2 at room temperature and over a few cycles with FEC based electrolytes,[36,45] whereas at elevated temperatures and over extended cycling in FEC/DEC (2:8 by volume) electrolyte also substantial amounts of H_2 were observed.[46] Even though the electrochemical behavior of the cells was still stable, the tests were stopped for safety reasons.

The NCA cells showed a more stable cycling behavior. For a better comparison of the two active materials, the NCA cell data are only plotted up to 300 cycles in Fig. 5; an overview of all the data up to 1600 cycles for the NCA pouch cells and up to 1000 cycles for the NCA coin cells is given in the Appendix in Fig. A·2, indicating the state-of-the-art performance of the large-format multilayer pouch cells. While the upscaling from coin to pouch cells for a state-of-the-art reference material is adequate, effects related to temperature and gas evolution that occur in LMR-NCM cells can clearly not be appropriately predicted from coin cell data, as they are operated isothermally and do not capture cell rupture effects from extensive gassing. Furthermore, small-scale laboratory cells generally have a higher electrolyte to active material ratio[35] that affects the aging behavior, which likely explains the slightly better capacity retention of the NCA coin vs NCA pouch cells (see Fig. A·2).

The specific capacity of the LMR-NCM pouch cells decreased faster, but remained higher than for the NCA pouch cells as shown in Fig. 5a. An extrapolation of the specific capacity of the LMR-NCM cells projects a crossover with the 80% threshold at approximately 350 cycles, as seen in Fig. A·1 in the Appendix. The NCA cells reached this point after 980 cycles (see Fig. A·2), as is also listed in Table VI. The aging behavior of both cell types is in good agreement

Table V. Energy losses derived from integrating the C/10 cycling curves. The total energy loss is divided into the hysteresis (ΔE_{OCV}) and the overpotential (ΔE_R) driven part.

Cell type	ΔE_{tot}	ΔE_{OCV}	ΔE_R	$\Delta E_{OCV} : \Delta E_R$	η	$\Delta E_{tot}/E_{CH}$
LMR-NCM	3.54 Wh	1.31 Wh	2.23 Wh	37 : 63	86.5%	13.5%
NCA	0.50 Wh	0.04 Wh	0.46 Wh	7 : 93	97.7%	2.3%

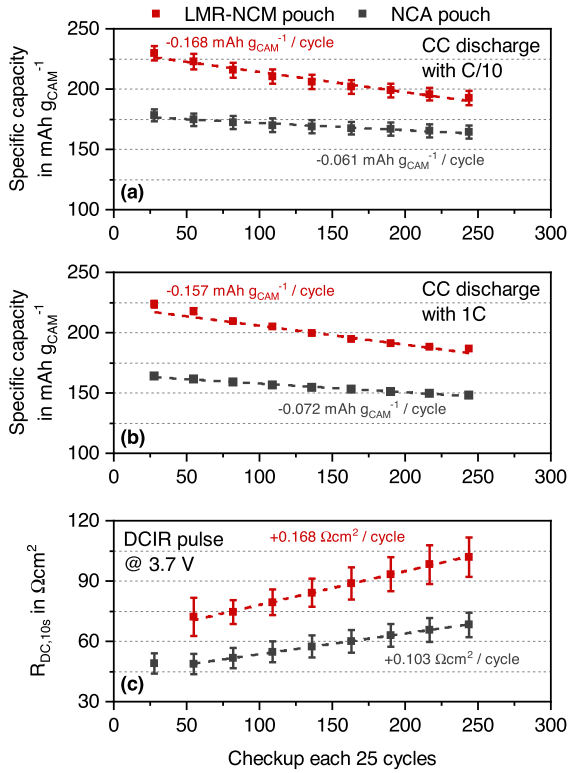

Figure 6. Checkup cycles (see Table II) of the LMR-NCM and NCA pouch cell tests shown in Fig. 5 with regards to their (a) specific C/10 discharge capacity related to the CAM mass, (b) specific 1C discharge capacity related to the CAM mass, and (c) DCIR for a 10 s C/2 discharge after charging the cells to a voltage of 3.7 V. The dashed lines indicate a linear regression of the mean values of the data points. In (a) and (c), average values from 6 LMR-NCM and 5 NCA pouch cells are shown, and the error bars represent the standard deviation. In (b), only average values of 2 cells of each type are shown, with the error bars representing their minimum/maximum values.

with published data on core-shell or surface-coated LMR-NCM in LMR-NCM/graphite cells[11,12] and of NCA in NCA/graphite cells.[6,47–49]

In Fig. 5b, the mean discharge voltage of the NCA cells showed a decrease of 59 mV after 255 cycles, which was less pronounced than the loss of 155 mV of the LMR-NCM cells. Voltage fading during prolonged cycling is a known issue of LMR-NCM and is caused by structural reordering from a layered to a spinel-like structure.[11,12,27,50–53] This has an additional, negative impact on the energy density decay displayed in Fig. 5c. In the beginning of the cycle-life test, the LMR-NCM cells offered a 11% higher cell energy density, but due to their faster degradation, their cell energy density became the same as that of the NCA cells at cycle 210. After 230 cycles, the LMR-NCM cells reached their 80% SOH criterion (red dashed line in Fig. 5c), whereas the NCA cells could be cycled 710 times until they reached 80% SOH (gray dashed line in Fig. 5c). The number of cycles up to 80% SOH with regards to their specific capacity and energy density for the two cell types are summarized in Table VI. Note that the LMR-NCM cells were charged to 4.6 V while the NCA cells were only charged to 4.3 V. At such high voltages, the electrolyte stability plays an important role and determines the aging behavior of these cells. Electrolyte oxidation at the cathode was probably one cause for an accelerated aging.[36,43,45] While higher temperatures also lead to an accelerated aging of lithium-ion cells,[47,54–57] this would not explain the comparatively faster degradation of the LMR-NCM cells since their average surface temperature during this aging test at C/2 of 29 °C (max. 31 °C) was similar to the 27 °C of that of the NCA cells (max. 28 °C).

Table VI. C/2 cycling stability defined by the 80% SOH criterion of the LMR-NCM and NCA pouch cells based on the data shown in Fig. 5.

80% SOH	LMR-NCM	NCA
Specific capacity	350 cycles[a)]	980 cycles
Energy density	230 cycles	710 cycles

a) extrapolation, see Fig. A·1 in the Appendix.

During the checkup cycles, the remaining capacity was assessed by a C/10 cycle, displayed in Fig. 6a. By applying a lower current, the cell polarization due to internal resistances, e.g., caused by growing passive layers or contact losses, is less. The influence of the internal resistance buildup on the capacity was evaluated with an additional 1C discharge, as seen in Fig. 6b. As described in the experimental section, only two pouch cells of each type were stressed with the 1C cycling procedure and therefore smaller error bars appear in Fig. 6b. By comparing the capacity of the C/10 with the 1C discharge, the capacity fading of the LMR-NCM cells is essentially independent of the C-rate, which suggests that the main degradation mechanism is the loss of cyclable lithium (e.g., via electrolyte oxidation) rather than an impedance buildup, at least for discharge C-rates up to 1C. For the NCA cells, the capacity fading at 1C is only ≈20% faster than at C/10, again suggesting that this decrease is not dominated by an impedance buildup.

The DCIR method was used to determine the internal cell resistance, employing a discharge pulse after a relaxation time of 1 h at 3.7 V (see Table II), which corresponded to a SOC of about 40% for both cell types. The first checkup of the LMR-NCM cells before the aging study was measured at a different voltage and was therefore left out. Here it should be noted, however, that the cell resistance is a strong function of SOC and thus cell voltage for both LMR-NCM[10] and for NCA[6] with a minimum resistance at mid-range SOCs. Based on the cathode-resolved impedance of NCM-811,[58] this resistance versus SOC behavior reflects that of the CAM. Moreover, because of the strong voltage hysteresis for LMR-NCM, the resistance also depends on whether the cell was charged or discharged before applying a DCIR pulse.[10] While the LMR-NCM cells exhibited ≈2-fold higher resistances, the resistances of both cell types rose equally by ≈40% between the 50th and the 250th cycle.

Therefore, the faster capacity and cell energy density degradation of the LMR-NCM cells compared to the NCA cells is unlikely due to polarization effects. Instead, based on the similar capacity fading rates of C/10 and 1C for both cell types (Figs. 6a and 6b), the performance degradation seems to be due to a loss of cyclable lithium. That the latter would be more pronounced at the higher cathode potentials of the LMR-NCM cells is not surprising, enhanced by the reaction of the electrolyte with lattice oxygen at the high degrees of delithiation at 100% SOC for this material.[43] Therefore, a more stable electrolyte system is still required for LMR-NCM CAMs, particularly for elevated temperatures due to the thermal instabilities of FEC in combination with $LiPF_6$.[44,46] Moreover, surface modifications of LMR-NCM materials could also reduce detrimental side reactions and improve the overall cycling stability.[11,12]

Conclusions

In this study, the LMR-NCM cathode active material, offering a high reversible capacity of 250 mAh g^{-1}, was employed with graphite anodes in large-format multilayer pouch cells, which were produced on a pilot scale production line. Comparable NCA/graphite pouch cells were produced and served as a reference for an evaluation of the performance of the LMR-NCM cells. The two pouch cell types were standardized to deliver an areal capacity of 2.3 mAh cm^{-2} or a total capacity of 5.5 Ah at a 1C discharge rate.

The characteristics of both cell types were compared against each other in a discharge rate capability test and an aging test.

Distinct differences between the two cell types were the wider voltage window of the LMR-NCM cells with a lower cutoff voltage of 2.0 V and an upper cutoff voltage of 4.6 V as well as the hysteresis of the voltage profile between charge and discharge even at C/10, while the NCA cells were cycled between 3.0–4.3 V and showed almost no voltage hysteresis. The LMR-NCM cells exhibited a specific capacity of 235 mAh g^{-1} for low discharge currents $\leqslant$ C/5, which amounted to a 30% increase compared to the 180 mAh g^{-1} of the NCA cells. However, because of the voltage hysteresis and the lower mean discharge voltage, the energy density of the LMR-NCM pouch cells was only ≈11% higher in comparison to the NCA cells.

The aging behavior was evaluated with a C/2 cycling test and initially showed a better performance of the LMR-NCM cells. However, both the specific capacity and the energy density showed a faster degradation, so that the LMR-NCM pouch cells were projected to reach their 80% SOH criterion with respect to the specific capacity after approximately 350 cycles, whereas the 80% of the initial energy density was reached after already 230 cycles, due to a faster voltage fading. On the other hand, these 80% SOH criteria were reached after 980 cycles and 710 cycles, respectively for the NCA cells. Checkup cycles including the measured cell resistances showed that the increasing cell resistance was not dominating the overall capacity decay, and that instead the performance degradation of both the LMR-NCM and the NCA cells is rather due to a loss of cyclable lithium. The overall cycle life of the LMR-NCM pouch cells was limited to ≈250 cycles due to cell rupture caused by the strong gassing of the LMR-NCM cells.

In conclusion, LMR-NCM proved to be a high capacitive CAM, which is comparatively cheap because of its high manganese share compared to cobalt and nickel. Long-term stability issues still have to be addressed, e.g., a surface treatment of LMR-NCM could bring improvements on the material level, and should be examined in combination with an adequate electrolyte system. Because of the heat accumulation for discharge rates above C/2, an application of LMR-NCM in large-format cells should be critically assessed together with the accompanying cooling system. This issue will be addressed in our future research. Generally, the material is more suited for high energy than high power applications.

Acknowledgments

This work was financially supported by the German Federal Ministry of Education and Research (BMBF) under grant number 03XP0081 (ExZellTUM II) and 03XP0255 (ExZellTUM III). For the production of the large-format pouch cells, special thanks go to the battery production research team of iwb, in particular to Benedikt Stumper, Ajinkya Metkar, Nicolas Billot, Till Günther, Johannes Kriegler, Fabian Konwitschny, Celestine Singer, Hoda Mohseni, Sophie Grabmann, and Joscha Schnell. The authors gratefully acknowledge Tobias Teufl and Manual Mendez from BASF SE for the helpful scientific discussions, Robin Schregle for his contribution to the CAD drawing of the cell holder, and Fabian Linsenmann for his critical feedback.

Appendix

The measured cycling data of the LMR-NCM pouch cells was limited to approximately 250 cycles due to gassing induced rupture of the cells. To have an assessment of the 80% SOH criterion regarding the specific capacity of the cells, an extrapolation was carried out, yielding a projected crossover after approximately 350 cycles (see Fig. A·1). The following fitting function ($R^2 = 0.9986$) was used for this extrapolation (see black line in Fig. A·1), with x representing the cycle number and y the specific capacity in mAh g_{CAM}^{-1}:

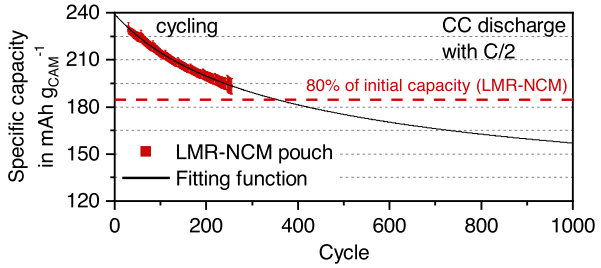

Figure A·1. Extrapolation of the specific capacity related to the mass of the active material during C/2 cycling of the LMR-NCM pouch cells.

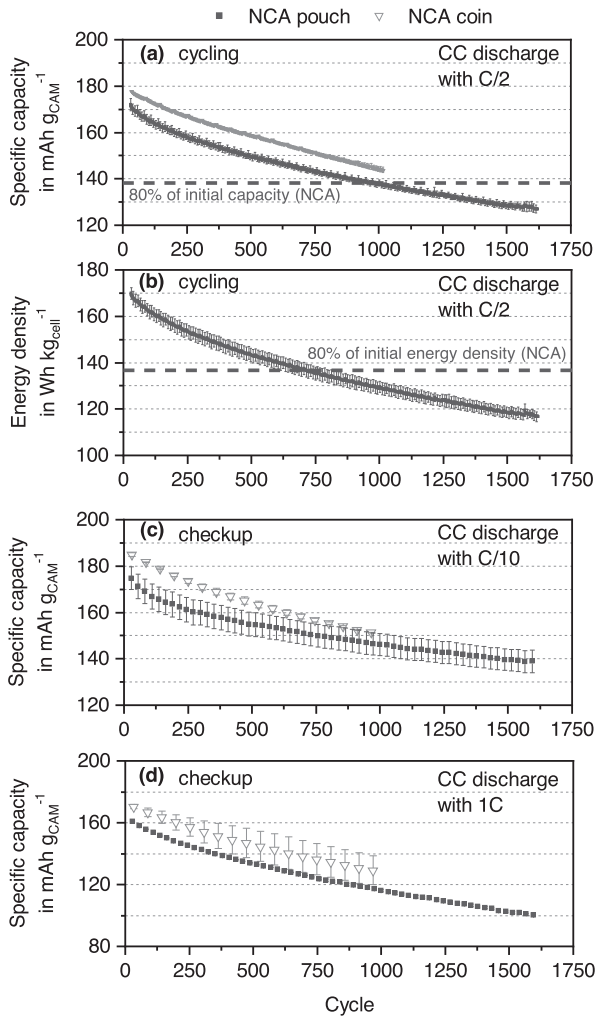

Figure A·2. Cycle stability including all cycles and checkups of the NCA pouch and coin cells. (a) Specific capacity related to the mass of the active material and (b) energy density related to the total mass of the cell during C/2 cycling (only displayed for the NCA pouch cells). (c) Specific C/10 discharge capacity and (d) specific 1C discharge capacity related to the mass of the active material during the checkups every 25 C/2 cycles. The cells were charged with a C/2 CC procedure including a CV phase at the end of charge at an ambient temperature of 25 °C in the voltage window 3.0–4.3 V (see Table II).

$$y = \frac{2107}{\sqrt{218.8 + x}} + 96.61 \qquad [A\cdot1]$$

To allow for a more clear comparison between the LMR-NCM and the NCA cells, Fig. 5 only shows the initial 300 cycles for the NCA cells. The total cycling stability of the NCA pouch cells including the laboratory NCA coin cells is displayed in Fig. A·2. The coin cells were cycled up to 1000 cycles while the pouch cell aging test was carried out for over 1600 cycles. The energy density in Fig. A·2b is only displayed for the pouch cells, because this value is related to the total cell mass, which is not representative for coin cells.

ORCID

Ludwig Kraft https://orcid.org/0000-0003-4324-426X
Tanja Zünd https://orcid.org/0000-0002-1650-3636
David Schreiner https://orcid.org/0000-0001-8035-0438
Rebecca Wilhelm https://orcid.org/0000-0002-4161-5197
Florian J. Günter https://orcid.org/0000-0002-5967-6801
Hubert A. Gasteiger https://orcid.org/0000-0001-8199-8703
Andreas Jossen https://orcid.org/0000-0003-0964-1405

References

1. D. Andre, S.-J. Kim, P. Lamp, S. F. Lux, F. Maglia, O. Paschos, and B. Stiaszny, "Future generations of cathode materials: an automotive industry perspective." *Journal of Materials Chemistry A*, **3**, 6709 (2015).
2. S.-T. Myung, F. Maglia, K.-J. Park, C. S. Yoon, P. Lamp, S.-J. Kim, and Y.-K. Sun, "Nickel-rich layered cathode materials for automotive lithium-ion batteries: achievements and perspectives." *ACS Energy Lett.*, **2**, 196 (2017).
3. M. A. Hannan, M. M. Hoque, A. Mohamed, and A. Ayob, "Review of energy storage systems for electric vehicle applications: issues and challenges." *Renew. Sustain. Energy Rev.*, **69**, 771 (2017).
4. R. Schmuch, R. Wagner, G. Hörpel, T. Placke, and M. Winter, "Performance and cost of materials for lithium-based rechargeable automotive batteries." *Nat. Energy*, **3**, 267 (2018).
5. C. S. Yoon, K.-J. Park, U.-H. Kim, K. H. Kang, H.-H. Ryu, and Y.-K. Sun, "High-energy Ni-rich Li[$Ni_xCo_yMn_{1-x-y}$]O_2 cathodes via compositional partitioning for next-generation electric vehicles." *Chemistry of Materials*, **29**, 10436 (2017).
6. R. Weber, A. J. Louli, K. P. Plucknett, and J. R. Dahn, "Resistance growth in lithium-ion pouch cells with $LiNi_{0.80}Co_{0.15}Al_{0.05}O_2$ positive electrodes and proposed mechanism for voltage dependent charge-transfer resistance." *J. Electrochem. Soc.*, **166**, A1779 (2019).
7. S. Hwang and E. A. Stach, "Using in situ and operando methods to characterize phase changes in charged lithium nickel cobalt aluminum oxide cathode materials." *J. Phys. D*, **53**, 113002 (2020).
8. J. R. Croy, M. Balasubramanian, K. G. Gallagher, and A. K. Burrell, "Review of the U.S. department of energy's deep dive effort to understand voltage fade in Li- and Mn-rich cathodes." *Acc. Chem. Res.*, **48**, 2813 (2015).
9. G. E. Blomgren, "The development and future of lithium ion batteries." *J. Electrochem. Soc.*, **164**, A5019 (2016).
10. T. Teufl, D. Pritzl, S. Solchenbach, H. A. Gasteiger, and M. A. Mendez, "State of charge dependent resistance build-up in Li- and Mn-rich layered oxides during lithium extraction and insertion." *J. Electrochem. Soc.*, **166**, A1275 (2019).
11. D. Becker, M. Börner, A. Friesen, S. Klein, U. Rodehorst, M. Diehl, M. Winter, T. Placke, and R. Schmuch, "Towards high-performance Li-rich NCM—graphite cells by germanium-polymer coating of the positive electrode material." *J. Electrochem. Soc.*, **167**, 060524 (2020).
12. J. Helbig, T. Beuse, V. Siozios, T. Placke, M. Winter, and R. Schmuch, "Li—Mn-rich cathode materials with low-cobalt content and core-shell particle design for high-energy lithium ion batteries." *J. Electrochem. Soc.*, **167**, 060519 (2020).
13. K. G. Gallagher and P. A. Nelson, "Manufacturing costs of batteries for electric vehicles." *Lithium-Ion Batteries: Advances and Applications*, ed. G. Pistoia (Elsevier, Amsterdam) p. 97 (2014).
14. O. Gröger, H. A. Gasteiger, and J.-P. Suchsland, "Review–electromobility: batteries or fuel cells?" *J. Electrochem. Soc.*, **162**, A2605 (2015).
15. A. Kwade, W. Haselrieder, R. Leithoff, A. Modlinger, F. Dietrich, and K. Droeder, "Current status and challenges for automotive battery production technologies." *Nat. Energy*, **3**, 290 (2018).
16. UK Electric Vehicle and Battery Production Potential to 2040. March 2020. https://faraday.ac.uk/publications/ev-economics-study/.
17. SMM Information & Technology Co, Ltd., Nickel price. Accessed 2/9/2021 https://price.metal.com/Nickel.
18. SMM Information & Technology Co, Ltd., Manganese price. Accessed 2/9/2021 https://price.metal.com/Manganese.
19. Y.-K. Sun, D.-J. Lee, Y. J. Lee, Z. Chen, and S.-T. Myung, "Cobalt-free nickel rich layered oxide cathodes for lithium-ion batteries." *ACS Applied Materials & Interfaces*, **5**, 11434 (2013).
20. N. Zhang, N. Zaker, H. Li, A. Liu, J. Inglis, L. Jing, J. Li, Y. Li, G. A. Botton, and J. R. Dahn, "Cobalt-free nickel-rich positive electrode materials with a core-shell structure." *Chemistry of Materials*, **31**, 10150 (2019).
21. H. Li, M. Cormier, N. Zhang, J. Inglis, J. Li, and J. R. Dahn, "Is cobalt needed in nickel-rich positive electrode materials for lithium ion batteries?" *J. Electrochem. Soc.*, **166**, A429 (2019).
22. W.-C. Chen, Y.-F. Song, C.-C. Wang, Y. Liu, D. T. Morris, P. A. Pianetta, J. C. Andrews, H.-C. Wu, and N.-L. Wu, "Study on the synthesis-microstructure-performance relationship of layered Li-excess nickel-manganese oxide as a Li-ion battery cathode prepared by high-temperature calcination." *Journal of Materials Chemistry A*, **1**, 10847 (2013).
23. Trading Economics, Cobalt price. Accessed 2/9/2021 https://tradingeconomics.com/commodity/cobalt.
24. Trading Economics, Lithium price. Accessed 2/9/2021 https://tradingeconomics.com/commodity/lithium.
25. Trading Economics, Aluminum price. Accessed 2/9/2021 https://tradingeconomics.com/commodity/aluminum.
26. G. Assat, S. L. Glazier, C. Delacourt, and J.-M. Tarascon, "Probing the thermal effects of voltage hysteresis in anionic redox-based lithium-rich cathodes using isothermal calorimetry." *Nat. Energy*, **4**, 647 (2019).
27. N. Leifer, T. Penki, R. Nanda, J. Grinblat, S. Luski, D. Aurbach, and G. Goobes, "Linking structure to performance of $Li_{1.2}Mn_{0.54}Ni_{0.13}Co_{0.13}O_2$ (Li and Mn rich NMC) cathode materials synthesized by different methods." *Physical Chemistry Chemical Physics: PCCP*, **22**, 9098 (2020).
28. J. B. Quinn, T. Waldmann, K. Richter, M. Kasper, and M. Wohlfahrt-Mehrens, "Energy density of cylindrical li-ion cells: a comparison of commercial 18650 to the 21700 cells." *J. Electrochem. Soc.*, **165**, A3284 (2018).
29. M. J. Lain, J. Brandon, and E. Kendrick, "Design strategies for high power vs high energy lithium ion cells." *Batteries*, **5**, 64 (2019).
30. Y. Ding, Z. P. Cano, A. Yu, J. Lu, and Z. Chen, "Automotive li-ion batteries: current status and future perspectives." *Electrochemical Energy Reviews*, **2**, 1 (2019).
31. H. Popp, N. Zhang, M. Jahn, M. Arrinda, S. Ritz, M. Faber, D. U. Sauer, P. Azais, and I. Cendoya, "Ante-mortem analysis, electrical, thermal, and ageing testing of state-of-the-art cylindrical lithium-ion cells." *E & I Elektrotechnik und Informationstechnik*, **8**, 104 (2020).
32. M. Singh, J. Kaiser, and H. Hahn, "Thick electrodes for high energy lithium ion batteries." *J. Electrochem. Soc.*, **162**, A1196 (2015).
33. J. Sturm, A. Rheinfeld, I. Zilberman, F. B. Spingler, S. Kosch, F. Frie, and A. Jossen, "Modeling and simulation of inhomogeneities in a 18650 nickel-rich, silicon-graphite lithium-ion cell during fast charging." *Journal of Power Sources*, **412**, 204 (2019).
34. G. Reinhart, T. Zeilinger, J. Kurfer, M. Westermeier, C. Thiemann, M. Glonegger, M. Wunderer, C. Tammer, M. Schweier, and M. Heinz, "Research and demonstration center for the production of large-area lithium-ion cells." *Future Trends in Production Engineering*, ed. G. Schuh, R. Neugebauer, and E. Uhlmann (Springer, Berlin, Heidelberg) Vol. 12, p. 3 (2013).
35. D. Schreiner et al., "Comparative evaluation of lmr-ncm and nca cathode active materials in multilayer lithium-ion pouch cells—part I: production, electrode characterization, and formation." *J. Electrochem. Soc.*, **168**, 030507 (2021).
36. T. Teufl, B. Strehle, P. Müller, H. A. Gasteiger, and M. A. Mendez, "Oxygen release and surface degradation of Li- and Mn-rich layered oxides in variation of the Li_2MnO_3 content." *J. Electrochem. Soc.*, **165**, A2718 (2018).
37. A. Guéguen, C. Bolli, M. A. Mendez, and E. J. Berg, "Elucidating the reactivity of tris(trimethylsilyl)phosphite and tris(trimethylsilyl)phosphate additives in carbonate electrolytes—a comparative online electrochemical mass spectrometry study." *ACS Appl. Energy Mater.*, **3**, 290 (2020).
38. S.-H. Kang, W.-S. Yoon, K.-W. Nam, X.-Q. Yang, and D. P. Abraham, "Investigating the first-cycle irreversibility of lithium metal oxide cathodes for Li batteries." *J. Mater. Sci.*, **43**, 4701 (2008).
39. S. S. Zhang, "Identifying rate limitation and a guide to design of fast-charging Li-ion battery." *InfoMat*, **2**, 942 (2020).
40. J. Zheng, W. Shi, M. Gu, J. Xiao, P. Zuo, C. Wang, and J.-G. Zhang, "Electrochemical kinetics and performance of layered composite cathode material $Li[Li_{0.2}Ni_{0.2}Mn_{0.6}]O_2$." *J. Electrochem. Soc.*, **160**, A2212 (2013).
41. W. Mao, G. Ai, Y. Dai, Y. Fu, X. Song, H. Lopez, and V. Battaglia, "Nature of the impedance at low states of charge for high-capacity, lithium and manganese-rich cathode materials." *J. Electrochem. Soc.*, **163**, A3091 (2016).
42. P. Meister, H. Jia, J. Li, R. Kloepsch, M. Winter, and T. Placke, "Best practice: performance and cost evaluation of lithium ion battery active materials with special emphasis on energy efficiency." *Chemistry of Materials*, **28**, 7203 (2016).
43. J. Wandt, A. T. Freiberg, A. Ogrodnik, and H. A. Gasteiger, "Singlet oxygen evolution from layered transition metal oxide cathode materials and its implications for lithium-ion batteries." *Mater. Today*, **21**, 825 (2018).
44. K. Kim, I. Park, S.-Y. Ha, Y. Kim, M.-H. Woo, M.-H. Jeong, W. C. Shin, M. Ue, S. Y. Hong, and N.-S. Choi, "Understanding the thermal instability of fluoroethylene carbonate in $LiPF_6$-based electrolytes for lithium ion batteries." *Electrochimica Acta*, **225**, 358 (2017).
45. T. Teufl, D. Pritzl, P. Krieg, B. Strehle, M. A. Mendez, and H. A. Gasteiger, "Operating EC-based electrolytes with Li- and Mn-rich NCMs: the role of O_2-release on the choice of the cyclic carbonate." *J. Electrochem. Soc.*, **167**, 110505 (2020).
46. T. Teufl, D. Pritzl, S. Solchenbach, M. A. Mendez, and H. A. Gasteiger, (2021), Thermal stability of FEC-based electrolytes for high-voltage Li-ion batteries, Manuscript in preparation.
47. M. Uitz, M. Sternad, S. Breuer, C. Täubert, T. Traußnig, V. Hennige, I. Hanzu, and M. Wilkening, "Aging of Tesla's 18650 lithium-ion cells: correlating solid-electrolyte-interphase evolution with fading in capacity and power." *J. Electrochem. Soc.*, **164**, A3503 (2017).
48. S. Hildebrand, C. Vollmer, M. Winter, and F. M. Schappacher, "Al_2O_3 , SiO_2 and TiO_2 as coatings for Safer $LiNi_{0.8}Co_{0.15}Al_{0.05}O_2$ cathodes: electrochemical

performance and thermal analysis by accelerating rate calorimetry." *J. Electrochem. Soc.*, **164**, A2190 (2017).
49. J. Li, J. Harlow, N. Stakheiko, N. Zhang, J. Paulsen, and J. Dahn, "Dependence of cell failure on cut-off voltage ranges and observation of kinetic hindrance in $LiNi_{0.8}Co_{0.15}Al_{0.05}O_2$." *J. Electrochem. Soc.*, **165**, A2682 (2018).
50. D. Mohanty, A. S. Sefat, J. Li, R. A. Meisner, A. J. Rondinone, E. A. Payzant, D. P. Abraham, D. L. Wood, and C. Daniel, "Correlating cation ordering and voltage fade in a lithium-manganese-rich lithium-ion battery cathode oxide: a joint magnetic susceptibility and TEM study." *Physical Chemistry Chemical Physics: PCCP*, **15**, 19496 (2013).
51. D. Mohanty, J. Li, D. P. Abraham, A. Huq, E. A. Payzant, D. L. Wood, and C. Daniel, "Unraveling the voltage-fade mechanism in high-energy-density lithium-ion batteries: origin of the tetrahedral cations for spinel conversion." *Chemistry of Materials*, **26**, 6272 (2014).
52. M. Sathiya et al., "Origin of voltage decay in high-capacity layered oxide electrodes." *Nat. Mater.*, **14**, 230 (2015).
53. K. Kleiner, B. Strehle, A. R. Baker, S. J. Day, C. C. Tang, I. Buchberger, F.-F. Chesneau, H. A. Gasteiger, and M. Piana, "Origin of high capacity and poor cycling stability of Li-rich layered oxides: a long-duration in situ synchrotron powder diffraction study." *Chemistry of Materials*, **30**, 3656 (2018).
54. M. Wohlfahrt-Mehrens, C. Vogler, and J. Garche, "Aging mechanisms of lithium cathode materials." *Journal of Power Sources*, **127**, 58 (2004).
55. J. Vetter, P. Novák, M. R. Wagner, C. Veit, K.-C. Möller, J. O. Besenhard, M. Winter, M. Wohlfahrt-Mehrens, C. Vogler, and A. Hammouche, "Ageing mechanisms in lithium-ion batteries." *Journal of Power Sources*, **147**, 269 (2005).
56. Y. Wu, P. Keil, S. F. Schuster, and A. Jossen, "Impact of temperature and discharge rate on the aging of a $LiCoO_2/LiNi_{0.8}Co_{0.15}Al_{0.05}O_2$ lithium-ion pouch cell." *J. Electrochem. Soc.*, **164**, A1438 (2017).
57. P. Keil and A. Jossen, "Impact of dynamic driving loads and regenerative braking on the aging of lithium-ion batteries in electric vehicles." *J. Electrochem. Soc.*, **164**, A3081 (2017).
58. F. Friedrich, B. Strehle, A. T. S. Freiberg, K. Kleiner, S. J. Day, C. Erk, M. Piana, and H. A. Gasteiger, "Choice–capacity fading mechanisms of NCM-811 cathodes in lithium-ion batteries studied by X-ray diffraction and other diagnostics." *J. Electrochem. Soc.*, **166**, A3760 (2019).

3.2 Thermal Effects of LMR-NCM in Large-Format Cells

In this section, the article titled *Implications of the Heat Generation of LMR-NCM on the Thermal Behavior of Large-Format Lithium-Ion Batteries* [48] is presented.

In the previously conducted discharge rate capability test, a strong increase in cell temperature was detected for the LMR-NCM/graphite pouch cells. For a 3C discharge, the LMR-NCM/graphite pouch cells reached a surface temperature of 53 °C while the NCA/graphite pouch cells only reached 33 °C [44]. The strong heat generation of the LMR-NCM/graphite cells is caused by an energy inefficiency that is linked to overpotentials and the pronounced voltage hysteresis of LMR-NCM. In order to quantify the released heat, calorimetric measurements were performed with LMR-NCM/graphite coin cells and also NCA/graphite coin cells. During charging operations, the LMR-NCM/graphite cells generate more than double the heat than the NCA/graphite cells. During discharge operations, this ratio of released heat even increases to four times as much.

The heat generation obtained from the calorimetric measurements was then scaled via the cathode area to larger cell formats and with the aid of 3D thermal models, simulation studies with different cooling strategies were conducted. Without any active cooling of larger LMR-NCM/graphite cells, discharge C-rates lower than C/2 are recommended in order to keep the cell temperature within an acceptable temperature range. For higher C-rates, an application and cell format specific cooling strategy has to be developed, otherwise critical temperatures above 60 °C are easily reached. The investigated convective surface cooling and base plate cooling scenarios revealed, that especially large prismatic cell formats, which are commonly used in EVs, are unfavorable for LMR-NCM, as the large amount of heat cannot be adequately dissipated and results in a pronounced temperature increase. In general, the active material LMR-NCM is more suited for high energy applications that operate with lower currents than high power applications.

Author contribution Tanja Zünd built the coin cells and Alexander Hoefling conducted the calorimetric measurements. The electrochemical data and the heat generation data was analyzed by Ludwig Kraft and discussed with Alexander Hoefling, Tanja Zünd, and Alexander Kunz. The thermal models were implemented and parameterized by Ludwig Kraft; the thermal parameterization was supported by Marco Steinhardt. Ludwig Kraft carried out the upscaling calculations and conducted the simulation studies. The manuscript was written by Ludwig Kraft and edited by the co-authors. All authors discussed the data and commented on the results.

Implications of the Heat Generation of LMR-NCM on the Thermal Behavior of Large-Format Lithium-Ion Batteries

Ludwig Kraft, Alexander Hoefling, Tanja Zünd, Alexander Kunz, Marco Steinhardt, Jens Tübke, Andreas Jossen

Journal of The Electrochemical Society 168 (5), p. 053505, 2021

Permanent weblink:
http://dx.doi.org/10.1149/1945-7111/ac0069

Journal of The Electrochemical Society, 2021 **168** 053505

Implications of the Heat Generation of LMR-NCM on the Thermal Behavior of Large-Format Lithium-Ion Batteries

Ludwig Kraft,[1,*,z] Alexander Hoefling,[2,3] Tanja Zünd,[4,*] Alexander Kunz,[1] Marco Steinhardt,[1] Jens Tübke,[2,3] and Andreas Jossen[1]

[1]*Institute for Electrical Energy Storage Technology, Technical University of Munich (TUM), Munich, Germany*
[2]*Helmholtz Institute Ulm (HIU), Ulm, Germany*
[3]*Karlsruhe Institute of Technology (KIT), Karlsruhe, Germany*
[4]*Chair of Technical Electrochemistry, Technical University of Munich (TUM), Garching, Germany*

Lithium- and manganese-rich NCM (LMR-NCM) cathode active materials exhibit a pronounced energy inefficiency during charge and discharge that results in a strong heat generation during operation. The implications of such a heat generation are investigated for large-format lithium-ion batteries. Small laboratory cells are generally considered isothermal, but for larger cell formats this heat cannot be neglected. Therefore, the heat generation of LMR-NCM/graphite coin cells and NCA/graphite coin cells as a reference is measured for varying charge/discharge rates in an isothermal heat flow calorimeter and scaled to larger standardized cell formats. With the aid of thermal 3D models, the temperature evolution within these cell formats under different charge/discharge operations and cooling conditions is analyzed. Without an additional heat sink and any active cooling of larger LMR-NCM/graphite cells, discharge C-rates lower than C/2 are advisable to keep the cell temperature below a critical threshold. If the loads are increased, the cooling strategy has to be adapted to the specific cell format, otherwise critical temperatures above 60 °C are easily reached. For the investigated convective surface cooling and base plate cooling scenarios, thick prismatic cell formats with LMR-NCM are generally unfavorable, as the large amount of heat cannot be adequately dissipated.
 [DOI: 10.1149/1945-7111/ac0069]

Manuscript submitted February 19, 2021; revised manuscript received April 27, 2021. Published May 27, 2021.

State-of-the-art electric vehicles (EVs) rely on lithium-ion batteries that come in different sizes and chemical compositions. The driving range and thereby the accompanying customer acceptance of EVs is highly dependent on the energy density of the used battery system. In order to increase the energy density, the latest trend goes toward larger cell formats and active materials with a higher specific capacity,[1–4] whereas the thermal behavior of these cells, including the thermal management system that is necessary to keep an optimal operating range, is often neglected.[5]

There are three main designs of cell formats, namely cylindric, prismatic, and pouch. While most automobile manufacturers rely on either prismatic or pouch cells, Tesla poses an exception and uses cylindric cells in their EVs.[3,4] Their early Tesla Model S in 2012 relied on 18 650 cylindric cells, while the more recent Tesla Model 3 uses advanced 21 700 cells.[3,4] Reportedly, Tesla now manufactures even larger 46 800 cells.[6] By changing the cell format from 18 650 to 21 700, the cell volume increases, meaning that more active material can be packed into the cell, which results in an increased energy content of around 49% per cell and potentially lower production costs.[7,8] A similar trend can be seen for prismatic and pouch cell formats used by automobile manufacturers, some of them are defined in the standard DIN 91252,[9] which gives design specifications for lithium-ion battery cells. Within this standard, the geometric dimensions of prismatic and pouch cell formats for hybrid electric vehicles (HEVs), plug-in hybrid electric vehicles (PHEVs), and battery electric vehicles (BEVs) are defined. As an example, the prismatic format BEV4 features an increased volume of 53% in comparison to the older BEV1 format.

Besides larger cell formats, anode active materials (AAMs) and cathode active materials (CAMs) with higher specific capacities are used for automotive cells. Almost all automotive cells contain graphite AAMs with a theoretical specific capacity of 372 mAh g^{-1}. Only a few use lithium-titanate (LTO), e.g., Honda in its 2013 Fit EV,[3,4,10] with only 175 mAh g^{-1} at a comparably high potential of ≈1.55 V vs Li/Li^+.[11,12] Pristine silicon offers a theoretical capacity of 4200 mAh g^{-1} that is accompanied by high volume changes up to 320%.[12] By adding some silicon to graphite anodes, the specific capacity can be boosted,[13–15] which is why cells with silicon-graphite (Si-C) composite anodes are reportedly used in more recent EVs like the Tesla Model X or Model 3.[3,4]

There is a variety of CAMs for automotive cells, ranging from layered lithium-nickel-cobalt-manganese-oxide (NCM, 160–200 mAh g^{-1}) and lithium-nickel-cobalt-aluminum-oxide (NCA, 180–200 mAh g^{-1}) to spinel lithium-manganese-oxide (LMO, 100–120 mAh g^{-1}) to olivine lithium-iron-phosphate (LFP, 160–165 mAh g^{-1}) or even a blend of two or more of these materials.[3,4,7,10] A CAM that offers a higher specific capacity of around 250 mAh g^{-1}[10,16–19] is lithium- and manganese-rich NCM (LMR-NCM). LMR-NCM is environmentally benign and a low cost alternative to nickel-rich materials due to a high manganese content,[18,20] but faces structural changes accompanied by voltage fading as well as a pronounced voltage hysteresis.[18–23] The material LMR-NCM is in the focus of current research and it was shown that cells containing LMR-NCM can be cycled for several hundred cycles before they reach a state-of-health of 80%.[18,19,24] Thereby, the capacity loss is not only related to structural changes of LMR-NCM, but also to electrolyte stability issues, as LMR-NCM is often cycled up to 4.7–4.8 V vs Li/Li^+.[18,21,24] Despite the remaining challenges, the high specific capacity combined with the lower material costs render LMR-NCM to a promising CAM for future lithium-ion batteries.[3,20,25]

Meister et al.[26] classified the energy efficiency of various CAMs and AAMs for a 1C charge/discharge cycle. In their study, LMR-NCM (0.5 Li_2MnO_3 · 0.5 $LiNi_{0.4}Co_{0.2}Mn_{0.4}O_2$) reached a 85% round-trip energy efficiency, for comparison, NCM-111 was classified with 96%, NCA was not studied. Of the investigated AAMs, graphite reached the highest round-trip energy efficiency with 94%. The Si-C composite (20 wt% silicon, 60 wt% graphite, 10 wt% binder, 10 wt% carbon black) with a practical capacity of around 1100 mAh g^{-1} in the first cycles, reached a lower efficiency of 89%. The energy inefficiency of the active material LMR-NCM, but also of the Si-C composite, was mainly caused by a lower voltage efficiency, which is defined as the ratio of the mean discharge voltage to the mean charge voltage in a full cycle.[26]

In our previous publication, multilayer LMR-NCM/graphite and NCA/graphite pouch cells with a nominal capacity of around 6–7 Ah

*Electrochemical Society Student Member.
[z]E-mail: ludwig.kraft@tum.de

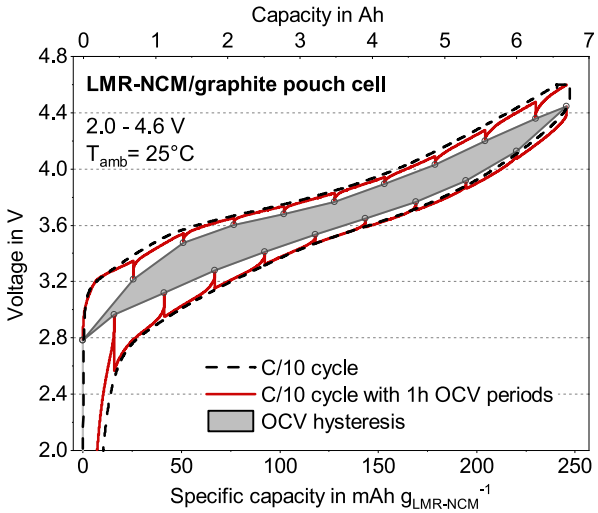

Figure 1. C/10 voltage profiles with and without 1 h OCV rest periods of an LMR-NCM/graphite pouch cell that was cycled in a voltage window of 2.0–4.6 V at an ambient temperature of 25 °C. Figure derived from Ref. 24.

Table I. Round-trip energy efficiencies of multilayer LMR-NCM/graphite and NCA/graphite pouch cells with a nominal capacity of 6–7 Ah during a discharge rate capability test at an ambient temperature of 25 °C.[24] The temperatures were measured on the surface of the pouch cells within cell holders and the stated maximum surface temperatures $T_{max,surf}$ were reached during the discharge.

DCH C-rate	LMR-NCM/graphite		NCA/graphite	
	EE	$T_{max,surf}$	EE	$T_{max,surf}$
C/10	88%	27 °C	98%	27 °C
1C	81%	36 °C	92%	28 °C
3C	70%	53 °C	85%	33 °C

Note. DCH—discharge, EE—round-trip energy efficiency.

were manufactured on the pilot scale production line at the Technical University of Munich.[27] The C/10 voltage profiles of an LMR-NCM/graphite pouch cell are displayed in Fig. 1. By adding 1 h open circuit voltage (OCV) rest periods, the voltage difference between charge and discharge can be approximately separated into a voltage drop due to overpotentials during cycling and the LMR-NCM OCV hysteresis.[24] The overpotentials are caused by poor charge transfer kinetics and/or a slow solid-state diffusion of LMR-NCM, especially at low states-of-charge (SOC).[17,28,29] While there still is a minimal voltage relaxation after 1 h OCV, an OCV hysteresis remains for LMR-NCM materials even after resting periods of several days.[20,30]

In a discharge rate capability test, the LMR-NCM/graphite pouch cells reached ≈81% round-trip energy efficiency for a 1C discharge, while the NCA/graphite pouch cells reached ≈92%.[24] These values are in very good agreement with the values stated by Meister et al.[26] if NCA is considered to have a similar energy efficiency like NMC-111. The discharge rate capability tests also revealed a strong increase in cell temperature for the LMR-NCM/graphite pouch cells with increasing discharge currents, which can be ascribed to the energy loss due to overpotentials and the LMR-NCM OCV hysteresis. The gray shaded area in Fig. 1 indicates the approximate share of the OCV hysteresis of LMR-NCM, which is presumably current-independent, and the electrical work that is lost due to such a voltage hysteresis is most likely dissipated as waste heat.[20,24] So with rising C-rates, the share of the irreversible heat due to overpotentials likely dominates the total heat generation. In Table I, the round-trip energy efficiencies and maximum surface temperatures for the two pouch cell types are stated (taken from Ref. 24). For a C/10 discharge, both cell types kept approximately the same temperature, but for a 3C discharge, the LMR-NCM/graphite pouch cells reached surface temperatures of 53 °C, while the NCA/graphite pouch cells only reached 33 °C. In smaller laboratory-scale cell formats, the generated heat poses no further problems, but when it comes to larger cell formats, the thermal behavior of cells containing LMR-NCM cannot be neglected.

The temperature has a high impact on the performance of lithium-ion cells, and with the aid of thermal models, various cooling strategies can be analyzed and optimized. There are thermal models of the cell itself, which are often coupled with electrochemical models,[31–39] but also thermal models that describe the whole battery pack including the corresponding cooling system.[40–43] In the coupled models, the heat generation is usually computed based on the electrochemical model, i.e., the irreversible losses described by currents and overpotentials plus the reversible heat. However, especially the electrochemical models of lithium-ion cells are based on an extensive parameter set consisting of more than 30 parameters.[32,33,37] Not all of these parameters can be experimentally determined and are either taken from literature or have to be assumed.

In this work, the thermal behavior of LMR-NCM/graphite cells is investigated and compared to NCA/graphite cells and the consequences for operating strategies and thermal management systems are derived. The focus is on the total heat generation and not on a characterization of the different heat sources. To quantify the heat generation for different charge and discharge rates, isothermal calorimetric measurements were performed on laboratory coin cells for the cell systems LMR-NCM/graphite and NCA/graphite. The determined heat generation was scaled to various cell formats and used as an input parameter for a homogenized 3D thermal model to qualitatively assess the thermal behavior. Simulation studies analyzed the implications of the heat generation on the temperature development especially in large-format batteries and the resulting requirements for their thermal management system. Particularly, the interplay between the cell size, the applied load, and the thermal boundary conditions of the cooling system was evaluated and design criteria for cells containing LMR-NCM were derived.

Experimental

Electrode specifications.—The LMR-NCM cathodes have a stoichiometry of 0.33 Li_2MnO_3 · 0.67 $LiNi_{0.38}Co_{0.21}Mn_{0.41}O_2$ (BASF, Germany), which can also be written as $Li_{1.14}[Ni_{0.26}Co_{0.14}Mn_{0.60}]_{0.86}O_2$, and the NCA cathodes have a stoichiometry of $LiNi_{0.81}Co_{0.15}Al_{0.04}O_2$ (BASF, Germany). The cathode coatings were prepared by mixing 92.5 wt% CAM (LMR-NCM or NCA), 4 wt% conductive carbon (Super-C65, Timcal, Switzerland), and 3.5 wt% polyvinylidene-fluoride binder (PVdF, Solef 5130, Solvay, Belgium) with N-methyl-2-pyrrolidone (NMP, anhydrous, 99.5%, Sigma-Aldrich, Germany) at a solid content of 57 wt% and 62 wt% for LMR-NCM and NCA, respectively. The mixing was performed in several steps using a planetary orbital mixer (Thinky, USA). The final slurry was cast onto one side of a 15 μm aluminum foil (MTI, USA) using a 200 μm four-edge blade. The CAM loading was set to 11.5 mg cm^{-2} (≡2.9 mAh cm^{-2} at C/10, based on a nominal capacity of 250 mAh g_{CAM}^{-1}) and 12.5 mg cm^{-2} (≡2.5 mAh cm^{-2} at C/10, based on a nominal capacity of 200 mAh g_{CAM}^{-1}) for the LMR-NCM and NCA electrode sheets, respectively. The coated cathode foils were dried overnight in a convection oven at 50 °C and afterwards compressed in a calender (GK 300-L, Saueressig, Germany) to a porosity of 42%, resulting in coating thicknesses of ≈54 μm (LMR-NCM) and ≈56 μm (NCA).

The corresponding anode coatings were prepared by mixing 95 wt% graphite (SGL Carbon, Germany) and 5 wt% PVdF binder (Solef 5130, Solvay, Belgium) with NMP (anhydrous, 99.5%,

Table II. Specifications of the LMR-NCM/graphite and NCA/graphite coin cells. The nominal cell capacities were calculated with reversible capacities of 250 mAh g^{-1} for LMR-NCM and 200 mAh g^{-1} for NCA.

Type	Cell	CAM mass	Nominal cell capacity
LMR-NCM/graphite	L1	17.834 mg	4.459 mAh
	L2	17.603 mg	4.401 mAh
NCA/graphite	N1	19.518 mg	3.904 mAh
	N2	19.795 mg	3.959 mAh

Note. CAM—cathode active material.

Sigma-Aldrich, Germany) at a solid content of 54 wt% and 52 wt% for the respective LMR-NCM and NCA electrodes. As before, this was performed in several steps in a planetary orbital mixer (Thinky, USA). The final slurry was cast onto one side of a 12 μm copper foil (Gelonlib, China) using a 200 μm four-edge blade. The graphite electrode loadings were set to 10.3 mg cm^{-2} ($\equiv$3.7 mAh cm^{-2} at C/10, based on a nominal capacity of 355 mAh $g^{-1}_{graphite}$) for LMR-NCM and 9.4 mg cm^{-2} ($\equiv$3.3 mAh cm^{-2} at C/10, based on a nominal capacity of 355 mAh $g^{-1}_{graphite}$) for NCA based coin cells. The coated anode foils were dried overnight in a convection oven at 50 °C and afterwards compressed in a calender (GK 300-L, Saueressig, Germany) to a porosity of 30%, resulting in anode coating thicknesses of $\approx$69 μm (for LMR-NCM) and $\approx$63 μm (for NCA). The resulting areal capacity ratios of negative/positive electrode (N/P ratio) were around 1.3 for both cell setups.

Coin cell preparation.—The cathode coins were punched out of the electrode sheets with a diameter of 14 mm, and the anode coins with a diameter of 15 mm. The coin cells in the 2032 format were assembled in an argon filled glove box (M. Braun Inertgas-Systeme, Germany) with $H_2O < 0.1$ ppm and $O_2 < 0.1$ ppm. Each cell was filled with 80 μl of electrolyte. The LMR-NCM/graphite cells were filled with a 1 M solution of $LiPF_6$ in 12 vol% FEC, 64 vol% DEC, 24 vol% co-solvent, and 2 wt% of a proprietary additive (BASF, Germany), while the NCA/graphite cells were filled with a 1 M solution of $LiPF_6$ in a 3:7 (by weight) mixture of EC:DEC and 2 wt% vinylene carbonate (VC, BASF, Germany). A glass fiber separator (Type 691, VWR, USA) with 17 mm diameter and two 1 mm spacers were used. The specifications of the four coin cells (2x LMR-NCM/graphite and 2x NCA/graphite) used for the calorimetric measurements are listed in Table II. The nominal cell capacities were calculated based on the amount of CAM with reversible capacities of 250 mAh g^{-1} (LMR-NCM) and 200 mAh g^{-1} (NCA). All later used C-rates in the measurements are referenced to the stated capacities for each cell.

After cell assembly, a formation procedure including one C/15 charge/discharge cycle and two C/10 charge/discharge cycles was carried out with a Maccor cycler (series 4000, USA) in a thermostatic chamber (Binder, Germany) at 25 °C. In the first formation cycle, the LMR-NCM/graphite cells were charged to 4.7 V in order to activate the LMR-NCM.[17] The following cycles were carried out in the voltage window 2.0–4.6 V. The NCA/graphite cells were cycled in the voltage window 3.0–4.3 V.

Calorimetric measurements.—After formation, the coin cells were transferred to an isothermal heat flow calorimeter setup (TAM IV, TA Instruments, USA), consisting of a thermostat (stability ±50 μK) equipped with a 20 ml microcalorimeter (accuracy ±300 nW, precision ±100 nW) and a custom-made coin cell holder. Over the duration of the experiment, the baseline drift was less than 500 nW. The step response of the heat flow resulted in a delay time of 750 s until 95% of the heat flow signal were detected. All measurements were performed in isothermal mode at 25 °C after internal gain calibration. The cells were connected over Cu-P bronze DuoTwist wires (36 AWG, Lakeshore, USA) to a multi-channel potentiostat (VSP, BioLogic, France).

Detailed measurement procedures including the formation are listed in Table III. After installing the coin cells into the calorimeter, a first C/10 stabilization cycle was carried out to ensure a proper cell and calorimeter functionality. The subsequent cycles were conducted to precisely measure the heat generation during different constant current (CC) charge and discharge operations, namely C/10, C/2, 1C, 2C, and 3C. Before each CC charge or discharge cycle, a pause of 4 h was added to allow a relaxation of the heat in the calorimeter. After each CC charge/discharge, a pause of 30 min was added to

Table III. Measurement procedures applied to the LMR-NCM/graphite and NCA/graphite coin cells. After the first three formation cycles, the cells were cycled in the calorimeter.

Procedure	Parameters	Stop condition
C/15 formation cycle	CC charge @ C/15	$U \geqslant U_{max}$*
	CC discharge @ C/15	$U \leqslant U_{min}$
C/10 formation cycle (2x)	CC charge @ C/10	$U \geqslant U_{max}$
	CC discharge @ C/10	$U \leqslant U_{min}$
C/10 stabilization cycle	CC charge @ C/10	$U \geqslant U_{max}$
	CC discharge @ C/10	$U \leqslant U_{min}$
	Pause	$t \geqslant 4$ h
C/10 cycle	CC charge @ C/10	$U \geqslant U_{max}$
	Pause	$t \geqslant 4$ h
	CC discharge @ C/10	$U \leqslant U_{min}$
	Pause	$t \geqslant 4$ h
Cycle test	CC charge @ I_{charge}**	$U \geqslant U_{max}$
	Pause	$t \geqslant 30$ min
	CC charge @ C/10	$U \geqslant U_{max}$
	Pause	$t \geqslant 4$ h
	CC discharge @ $I_{discharge}$**	$U \leqslant U_{min}$
	Pause	$t \geqslant 30$ min
	CC discharge @ C/10	$U \leqslant U_{min}$
	Pause	$t \geqslant 4$ h

Note. The C-rates refer to the nominal cell capacities listed in Table II. CC—constant current, CV—constant voltage. LMR-NCM: $U_{max} = 4.6$ V, $U_{min} = 2.0$ V. NCA: $U_{max} = 4.3$ V, $U_{min} = 3.0$ V. * In their first C/15 formation cycle, the LMR-NCM/graphite cells were charged to 4.7 V to activate the CAM. ** $I_{charge} = I_{discharge} = [C/2, 1C, 2C, 3C]$.

measure the inert heat that was generated. Thereafter, the cells were either fully charged or discharged with a C/10 CC procedure to ensure consistent starting conditions: The cells were charged with a C/10 CC to a SOC of 100% before a discharge procedure and were discharged with a C/10 CC to a SOC of 0% before a charge procedure.

Cell formats.—Cell formats of lithium-ion cells are categorized into cylindric, prismatic, and pouch. Based on double-sided anodes and cathodes with separators in between, the electrode stack or jelly roll is adapted to the desired cell format. Pouch cells use stacked electrodes, cylindrical cells wound electrodes, and prismatic cells either flat wound or stacked electrodes.[44–46] A schematic overview is illustrated in Fig. 2, together with the stated electrode thicknesses of the coin cells, assuming double-sided electrodes and a 25 μm separator.

Via the thickness of the electrode stack, the total electrode area of any desired cell format can be calculated. A multiplication of the total electrode area with the areal capacity yields the nominal capacity C_N of the cell. By further multiplying C_N with the mean discharge voltage, the nominal energy E_N of the cell can be calculated. In this work, the geometric dimensions of the pouch and prismatic cells were taken from the standard DIN 91252.[9] In this standard, the thickness of the pouch cell formats is not specified, however, in the corresponding pre-standard a maximum thickness of 13 mm was defined. For our calculations, the HEV and PHEV pouch cells were assumed with a thickness of 10 mm, while the BEV pouch cells were assumed with a thickness of 13 mm. In addition to the standardized prismatic and pouch cell formats, the cylindric cell formats 18 650, 21 700, and 26 650 were investigated, as shown in Table IV.

The calculation of the nominal capacity and energy content of the listed cell formats is based on the electrodes of the coin cells described above, only double-sided, and a 25 μm separator. According to Fig. 2, the electrode stack consists of one double-sided anode, one double-sided cathode, and two separators. The LMR-NCM/graphite electrode stack has a total thickness of 323 μm, an areal capacity of 2.9 mAh cm^{-2}, and a mean discharge voltage of 3.5 V for a C/10 discharge. The NCA/graphite electrode stack has a total thickness of 315 μm, an areal capacity of 2.5 mAh cm^{-2}, and a mean discharge voltage of 3.7 V. The cells were not optimized toward a high energy density, in fact, they served as a CAM characterization in comparable cell designs. The resulting surface to volume (S/V) ratio of each cell format was calculated with the outer surface of the cell case and the effective volume of the jelly roll/electrode stack and not the total inner volume of each cell case.

For the calculation of the larger pouch cell formats as stated in the standard DIN 91252,[9] a pouch foil thickness of 153 μm (D-EL408PH-3, DNP, Japan) was used, and tabs as well as empty spaces between the foil and the electrode stack were neglected. The geometric dimensions are given in Fig. 3a. The thickness of the hard case of the prismatic cells was assumed to be 0.7 mm.[31] The highest utilization of the hard case volume can be achieved by stacking the electrodes. However, stacking includes more processing steps and time compared to flat winding and errors are more likely.[45,46] In our calculations, a flat wound jelly roll with an axial orientation in the *y*-direction of the prismatic cell formats was presumed. The spaces between the hard case and the jelly roll are displayed in Fig. 3b. According to the study of Quinn et al.,[8] the can of cylindric cells has a thickness of 0.2 mm and contains a 5 mm head space for contacting and safety devices. For the 3D thermal model, the 5 mm were divided into a 1 mm bottom and 4 mm top head space, as seen in Fig. 3c. The 1 mm inner void of the jelly roll originates from the winding process. Possible separator overlaps and anode overhang areas, as well as single-sided anodes at the beginning and end of each stack or jelly roll were neglected in the calculations.

Modeling

According to the description of the different cell formats in the experimental section, the geometric dimensions of the cell cases including the electrode stack/jelly roll were integrated in a 3D thermal model, which uses the scaled heat generation of the calorimetry measurements as an input parameter. The 3D thermal model was implemented in the commercial FEM solver *COMSOL Multiphysics 5.4*. To reduce computational complexity, the jelly roll/

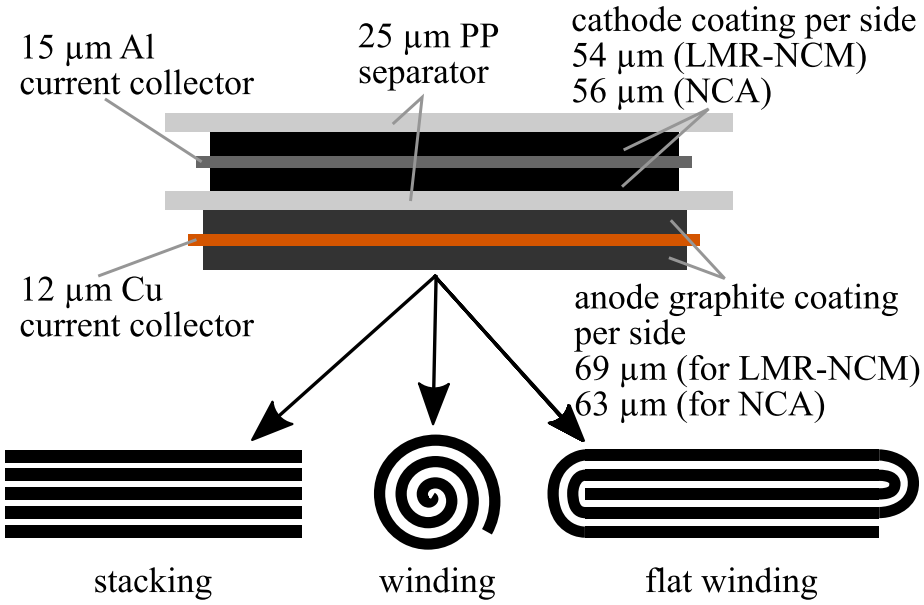

Figure 2. Schematic electrode stack consisting of double-sided anodes and cathodes with separators in between. Stacking the layers is used for pouch cells, winding for cylindric cells, and flat winding or stacking for prismatic cells. The stated coating thicknesses represent the coating thickness per side of double-sided electrodes.

Table IV. Geometric dimensions of the investigated cell formats including their scaled nominal capacity and energy content. For the calculations, the areal capacity and mean discharge voltage for a C/10 discharge of the LMR-NCM/graphite and NCA/graphite coin cells were used. The surface to volume (S/V) ratio was calculated based on the effective volume of the jelly roll/electrode stack and not the total inner volume.

						LMR-NCM/graphite		NCA/graphite	
Cell format		x in mm	y in mm	z in mm	S/V ratio in m^{-1}	C_N in Ah	E_N in Wh	C_N in Ah	E_N in Wh
Pouch	HEV	161	141	10	2.3	39	138	35	128
	PHEV1	164.2	226	10	2.3	64	225	56	209
	PHEV2	164	232	10	2.3	66	231	58	214
	BEV1	99.7	301.5	13	1.9	68	237	60	222
	BEV2	329.2	161.4	13	1.8	120	420	106	392
Prismatic	HEV1	85	120	12.5	2.6	15	53	14	50
	HEV2	80.5	120	12.1	2.7	14	48	12	45
	PHEV1	85	173	21	1.6	41	144	37	135
	PHEV2	91	148	26.5	1.3	48	169	43	158
	BEV1	115	173	32	1.1	90	315	79	293
	BEV2	115	173	45	0.8	127	445	113	416
	BEV3	125	173	32	1.0	98	345	87	321
	BEV4	125	173	45	0.8	139	487	123	455
		d in mm	h in mm		S/V ratio in m^{-1}	LMR-NCM/graphite C_N in Ah	E_N in Ah	NCA/graphite C_N in Ah	E_N in Wh
Cylindric	18 650	18	65		2.9	2.6	9.1	2.3	8.5
	21 700	21	70		2.5	3.9	13.5	3.4	12.6
	26 650	26	65		2.1	5.5	19.3	4.9	18.0

Note. LMR-NCM/graphite: 2.9 mAh cm^{-2}, 3.5 V @ C/10 discharge. NCA/graphite: 2.5 mAh cm^{-2}, 3.7 V @ C/10 discharge.

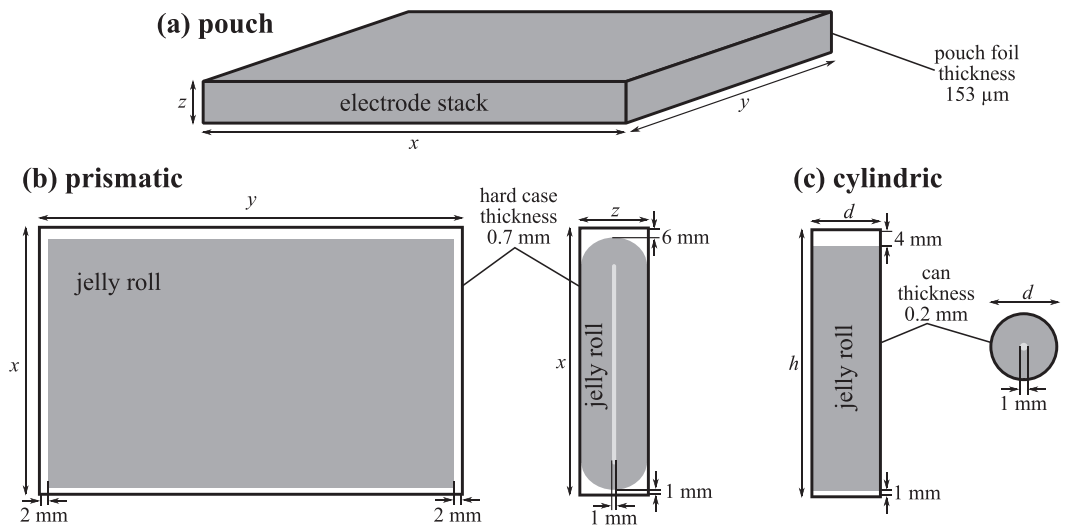

Figure 3. Geometric dimensions of the (a) pouch, (b) prismatic, and (c) cylindric cell formats including the assumed head spaces and inner voids of the jelly rolls as well as the respective case thicknesses.

electrode stack was homogenized with an anisotropic thermal conductivity perpendicular and parallel to the layers. Therefore, each thermal model consists of two different domains, the jelly roll/electrode stack and the case. Within these domains, the general heat balance is solved.[31,47]

$$\rho c_p \frac{\partial T}{\partial t} = \nabla(k \nabla T) + q, \qquad [1]$$

where ρ is the density in kg m^{-3}, c_p the specific heat capacity in J kg^{-1} K^{-1}, T the temperature in K, q the volumetric heat generation in W m^{-3}, and k the thermal conductivity in W m^{-1} K^{-1}. The thermal conductivity k is defined via its values in x-, y-, and z-direction:

$$k = \begin{bmatrix} k_x & 0 & 0 \\ 0 & k_y & 0 \\ 0 & 0 & k_z \end{bmatrix} \qquad [2]$$

Finally, the ∇ operator (transpose) is defined in the 3D model as:

$$\nabla = \left(\frac{\partial}{\partial x}, \frac{\partial}{\partial y}, \frac{\partial}{\partial z} \right)^T \qquad [3]$$

The 3D thermal models with the homogenized jelly roll/electrode stack had in between 135 000-280000 degrees of freedom (DOF)

depending on the cell format and the boundary conditions (as specified below) and were able to solve within a few minutes on a desktop computer.

Thermal model parameters.—For the cylindric cells, as well as the wound part at the top and bottom of the jelly roll of the prismatic cells, a cylindric coordinate system was used. The corresponding values for the parameterization of the thermal model are stated in Table V. The density, the heat capacity, and the thermal conductivities of the jelly roll/electrode stack were calculated in the Appendix based on the values in Table A·I. These parameters can be calculated with the material properties and thicknesses of the current collectors, composite electrodes, separator, and electrolyte.[14,31,47] However, it is difficult to get proper measurement values especially for the porous electrodes with varying compositions and active materials, which are soaked with electrolyte. In the literature, reported values of electrode densities ρ are within the range 920–1040 kg m^{-3}, and values of specific heat capacities c_p within the range 2560–2781 J kg^{-1} K^{-1}.[14,37,48,49] Reported values of the thermal through-plane conductivity $k_\perp$ of electrode stacks are within the range 0.9–1.1 W m^{-1} K^{-1} and of the thermal in-plane conductivity $k_\parallel$ within 24.6–33.9 W m^{-1} K^{-1}.[31,37,39,47] Steinhardt et al.[50] investigated the thermal conductivity of the jelly roll/electrode stack based on different material combinations and calculated median values of $k_\perp = 0.878$ W m^{-1} K^{-1} and $k_\parallel = 26.5$ W m^{-1} K^{-1}. The reported literature values are in good agreement with our calculations. A constant anisotropic thermal conductivity of the electrode stack ($k_\perp = 0.83$ W m^{-1} K^{-1}, $k_\parallel = 27.3$ W m^{-1} K^{-1}) was used for our modeling purposes, but a variable, temperature-dependent conductivity may be implemented in future work, especially if high temperature changes are expected.

The volumetric heat generation q is a function of the cell SOC and was measured for varying charge/discharge currents using isothermal calorimetry as described in the experimental section. The measured heat generation was related to the cathode area of the coin cells (1.54 cm^2), scaled to the total cathode area of each cell format, and finally ascribed to the domain of the homogenized jelly roll/electrode stack in the model.

Pouch foils usually consist of an aluminum foil that is laminated with diverse plastics on both sides. As an example, the 153 μm thick pouch foil D-EL408PH-3 (DNP, Japan) uses layers of polyethylene terephthalate (PET), polyamide (PA), and polypropylene (PP) around an inner aluminum foil. Accurate layer thicknesses of the different materials are not known, so a uniform heat capacity and an isotropic thermal conductivity of the pouch foil were estimated as a compound between the thermal characteristics of the plastics and the aluminum. The density of the pouch foil was determined by the areal weight and the thickness as stated in the data sheet. In the 3D model of the pouch cell, all boundary areas of the inner electrode stack were enclosed with the pouch foil.

For the hard case of a prismatic cell, an aluminum alloy is often used to ensure mechanical stability without adding too much weight.[37,52] For the model parameters of the prismatic case, the thermal characteristics of the aluminum alloy 2024 with a thickness of 0.7 mm were chosen.[31] The flat wound jelly roll is only in contact with the case on its two large lateral faces, as shown in Fig. 3b. The empty head spaces of prismatic cells are filled with argon, which possesses a low thermal conductivity (0.0178 W m^{-1} K^{-1}) and a low heat capacity (0.844 kJ m^{-3} K^{-1}).[52] For modeling simplicity, all remaining boundaries of the jelly roll were thermally insulated and a heat transfer with the case was deactivated.

Cylindric cell cans are typically made of steel with a thickness of 0.17–0.25 mm.[53,54] The thermal parameters in Table V are specified for the stainless steel AISI-304[31] with a thickness of 0.2 mm.[8] In the model, the wound jelly roll is in contact with the can on its lateral face. As stated in the description of the cell formats in the experimental section, gaps were implemented between the top and bottom area of the jelly roll and the can, see Fig. 3c, which prohibit a heat transfer on these boundaries.

Boundary conditions.—The boundary conditions of thermal models depend on the use of the cells in a certain application including its thermal management system. This can imply that a single cell is directly mounted in an application with no cooling system at all, e.g., in mobile phones, tablets, or laptops. Reportedly, the early Nissan Leaf models faced problems during charging operations as the heat of the battery system was only passively dissipated.[55,56] The charging and discharging performance is limited with a passive system, especially for warmer ambient temperatures, which is why most EVs rely on a liquid or refrigerant cooling system for their battery pack.[56] Tesla uses cooling tubes around their cylindrical cells with a thermally conductive, electrically insulative material in between.[57] Other car manufacturers use pouch or prismatic cells with a base plate cooling.[58–60]

In our first simulation study, a convective heat transfer between the entire surface area of the cell case and a constant ambient temperature T_∞ was modeled. The temperature T_{surf} describes the temperature on the surface of the cell case, i.e., the surface of the can of a cylindric cell, the hard case of a prismatic cell, or the pouch foil of a pouch cell. The convective heat flux q_{conv} in W m^{-2} was modeled with the following equation and h as the heat transfer coefficient in W m^{-2} K^{-1}.

$$q_{conv} = h(T_{surf} - T_\infty) \quad [4]$$

Feng et al.[61] classified the heat transfer coefficients according to different cooling scenarios. In their work, natural convection in air is listed with a heat transfer coefficient of 5–25 W m^{-2} K^{-1} and forced convection in air with 15–250 W m^{-2} K^{-1}. A better heat transfer up to 1000 W m^{-2} K^{-1} can be achieved with a liquid coolant directly surrounding the cell, which is rather difficult to implement in most applications.[5,61]

In our second simulation study, a base plate cooling scenario for prismatic cells was investigated. Thereby, the base plate of the prismatic cell is in direct contact with a cooled cooling plate.[60] A constant temperature of the cooling plate of 20 °C was assumed, and the starting temperature of the cell was also set to 20 °C to start with a uniform temperature of the whole system. In the model, the boundary condition for the bottom of the case was therefore set to a constant temperature of 20 °C:

$$T_{surf,bottom} = 20\ °C = const. \quad [5]$$

All other boundaries were thermally insulated, derived by the neighboring cells in a module on both sides and the electrical connection on the top.

Table V. Thermal modeling parameters of the homogenized jelly roll/electrode stack and the different cell cases. The parameters of the jelly roll/electrode stack are based on material properties described in the Appendix in Table A·I.

Parameter	Unit	Jelly roll	Pouch foil	Case prism.	Case cyl.
Heat capacity c_p	J kg^{-1} K^{-1}	1049	1400	875	477
Density ρ	kg m^{-3}	2427	1441^m	2770	7900
Thermal conductivity through-plane $k_\perp$	W m^{-1} K^{-1}	0.83	0.33	170	14.6
Thermal conductivity in-plane $k_\parallel$	W m^{-1} K^{-1}	27.3	0.33	170	14.6

Note. m—measured, remaining values were taken from Ref. 31, 51.

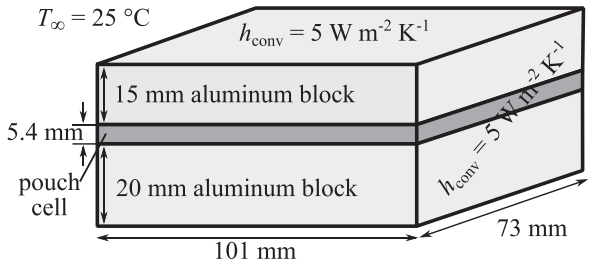

Figure 4. Schematic dimensions of the thermal validation model, representing the pouch cell within two aluminum blocks. The modeled thicknesses of the pouch cell were set to 5.5 mm (LMR-NCM/graphite) and 5.3 mm (NCA/graphite). The ambient temperature was set to 25 °C, and the convective heat transfer coefficient on the exterior surfaces to 5 W m^{-2} K^{-1}.

Model validation.—The volumetric heat generation q is a key input parameter of thermal models. In order to verify if a scaling of the heat generation measured in coin cells to larger cell formats is plausible, the thermal model needs to be validated with measurement data. Therefore, the temperature evolution of one LMR-NCM/graphite and one NCA/graphite pouch cell measured in discharge rate capability tests in our previous work was used for comparison.[24] During this test, the pouch cells were mounted in cell holders and the temperature was measured with a negative temperature coefficient (NTC) temperature sensor on the surface of the pouch cells with a precision of ±1 K (compare Fig. 1 in Ref. 24). The LMR-NCM/graphite pouch cell had a nominal capacity of 6.8 Ah (27.3 g CAM), and the NCA/graphite pouch cell 6.3 Ah (31.7 g CAM), to which the C-rates in the discharge rate capability test were referred to. As the exact CAM mass was known for these cells, the heat generation for the thermal validation model was scaled via the CAM mass and not via the electrode area.

In the thermal validation model, the cell holder was represented by two aluminum blocks with thicknesses of 20 mm and 15 mm, which were placed on the bottom and top of the pouch cell, respectively, as seen in Fig. 4. The stated thickness of the pouch cell of 5.4 mm represents a mean value; in the thermal model, the thicknesses of the pouch cells were set to 5.5 mm (LMR-NCM/graphite) and 5.3 mm (NCA/graphite). The width and the depth of the two blocks were set to 73 mm and 101 mm, which are the dimensions of the area of one cathode layer. For simplicity, anode and separator overhang areas as well as the pouch foil and cellulose sheets between pouch cell and cell holder were neglected in the validation model. The original cell holder (see Fig. 1 in Ref. 24) contained a polyoxymethylene (POM) frame around the aluminum blocks, which was in no direct contact with the cell and therefore left out. The thermal model parameters of the aluminum blocks were set to the ones of the prismatic aluminum case described in Table V. For each simulation, the starting temperatures of the pouch cells as well as the adjacent blocks were set to the starting temperature of the corresponding measurement. On the exterior surfaces of the aluminum blocks and the open side surface areas of the pouch cell, a convective heat transfer coefficient of 5 W m^{-2} K^{-1} was implemented, representing a natural convection without an active cooling. The ambient temperature was set to 25 °C as the pouch cells were cycled in a controlled climate chamber at 25 °C. For detailed information about the pouch cell measurement procedures during this test as well as the cell holder, the reader is referred to the previous publication.[24]

Results and Discussion

This section is divided into the following parts: a presentation of the measured heat generation of the coin cells, and a validation of the thermal model with a scaled heat generation to the measured temperature of the pouch cells. Then, the results of two simulation studies, which were carried out for different standardized cell formats, are presented. The studies included one simulation with a

Table VI. Specific charge and discharge capacities and heat generation of one LMR-NCM/graphite (L1) and one NCA/graphite (N1) coin cell during the CC phases (Q_{CC}) and the 30 min pauses (Q_{pause}) afterwards. Q_{total} is the sum of Q_{CC} and Q_{pause}. ΔSOC was referred to the listed C/10 charge capacity of each cell type. The specific capacities and the heat are related to the CAM mass of the respective coin cell.

Type	C-rate	Capacity in mAh g_{CAM}^{-1}	ΔSOC	Q_{CC} in mWh g_{CAM}^{-1}	Q_{pause} in mWh g_{CAM}^{-1}	Q_{total} in mWh g_{CAM}^{-1}	Q_{CC}/Q_{total}
Charge							
LMR-NCM/	C/10	231.7	100%	26.4	2.6	29.0	91%
graphite	C/2	212.9	91.9%	42.9	6.8	49.7	86%
	1C	199.5	86.1%	59.2	14.4	73.6	80%
	2C	186.0	80.3%	72.1	35.3	107.4	67%
	3C	168.2	72.6%	62.8	62.5	125.3	50%
NCA/	C/10	182.9	100%	10.0	0.4	10.4	96%
graphite	C/2	175.5	96.0%	18.7	2.1	20.8	90%
	1C	165.4	90.4%	25.9	6.1	32.0	81%
	2C	148.9	81.4%	33.3	17.1	50.4	66%
	3C	131.0	71.6%	30.8	31.4	62.2	50%
Discharge							
LMR-NCM/	C/10	229.6	99.1%	45.4	3.7	49.1	92%
graphite	C/2	214.5	92.6%	63.5	16.2	79.7	80%
	1C	193.5	83.5%	66.2	30.7	96.9	68%
	2C	164.1	70.8%	63.3	53.3	116.6	54%
	3C	124.2	53.6%	39.0	77.5	116.5	33%
NCA/	C/10	181.3	99.1%	3.1	0.8	3.9	79%
graphite	C/2	174.1	95.2%	11.9	2.9	14.8	80%
	1C	166.7	91.1%	20.7	6.8	27.5	75%
	2C	138.6	75.8%	26.5	17.5	44.0	60%
	3C	106.1	58.0%	20.1	28.2	48.3	42%

Note. CC—constant current, SOC—state of charge. CAM mass: 17.834 mg LMR-NCM, 19.518 mg NCA.

convective surface cooling and one with a base plate cooling of prismatic cells.

Heat generation.—The heat generation of the LMR-NCM/graphite and NCA/graphite coin cells was measured for different charge and discharge C-rates using isothermal calorimetry. To verify the reproducibility of the measurements, two cells of each chemistry were measured, the comparison is displayed in Fig. A·1 in the Appendix.

In the following, the measurement results of one cell of each chemistry were further analyzed. The charge and discharge capacities and the accumulated heat in each cycle are listed in Table VI, the normalized heat generation is displayed in Fig. 5. In Table VI, the ΔSOC values are referenced to the charge capacity in the C/10 cycle of each cell. This gives an overview of the capacity throughput in each cycle, which strongly affects the energy that is released as waste heat. The integrated heat was split into the heat during the CC procedure (Q_{CC}), and the heat that was measured in the 30 min pause (Q_{pause}) after the current was switched off. For low currents, most of the total heat (Q_{total}) was accumulated in the CC phase, indicated by the ratio Q_{CC}/Q_{total} in the last column of Table VI. With increasing currents, a larger part of this heat was shifted into the pause owing to the time-delayed measurement in the calorimeter. As an example, the C/10 discharges lasted for over 9 h while the 3C discharges only lasted for about 10 min. In Fig. 5, the heat generation is displayed during the CC phases and the 30 min pauses afterwards. The vertical gray lines mark the time when the current in the CC phase was switched off. For most charging operations, the maximum heat generation was located slightly after the end of the CC phase. For the discharge operations, the maximum shifted further to the right with rising C-rates, caused by higher gradients of the heat generation curves at the end of discharge. These time-dependent heat generation profiles from Fig. 5 were used as a model input for the simulations, which were then carried out for each operation until the end of the pause in order to ensure that the maximum cell temperature is captured.

The total heat generation can be split into an irreversible and a reversible part, in which the reversible heat (entropy) is described by the temperature dependence of the open circuit voltage.[62–64] For low charge/discharge currents, the irreversible heat caused by joule

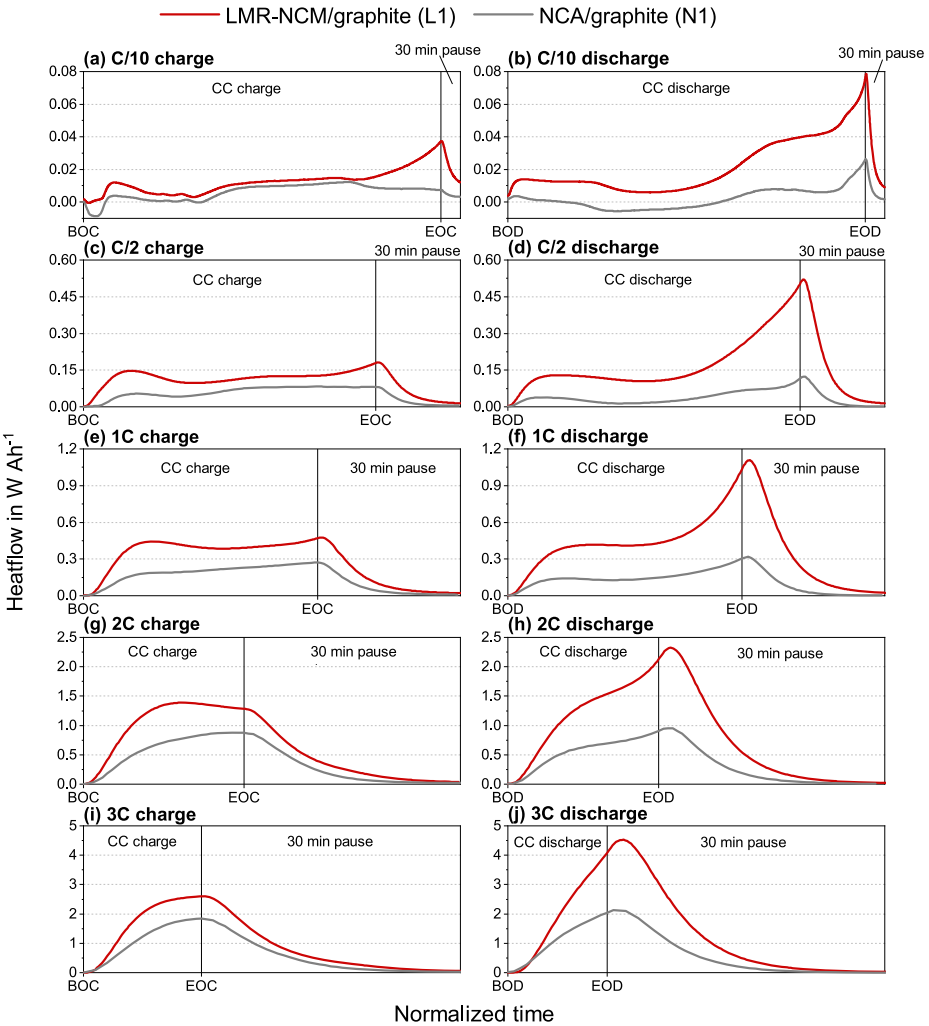

Figure 5. Heat generation of the LMR-NCM/graphite coin cell (L1) and the NCA/graphite coin cell (N1) for varying charge and discharge C-rates including the 30 min pause afterwards. The heat generation was normalized to the respective charged/discharged capacity in each cycle, and the *x*-axis was normalized to the charging/discharging time. The begin of charge (BOC) represents a SOC of 0%, the begin of discharge (BOD) represents a SOC of 100%, and the respective end of charge (EOC) and end of discharge (EOD) mark the time when the current in the CC phase was switched off.

heating and reaction overpotentials is likewise low and the contribution of the reversible heat to the total heat is more significant.[64] This can be seen in Figs. 5a and 5b, where the entropy of the graphite anode is evident. During lithiation of graphite, which is the case in charging operations of full cells, the entropy changes from a positive to a negative sign,[14,65–67] leading to a cooling down of the cell at the very beginning, e.g., clearly visible for the C/10 charge of the NCA/graphite cell in Fig. 5a. In comparison to the entropy change of graphite anodes, the entropy difference of NCM and NCA cathodes is less pronounced.[14,68,69] In our heat flow measurements of full cells, the features caused by an entropy change during the C/10 charge/discharge operations are similar for both cell chemistries. With rising currents, the irreversible heat dominates the heat evolution and the entropy features become less distinct.

The NCA/graphite cells released more heat during charging operations than discharging operations, as shown in Table VI. Manikandan et al.[64] investigated 18 650 NCA/graphite cells and showed that during discharge operations, the sum of the reversible heat is negative and thereby the total heat generation is lowered. However, the LMR-NCM/graphite cells showed quite the opposite behavior releasing more heat during discharge operations, as seen in Table VI. Poor charge transfer kinetics and/or a slow solid-state diffusion together with the OCV hysteresis of LMR-NCM cause the pronounced heat generation that is more dominant during discharge operations.[17,28,29] An additional SOC dependent resistance of LMR-NCM causes the strong temperature increase at the end of the discharges.[17] As the LMR-NCM OCV hysteresis is presumably current-independent, the increasing irreversible energy loss for rising C-rates is dominated by overpotentials. Figure 5 revealed, that for the same charge or discharge C-rate, the LMR-NCM/graphite cells released much more heat than the NCA/graphite cells, which is clearly caused by the LMR-NCM cathode material, as both cell types contained comparable graphite anodes.

Simulation studies.—The heat generation in the previous Section was determined with coin cells with a nominal capacity of 4.5 mAh (LMR-NCM/graphite) and 3.9 mAh (NCA/graphite), which was scaled to the reference pouch cells with 6.8 Ah (LMR-NCM/graphite) and 6.3 Ah (NCA/graphite) via the CAM mass of the cells and used as an input parameter for the thermal validation model. In this case, a scaling via the CAM mass was more reliable than a scaling via the electrode area, as the total CAM mass of the pouch cells was known, and the electrode thicknesses of the pouch cells were slightly different.

The comparison of the measured surface temperatures during the discharge rate capability test and the simulated surface temperatures of the pouch cells is displayed in Fig. 6. The measured temperatures were plotted until the end of discharge, as the discharge was immediately followed by a charging procedure. During these measurements, the maximum temperature occurred directly at the end of discharge without a time delay. The simulations used the heat generation displayed in Fig. 5 including the pauses, which is why the simulated temperatures were not plotted until the end of the pause but until the maximum surface temperature was reached in each cycle. The time when the current was switched off in the simulations is marked with a cross in Fig. 6. As the heat measurements in the calorimeter exhibited a time delay, especially affecting higher C-rates, the maximum temperatures of the simulations appeared in the pause after the current was switched off.

For low currents, the simulation results of the LMR-NCM/graphite cells are in good agreement with the measured surface temperatures of the pouch cells. With increasing discharge C-rates, the deviation $|\Delta T_{dev,max}|$ also increases. Up to and including the 1C discharge, the absolute deviations remain below 2 K, which is acceptable for our simulation purposes considering that the precision of the temperature sensor used in the pouch cell measurements was ±1 K. However, at the end of the 2C discharge, the deviation is 6.2 K, and for a 3C discharge the deviation doubles to 12.7 K. While the heat generation measurements of the coin cells in the calorimeter were performed under isothermal conditions at 25 °C and then scaled up, the temperature of the pouch cells increased during operation. In general, lithium-ion batteries are very temperature-sensitive, with a higher operating temperature, the transport and kinetics enhance, the internal cell resistance decreases and more capacity can be discharged from the cell.[70–72] For a 1C discharge, the LMR-NCM/graphite coin cells delivered around 84% of their C/10 capacity, 71% for a 2C discharge, and only 54% for a 3C discharge. In comparison, during the rate capability test, the 6.8 Ah LMR-NCM/graphite pouch cells delivered around 93% for a 1C discharge, 88% for a 2C discharge, and 77% for a 3C discharge.[24] The longer the cells can sustain a certain C-rate, more capacity can be discharged from the cell and more heat will be released during this process, resulting in higher cell temperatures. Up to a discharge C-rate of 1C, the homogenized thermal model can adequately represent the behavior of the modeled LMR-NCM/graphite pouch cells. For this reason, the subsequent simulation studies with varying cooling conditions were only carried out for discharge rates of C/10, C/2, and 1C.

Comparing the NCA/graphite simulation results, a similar trend can be observed. With rising discharge C-rates, the temperature deviation also becomes higher. However, the maximum deviation is lower, e.g., 1.7 K for the 3C discharge, because the NCA/graphite pouch cells exhibited a less pronounced temperature increase, making the measured coin cell heat generation more comparable to the one in the larger pouch cells. In the C/10 discharge simulation, the cell temperature decreases from a starting temperature of 26.5 °C down to 25 °C while the measured temperature stayed almost constant. This discrepancy with a maximum deviation of 1.5 K can be explained with possible inhomogeneous thermal conditions during the experiment. In the simulation model, the temperatures of the cell and the adjacent aluminum blocks were set to the same value, while the experimental temperature conditions may have been different between the pouch cell and the cell holder. The C/10 discharge of the pouch cells was carried out directly after a C/10 CCCV charging operation with no pause in between, resulting in inhomogeneous thermal starting conditions. The aim of the following simulation studies with the homogenized thermal 3D model was a qualitative assessment of maximum temperatures that occur in larger cell formats, so a deviation below 2 K was considered as acceptable.

The cell holder of the pouch cells consisted of two aluminum blocks, which represent an additional heat sink for the generated heat in the cell. Waldmann et al.[73] experimentally investigated the temperatures and temperature gradients of different pouch and cylindric lithium-ion cells and, among other things, used an aluminum block with an 18 mm hole including mounted dissipaters and fans for cooling of an 18 650 cylindric cell. With this setup, they could drastically reduce the cell temperature during operation. Even if the aluminum blocks of the pouch cell holder were not actively cooled, the cell temperatures without this additional heat sink would certainly be higher.

Convective cooling.—In our first study, thermal simulations with convective cooling boundary conditions for the cell formats listed in Table IV were carried out. In contrast to the preceding model validation, no cell holder or respective aluminum blocks were added to the model. Only the jelly roll or electrode stack and the corresponding cell case were modeled, and the whole surface of the housing was exposed to a convective heat flow. In this way, a general comparison between all cell formats was possible, independent of the cooling conditions of a specific application. Furthermore, the heat generation was scaled via the total electrode area of the cathode that fits into each cell format, not via the amount of active material. The maximum temperatures of the cell formats for discharge C-rates of C/10, C/2, and 1C are displayed in

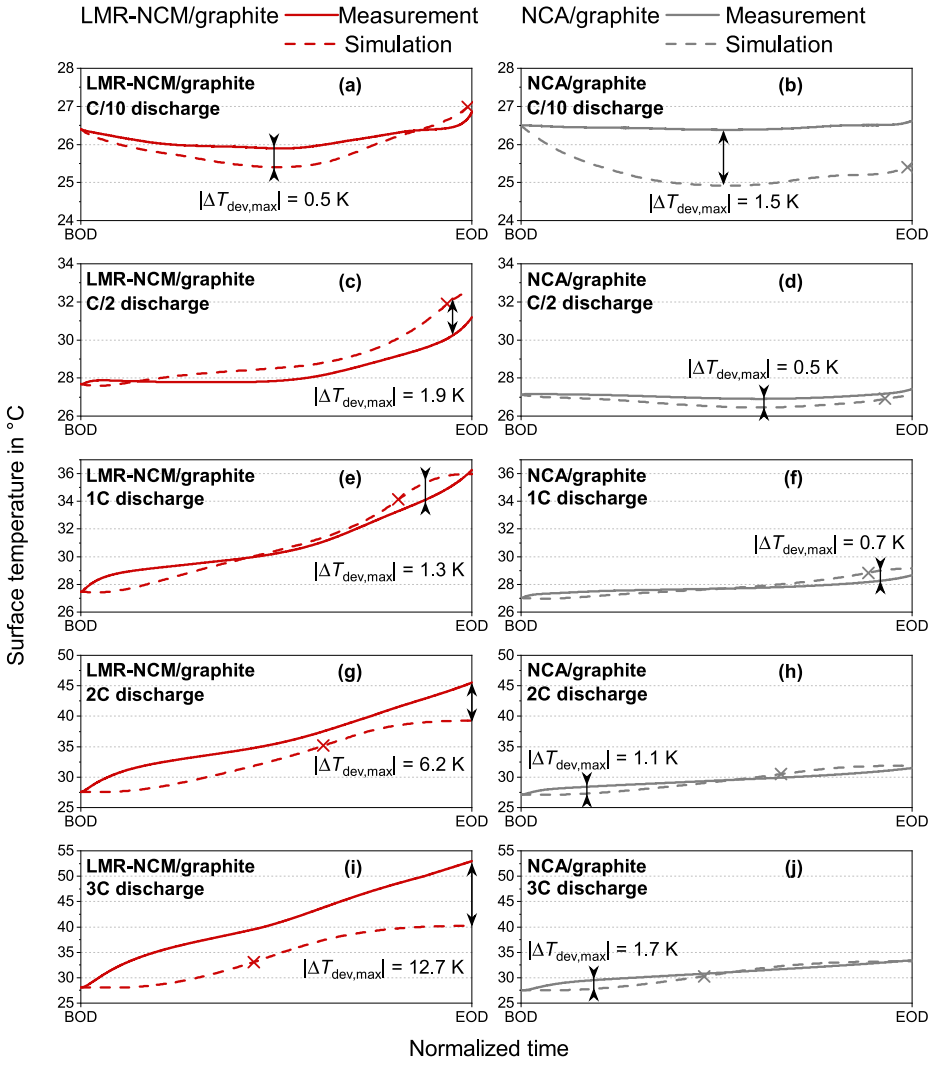

Figure 6. Comparison of the measured temperatures on the surface of the pouch cells within the cell holders during the discharge rate capability test with the simulated surface temperatures of the pouch cells of the thermal validation model. The crosses mark the time when the current was switched off during the simulation. For each C-rate, the maximum deviation $|\Delta T_{dev,max}|$ is indicated with the black arrow.

Fig. 7. The filled symbols indicate the LMR-NCM/graphite cells, while the open symbols indicate the NCA/graphite cells. As the cells were uniformly cooled via the whole surface of the case, the maximum temperatures occurred in the core of the jelly roll or electrode stack.

In Fig. 7a, a natural convection of 5 W m^{-2} K^{-1} on the surface of the cells was simulated, meaning that the cells were not actively cooled during operation; the heat is passively dissipated from the cell surface to the surrounding air. If cells are cooled via their surface, the decisive parameter is the surface to volume (S/V) ratio, as listed in Table IV. The higher the S/V ratio for a constant cell volume, the more cooling surface is available and the lower the cell temperatures become. For the pouch and prismatic cell formats, the HEV cells have the highest S/V ratio and the BEV cells the lowest ratio, with the PHEV cells somewhere in between, resulting in maximum temperatures $T_{max,HEV} < T_{max,PHEV} < T_{max,BEV}$ for convective cooling. The S/V ratio of cylindrical cells decreases with increasing cell diameter, hence $T_{max,18650} < T_{max,21700} < T_{max,26650}$. The nominal cell capacity plays a minor role, e.g., during a 1C discharge under natural convection (5 W m^{-2} K^{-1}), the maximum temperatures of the cylindric 26 650 LMR-NCM/graphite cell with 5.5 Ah are similar to the PHEV2 LMR-NCM/graphite pouch cell with 66 Ah.

For a C/10 discharge, with a heat transfer coefficient of 5 W m^{-2} K^{-1} in Fig. 7a, all LMR-NCM/graphite cells reach temperatures above 31 °C up to 42 °C, while the NCA/graphite cells only heat up to 28 °C. For the C/2 and 1C discharges, the temperatures of the LMR-NCM/graphite cells drastically increase, most cell formats reaching critical temperatures above 60 °C, whereas the NCA/graphite cell temperatures stay below 50 °C. The thermal model was not validated for the simulated cell formats, but the differentiation of the maximum temperatures between the LMR-NCM/graphite and the NCA/graphite cells becomes obvious.

In the study of Waldmann et al.,[73] a commercial 18 650 high energy NCA/graphite cell with 3.25 Ah reached temperatures between 32 –43 °C for discharges with C/10, C/2, and 1C at an ambient temperature of 25 °C, which is about the temperature range of our simulations for cylindric NCA/graphite cells. Furthermore, they stated, that the maximum cell temperatures depend linearly on the discharge C-rate for a full discharge.[73] A rescaling of the *x*-axis in Fig. 7 shows, that the temperature correlation for the three investigated discharge C-rates is not perfectly linear, however, with

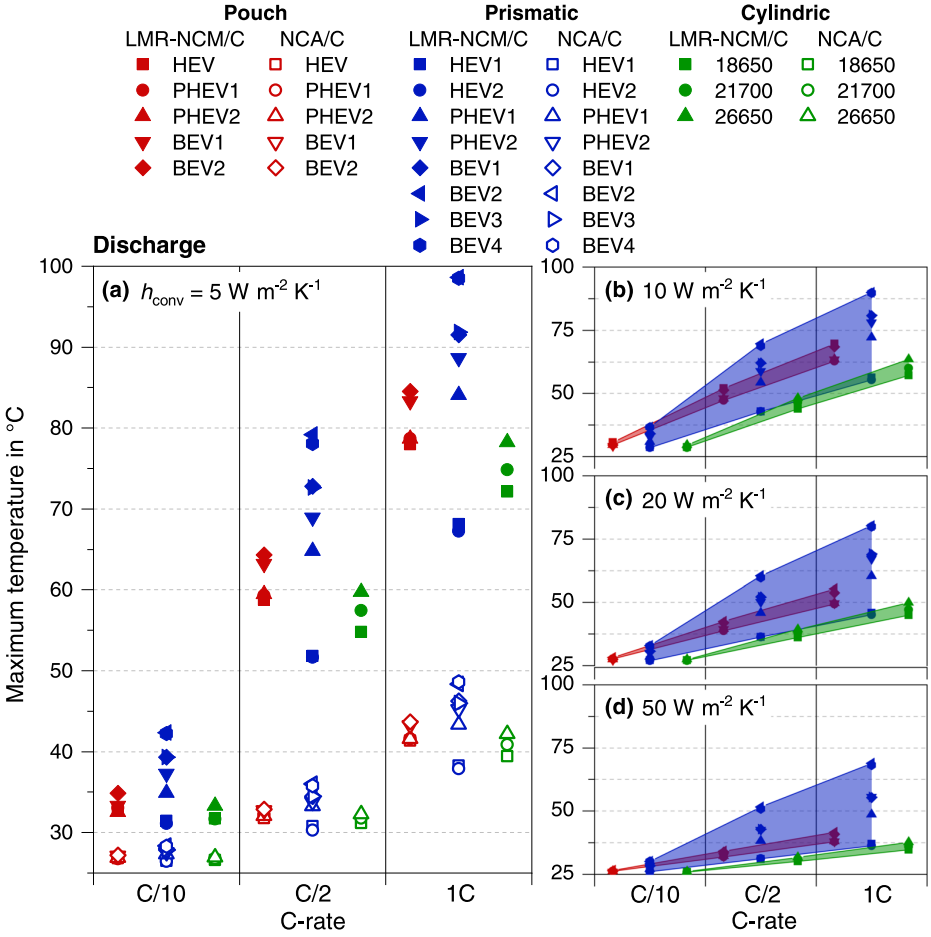

Figure 7. Simulated maximum temperatures of LMR-NCM/graphite and NCA/graphite chemistries in different cell formats (stated in Table IV) during or after discharge processes with a convective surface cooling scenario of (a) h_{conv} = 5 W m^{-2} K^{-1}, (b) 10 W m^{-2} K^{-1}, (c) 20 W m^{-2} K^{-1}, and (d) 50 W m^{-2} K^{-1}. In (b), (c), and (d) only the LMR-NCM/graphite cells are shown, and the colored areas indicate the temperature range of the respective cell format. The starting temperature of the cells as well as the ambient temperature were set to 25 °C.

this assumption, one could still estimate the maximum temperatures that are reached with higher C-rates for a given cell format.

In this work, the NCA/graphite cells were used as a state-of-the-art reference, but the focus is on the thermal behavior of the LMR-NCM/graphite cells, so in the following studies, only the latter are further analyzed. If a higher surface cooling is assumed, as 10 W m^{-2} K^{-1} seen in Fig. 7b, 20 W m^{-2} K^{-1} in Fig. 7c, and 50 W m^{-2} K^{-1} in Fig. 7d, the pouch (red area) and cylindric (green area) LMR-NCM/graphite cell formats can be kept within acceptable temperature ranges. The prismatic cells show quite a diverging behavior and four sub-groups with a similar S/V ratio can be identified. The first group consists of the HEV1 (15 Ah) and HEV2 (14 Ah) cells that are comparatively thin with a thickness of 12.5 mm and 12.1 mm and a S/V ratio of 2.6 m^{-1} and 2.7 m^{-1}, respectively. The PHEV1 cell with a nominal capacity of 41 Ah, a thickness of 21 mm, and a S/V ratio of 1.6 m^{-1} forms the second group. The third group consists of the PHEV2 (48 Ah, 26.5 mm, 1.3 m^{-1}), the BEV1 (90 Ah, 32 mm, 1.1 m^{-1}), and the BEV3 (98 Ah, 32 mm, 1.0 m^{-1}) cells. The BEV2 (127 Ah, 45 mm, 0.8 m^{-1}) and BEV4 (139 Ah, 45 mm, 0.8 m^{-1}) cells form the fourth group. Even with a heat transfer coefficient of 50 W m^{-2} K^{-1}, the thick BEV2 and BEV4 formats reach maximum temperatures around 68 °C for a 1C discharge.

Within this first simulation study it became clear that the cell format plays a crucial role for the temperature evolution of large-format LMR-NCM/graphite cells. Without any active cooling, either the discharge should be limited to C-rates lower than C/2, or thinner cell formats with a comparatively high S/V ratio and a low nominal capacity like the prismatic HEV1/HEV2 or the cylindric 18 650 are favorable. By using an active cooling system, larger cell formats and higher discharge C-rates are possible, however very thick cells with a high capacity like the BEV2 and BEV4 cells cannot be sufficiently convectively cooled via their surface[74] and reach critical temperatures. Therefore, in the next section, a more adapted cooling strategy for prismatic cells is described.

Base plate cooling.—In our second study, a bottom plate cooling of prismatic cell formats was simulated. Large-format prismatic cells are used by car manufacturers in EVs to reach high energy densities and sufficient driving ranges. An active thermal management of the battery pack is often realized via cooled plates that are mounted underneath the cells. Therefore, the bottom of the prismatic cell case was kept at a constant temperature of 20 °C during the simulations. To have homogeneous starting conditions, the cell temperature was also set to 20 °C. The simulation results for a 1C discharge of four different prismatic LMR-NCM/graphite cells are shown in Fig. 8. In the previous convective simulations, four sub-groups of prismatic cells were identified based on their different thermal behavior. For this study, one representative of each group, namely the HEV2, PHEV1, BEV1, and BEV2 cell formats were chosen.

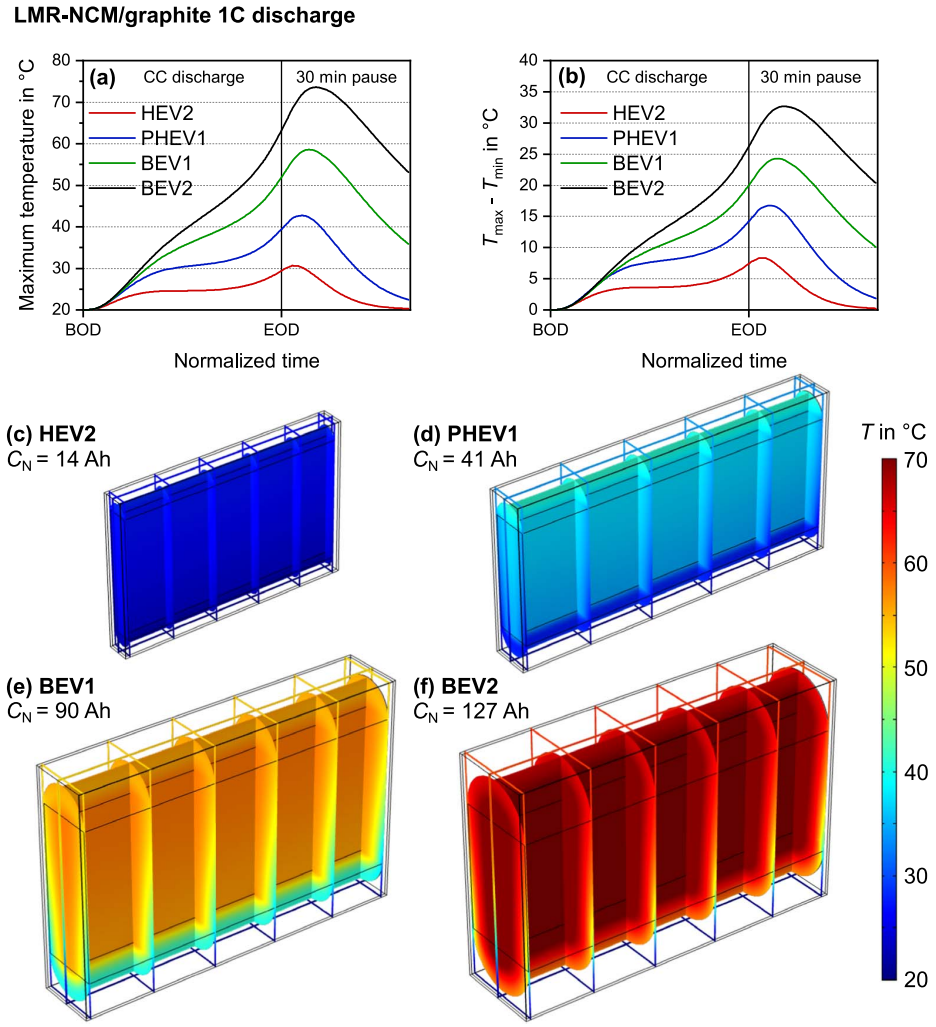

Figure 8. Simulated temperatures during a 1C discharge and the 30 min pause afterwards with a base plate cooling scenario of prismatic LMR-NCM/graphite cells. (a) Maximum temperature and (b) temperature spread (T_{max} - T_{min}) within the jelly roll. The 3D plots show the temperatures of the cell formats (c) HEV2, (d) PHEV1, (e) BEV1, and (f) BEV2 at the time, when the maximum cell temperature was reached. The starting temperature of the cells as well as the constant temperature of the base plate were set to 20 °C.

In Fig. 8a, the maximum temperatures of the four cell formats within the jelly roll during the 1C discharge and the 30 min pause afterwards are shown. Particularly at the end of discharge, the temperatures drastically rise, as the heat generation of the LMR-NCM/graphite cells increases rapidly, as seen in Fig. 5. Because of the time-delayed measurement of the heat generation, the maximum temperatures occurred after the end of discharge. In Fig. 8b, the temperature spread within the jelly roll is displayed. The higher this temperature spread is within the cell, the more inhomogeneities there will be. This results in uneven internal resistances, loads, and SOCs during cycling and most likely also a different aging behavior.[73,75] Furthermore, usually there are no internal temperature sensors in the cells, so with high temperature gradients, a battery management system has more difficulties to track or estimate the hottest temperature within the cell to prevent safety critical conditions. For all these reason, if possible, the temperature spread within a cell should be kept minimal.

In Figs. 8c–8f, 3D temperature distributions of the four cell formats are plotted at the exact time, when the maximum jelly roll temperature was reached (i.e., at the time of the maximum in Fig. 8a). In the simulations of the base plate cooling of prismatic cells, the coldest temperature was always at the bottom of the cell, as this is where the cooling plate was attached. On the other hand, the hottest temperature was at the top of the cell, as this is the furthest away from the cooling side, and the top and side areas were thermally insulated, derived by the neighboring cells in a module and the electrical connection on the top.

With the base plate cooling strategy, the four cell formats still exhibit distinct differences in their thermal behavior, the maximum temperatures are around 10 °C higher for the next larger cell. If full discharge cycles are necessary, the HEV2 (representing also HEV1) and PHEV1 cell formats are advantageous, as their maximum temperatures stay below 43 °C. The BEV2 cell reaches 74 °C at its hottest spot, however, if the 1C discharge would be stopped after e.g., 80% of the time, the maximum temperature would be much lower. For our simulations, the cooling plate was kept at a constant temperature of 20 °C. With a better thermal management system and a higher cooling power, this temperature could be lowered, yet the temperature spread within the cell would also increase.[73,75] There is a spread of more than 30 °C within the BEV2 cell already, so this strategy might not be helpful.

A tab cooling system could provide a better and more homogeneous cooling, especially for pouch cells.[74] Thus, not only the

cooling strategy has to be adapted to the cell format, but also the load profile of the corresponding application. A dynamic load profile around a mean SOC could result in a quite different temperature evolution. In summary, an application defines the specific requirements of the preferred cell format and the design of the corresponding thermal management system.

Conclusions

In this work, the heat generation of LMR-NCM/graphite cells was investigated. The LMR-NCM cathode active material comes with a pronounced difference between charge and discharge voltage during operation, caused by overpotentials and an OCV hysteresis. This voltage difference results in an energy inefficiency that is released as waste heat and causes a strong heat generation. As a reference, an established NCA/graphite material combination was chosen. So far, LMR-NCM was predominantly studied in small laboratory-scale cells where the heat generation is negligible. However, in large-format LMR-NCM/graphite cells, critical temperatures above 60 °C can easily be reached. In order to qualitatively assess the thermal behavior of large-format cells, the heat generation of LMR-NCM/graphite and NCA/graphite coin cells was measured in a heat flow calorimeter, scaled to various standardized cell formats via their electrode area, and used as an input parameter for homogenized 3D thermal models.

The calorimetric measurements showed, that during charging operations, the LMR-NCM/graphite cells generate more than double the heat than comparable NCA/graphite cells. During discharge operations, the LMR-NCM/graphite cells released even more heat, making it four times more than the NCA/graphite cells. The coin cells used for the calorimetry stayed quasi-isothermal during these measurements, whereas larger cells heat up during operation. The model validation with measurement data from reference 6–7 Ah pouch cells showed, that for the LMR-NCM/graphite cells, the upscaling of the heat generation is only valid up to 1C, as higher cell temperatures resulted in a promoted electrochemical behavior that is not accounted for in this process. For the same C-rate, the LMR-NCM/graphite cells generate more heat during discharge operations than charge operations. Therefore, only the thermal behavior during discharge operations was further investigated in two simulation studies.

In our first simulation study, a convective cooling scenario for standardized prismatic, pouch, and cylindric cell formats for discharge rates of C/10, C/2, and 1C was analyzed. With only passive cooling, i.e., natural convection on the surface of the cells, either the discharge current has to be limited to C-rates lower than C/2, or thin cell formats with a high surface to volume ratio and comparatively low nominal capacity are favorable. Good examples are the prismatic HEV1 and HEV2 cells as well as the cylindric 18650 cell. By using an active convective cooling strategy, more heat can be dissipated and most cell formats show acceptable temperature ranges. Exceptions are posed by thick prismatic cell formats, e.g., the BEV2 and BEV4 cells, that cannot be sufficiently cooled via convection. Even with a forced convection, simulated with a heat transfer coefficient of $50\,\mathrm{W\,m^{-2}\,K^{-1}}$, maximum temperatures of these two cell formats of around 68 °C were reached for a 1C discharge.

In our second study, a base plate cooling of four prismatic cell formats during a 1C discharge was simulated. This cooling strategy is more adapted to automotive prismatic cell formats as often used in EVs. With this base plate cooling, the HEV1, HEV2, and PHEV1 cell formats were advantageous, as the cell temperatures remained below 43 °C. The thicker prismatic cells reached higher temperatures between 58 °C–74 °C, accompanied by an unfavorable temperature spread within the jelly roll of more than 32 °C from the coldest spot on the bottom to the hottest spot on the top. In the simulations, only full discharge cycles were considered, whereas with partial discharges or dynamic load profiles around a mean SOC, the thermal behavior of the cells would certainly be different.

To summarize, the thermal behavior of cells containing LMR-NCM should be accounted for. Especially larger cell formats and higher charge/discharge currents can result in undesired cell temperatures. This heat generation is mainly caused by the voltage difference between charge and discharge of LMR-NCM, so the thermal behavior of materials with a similarly lower voltage efficiency should also be carefully investigated. Silicon, for example, exhibits a pronounced voltage difference of $\approx$300 mV between charge and discharge even at low currents.[76] The aim of our work was to highlight the general implications of the heat generation caused by an active material like LMR-NCM with a low voltage efficiency on the thermal behavior of different cell formats. For a specific application, including its corresponding load profile, an optimal cell design and operating strategy for the thermal management system could be derived.

Acknowledgments

This work was financially supported by the German Federal Ministry of Education and Research (BMBF) under grant number 03XP0255 (ExZellTUM III). The authors gratefully acknowledge the scientific discussions with Johannes Sturm and Franziska Friedrich, and thank BASF SE for the supply of cathode materials.

Appendix

In the results section in Fig. 5, the heat generation of one LMR-NCM/graphite and one NCA/graphite coin cell was shown. In order to validate that these cells provide meaningful values, the heat generation of a second coin cell of each type was measured in the calorimeter. In Fig. A·1, the comparison of the heat generation for two cells each during charge and discharge was plotted for the C-rates C/10, C/2, and 1C. The heat generation rates of the two LMR-NCM/graphite cells are in excellent agreement, the two NCA/graphite cells differ slightly. Therefore, the higher heat generation of cell N1 was chosen for the simulations.

The input parameters of the homogenized jelly roll/electrode stack for the thermal model were calculated based on the material properties of multilayer LMR-NCM/graphite pouch cells.[24,27] The

Table A·I. Calculation of the thermal modeling parameters of the homogenized jelly roll/electrode stack based on multilayer LMR-NCM/graphite pouch cells.[24,27] The material properties were taken from data sheets and literature.[14,31,51]

Parameter	Unit	CC_{neg} Cu	$Coating_{neg}$ graphite	Separator PP	$Coating_{pos}$ LMR-NCM	CC_{pos} Al	Electrolyte
l	μm	12	64	25	55	15	
porosity	%		30	55	42		
ρ	$\mathrm{kg\,m^{-3}}$	8920	2208	980	3960	2698	1289
c_p	$\mathrm{J\,kg^{-1}\,K^{-1}}$	385	867	1978	840	903	2055
k	$\mathrm{W\,m^{-1}\,K^{-1}}$	398	1.04	0.33	1.58	238	0.6

Note. CC—current collector, PP—polypropylene.

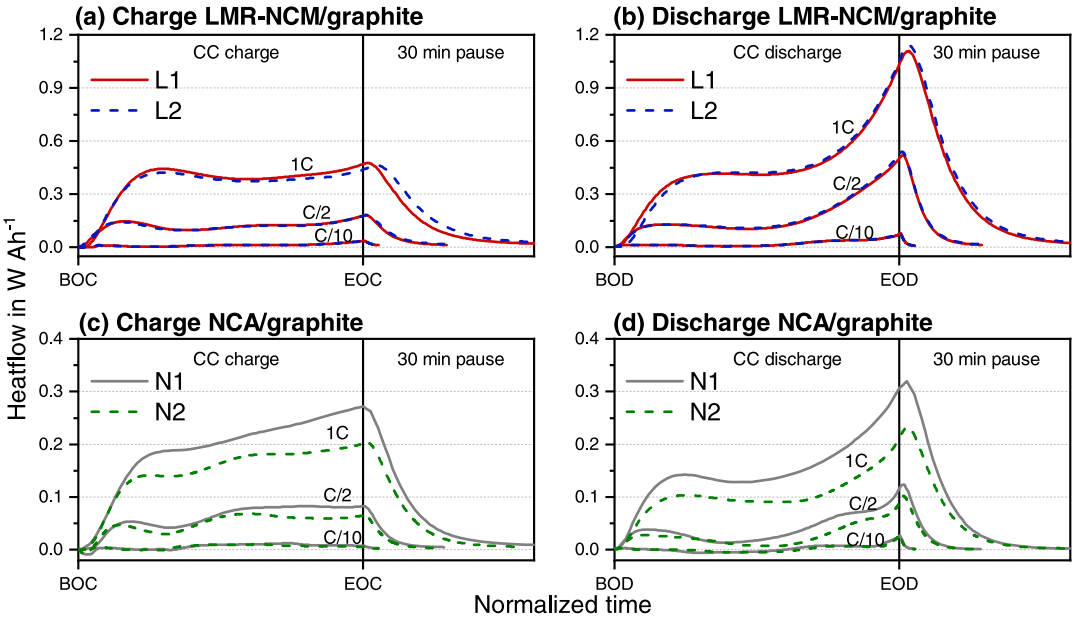

Figure A·1. Comparison of the heat generation of two LMR-NCM/graphite coin cells and two NCA/graphite coin cells for varying charge and discharge C-rates including the 30 min pause afterwards. The heat generation was normalized to the respective charge/discharge capacity in each cycle, and the *x*-axis was normalized to the charge/discharge time. The begin of charge (BOC) represents a SOC of 0%, the begin of discharge (BOD) represents a SOC of 100%, while the respective end of charge (EOC) and end of discharge (EOD) mark the time when the current in the CC phase was switched off.

following equations calculate the total density ρ_{tot}, the heat capacity $c_{p,tot}$, the through-plane thermal conductivity $k_{\perp}$, and the in-plane thermal conductivity $k_{\parallel}$ based on the respective layer thicknesses l.[14,31,47] The corresponding material properties are listed in Table A·I.

$$\rho_{tot} = \frac{\sum_i \rho_i l_i}{l_{tot}} = 2427 \text{ kg m}^{-3} \quad [A·1]$$

$$c_{p,tot} = \frac{\sum_i \rho_i c_{p,i} l_i}{\rho_{tot} l_{tot}} = 1049 \text{ J kg}^{-1} \text{ K}^{-1} \quad [A·2]$$

$$k_{\perp} = \frac{l_{tot}}{\sum_i \frac{l_i}{k_i}} = 0.83 \text{ W m}^{-1} \text{ K}^{-1} \quad [A·3]$$

$$k_{\parallel} = \frac{\sum_i l_i k_i}{l_{tot}} = 27.3 \text{ W m}^{-1} \text{ K}^{-1} \quad [A·4]$$

ORCID

Ludwig Kraft https://orcid.org/0000-0003-4324-426X
Tanja Zünd https://orcid.org/0000-0002-1650-3636
Alexander Kunz https://orcid.org/0000-0003-3169-4263
Marco Steinhardt https://orcid.org/0000-0003-1356-1686
Andreas Jossen https://orcid.org/0000-0003-0964-1405

References

1. D. Andre, S.-J. Kim, P. Lamp, S. F. Lux, F. Maglia, O. Paschos, and B. Stiaszny, "Future generations of cathode materials: An automotive industry perspective." *Journal of Materials Chemistry A*, **3**, 6709 (2015).
2. R. E. Ciez and J. F. Whitacre, "Comparison between cylindrical and prismatic lithium-ion cell costs using a process based cost model." *Journal of Power Sources*, **340**, 273 (2017).
3. R. Schmuch, R. Wagner, G. Hörpel, T. Placke, and M. Winter, "Performance and cost of materials for lithium-based rechargeable automotive batteries." *Nat. Energy*, **3**, 267 (2018).
4. Y. Ding, Z. P. Cano, A. Yu, J. Lu, and Z. Chen, "Automotive Li-Ion Batteries: Current Status and Future Perspectives." *Electrochemical Energy Reviews*, **2**, 1 (2019).
5. G. Offer, Y. Patel, A. Hales, L. Bravo Diaz, and M. Marzook, "Cool metric for lithium-ion batteries could spur progress." *Nature*, **582**, 485 (2020).
6. T. G. Tranter, R. Timms, P. R. Shearing, and D. J. L. Brett, "Communication–Prediction of Thermal Issues for Larger Format 4680 Cylindrical Cells and Their Mitigation with Enhanced Current Collection." *J. Electrochem. Soc.*, **167**, 160544 (2020).
7. M. Armand, P. Axmann, D. Bresser, M. Copley, K. Edström, C. Ekberg, D. Guyomard, B. Lestriez, P. Novák, M. Petranikova, W. Porcher, S. Trabesinger, M. Wohlfahrt-Mehrens, and H. Zhang, "Lithium-ion batteries—Current state of the art and anticipated developments." *Journal of Power Sources*, **479**, 228708 (2002).
8. J. B. Quinn, T. Waldmann, K. Richter, M. Kasper, and M. Wohlfahrt-Mehrens, "Energy Density of Cylindrical Li-Ion Cells: A Comparison of Commercial 18650 to the 21700 Cells." *J. Electrochem. Soc.*, **165**, A3284 (2018).
9. DIN Deutsches Institut für Normung e.V., Electrically propelled road vehicles—Battery systems—Design specifications for Lithium-Ion battery cells (2016-11).
10. G. E. Blomgren, "The Development and Future of Lithium Ion Batteries." *J. Electrochem. Soc.*, **164**, A5019 (2016).
11. T.-F. Yi, L.-J. Jiang, J. Shu, C.-B. Yue, R.-S. Zhu, and H.-B. Qiao, "Recent development and application of $Li_4Ti_5O_{12}$ as anode material of lithium ion battery." *J. Phys. Chem. Solids*, **71**, 1236 (2010).
12. W.-J. Zhang, "A review of the electrochemical performance of alloy anodes for lithium-ion batteries." *Journal of Power Sources*, **196**, 13 (2011).
13. Z. Luo, D. Fan, X. Liu, H. Mao, C. Yao, and Z. Deng, "High performance silicon carbon composite anode materials for lithium ion batteries." *Journal of Power Sources*, **189**, 16 (2009).
14. J. Sturm, A. Rheinfeld, I. Zilberman, F. B. Spingler, S. Kosch, F. Frie, and A. Jossen, "Modeling and simulation of inhomogeneities in a 18650 nickel-rich, silicon-graphite lithium-ion cell during fast charging." *Journal of Power Sources*, **412**, 204 (2019).
15. E. Moyassari, L. Streck, N. Paul, M. Trunk, R. Neagu, C.-C. Chang, S.-C. Hou, B. Märkisch, R. Gilles, and A. Jossen, "Impact of Silicon Content within Silicon-Graphite Anodes on Performance and Li Concentration Profiles of Li-Ion Cells using Neutron Depth Profiling." *J. Electrochem. Soc.*, **168**, 020519 (2021).
16. J. R. Croy, M. Balasubramanian, K. G. Gallagher, and A. K. Burrell, "Review of the U.S. Department of Energy's "deep dive" effort to understand voltage fade in Li- and Mn-rich cathodes." *Acc. Chem. Res.*, **48**, 2813 (2015).
17. T. Teufl, D. Pritzl, S. Solchenbach, H. A. Gasteiger, and M. A. Mendez, "State of Charge Dependent Resistance Build-Up in Li- and Mn-Rich Layered Oxides during Lithium Extraction and Insertion." *J. Electrochem. Soc.*, **166**, A1275 (2019).

18. D. Becker, M. Börner, A. Friesen, S. Klein, U. Rodehorst, M. Diehl, M. Winter, T. Placke, and R. Schmuch, "Towards High-Performance Li-rich NCM-Graphite Cells by Germanium-Polymer Coating of the Positive Electrode Material." *J. Electrochem. Soc.*, **167**, 060524 (2020).
19. J. Helbig, T. Beuse, V. Siozios, T. Placke, M. Winter, and R. Schmuch, "Li-Mn-Rich Cathode Materials with Low-Cobalt Content and Core-Shell Particle Design for High-Energy Lithium Ion Batteries." *J. Electrochem. Soc.*, **167**, 060519 (2020).
20. G. Assat, S. L. Glazier, C. Delacourt, and J.-M. Tarascon, "Probing the thermal effects of voltage hysteresis in anionic redox-based lithium-rich cathodes using isothermal calorimetry." *Nat. Energy*, **4**, 647 (2019).
21. N. Leifer, T. Penki, R. Nanda, J. Grinblat, S. Luski, D. Aurbach, and G. Goobes, "Linking structure to performance of $Li_{1.2}Mn_{0.54}Ni_{0.13}Co_{0.13}O_2$ (Li and Mn rich NMC) cathode materials synthesized by different methods." *Physical chemistry chemical physics : PCCP*, **22**, 9098.
22. J. R. Croy, K. G. Gallagher, M. Balasubramanian, B. R. Long, and M. M. Thackeray, "Quantifying Hysteresis and Voltage Fade in $xLi_2MnO_3 \cdot (1-x)LiMn_{0.5}Ni_{0.5}O_2$ Electrodes as a Function of Li_2MnO_3 Content." *J. Electrochem. Soc.*, **161**, A318 (2014).
23. D. Mohanty, J. Li, D. P. Abraham, A. Huq, E. A. Payzant, D. L. Wood, and C. Daniel, "Unraveling the Voltage-Fade Mechanism in High-Energy-Density Lithium-Ion Batteries: Origin of the Tetrahedral Cations for Spinel Conversion." *Chemistry of Materials*, **26**, 6272 (2014).
24. L. Kraft, T. Zünd, D. Schreiner, R. Wilhelm, F. J. Günter, G. Reinhart, H. A. Gasteiger, and A. Jossen, "Comparative Evaluation of LMR-NCM and NCA Cathode Active Materials in Multilayer Lithium-Ion Pouch Cells: Part II. Rate Capability, Long-Term Stability, and Thermal Behavior." *J. Electrochem. Soc.*, **168**, 020537 (2021).
25. F. Wu, J. Maier, and Y. Yu, "Guidelines and trends for next-generation rechargeable lithium and lithium-ion batteries." *Chem. Soc. Rev.*, **49**, 1569 (2020).
26. P. Meister, H. Jia, J. Li, R. Kloepsch, M. Winter, and T. Placke, "Best Practice: Performance and Cost Evaluation of Lithium Ion Battery Active Materials with Special Emphasis on Energy Efficiency." *Chemistry of Materials*, **28**, 7203 (2016).
27. D. Schreiner, T. Zünd, F. J. Günter, L. Kraft, B. Stumper, F. Linsenmann, M. Schüßler, R. Wilhelm, A. Jossen, G. Reinhart, and H. A. Gasteiger, "Comparative Evaluation of LMR-NCM and NCA Cathode Active Materials in Multilayer Lithium-Ion Pouch Cells: Part I. Production, Electrode Characterization, and Formation." *J. Electrochem. Soc.*, **168**, 030507 (2021).
28. J. Zheng, W. Shi, M. Gu, J. Xiao, P. Zuo, C. Wang, and J.-G. Zhang, "Electrochemical Kinetics and Performance of Layered Composite Cathode Material $Li[Li_{0.2}Ni_{0.2}Mn_{0.6}]O_2$." *J. Electrochem. Soc.*, **160**, A2212 (2013).
29. W. Mao, G. Ai, Y. Dai, Y. Fu, X. Song, H. Lopez, and V. Battaglia, "Nature of the Impedance at Low States of Charge for High-Capacity, Lithium and Manganese-Rich Cathode Materials." *J. Electrochem. Soc.*, **163**, A3091 (2016).
30. J. R. Croy, K. G. Gallagher, M. Balasubramanian, Z. Chen, Y. Ren, D. Kim, S.-H. Kang, D. W. Dees, and M. M. Thackeray, "Examining Hysteresis in Composite $xLi_2MnO_3 \cdot (1- x)LiMO_2$ Cathode Structures." *The Journal of Physical Chemistry C*, **117**, 6525 (2013).
31. S. C. Chen, C. C. Wan, and Y. Y. Wang, "Thermal analysis of lithium-ion batteries." *Journal of Power Sources*, **140**, 111 (2005).
32. G.-H. Kim, K. Smith, K.-J. Lee, S. Santhanagopalan, and A. Pesaran, "Multi-Domain Modeling of Lithium-Ion Batteries Encompassing Multi-Physics in Varied Length Scales." *J. Electrochem. Soc.*, **158**, A955 (2011).
33. S. V. Erhard, P. J. Osswald, J. Wilhelm, H. E. Hoster, and A. Jossen, "Simulation and Measurement of Local Potentials of Modified Commercial Cylindrical Cells: II: Multi-Dimensional Modeling and Validation." *J. Electrochem. Soc.*, **162**, A2707 (2015).
34. A. Rheinfeld, S. Kosch, S. V. Erhard, P. J. Osswald, B. Rieger, and A. Jossen, "Electro-Thermal Modeling of Large Format Lithium-Ion Pouch Cells: A Cell Temperature Dependent Linear Polarization Expression." *J. Electrochem. Soc.*, **163**, A3046 (2016).
35. B. Rieger, S. V. Erhard, S. Kosch, M. Venator, A. Rheinfeld, and A. Jossen, "Multi-Dimensional Modeling of the Influence of Cell Design on Temperature, Displacement and Stress Inhomogeneity in Large-Format Lithium-Ion Cells." *J. Electrochem. Soc.*, **163**, A3099 (2016).
36. D. Chen, J. Jiang, G.-H. Kim, C. Yang, and A. Pesaran, "Comparison of different cooling methods for lithium ion battery cells." *Applied Thermal Engineering*, **94**, 846 (2016).
37. H. Lundgren, P. Svens, H. Ekström, C. Tengstedt, J. Lindström, M. Behm, and G. Lindbergh, "Thermal Management of Large-Format Prismatic Lithium-Ion Battery in PHEV Application." *J. Electrochem. Soc.*, **163**, A309 (2016).
38. R. Kantharaj and A. M. Marconnet, "Heat Generation and Thermal Transport in Lithium-Ion Batteries: A Scale-Bridging Perspective." *Nanoscale and Microscale Thermophysical Engineering*, **23**, 128 (2019).
39. J. Sturm, A. Frank, A. Rheinfeld, S. V. Erhard, and A. Jossen, "Impact of Electrode and Cell Design on Fast Charging Capabilities of Cylindrical Lithium-Ion Batteries." *J. Electrochem. Soc.*, **167**, 130505 (2020).
40. H. Park, "A design of air flow configuration for cooling lithium ion battery in hybrid electric vehicles." *Journal of Power Sources*, **239**, 30 (2013).
41. J. Zhao, Z. Rao, and Y. Li, "Thermal performance of mini-channel liquid cooled cylinder based battery thermal management for cylindrical lithium-ion power battery." *Energy Conversion and Management*, **103**, 157 (2015).
42. A. de Vita, A. Maheshwari, M. Destro, M. Santarelli, and M. Carello, "Transient thermal analysis of a lithium-ion battery pack comparing different cooling solutions for automotive applications." *Applied Energy*, **206**, 101 (2017).
43. K.-H. Chen, M. J. Namkoong, V. Goel, C. Yang, S. Kazemiabnavi, S. M. Mortuza, E. Kazyak, J. Mazumder, K. Thornton, J. Sakamoto, and N. P. Dasgupta, "Efficient fast-charging of lithium-ion batteries enabled by laser-patterned three-dimensional graphite anode architectures." *Journal of Power Sources*, **471**, 228475 (2020).
44. G. Reinhart, T. Zeilinger, J. Kurfer, M. Westermeier, C. Thiemann, M. Glonegger, M. Wunderer, C. Tammer, M. Schweier, and M. Heinz, "Research and Demonstration Center for the Production of Large-Area Lithium-Ion Cells." *Future Trends in Production Engineering*, ed. G. Schuh, R. Neugebauer, and E. Uhlmann (Springer, Berlin, Heidelberg) 3 (2013).
45. R. Schröder, M. Aydemir, and G. Seliger, "Comparatively Assessing different Shapes of Lithium-ion Battery Cells." *Procedia Manufacturing*, **8**, 104 (2017).
46. A. Kwade, W. Haselrieder, R. Leithoff, A. Modlinger, F. Dietrich, and K. Droeder, "Current status and challenges for automotive battery production technologies." *Nat. Energy*, **3**, 290 (2018).
47. T. M. Bandhauer, S. Garimella, and T. F. Fuller, "A Critical Review of Thermal Issues in Lithium-Ion Batteries." *J. Electrochem. Soc.*, **158**, R1 (2011).
48. H. Maleki, S. A. Hallaj, J. R. Selman, R. B. Dinwiddie, and H. Wang, "Thermal Properties of Lithium-Ion Battery and Components." *J. Electrochem. Soc.*, **146**, 947 (1999).
49. K. Darcovich, D. D. MacNeil, S. Recoskie, and B. Kenney, "Coupled electro-chemical and thermal battery models for thermal management of prismatic automotive cells." *Applied Thermal Engineering*, **133**, 566 (2018).
50. M. Steinhardt, E. I. Gillich, M. Stiegler, and A. Jossen, "Thermal conductivity inside prismatic lithium-ion cells with dependencies on temperature and external compression pressure." *Journal of Energy Storage*, **32**, 101680 (2020).
51. S. D. Lubner, S. Kaur, Y. Fu, V. Battaglia, and R. S. Prasher, "Identification and characterization of the dominant thermal resistance in lithium-ion batteries using operando 3-omega sensors." *J. Appl. Phys.*, **127**, 105104 (2020).
52. T. Bandhauer, S. Garimella, and T. F. Fuller, "Electrochemical-Thermal Modeling to Evaluate Battery Thermal Management Strategies: I. Side Cooling." *J. Electrochem. Soc.*, **162**, A125 (2015).
53. X. Zhang and T. Wierzbicki, "Characterization of plasticity and fracture of shell casing of lithium-ion cylindrical battery." *Journal of Power Sources*, **280**, 47 (2015).
54. J. Zhu, X. Zhang, E. Sahraei, and T. Wierzbicki, "Deformation and failure mechanisms of 18650 battery cells under axial compression." *Journal of Power Sources*, **336**, 332 (2016).
55. M. Ikezoe, N. Hirata, C. AMEMIYA, T. Miyamoto, Y. Watanabe, T. Hirai, and T. Sasaki, "Development of High Capacity Lithium- Ion Battery for NISSAN LEAF." *SAE International*, **2012-01-0664**, 1 (2012).
56. M. Keyser, A. Pesaran, Q. Li, S. Santhanagopalan, K. Smith, E. Wood, S. Ahmed, I. Bloom, E. Dufek, M. Shirk, A. Meintz, C. Kreuzer, C. Michelbacher, A. Burnham, T. Stephens, J. Francfort, B. Carlson, J. Zhang, R. Vijayagopal, K. Hardy, F. Dias, M. Mohanpurkar, D. Scoffield, A. N. Jansen, T. Tanim, and A. Markel, "Enabling fast charging—Battery thermal considerations." *Journal of Power Sources*, **367**, 228 (2017).
57. D. T. Adams, G. Berdichevsky, T. E. Colson, A. Hebert, S. Kohn, D. Lyons, N. J. Mendez, J. B. Straubel, D. West, and A. Simpson, *Battery Pack Thermal Management System*, Patent Application Publication (2009), US 2009/0023056A1.
58. J. Kim, J. Oh, and H. Lee, "Review on battery thermal management system for electric vehicles." *Applied Thermal Engineering*, **149**, 192 (2019).
59. Y. Deng, C. Feng, E. J. H. Zhu, J. Chen, M. Wen, and H. Yin, "Effects of different coolants and cooling strategies on the cooling performance of the power lithium ion battery system: A review." *Applied Thermal Engineering*, **142**, 10 (2018).
60. A. Adam, J. Wandt, E. Knobbe, G. Bauer, and A. Kwade, "Fast-Charging of Automotive Lithium-Ion Cells: In-Situ Lithium-Plating Detection and Comparison of Different Cell Designs." *J. Electrochem. Soc.*, **167**, 130503 (2020).
61. X. Feng, X. He, M. Ouyang, L. Lu, P. Wu, C. Kulp, and S. Prasser, "Thermal runaway propagation model for designing a safer battery pack with 25 Ah $LiNi_xCo_yMn_zO_2$ large format lithium ion battery." *Applied Energy*, **154**, 74 (2015).
62. K. Takano, Y. Saito, K. Kanari, K. Nozaki, K. Kato, A. Negishi, and T. Kato, "Entropy change in lithium ion cells on charge and discharge." *Journal of Applied Electrochemistry*, **32**, 251 (2002).
63. P. J. Osswald, M. D. Rosario, J. Garche, A. Jossen, and H. E. Hoster, "Fast and Accurate Measurement of Entropy Profiles of Commercial Lithium-Ion Cells." *Electrochimica Acta*, **177**, 270 (2015).
64. B. Manikandan, C. Yap, and P. Balaya, "Towards Understanding Heat Generation Characteristics of Li-Ion Batteries by Calorimetry, Impedance, and Potentiometry Studies." *J. Electrochem. Soc.*, **164**, A2794 (2017).
65. Y. Reynier, R. Yazami, and B. Fultz, "The entropy and enthalpy of lithium intercalation into graphite." *Journal of Power Sources*, **119-121**, 850 (2003).
66. Y. Reynier, J. Graetz, T. Swan-Wood, P. Rez, R. Yazami, and B. Fultz, "Entropy of Li intercalation in Li_xCoO_2." *Physical Review B*, **70**, 753 (2004).
67. R. Yazami and Y. Reynier, "Thermodynamics and crystal structure anomalies in lithium-intercalated graphite." *Journal of Power Sources*, **153**, 312 (2006).
68. R. E. Williford, V. V. Viswanathan, and J.-G. Zhang, "Effects of entropy changes in anodes and cathodes on the thermal behavior of lithium ion batteries." *Journal of Power Sources*, **189**, 101 (2009).
69. V. V. Viswanathan, D. Choi, D. Wang, W. Xu, S. Towne, R. E. Williford, J.-G. Zhang, J. Liu, and Z. Yang, "Effect of entropy change of lithium intercalation in cathodes and anodes on Li-ion battery thermal management." *Journal of Power Sources*, **195**, 3720 (2010).
70. S. S. Zhang, K. Xu, and T. R. Jow, "Charge and discharge characteristics of a commercial $LiCoO_2$-based 18650 Li-ion battery." *Journal of Power Sources*, **160**, 1403 (2006).

71. K. Kumaresan, G. Sikha, and R. E. White, "Thermal Model for a Li-Ion Cell." *J. Electrochem. Soc.*, **155**, A164 (2008).
72. X.-G. Yang, T. Liu, Y. Gao, S. Ge, Y. Leng, D. Wang, and C.-Y. Wang, "Asymmetric Temperature Modulation for Extreme Fast Charging of Lithium-Ion Batteries." *Joule*, **3**, 3002 (2019).
73. T. Waldmann, G. Bisle, B.-I. Hogg, S. Stumpp, M. A. Danzer, M. Kasper, P. Axmann, and M. Wohlfahrt-Mehrens, "Influence of Cell Design on Temperatures and Temperature Gradients in Lithium-Ion Cells: An In Operando Study." *J. Electrochem. Soc.*, **162**, A921 (2015).
74. A. Hales, R. Prosser, L. Bravo Diaz, G. White, Y. Patel, and G. Offer, "The Cell Cooling Coefficient as a design tool to optimise thermal management of lithium-ion cells in battery packs." *eTransportation*, **6**, 100089 (2020).
75. C. Veth, D. Dragicevic, and C. Merten, "Thermal characterizations of a large-format lithium ion cell focused on high current discharges." *Journal of Power Sources*, **267**, 760 (2014).
76. Y. Jiang, G. Offer, J. Jiang, M. Marinescu, and H. Wang, "Voltage Hysteresis Model for Silicon Electrodes for Lithium Ion Batteries, Including Multi-Step Phase Transformations, Crystallization and Amorphization." *J. Electrochem. Soc.*, **167**, 130533 (2002).

4 Enhancing the Performance of Lithium-Ion Cells via Electrode and Cell Design

With a given cathode and anode active material combination, the performance of a LIB can be adjusted via the electrode and cell design. Especially the electrode thickness and the porosity play a crucial role for the performance, i.e., the energy content and the power capability. If the lithium-ion transport in the liquid electrolyte within the pores of the electrodes is a limiting mechanism, electrode structuring methods can be applied to enhance the overall performance of LIBs.

For the presented investigations, laser-structuring was used to induce hole-like structures in graphite anodes in a hexagonal pattern [141, 255, 256]. Within this chapter, the influences of the anode structuring process on the cell performance of LIBs are analyzed by means of different experimental studies and electrochemical modeling approaches [76, 80].

4.1 Increasing the Discharge Rate Capability with Structured Anodes

In this section, the article titled *Increasing the Discharge Rate Capability of Lithium-Ion Cells with Laser-Structured Graphite Anodes: Modeling and Simulation* [76] is presented. Parts of the article were presented at the 6^{th} *European Conference on Computational Mechanics (ECCM 6) - 7^{th} European Conference on Computational Fluid Dynamics (ECFD 7)* in Glasgow, UK in June 2018, and the *Pacific Rim Meeting (PRiME)* in October 2020, which was held as an online event.

In this work, we introduced a new modeling approach, which is able to describe the enhanced discharge rate capability of LIBs by using laser-structured graphite anodes. Within a restricted C-rate window, the performance of LIBs can be improved by the structuring process. Measurement data of NCM-111/graphite coin cells comprising unstructured and structured graphite anodes was used for the presented purpose of modeling, simulation, and validation.

First, a standard p2D model was parameterized against rate capability data of coin cells with unstructured graphite anodes. However, a p2D model only considers a 1D representation in the x-direction perpendicular to the cell layers, while the y- and z-directions are assumed homogeneous. In order to investigate the in-plane concentration gradients arising from the 3D structures in the electrode, a homogenized 3D model, i.e., a p4D model, of a representative hole structure was developed and validated against rate capability tests of the coin cells comprising structured graphite anodes. The simulation data of both models shows excellent agreement with the transient voltage response and the discharge capacity of the measurement data.

Experimental and simulation data revealed three stages of rate capability enhancement introduced through the laser-structuring process. In the first stage, at low discharge rates, there is no significant influence of the structuring process, because the lithium-ion transport in the liquid electrolyte is not

limiting the discharge process. With rising currents, lithium-ion gradients in the liquid phase of the graphite anode build up and limit the discharge process. In this second stage, structured anodes with a reduced tortuosity enhance the lithium-ion transport, decrease the resulting overpotentials and more capacity can be discharged from the cell until the cutoff voltage is reached. If the current is further increased, the third stage is reached and the positive effect on capacity retention fades. Other limitation mechanisms like electrolyte depletion in the porous cathode or a limited electronic conductivity become more dominant.

Author contribution Jan B. Habedank initiated the idea of laser-structuring graphite anodes and supplied the coin cell measurement data. Ludwig Kraft carried out simulation studies, supported the model development, and optimized the model parameters. Alexander Rheinfeld developed the homogenized three-dimensional electrode model to describe structured electrode morphologies. Christina Krezdorn supported both model development and simulation studies. The data was analyzed and interpreted by Alexander Rheinfeld, Ludwig Kraft, and Jan B. Habedank. The manuscript was written by Ludwig Kraft, Alexander Rheinfeld, and Jan B. Habedank and edited by Andreas Jossen and Michael F. Zaeh. All authors discussed the data and commented on the results.

Increasing the Discharge Rate Capability of Lithium-Ion Cells with Laser-Structured Graphite Anodes: Modeling and Simulation

Jan B. Habedank, Ludwig Kraft, Alexander Rheinfeld, Christina Krezdorn, Andreas Jossen, Micheal F. Zaeh

Journal of The Electrochemical Society 165 (7), pp. A1563–A1573, 2018

Permanent weblink:
http://dx.doi.org/10.1149/2.1181807jes

Increasing the Discharge Rate Capability of Lithium-Ion Cells with Laser-Structured Graphite Anodes: Modeling and Simulation

Jan B. Habedank,[1,=] Ludwig Kraft,[2,=,*,z] Alexander Rheinfeld,[2,=,*] Christina Krezdorn,[1] Andreas Jossen,[2] and Michael F. Zaeh[1]

[1]*Institute for Machine Tools and Industrial Management, Technical University of Munich (TUM), Munich, Germany*
[2]*Institute for Electrical Energy Storage Technology, Technical University of Munich (TUM), Munich, Germany*

A physical-chemical model is suggested, which is able to describe the enhanced discharge rate capability of lithium-ion cells by using laser-structured graphite anodes. Recently published test data of coin cells comprising unstructured and structured graphite anodes with $LiNi_{1/3}Co_{1/3}Mn_{1/3}O_2$ cathodes is used for the presented purpose of modeling, simulation and validation. To minimize computational demand, a homogenized three-dimensional model of a representative hole structure is developed, accounting for charge and mass transport throughout the cell layers and one-dimensional diffusion within radial-symmetric particles. First, a standard pseudo-two-dimensional model is calibrated against rate capability test data of coin cells with unstructured anodes. The calibrated parameter set is transferred to the three-dimensional model in order to simulate the transient voltage response and the discharged capacity depending on the applied C-rate. The simulation data shows excellent agreement with experimental data for both cell types. Three stages of rate capability enhancement are identified showing an improved relative capacity retention of 11−24% at 3C. Experimental and simulation data reveal a restricted C-rate window, which can be positively affected by the structuring process, whereas both shape and pattern of the structuring process can be further optimized with the model.
 [DOI: 10.1149/2.1181807jes]

Manuscript submitted March 26, 2018; revised manuscript received May 4, 2018. Published May 23, 2018.

Lithium-ion batteries (LIBs) are the predominant energy storage solution for consumer electronics, electric vehicles and stationary energy storage devices. However, especially LIBs with high energy densities struggle to deliver sufficient energy at high discharge rates.[1] This rate limitation is caused by internal cell resistances of diverse origins, which has recently been reported to be dominated by the ionic resistance in the liquid electrolyte for common LIB electrode morphologies and operation strategies.[2,3] The electrodes of LIBs typically consist of active material particles mixed with binders and conductive agents and are coated onto metallic current collector foils. The pores of the electrodes and the electronically insulating separator are filled with the electrolyte solution, enabling ion transport between the electrodes. In most automotive LIBs, lithium nickel cobalt manganese oxide $Li(Ni_xCo_yMn_z)O_2$ (NMC) is employed as the cathode active material due to its high specific capacity and voltage level vs. Li/Li^+. For nearly all commercially available cells, graphite is used as the anode active material. Natural graphite particles have a flake-like shape, which makes them align parallel to the current collector foil during the coating and the subsequent calendering process. This particle orientation implies a strong tortuosity anisotropy within the graphite anodes, creating particularly long diffusion pathways for Li-ion transport through the electrode.[4] This results in large Li-ion concentration gradients within the electrode at high charge and discharge rates, causing concentration overpotentials and, consequently, a premature approach of the voltage limits resulting in an insufficient usage of the available capacity.[3]

Previously, it has been demonstrated that structured electrodes can have a positive impact on the cell's performance at higher current rates.[5] Multiple fabrication processes have been introduced, such as co-extrusion of the active material[6] and combinations of extrusion and sintering processes.[7] Many of the battery concepts involve a three-dimensional (3D) cell setup, in which the electrodes interlock on a micro or nano scale, creating a large reaction surface area and excellent charge transfer characteristics.[8] As laser-based manufacturing processes have been gaining importance in the processing industry over the past decades, particular attention has been given to laser-structuring of state-of-the-art electrodes. This concept involves high-precision ablation of a small fraction of the active material from the initial coating, generating additional diffusion pathways, which are solely filled with electrolyte. Significant improvements in rate capability were observed for laser-structured cathodes, e.g. consisting of lithium manganese oxide $LiMn_2O_4$,[9] as well as for graphite anodes.[10]

A few simulation-based approaches have been published in the past, explaining the improved rate capability for structured cathodes[6,11] and anodes[12] due to the reduced overall tortuosity of the electrodes. Based on the structuring process, a more homogeneous active material utilization is achieved and overpotentials are reduced during operation. To the knowledge of the authors, no experimentally validated physical-chemical model of LIBs with structured graphite anodes has been presented so far. Such a model, however, is needed to optimize the geometry of the superimposed structure while taking manufacturing constraints into account. In the work presented here, a homogenized 3D model of an NMC/graphite cell with laser induced microstructures within the anode is introduced taking one-dimensional (1D) diffusion within the solid particles into account. The adapted 3D+1D electrochemical model is based on Newman's pseudo two-dimensional (p2D) model of a LIB[13] accounting for both theories of porous electrodes and concentrated solutions.[14] The presented model is implemented and solved with the aid of a commercially available finite element method (FEM) tool. Geometrical features of the electrodes are matched to previously measured data.[10] Most relevant material parameters, such as the open circuit potentials of the used materials, were determined experimentally. The model is utilized to not only predict the transient voltage curves for discharge rates from C/5 to 10C and the derived capacity at the end of discharge, but also to determine Li-ion concentration gradients throughout the cell representing the cause of overpotentials during operation. The simulation results show excellent accordance with experimental data collected during the considered rate capability tests. Based on these results, the presented model can be used for optimizing a superimposed electrode structure, allowing for further improvements in terms of rate capability of LIBs.

Experimental

In this section, the experimental procedures for electrode fabrication, laser-structuring of the anodes as well as cell assembly and testing are described.

Electrode fabrication.—The components for the electrode inks were mixed with N-methyl-2-pyrrolidone (NMP, Sigma-Aldrich, USA) in a planetary vacuum mixer (Thinky Mixer ARV-310, Thinky, USA) for 10 min at ambient pressure and temperature. The graphite

=These authors contributed equally to this work.
*Electrochemical Society Student Member.
zE-mail: ludwig.kraft@tum.de

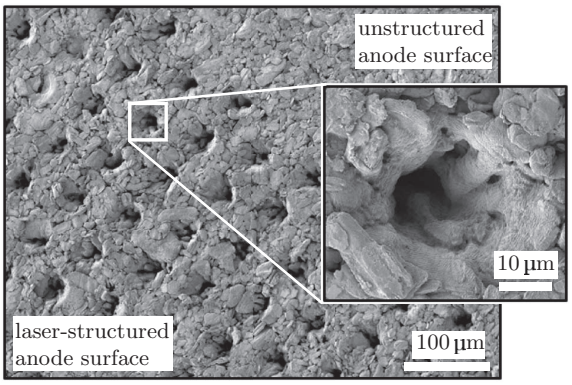

Figure 1. SEM image of a laser-structured anode with structured and unstructured parts.

ink contained 95 wt% graphite (SGL Carbon, Germany) and 5 wt% polyvinylidene fluoride (PVDF, Kynar, Arkema, France). The NMC ink was made of 96 wt% $LiNi_{1/3}Co_{1/3}Mn_{1/3}O_2$ (BASF, Germany), 2 wt% PVDF and 2 wt% conductive carbon (C65, Timcal, Switzerland). Slot die coating was performed in an industrial roll-to-roll coating machine (Coatema, Germany) equipped with an infrared dryer at a coating speed of 1 m min^{-1}. Subsequently, the coatings were calendered to a final porosity of approximately 35%. After calendering, the average coating thickness was 64 µm for both anode and cathode.

Laser-structuring of anodes.—For laser-structuring, a femtosecond laser (Spirit One 1040-8, Spectra-Physics, USA), operating at an infrared wavelength of $\lambda = 1040$ nm with a pulse duration τ_p of 400 fs was used. Only the anodes were structured, the NMC cathodes remained pristine as a larger effect on the overall tortuosity can be achieved in comparison. The beam diameter d_0 in the focal plane (on the electrode surface) was 17.2 µm and the peak fluence Φ_0 was 33.6 J cm^{-2}. The repetition rate f_{rep} used for ablation was 1 kHz and a pulse number $n = 100$ was applied to achieve an average structure depth d_s of approximately 52 µm and an average structure diameter of approximately 20 µm at the electrode's surface, measured with a confocal microscope. Toward deeper parts of the electrode (close to the current collector), the structures narrowed. The structures were spatially distributed in a hexagonal shape with a lateral length of 70 µm, resulting in approximately 20400 structures per cm^2. The ablated fraction of the coating materials for the chosen process parameters was around 5 wt% of the composite electrode material, determined by weighing electrodes before and after structuring. For more details on the experimental setup, the reader is referred to Habedank et al.[10] An image of the resulting structure distribution and geometry gained by means of scanning electron microscopy (SEM) is presented in Fig. 1. It becomes apparent, that the laser-induced structures are not uniformly shaped as the electrode consists of particles of different sizes and shapes. The local electrode conditions thus play a decisive role in the resulting characteristics of the structure.

Half cell assembly and open circuit potentials.—The open circuit potential curves of the utilized unstructured graphite and NMC electrodes were measured in 2032 type coin cells vs. a lithium metal electrode. The half cells were assembled in an argon filled glove box (M. Braun Inertgas-Systeme, Germany) with $H_2O < 0.1$ ppm and $O_2 < 0.1$ ppm. Each cell was filled with 150 µl of electrolyte (LP57, BASF, Germany), containing ethylene carbonate (EC) and ethyl-methyl-carbonate (EMC) in a ratio of 3:7 (by weight) with 1 M lithium-hexaflourophosphate ($LiPF_6$). As a separator, a glass microfiber sheet (Type 691, VWR, USA) was employed. In its uncompressed state, the separator has a thickness of 260 µm. Due to the compression during cell assembly, the separator thickness was estimated to be 200 µm.[15] For the measurement of the quasi open circuit potential as a function of the degree of lithiation, the cells were charged and discharged three times at rates of C/50 in a dry room at a controlled temperature of 20°C between 4.3 V and 2.9 V (NMC) and between 1.6 V and 0.05 V (graphite). In order to derive representative open circuit potential curves from this procedure, an averaging between lithiation (NMC) and delithiation (graphite) of the considered working electrode was carried out for all three C/50 cycles. The averaged open circuit potential curves that were used for modeling and simulation are shown in Fig. A1 in the Appendix. The individual cell capacities for specifying the applied C/50 current were calculated by determining the coating mass assuming mass specific capacities of 150 mAh g^{-1} for NMC and 360 mAh g^{-1} for graphite.

Full cell fabrication.—Three 2032 type coin cells with unstructured anodes and three coin cells with laser-structured anodes were assembled analogously to the half cell assembly described in the previous section. As common practice for Li-ion cells, the areal capacities of the graphite anodes were slightly overdimensioned compared to the NMC cathodes in order to account for irreversible losses during formation and to avoid anode potentials below 0 V, which would result in an undesired Li-plating reaction during charge. In the case presented here, an overdimensioning factor of approximately 1.2 of the pristine anode was chosen so that Li-plating could be avoided at all times during cycling. As only 5 wt% of the coating was removed during the laser-structuring process, this overdimensioning was considered sufficient so that Li-plating during charging could also be avoided in this case. As the mass loading of the pristine graphite anodes was kept constant, the structuring process inevitably resulted in a change in the capacity balancing of the electrodes. This effect needs to be taken into account especially during modeling and simulation and will be further discussed in the modeling section. As the electrolyte, LP572 (BASF, Germany) was used, which consists of EC and EMC in a gravimetric mixing ratio of 3:7 with 1 M $LiPF_6$ conductive salt and 2 wt% vinylene carbonate (VC). As the full cell test data has already been published elsewhere,[10] no further details on the cell fabrication procedure are discussed here. The focus of the work presented here lies on model validation by means of this experimental test data, which is why only essential information is given. Material and fabrication parameters relevant for modeling and simulation purposes are listed in the Appendix of this paper.

Formation procedure.—All cells went through a formation procedure of three charge and discharge cycles at a C-rate of C/10 in order to sufficiently form the solid electrolyte interphase (SEI) on the surface of the graphite particles before the subsequent rate capability test was carried out. Charging was conducted using a constant current/constant voltage (CCCV) operation with a cutoff current of C/20 and discharging was performed in a constant current (CC) procedure within a voltage window of 4.2 V to 3.0 V at a constant temperature of 20°C.

Rate capability test.—After formation, the cells underwent a rate capability test at a controlled temperature of 20°C whereas the applied current was derived from the capacity of the cell after the last formation cycle at C/10. The area-specific values for the adapted C/10 discharge current are shown in Table I for each individual cell considered in this study. As can be seen from this table, all cells investigated in this work showed comparable areal capacities with only slight deviations between the samples. This was considered to be of major importance in order to allow for a straightforward comparison in absolute capacity retention. Higher C-rates are a multiple of the corresponding C/10 discharge current. Charging was carried out following a CCCV procedure and discharging was performed in a CC procedure within a voltage window between 4.2 V and 3.0 V from C/10 to 10C. The constant voltage (CV) phase during charge was terminated when a charging current smaller than C/20 was reached. Charging currents were C/10 and C/5 for the corresponding discharge cycles of C/10 and C/5, respectively. After that, a charging current of C/2 was applied.

Table I. C/10 discharge currents matched to cell capacities of coin cells comprising unstructured and structured anodes.

		Discharge current in mA cm^{-2}
Unstructured anode	Cell 1	0.2399
	Cell 2	0.2535
	Cell 3	0.2597
	Average	0.2510
Structured anode	Cell 4	0.2597
	Cell 5	0.2445
	Cell 6	0.2501
	Average	0.2514

The resulting discharge rate capability is shown in Fig. 2. As can be seen from this figure, all investigated cells show quite comparable behavior. The cells containing structured anodes show an even more reproducible behavior compared to the cells with unstructured anodes. As can be clearly seen from the experiments in Fig. 2, the structuring process results in an overall improvement of the cell's absolute capacity retention, which becomes dominant beyond 2.5 mA cm^{-2} or 1C and fades again before 25 mA cm^{-2} or 10C. This effect will be further evaluated in the following sections.

Cyclic aging test.—Subsequent to the rate capability tests, the six coin cells comprising unstructured and structured anodes underwent a cycling test of 1000 cycles. The cells were charged with a CCCV procedure following a charging current of 1C until the cutoff voltage of 4.2 V and a cutoff current of C/5 in the CV phase. The discharge was carried out with a CC phase at a 1C discharge current until a cutoff voltage of 3.0 V. Similar to the rate capability tests, the ambient temperature was set to 20°C. The capacity retention of the first CC discharge cycle was used as a reference. The capacity fade of each cell as a result of cyclic aging is displayed in Fig. 3.

Modeling

In accordance with the homogenized p2D modeling approach for porous microstructures developed by Newman, Doyle and Fuller,[13,14,16] the model presented here consists of an anode, a separator, and a cathode domain in which both charge and mass transport are accounted for. The governing equations rely on porous electrode and concentrated solution theories and are listed in the appendix for the reader's convenience. Relevant model parameters representing the investigated coin cells are summarized in Table AI in the appendix. The Newman model originally considers a 1D representation through the layers of the electrochemical cell which is coupled to a second dimension representing radial-symmetric active material particles (i.e. 1D+1D, hence p2D). This approach has proven to be valid if the cell shows a homogeneous behavior in the second and third in-plane dimension which allows to neglect gradients in these dimensions as the cell behavior is dominated by through-plane charge and mass transport.[17,18] Only if these gradients cannot be ruled out due to e.g. the non-ideal spatial configuration of the current collectors and the positioning of the corresponding tabs, further means of model development need to be considered.[19,20]

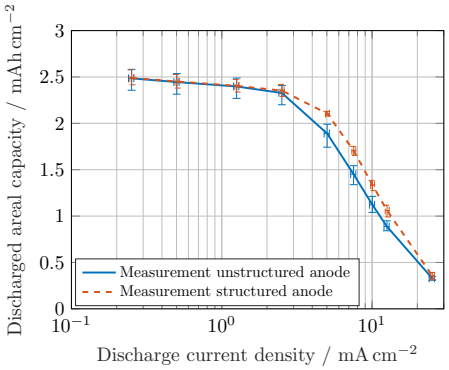

Figure 2. Measured area-specific discharge capacity as a function of applied current density of coin cells comprising unstructured and structured anodes.

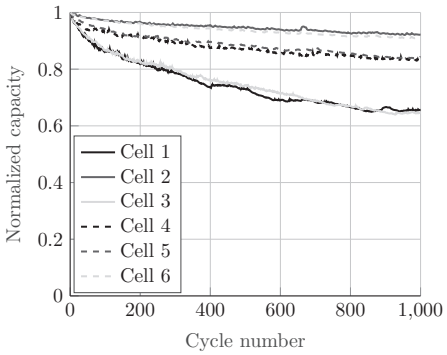

Figure 3. Normalized capacity retention during cycling of cells comprising unstructured anodes (Cell 1, Cell 2 and Cell 3) and structured anodes (Cell 4, Cell 5 and Cell 6).

In the case presented here, 1D and 2D models cannot be used to appropriately describe the hole structure created by the laser ablation process as gradients are expected to occur due to the spatial distribution of the superimposed structure. Furthermore, as already stated in the laser-structuring section, the hole structure is not uniform throughout the entire electrode but is highly dependent on the size and shape of the particles which are affected by the ablation process resulting in a rather coarse hole structure when visually comparing the holes one by one. In order to account for a representative hole structure on the one hand and in order to limit computational effort on the other hand, a homogenized 3D representation of the electrode layers is considered which is coupled to the aforementioned additional radial dimension representing the active material particles. This simplification follows the same line of thought initially suggested by the Newman group in order to efficiently describe porous insertion materials. If the electrode is large enough in terms of its planar dimensioning, every location along an electrode's normal vector can be represented by one particle that will be in contact with the surrounding electrolyte leading to the p2D approach, which is widely accepted and applied. The same principle accounts for a representative hole structure describing the general behavior of the structured electrode. Following this idea, there will be a particle at every location within the representative 3D structure which will be in contact with the surrounding electrolyte at this very location. Furthermore, a generalized or simplified hole structure representing the 20400 holes per cm^2 can be introduced. The specified differential equations have to be consequently solved in all three spatial dimensions of the homogenized 3D cell setup which implies:

$$\nabla := \left(\frac{\partial}{\partial x}, \frac{\partial}{\partial y}, \frac{\partial}{\partial z} \right) \quad [1]$$

Due to the increased spatial discretization effort, 3D models tend to have larger degrees of freedom (DOF), which inevitably causes a higher computational demand and, hence, longer computing times. To minimize the computational effort for solving the set of partial differential equations, the modeled electrode section takes most advantage of symmetry planes representing the structuring pattern. The definition of the modeled geometry is shown in Fig. 4. The laser ablation process creates holes in a hexagonal pattern as can be seen from Fig. 1. The x-direction of the modeled section represents the direction perpendicular to the layers of the cell following the same notation

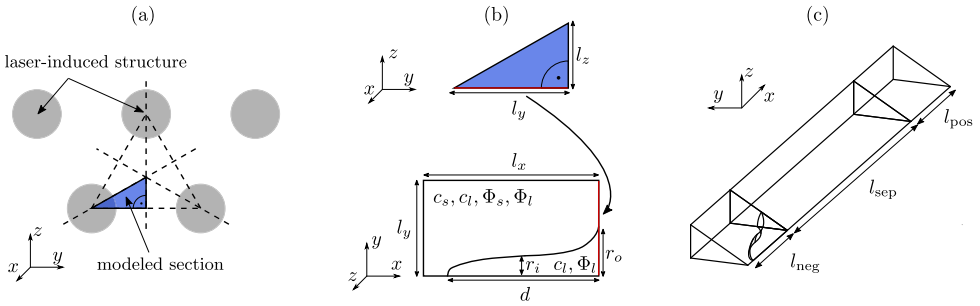

Figure 4. Definition of the modeled geometry using symmetry characteristics of the laser-structured anode. Representative anode surface (a), anode cross section (the state variables solved per domain are the solid and liquid phase Li-ion concentration c_s and c_l and the solid and liquid phase potential Φ_s and Φ_l, respectively) (b) and final 3D geometry implemented in the FEM tool (c).

as the original Newman model. As the holes are homogeneously distributed across the cell, a triangular section of the structured anode is sufficient to describe the entire cell behavior, see Fig. 4a. In this case, a 30° sector of the hexagonal structuring pattern is specified. The cross section of the anode is shown in Fig. 4b with l_x, l_y and l_z representing the length in x-, y- and z-direction, respectively. In this case, l_x is equal to the thickness of the negative electrode l_{neg}. The distance between the centers of two adjacent holes accounts for $2l_y$. The inner radius of the hole is described by r_i, the outer radius by r_o and the depth by d. As the structures are not perfectly cylindrical, the shape was built by using a cubic Bézier curve

$$B(t) = (1-t)^3 P_0 + 3(1-t)^2 t P_1 + 3(1-t)t^2 P_2 + t^3 P_3 \qquad [2]$$

The Bézier curve runs in the interval $0 \leq t \leq 1$. It starts at P_0 for $t = 0$ and terminates in the last control point for $t = 1$. Each control point P_n is defined by its x_n and y_n component, the shape of the curve was controlled by the weighting coefficients w_1 and w_2. The control points are provided in Table II.

$$P_n = \begin{pmatrix} x_n \\ y_n \end{pmatrix}, \; n = 0, 1, 2, 3 \qquad [3]$$

All remaining parameters are listed in the Appendix in Table AI. The resulting idealized 3D geometry is displayed in Fig. 4c. The volume fraction of the modeled hole is 5.1% of the initial anode volume, which is in good agreement with the results of the laser-structuring process. To account for a reduced anode volume, the initial degree of lithiation of the unstructured anode was increased from $0.78 \cdot c_{s,\,max,\,neg}$ (see Table AI) to $0.82 \cdot c_{s,\,max,\,neg}$ for the structured anode which represents this relative decrease. The thicknesses of the separator l_{sep} and the positive electrode l_{pos} are added to the geometry in x-direction.

The presented model of the Li-ion cell was implemented in the FEM-based software platform *COMSOL Multiphysics 5.3*. In order to depict the geometrical features of the hole, a high spatial discretization around the hole boundaries was chosen resulting in approximately 30000 DOF which need to be solved during computation. For comparison, a 3D model of an unstructured cell with a similar spatial discretization along the x-axis results in approximately 9000 DOF. For describing the unstructured cell, a classic p2D model with around 2000 DOF was chosen in order to save computing time.

Table II. x and y components of the four control points.

	x_n	y_n
P_0	$l_{neg} - d$	0
P_1	$l_{neg} - d$	$r_i w_1$
P_2	l_{neg}	$r_i w_2$
P_3	l_{neg}	r_o

In order to describe charge and mass transport in the porous microstructures of a Li-ion cell, a correction of the electrolyte's transport properties is necessary. An often used correction factor is the Bruggeman exponent which was empirically determined for porous structures formed of spherical particles. Recent research findings showed that the Bruggeman correction often underestimates the limitation of the transport properties especially in graphite electrodes formed of platelet-like particles.[4,21–24] In order to evaluate effective transport parameters, the tortuosity τ of the porous electrode structure needs to be known, which can be defined as the ratio of the direct path length to the effective path length of ion transport

$$D_{l,\,eff} = D_l \frac{\varepsilon_l}{\tau} = \frac{D_l}{N_M} \qquad [4]$$

$$\kappa_{eff} = \kappa \frac{\varepsilon_l}{\tau} = \frac{\kappa}{N_M} \qquad [5]$$

with D_l representing the diffusion coefficient in the liquid phase (i.e. the electrolyte), κ its conductivity and ε_l the volume fraction of the electrolyte, also known as the porosity of the porous structure. The ratio of the tortuosity to the volume fraction is also known as the MacMullin number N_M.[24–26] Ebner et al. further demonstrated that the electrode's tortuosity for spherical particles (e.g. NMC) shows an isotropic behavior, but for cylindrical (e.g. lithium cobalt oxide $LiCoO_2$ (LCO)) and platelet-shaped particles (e.g. graphite), an anisotropy of tortuosity can be observed that cannot be neglected when considering charge and mass transport in all spatial dimensions of an electrode.[4] Especially the through-plane tortuosity of graphite τ_x is significantly higher than the in-plane tortuosity (with $\tau_y = \tau_z$). In order to account for this effect, an anisotropic tortuosity was implemented in the graphite anode with $\tau_x = 8$ and $\tau_y = \tau_z = 2.5$.[4] The separator and the NMC cathode were considered to inhibit an isotropic tortuosity of $\tau_x = \tau_y = \tau_z = 1.2$ and $\tau_x = \tau_y = \tau_z = 1.7$, respectively (see Table AI).

Results and Discussion

In this section, the data gained from the rate capability tests carried out for this work is presented and then discussed with the aid of simulation studies derived from the developed modeling approach. The results of the cyclic aging experiments carried out after the rate capability tests are discussed at the end of the section.

Effects of structuring on rate capability.—All rate capability tests were carried out as described in the experimental section at C/10, C/5, C/2, 1C, 2C, 3C, 4C, 5C and 10C at an ambient temperature of 20°C. As the coulombic efficiency of the C/10 cycles after the formation procedure was only 99.1% on average, this data is not considered in the further process of this work. The authors believe that the process of formation was not completely finished at this stage, which might falsify the observed trends if taken into consideration here. From the

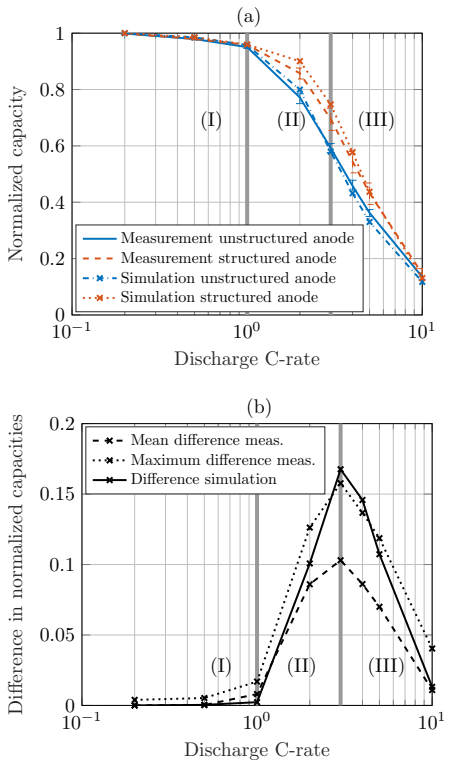

Figure 5. Comparison of measured and simulated C/5-normalized discharge rate capability of coin cells comprising unstructured and structured anodes (a) and observed difference in normalized discharge rate capability (b) within the three stages (I), (II) and (III).

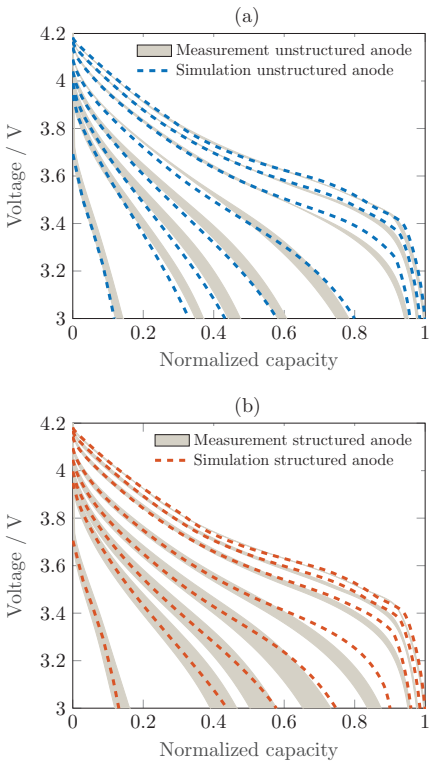

Figure 6. Comparison of measured and simulated discharge voltage curves as a function of C/5-normalized capacity for coin cells comprising unstructured (a) and structured anodes (b) for C-rates of C/5, C/2, 1C, 2C, 3C, 4C, 5C, and 10C (from right to left).

C/5 cycles onwards, all cycles showed efficiencies above this value rising toward 99.7%. Therefore, all further observations were focused on C-rates larger than C/10.

In Fig. 2, the mean area-specific discharged capacity is shown as a function of applied current density. As indicated by the error bars, a variation in both directions occurs, whereas the variation in applied current follows the notation presented in Table I, which is based on the derived capacity at the end of the carried out formation cycles. The cathode samples used for building the coin cells were chosen in such way, that the loading of the capacity limiting electrode, i.e. the cathode, was very similar for both unstructured and structured cells (see experimental section). This approach resulted in a highly reproducible area-specific capacity of approximately 2.5 mAh cm^{-2} at low current densities for all cells considered within this study, which guarantees a most straightforward comparison of the results gained from the rate capability tests. For the reader's convenience, besides area-specific values (see Fig. 2), also the capacity retention normalized to the C/5 discharge rate (see Fig. 5a) and the difference in normalized capacity retention (see Fig. 5b) is shown in this work. When looking into the difference in normalized capacity retention, the impact of electrode structuring can be categorized in three different stages depending on the applied C-rate and increase in derived capacity. The area-specific energy density is not shown here, as the voltage level only merely varies between coin cells with structured and unstructured anodes. Therefore, the area-specific capacity and area-specific energy density as a function of applied C-rate show very similar characteristics in this work. As the volume of the anode does not change with the structuring process, the volumetric energy density of the cell directly follows this trend. Based on the lower density of the electrolyte compared to the composite anode, the overall weight of the electrolyte soaked anode is reduced by approximately 3%. This will slightly improve the gravimetric energy density of the full cell. For all applied currents, the coin cells comprising structured anodes generally showed a larger discharged capacity compared to their unstructured counterpart, as can be seen in Fig. 2. In the case presented in this study, this effect suddenly becomes dominant at discharge current densities above 2.5 mA cm^{-2} or 1C reaching its peak impact around 7.5 mA cm^{-2} or 3C and steadily declines at current densities above this value as shown in Fig. 5b. As can also be seen from Figs. 2 and 5a, there is a rather gentle decrease of the discharged capacity with increasing current density up to 2.5 mA cm^{-2} or 1C, which then becomes more pronounced up to 7.5 mA cm^{-2} or 3C and then finally decreases again in its steepness. In order to understand the interplay of mechanisms leading to this effect, the presented model was applied. For this purpose, a standard p2D Newman model was considered first, in order to match the parameter set to the results of the rate capability tests with cells comprising unstructured anodes. As shown in Figs. 5a and 6a, the relative decline in capacity retention with rising C-rate at the end of the discharge as well as the transient characteristics of the voltage response during discharge can be depicted very well with the parameter set given in the Appendix.

This parameter set was then transferred to the 3D representation of the homogenized structured electrode model. With a simulated hole diameter of roughly 20 µm, 80% of penetration depth and 70 µm of distance between the centers of the holes, the rate capability tests performed on cells comprising structured anodes could also be depicted very well. Again, this accounts for both the absolute and the relative decline in discharged capacity with rising C-rate at the end of the discharge procedure (see Fig. 5a) as well as the transient characteristics of the voltage response during discharge (see Fig. 6b).

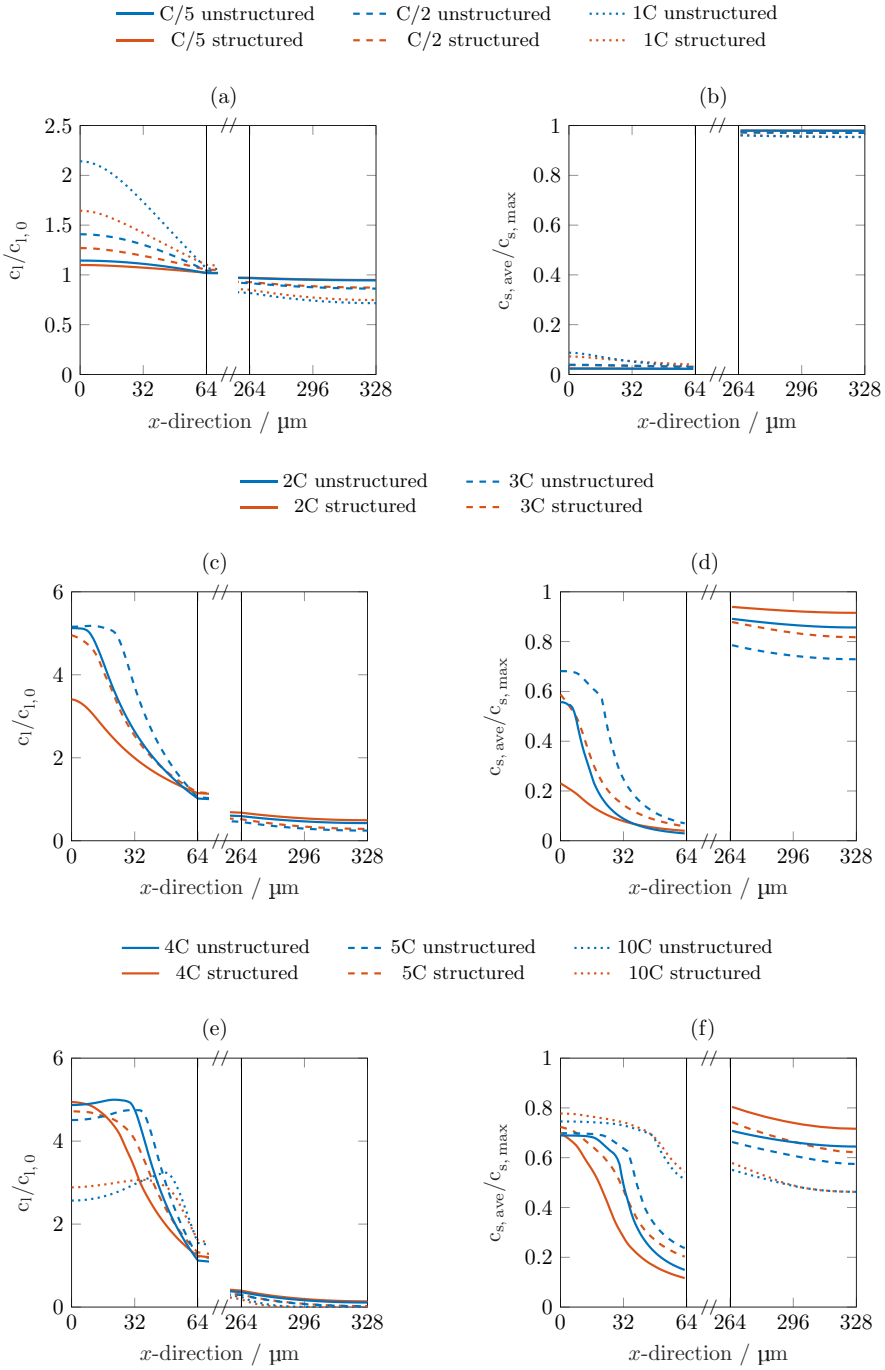

Figure 7. Li-ion concentration in both liquid (left) and solid phase (right) averaged along y- and z-direction at the end of the corresponding discharge step; solid phase concentration accounts for the mean concentration within the particle dimension.

Mechanisms of rate limitation.—When looking into Fig. 5a, the C-rates of C/5, C/2 and 1C are almost not affected by the structuring process. Also, the similar trend of the decline in discharged capacity hints at a limiting effect which is not influenced by the structuring process and consequently charge and mass transport in the liquid phase. This assumption can be proven when looking into Figs. 7a and 7b. The spatial distribution in liquid phase concentration at the end of the discharge procedure is almost identical for both the unstructured and structured cells with rising gradients between the anode and cathode for increasing C-rate. The same holds true for the spatial distribution in solid phase concentration. The utilization of the electrodes is constantly above 90% with almost no gradients along the thickness of the electrodes. At C-rates of 1C and below, this observation leads to the assumption that the capacity retention is mainly influenced by an increased potential drop based on ohmic losses and charge transfer kinetics with increasing C-rate. From 2C onwards, a

more homogeneous liquid phase concentration can be observed for the cells with structured anodes compared to those with unstructured anodes with lower maximum values, which positively influences the transport properties of the electrolyte (see Fig. 7c). This results in a considerably homogenized solid phase concentration along the electrode with lower mean values on the anode side which leads to higher overall solid phase concentrations on the cathode side at the end of the discharge procedure (see Fig. 7d). At C-rates of 4C and above, the homogenizing influence of laser beam structuring on both the liquid and the solid phase concentration is considerably diminished as shown in Figs. 7e and 7f. At these C-rates, the limiting influence in the liquid phase on the cathode side becomes increasingly dominant, reaching almost a complete depletion of Li-ions, which results in large overpotentials related to charge transfer kinetics (see Fig. 7e). In addition, the liquid phase concentration within the anode domain rises above 4 mol l^{-1} which significantly reduces both its conductivity and diffusivity resulting in large ohmic and diffusion based overpotentials. The electrolyte conductivity is reduced to 35% and the diffusivity to 14% at 4 mol l^{-1} compared to the values at the initial liquid Li-ion concentration of 1 mol l^{-1}. In order to improve the rate capability of the cell at these high discharge rates, further modifications need to be considered such as different electrolytes with enhanced transport properties at such high levels of Li-ion concentration or an additional structuring of the cathode to avoid a complete depletion of Li-ions.

These observations suggest a classification of the influence of laser beam structured anodes on the rate capability of the cells: At low C-rates, electrode morphology plays only a minor role in capacity retention making laser beam structuring obsolete in general, i.e. stage (I) between 0.1C and 1C in this case. At moderate C-rates, the effect of anode morphology and related effective transport properties becomes dominant, showing the largest benefit of laser beam structured anodes, i.e. stage (II) between 1C and 3C in this case. At high C-rates, not only the anode morphology is mainly influencing the occuring overpotentials, but also the electrolyte's inherent transport properties as well as the morphology of the separator and cathode are becoming increasingly important approaching a depletion of the electrolyte near the cathode current collector, i.e. stage (III) between 3C and 10C in this case. It is worth mentioning here, that the chosen glass fiber separator is not representative for commercial Li-ion cells, where separators are used which are about a magnitude thinner (i.e. approximately 10–30 μm). The glass fiber separator was used in this case due to ease of handling and comparability between half cell and full cell measurements. For the here presented results, this circumstance should only have a mere influence on the investigated rate capability as the overpotentials within the separator are dominated by the effective transport properties of the electrolyte, resembling an effective path-length of ion movement. The chosen glass fiber separator shows a MacMullin number of approximately 1.7 in its compressed state of 200 μm, which results in an effective path-length for the Li-ions of 340 μm. A standard polyolefin based separator with a thickness of 25 μm and a porosity of 40% inhibits a MacMullin number between 10 to 15,[24] resembling an effective path-length of 250–375 μm, which is very comparable to the chosen glass fiber separator.

In order to not only evaluate the through-plane but also the in-plane penetration depth of the structuring procedure, the 3D spatial distribution of Li-ion concentration in the solid and liquid phase was studied at the end of a 3C discharge step. For this purpose, five cut planes were introduced along the thickness of the structured anode (compare Fig. 4c) at a constant distance of 16 μm between them (see Figs. 8a and 8b). Looking into the spatial distribution of both the liquid and solid phase concentration, a fairly homogeneous coloring of the cut planes can be observed, whereby the coloring level is mainly dominated by the through-plane distribution in Li-ion concentration. This implies that the concentration gradients along the hole's axis are generally larger than the concentration gradients along the hole's radial direction.

Near the interface between the anode and the separator (i.e. planes V and IV), there is only little variation in Li-ion concentration throughout the cut planes in both the liquid and the solid phase. This tendency is confirmed when looking into the normalized liquid and solid phase concentration along the hypotenuse symmetry axis of the considered triangular electrode domain (see Figs. 8c and 8d). Furthermore, we observe an increasing gradient from the bulk material between the holes to the center of the hole with increasing distance to the separator along the depth of the holes (i.e. planes III and II). In case of the liquid phase concentration, the spatial distribution within the unstructured part of the electrode (i.e. plane I) becomes fairly homogeneous again, however, at significantly elevated levels of concentration. This jump becomes especially apparent when looking into the level of liquid phase Li-ion concentration within the hole (i.e. at $y = z = 0$ within planes V, IV and III) compared to the unstructured part of the electrode (i.e. at $y = z = 0$ within plane I). A similar trend in the solid phase concentration can be observed, whereas a considerable gradient in Li-ion concentration remains near the current collector in the range of a third to a half of the total through-plane concentration difference, which can be explained by the comparably slow diffusion-based equalization process within the solid phase compared to the liquid phase.[17] These observations imply that the penetration depth of the structuring process not only varies for the liquid and solid phase concentration but is highly dependent on the size and the depth of the hole as well as the distance between the holes. These results suggest that the size, the depth and the shape of the hole itself as well as the structuring pattern can be optimized in order to obtain an improved rate capability within a certain operating window and price range.

Cyclic aging behavior.—From the overall cycling behavior displayed in Fig. 3, no distinct indication can be observed that coin cells comprising structured or unstructured graphite anodes show superior aging characteristics. What is more, the developing spread between the cells might be a result of the manual cell assembly process or partial deterioration during the rate capability tests with high C-rates. Nevertheless, all cells comprising structured anodes reveal a capacity retention above 83% after 1000 cycles, whereas two cells with unstructured anodes already showed a capacity fade toward 65%. This leads to the conclusion that the laser-structuring process of the graphite anodes has no negative impact on the cyclic aging behavior of the coin cells. If coin cells comprising structured anodes even show an enhanced aging behavior needs to be evaluated by means of further measurements including more cells and cells that did not undergo a rate capability test before the carried out aging study.

Conclusions

Within this work, a combination of experimental and simulation-based evaluation of laser-beam structured graphite electrodes for enhancing the discharge rate capability of a NMC/graphite Li-ion cell was presented. As the experimental basis of this work, coin cells with a constant loading of approximately 2.5 mAh cm^{-2} were manufactured, whereas the NMC cathode was the capacity limiting electrode and the pristine graphite anode was oversized by approximately 20% in capacity so that the laser beam ablation of roughly 5 wt% did not result in an elevated risk of Li-plating during cycling. For simulation purposes, a representative homogenized microstructure model of the considered laser-beam-structured graphite electrode was developed and validated against rate capability tests, which were performed on both coin cells with unstructured and structured graphite electrodes.[10] In a first step, the underlying physical and chemical model parameters were adapted toward the unstructured coin cells with the aid of a standard p2D Newman-type model resulting in an excellent agreement between experimental and simulated rate capability tests. This parameter set was then transferred to the homogenized 3D+1D microstructure model, forming a representative triangular section of the structuring pattern making most use of symmetry planes in order to minimize computational effort. Due to the inevitably higher spatial discretization effort around the hole geometry, which was qualitatively approximated by a cubic Bézier curve toward SEM pictures, the computational demand

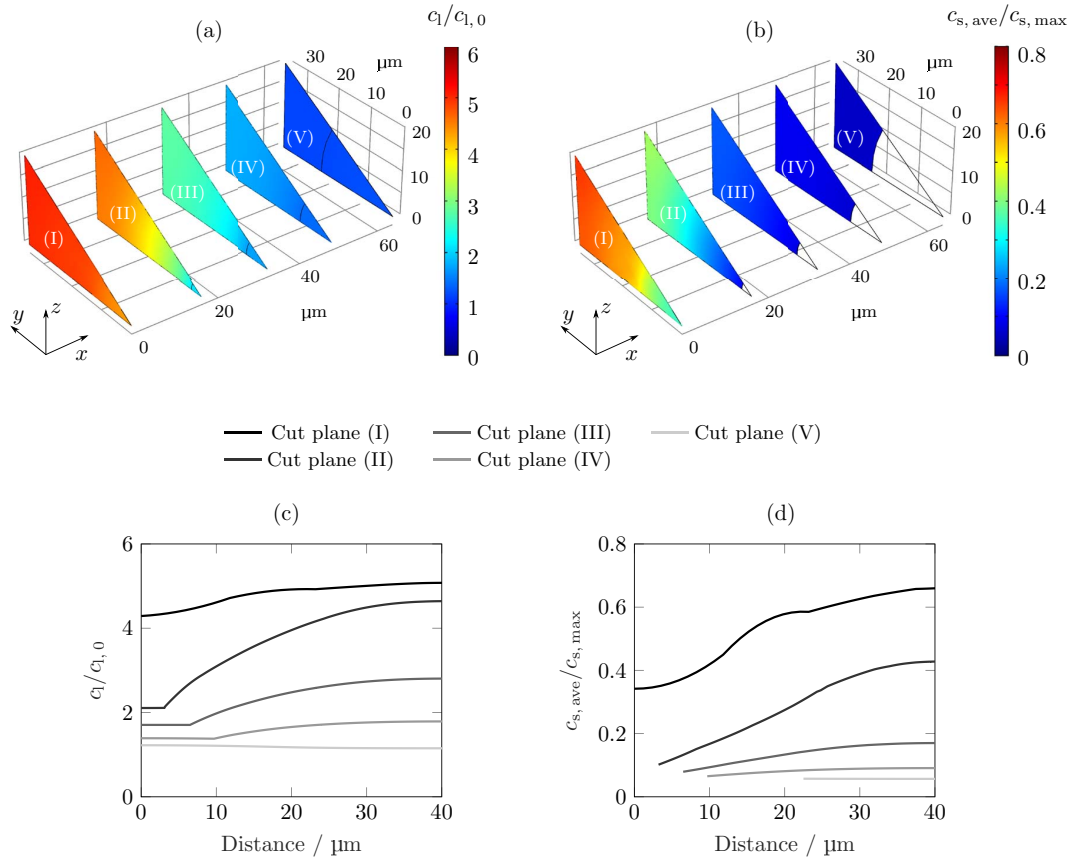

Figure 8. Liquid (a) and solid phase (b) Li-ion concentration on defined cut planes (I), (II), (III), (IV) and (V) (distance in x-direction: 0 µm, 16 µm, 32 µm, 48 µm and 64 µm, respectively) and liquid (c) and solid phase (d) Li-ion concentration along hypotenuse of cut planes at the end of a 3C discharge step within the structured graphite anode.

increased by a factor of approximately 15 compared to a standard p2D model (30000 DOF vs. 2000 DOF).

Simulated rate capability tests, which were carried out with the aid of the parametrized structured electrode model, were validated against experimental data showing again excellent agreement in terms of the transient voltage decline during discharge as well as the observed reduced capacity retention with increasing C-rate. It was shown, that for the electrode morphologies and materials considered in this case, the maximum benefit of structuring the graphite electrode was around a discharge rate of 3C. At low discharge rates, there is merely an influence of the structuring process (here up to 1C), which then suddenly changes at 2C rising toward its maximum impact at 3C of gaining between 10% and 15% in capacity compared to cells without structured graphite anodes at C/5. This corresponds to a relative improvement of capacity retention of 11–24% at 3C, at which the minimum and maximum capacity retention of the structured cells at 3C are related to the mean capacity retention of the unstructured cells at 3C. Beyond 3C, the impact of the structuring process declines again, however, at a comparably lower rate. This implies, that there forms a certain C-rate region in which the use of structured electrodes can considerably enhance a cell's rate capability forming an optimum. In other words, structured electrodes do not necessarily come with an overall improvement in rate capability of Li-ion cells at all applied currents as mass transport limitations within the electrolyte are still dominating at large currents despite the locally homogenized distribution in Li-ion concentration (e.g. overall electrolyte depletion in the NMC cathode[3]). When looking into the simulated spatial Li-ion concentration in the liquid and the solid phase at the end of discharge, the effect of the structuring process on the rate limitation becomes apparent. At low C-rates (i.e. C/5, C/2 and 1C or stage (I)), the structuring process has almost no influence on the solid phase concentration in both anode and cathode. Consequently, the amount of discharged capacity is rather limited by an increasing polarization due to ohmic losses and charge transfer kinetics instead of transport limitations in the liquid electrolyte. At higher C-rates (i.e. 2C and 3C or stage (II)), the homogenized liquid phase concentration has a more dominant impact on the distribution in liquid and solid phase concentration especially in the graphite anode which results in higher degrees of utilization within both electrodes. When further increasing the discharge rate (i.e. 4C, 5C and 10C or stage (III)), the positive impact of electrode structuring on the homogeneity of liquid phase concentration fades, which then results in a similarly inhomogeneous utilization of the graphite anode. What also becomes apparent is that the level in liquid phase concentration within the cathode generally decreases with increasing C-rate which is based on the ongoing depletion of the electrolyte resulting in increased charge transfer overpotentials. Similarly, the liquid phase concentration within the anode becomes excessively high ($> 4\,\mathrm{mol\,l^{-1}}$), which significantly reduces the inherent transport properties of the electrolyte, resulting in large ohmic and diffusion based overpotentials. This effect cannot be significantly influenced by a structuring of the anode but needs further modifications such as using enhanced electrolytes or including an additional structuring of the cathode.

The results shown in this work imply that not only the anode structuring process can enhance the discharge rate capability of the entire cell in a certain range but also that modeling and simulation

can help to understand the underlying mechanisms and interactions resulting in this enhancement. By evaluating the through-plane and in-plane distribution in Li-ion concentration throughout the electrodes, the ideal hole size, geometry and pattern can be identified in order to maximize the rate capability within a limited operating window. By further considering the costs of the electrode structuring process and also of the excess electrolyte within the holes, a cost-effective rate capability enhancement can be achieved. This can be best explained when considering Fig. 5b, where the peak location, height and width of the curve can be altered by changing the size, the shape and the pattern of the superimposed structure. In order to be able to reliably optimize the structure, inherent transport properties of the applied electrolyte need to be characterized well throughout the entire concentration range occurring during operation before salt precipitation takes place (i.e. beyond $4\,\mathrm{mol\,l^{-1}}$ in this case). The same holds true for a thorough characterization of the anisotropic electrode morphology. Further work will focus on this optimization procedure, not only for the graphite anode, but also for the NMC cathode during both discharge and charge operation for various electrode loadings. Furthermore, the model error accompanied with the homogenization of the microstructure will be evaluated and investigated in terms of means of a further model order reduction.

Acknowledgment

This work was financially supported by the German Federal Ministry of Education and Research (BMBF) under grant number 03XP0081 (ExZellTUM II) and 03XP0027G (MiBZ).

Appendix

In the experimental section, the open circuit potential measurements of the half cells were described. In Fig. A1, the derived curves are plotted as a function of degree of lithiation.

The developed model is based on the subsequent equations. For a more detailed description, the reader is referred to the work of the Newman group.[13,14,16] The most relevant model parameters used in this work are listed in Table AI. The mass balance is applied in the porous intercalation electrodes

$$\varepsilon_\mathrm{l}\frac{\partial c_\mathrm{l}}{\partial t} = \nabla\left(D_{\mathrm{l,\,eff}}\nabla c_\mathrm{l} - \frac{i_\mathrm{l} t_+}{F}\right) + \frac{3\varepsilon_\mathrm{s}}{r_\mathrm{p}}j_\mathrm{n} \qquad [A1]$$

where ε_l is the porosity or the liquid phase fraction of the electrode domain, $D_{\mathrm{l,\,eff}}$ the effective diffusivity, i_l the ionic current density, F the Faraday constant, ε_s the solid phase fraction, r_p the particle radius and j_n the pore wall flux. In the separator, there is no charge transfer reaction taking place, hence, the mass balance simplifies to

$$\varepsilon_\mathrm{l}\frac{\partial c_\mathrm{l}}{\partial t} = \nabla\left(D_{\mathrm{l,\,eff}}\nabla c_\mathrm{l} - \frac{i_\mathrm{l} t_+}{F}\right) \qquad [A2]$$

The ionic current density accounts for the interaction between the different species in the electrolyte which is why the activity dependence is essential

$$i_\mathrm{l} = -\kappa_\mathrm{eff}\nabla\Phi_\mathrm{l} + \frac{2\kappa_\mathrm{eff}RT}{F}\left(1 + \frac{\partial \ln f_\pm}{\partial \ln c_\mathrm{l}}\right)(1-t_+)\nabla \ln c_\mathrm{l} \qquad [A3]$$

with κ_eff being the effective ionic conductivity, Φ_l the potential in the liquid phase and R the ideal gas constant. At high C-rates the Li-ion concentration in the electrolyte can locally become very low due to transport limitations. To prevent the concentration from becoming zero or even negative, which causes instability of the model, a kinetic modification introduced by the Newman group[27] was implemented. The Butler-Volmer equation, which describes the charge transfer between the solid and the liquid phase on the particle surface is divided by a limitation term with $c_\mathrm{lim} = 1\,\mathrm{mol\,m^{-3}}$

$$j_\mathrm{n} = \frac{i_0}{F}\frac{\exp\left(\frac{\alpha_\mathrm{a}F}{RT}\eta\right) - \exp\left(-\frac{\alpha_\mathrm{c}F}{RT}\eta\right)}{1 + \frac{c_\mathrm{lim}}{c_\mathrm{l}}\exp\left(-\frac{\alpha_\mathrm{c}F}{RT}\eta\right)} \qquad [A4]$$

α_a and α_c are the anodic and cathodic charge-transfer coefficients. The exchange current density i_0 is defined as

$$i_0 = F k_\mathrm{c}^{\alpha_\mathrm{a}} k_\mathrm{a}^{\alpha_\mathrm{c}} (c_{\mathrm{s,\,max}} - c_\mathrm{s})^{\alpha_\mathrm{a}} c_\mathrm{s}^{\alpha_\mathrm{c}} \left(\frac{c_\mathrm{l}}{c_{\mathrm{l,\,ref}}}\right)^{\alpha_\mathrm{a}} \qquad [A5]$$

with $c_{\mathrm{l,\,ref}} = 1\,\mathrm{mol\,m^{-3}}$. $c_{\mathrm{s,\,max}}$ is the maximum Li-ion concentration in the solid phase and k_a and k_c are the anodic and cathodic reaction rates, respectively. The overpotential η is defined as a subtraction of the potential of the liquid phase Φ_l and the equilibrium voltage E_eq from the potential of the solid phase Φ_s

$$\eta = \Phi_\mathrm{s} - \Phi_\mathrm{l} - E_\mathrm{eq} \qquad [A6]$$

Finally, the following boundary conditions have to be maintained

$$\left.\frac{\partial c_\mathrm{l}}{\partial x}\right|_{x=0\&x=L} = 0 \qquad [A7]$$

$$\left.\frac{\partial \Phi_\mathrm{l}}{\partial x}\right|_{x=0\&x=L} = 0 \qquad [A8]$$

with $L = l_\mathrm{neg} + l_\mathrm{sep} + l_\mathrm{pos}$.

$$\left.\frac{\partial \Phi_\mathrm{s}}{\partial x}\right|_{x=0\&x=L} = -\frac{i_\mathrm{s}}{\sigma} \qquad [A9]$$

with i_s being the electric current density.

$$\left.\frac{\partial \Phi_\mathrm{s}}{\partial x}\right|_{x=l_\mathrm{neg}\&x=l_\mathrm{neg}+l_\mathrm{sep}} = 0 \qquad [A10]$$

$$\nabla i_\mathrm{l} = -\nabla i_\mathrm{s} \qquad [A11]$$

$$\left.\frac{\partial c_\mathrm{s}}{\partial r}\right|_{r=0} = 0 \qquad [A12]$$

$$\frac{\partial c_\mathrm{s}}{\partial r} = D_\mathrm{s}\left(\frac{\partial^2 c_\mathrm{s}}{\partial r^2} + \frac{2}{r}\frac{\partial c_\mathrm{s}}{\partial r}\right) \qquad [A13]$$

$$-D_\mathrm{s}\left.\frac{\partial c_\mathrm{s}}{\partial r}\right|_{r=r_\mathrm{p}} = j_\mathrm{n} \qquad [A14]$$

In literature, only a few electrolytes used in Li-ion cells have been characterized adequately so that they can be used for the purpose of model parameterization.[27–31] Necessary characteristics are diffusivity, ionic conductivity and activity dependence of the electrolyte. These characteristics depend on the Li-ion concentration and on the

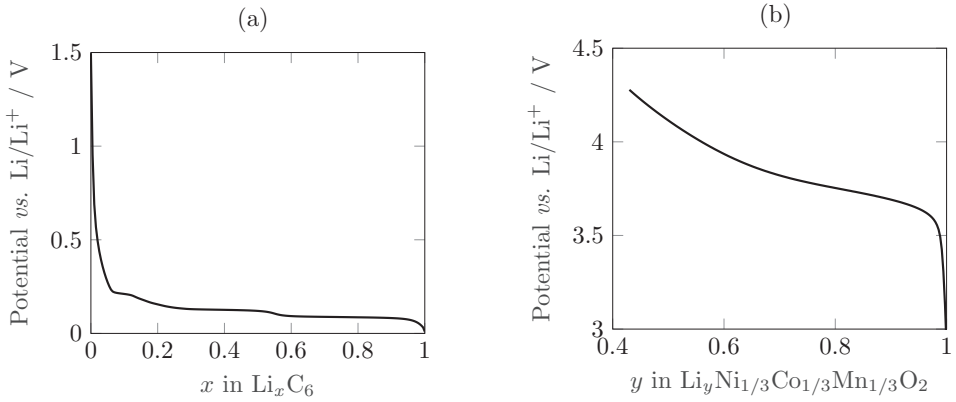

Figure A1. Open circuit potential curves for the graphite anode (a) and the NMC cathode (b) considered in this work.

Table AI. Model parameters used within this work; superscript *m* indicates measured values, *e* indicates estimated values (* value derived from D50 mass-median-diameter from datasheet, ** value derived from weight ratio of electrode composition); numeric values and magnitudes of parameters chosen in this study were referenced to literature where applicable.

Parameter	Anode	Separator	Cathode
Geometry			
Thickness l	64 µm ^{m}	200 µm[15]	64 µm ^{m}
Particle radius r_p	5 µm *		5.5 µm *
Solid phase fraction ϵ_s	0.59 **		0.52 **
Liquid phase fraction ϵ_l	0.32 ^{m}	0.7 ^{e}	0.35 ^{m}
Tortuosity through-plane τ_x	8[4]	1.2 ^{e}	1.7[4]
Tortuosity in-plane $\tau_{y,z}$	2.5[4]	1.2 ^{e}	1.7[4]
Thermodynamics			
Equilibrium voltage E_{eq}	Fig. A1a		Fig. A1b
Maximum lithium concentration $c_{s,max}$	32000 mol m^{-3}[32,33]		50000 mol m^{-3}[33]
Initial state of charge $\frac{c_{s,0}}{c_{s,max}}$	0.78 ^{e}		0.43 ^{e}
Kinetics			
Anodic reaction rate k_a	1×10^{-9} m s^{-1}[27]		1×10^{-9} m s^{-1}[27]
Cathodic reaction rate k_c	1×10^{-9} m s^{-1}[27]		1×10^{-9} m s^{-1}[27]
Anodic charge-transfer coefficient α_a	0.5[32,34]		0.5[32,34]
Cathodic charge-transfer coefficient α_c	0.5[32,34]		0.5[32,34]
Transport			
Solid diffusivity D_s	1×10^{-14} m^{2}s^{-1}[27,32]		1.8×10^{-13} m^{2}s^{-1}[33,35]
Solid conductivity σ	100 S m^{-1}[21,36]		10 S m^{-1}[35,36]

Parameter	Hole
Inner radius r_i	7.5 µm ^{m}
Outer radius r_o	22.5 µm ^{m}
Depth d	$0.8 \cdot l_{neg}$ ^{m}
Weighting factor w_1	1.1
Weighting factor w_2	0.6
Distance $2l_y$	70 µm ^{m}

Parameter	Electrolyte
Electrolyte diffusivity D_l	Eq. A15
Electrolyte conductivity κ_{fit}	Eq. A17
Activity dependence $\frac{\partial \ln f_\pm}{\partial \ln c_l}$	Eq. A18
Transport number t_+	0.4[27]

Parameter	Global
Temperature T	293.15 K ^{m}
Ohmic contact resistance R_Ω	1.3×10^{-3} Ωm^2 ^{e}

temperature, which is kept constant in this case. Due to various electrolyte compositions, the resulting curves differ slightly but overall show a similar trend.

The electrolyte diffusion coefficient and the electrolyte ionic conductivity were adopted according to Mao et al.[27] The corresponding unit for the following characteristic electrolyte functions is mol l^{-1} for the Li-ion concentration c_l and K for the temperature T

$$D_l = 5.34 \times 10^{-10} \exp(-0.65 c_l) \exp\left(\frac{2000(T-298)}{298T}\right) f \quad [A15]$$

$$\kappa = (0.0911 + 1.9101 c_l - 1.052 c_l^2 + 0.1554 c_l^3) \exp\left(\frac{1690(T-298)}{298T}\right) \quad [A16]$$

The electrolyte diffusion coefficient was slightly reduced by multiplying a factor $f = 0.85$. Mao et al.[27] used a polynomial fitting function for the ionic conductivity that is only valid in a certain concentration range. For concentrations above 3 mol l^{-1}, the conductivity starts to increase again due to the considered cubic fitting function. As larger Li-ion concentrations were observed in this work, the following fit was used, which is based on Eq. A16 with a constant temperature $T = 293.15$ K

$$\kappa_{fit} = 2.034 \left(\frac{c_l}{2.512}\right)^{0.55} \exp\left(-\left(\frac{c_l}{2.512}\right)^{1.55}\right) \quad [A17]$$

The effective diffusivity and ionic conductivity can be determined using the correction presented in Eqs. 4 and 5. The electrolyte activity dependence was taken from Valøen and Reimers[28] as it was neglected by Mao et al.[27]

$$\frac{\partial \ln f_\pm}{\partial \ln c_l} = \frac{0.601 - 0.24 c_l^{0.5} + 0.982 c_l^{1.5}(1 - 0.0052(T-294))}{1 - t_+} - 1 \quad [A18]$$

The equation contains a dependence of the transport number t_+, which was set constant, see Table AI.

ORCID

Jan B. Habedank http://orcid.org/0000-0003-2057-7037
Ludwig Kraft http://orcid.org/0000-0003-4324-426X
Alexander Rheinfeld http://orcid.org/0000-0003-0995-7266

References

1. M. Singh, J. Kaiser, and H. Hahn, "Thick Electrodes for High Energy Lithium Ion Batteries," *Journal of the Electrochemical Society*, **162**, A1196 (2015).
2. A. Nyman, T. G. Zavalis, R. Elger, M. Behm, and G. Lindbergh, "Analysis of the Polarization in a Li-Ion Battery Cell by Numerical Simulations," *Journal of The Electrochemical Society*, **157**, A1236 (2010).
3. K. G. Gallagher, S. E. Trask, C. Bauer, T. Woehrle, S. F. Lux, M. Tschech, P. Lamp, B. J. Polzin, S. Ha, B. Long, Q. Wu, W. Lu, D. W. Dees, and A. N. Jansen, "Optimizing Areal Capacities through Understanding the Limitations of Lithium-Ion Electrodes," *Journal of The Electrochemical Society*, **163**, A138 (2015).
4. M. Ebner, D.-W. Chung, R. E. García, and V. Wood, "Tortuosity Anisotropy in Lithium-Ion Battery Electrodes," *Advanced Energy Materials*, **4**, 1 (2014).
5. M. Osiak, H. Geaney, E. Armstrong, and C. O'Dwyer, "Structuring materials for lithium-ion batteries: Advancements in nanomaterial structure, composition, and defined assembly on cell performance," *Journal of Materials Chemistry*, **A 2**, 9433 (2014).

6. C. L. Cobb and M. Blanco, "Modeling mass and density distribution effects on the performance of co-extruded electrodes for high energy density lithium-ion batteries," *Journal of Power Sources*, **249**, 357 (2014).
7. C.-J. Bae, C. K. Erdonmez, J. W. Halloran, and Y.-M. Chiang, "Design of battery electrodes with dual-scale porosity to minimize tortuosity and maximize performance," *Advanced materials*, **25**, 1254 (2013).
8. S. Ferrari, M. Loveridge, S. D. Beattie, M. Jahn, R. J. Dashwood, and R. Bhagat, "Latest advances in the manufacturing of 3D rechargeable lithium microbatteries," *Journal of Power Sources*, **286**, 25 (2015).
9. J. Pröll, H. Kim, A. Piqué, H. J. Seifert, and W. Pfleging, "Laser-printing and femtosecond-laser structuring of $LiMn_2O_4$ composite cathodes for Li-ion microbatteries," *Journal of Power Sources*, **255**, 116 (2014).
10. J. B. Habedank, J. Endres, P. Schmitz, H. P. Huber, and M. F. Zaeh, "Femtosecond laser structuring of graphite anodes for improved lithium-ion batteries: Ablation characteristics and process design," *Journal of Laser Applications* (2018) (accepted for publication) 2018.
11. C. L. Cobb and S. E. Solberg, "Communication—Analysis of Thick Co-Extruded Cathodes for Higher-Energy-and-Power Lithium-Ion Batteries," *Journal of The Electrochemical Society*, **164**, A1339 (2017).
12. V. P. Nemani, S. J. Harris, K. C. Smith, and Design of Bi-Tortuous, "Anisotropic Graphite Anodes for Fast Ion-Transport in Li-Ion Batteries," *Journal of The Electrochemical Society*, **162**, A1415 (2015).
13. J. Newman and K. E. Thomas-Alyea, *Electrochemical Systems*, 3rd ed.; John Wiley & Sons, Inc.: Hoboken, New Jersey, 2004.
14. M. Doyle, T. F. Fuller, and J. Newman, "Modeling of Galvanostatic Charge and Discharge of the Lithium/Polymer/Insertion Cell," *Journal of the Electrochemical Society*, **140**, 1526 (1993).
15. J. Landesfeind, D. Pritzl, and H. A. Gasteiger, "An Analysis Protocol for Three-Electrode Li-Ion Battery Impedance Spectra: Part I. Analysis of a High-Voltage Positive Electrode," *Journal of the Electrochemical Society*, **164**, A1773 (2017).
16. T. F. Fuller, M. Doyle, and J. Newman, "Simulation and Optimization of the Dual Lithium Ion Insertion Cell," *Journal of the Electrochemical Society*, **141**, 1 (1994).
17. F. M. Kindermann, P. J. Osswald, G. Ehlert, J. Schuster, A. Rheinfeld, and A. Jossen, "Reducing Inhomogeneous Current Density Distribution in Graphite Electrodes by Design Variation," *Journal of The Electrochemical Society*, **164**, E3105 (2017).
18. F. M. Kindermann, P. J. Osswald, S. Klink, G. Ehlert, J. Schuster, A. Noel, S. V. Erhard, W. Schuhmann, and A. Jossen, ", Measurements of lithium-ion concentration equilibration processes inside graphite electrodes," *Journal of Power Sources*, **342**, 638 (2017).
19. S. V. Erhard, P. J. Osswald, J. Wilhelm, H. E. Hoster, and A. Jossen, "Simulation and Measurement of Local Potentials of Modified Commercial Cylindrical Cells: II: Multi-Dimensional Modeling and Validation," *Journal of The Electrochemical Society*, **162**, A2707 (2015).
20. S. V. Erhard, et al. Simulation and Measurement of the Current Density Distribution in Lithium-Ion Batteries by a Multi-Tab Cell Approach," *Journal of The Electrochemical Society*, **164**, A6324 (2017).
21. M. Doyle and J. Newman, "Comparison of Modeling Predictions with Experimental Data from Plastic Lithium Ion Cells," *Journal of the Electrochemical Society*, **143**, 1890 (1996).
22. K. K. Patel, J. M. Paulsen, and J. Desilvestro, "Numerical simulation of porous networks in relation to battery electrodes and separators," *Journal of Power Sources*, **122**, 144 (2003).
23. I. V. Thorat, D. E. Stephenson, N. A. Zacharias, K. Zaghib, J. N. Harb, and D. R. Wheeler, "Quantifying tortuosity in porous Li-ion battery materials," *Journal of Power Sources*, **188**, 592 (2009).
24. J. Landesfeind, J. Hattendorff, A. Ehrl, W. A. Wall, and H. A. Gasteiger, "Tortuosity Determination of Battery Electrodes and Separators by Impedance Spectroscopy," *Journal of The Electrochemical Society*, **163**, A1373 (2016).
25. R. B. MacMullin and G. A. Muccini, "Characteristics of porous beds and structures," *AIChE Journal*, **2**, 393 (1956).
26. M. J. Martínez, S. Shimpalee, and J. W. van Zee, "Measurement of MacMullin Numbers for PEMFC Gas-Diffusion Media," *Journal of the Electrochemical Society*, **156**, B80 (2009).
27. J. Mao, W. Tiedemann, and J. Newman, "Simulation of temperature rise in Li-ion cells at very high currents," *Journal of Power Sources*, **271**, 444 (2014).
28. L. O. Valøen and J. N. Reimers, "Transport Properties of $LiPF_6$-Based Li-Ion Battery Electrolytes," *Journal of the Electrochemical Society*, **152**, A882 (2005).
29. A. Nyman, M. Behm, and G. Lindbergh, "Electrochemical characterisation and modeling of the mass transport phenomena in $LiPF_6$–EC–EMC electrolyte," *Electrochimica Acta*, **53**, 6356 (2008).
30. M. Guo and R. E. White, "A distributed thermal model for a Li-ion electrode plate pair," *Journal of Power Sources*, **221**, 334 (2013).
31. H. Lundgren, M. Behm, and G. Lindbergh, "Electrochemical Characterization and Temperature Dependency of Mass-Transport Properties of $LiPF_6$ in EC:DEC," *Journal of the Electrochemical Society*, **162**, A413 (2014).
32. P. Ramadass, B. Haran, P. M. Gomadam, R. White, and B. N. Popov, "Development of First Principles Capacity Fade Model for Li-Ion Cells," *Journal of The Electrochemical Society*, **151**, A196 (2004).
33. S. Tippmann, D. Walper, L. Balboa, B. Spier, and W. G. Bessler, "Low-temperature charging of lithium-ion cells part I: Electrochemical modeling and experimental investigation of degradation behavior," *Journal of Power Sources*, **252**, 305 (2014).
34. M. Doyle and Y. Fuentes, "Computer Simulations of a Lithium-Ion Polymer Battery and Implications for Higher Capacity Next-Generation Battery Designs," *Journal of The Electrochemical Society*, **150**, A706 (2003).
35. M. Park, X. Zhang, M. Chung, G. B. Less, and A. M. Sastry, "A review of conduction phenomena in Li-ion batteries," *Journal of Power Sources*, **195**, 7904 (2010).
36. K. Smith and C.-Y. Wang, "Power and thermal characterization of a lithium-ion battery pack for hybrid-electric vehicles," *Journal of Power Sources*, **160**, 662 (2006).

4.2 Analysis of Performance Improvements through Anode Structuring

In this section, the article titled *Modeling and Simulation of Pore Morphology Modifications using Laser-Structured Graphite Anodes in Lithium-Ion Batteries* [80] is presented. Parts of the article were presented at the *Batterieforum Deutschland 2019* in Berlin in January 2019, the *16th Symposium on Modeling and Experimental Validation of Electrochemical Energy Technologies (ModVal 16)* in Braunschweig in March 2019, and the *Pacific Rim Meeting (PRiME)* in October 2020, which was held as an online event.

In the previous section, a homogenized 3D model (p4D model) of a representative hole structure was developed and used to describe a structured graphite anode [76]. Among the main findings were the reduced lithium-ion concentration gradients in the liquid electrolyte in the through-plane direction of the cell, primarily occurring in the highly tortuous graphite anode. However, it is difficult to adequately represent the induced structures in one single 3D model since each hole has a slightly different geometrical shape. As the dominant gradients still arise in the through-plane direction, in this work, a standard p2D model with an adapted tortuosity for the structured electrodes was used. Besides an appropriate representation, the p2D model provides faster computational speed with around 2000 degrees of freedom (DOFs) vs. 9000 DOFs for the p4D model.

To further investigate the impact of the structuring process on electrodes with varying morphology, the performance of NCM-111/graphite coin cells with different areal capacities was measured. Without changing the electrode composition, the loading of the cell was adjusted by the thickness of the anodes and cathodes. The simulation results are well in line with the discharge rate capability measurements. The C-rate window, where the structuring process provides a benefit in capacity retention is defined by the loading of the cell. With thicker electrodes, the maximum benefit shifts to lower C-rates (and vice versa) and the tortuosity reduction specifies the maximum itself, hence, a lower tortuosity yields a higher rate capability.

An overpotential analysis, that is based on local concentrations and potentials solved in the electrochemical model, revealed the anode as a major contributor to the total cell polarization. Especially for medium C-rates, the diffusion polarization in the liquid electrolyte is the dominant limiting mechanism for the cell performance. A modification of the pore morphology results in a reduction in anode tortuosity, which decreases concentration gradients and the accompanying overpotentials and more capacity can be discharged from the cell. For very high currents, the overpotentials originating from the cathode and the contact resistance overtake the anode contribution. In this current range, a structuring of the cathode could bring a positive effect on capacity retention, however, the usable capacity for such high loads is relatively low.

So far, only discharge processes were analyzed for cells comprising structured anodes. A reduction in overpotentials also offers an opportunity for improved charging performance, where the potential at the anode/separator interface is crucial. At this interface, the local potential criterion $\phi_s - \phi_l \leq 0\,\mathrm{V}$ can be interpreted as an indicator for detrimental lithium-plating during a charging procedure. Fast charging simulations for the different loadings revealed that a reduced tortuosity through electrode structuring provides a higher lithium-plating threshold. This results in faster charging times, while keeping the anode potential in a safe area and avoiding lithium-plating.

Author contribution Ludwig Kraft developed the idea of investigating the performance of lithium-ion cells with laser-structured anodes with varying areal capacities and tortuosity improvements. Jan B. Habedank carried out the laser-structuring process of the graphite anodes. Ludwig Kraft built the coin cells, recorded the measurement data, developed and validated the electrochemical model, and carried out the simulation studies. The data was analyzed and interpreted by Ludwig Kraft and Jan B. Habedank. Alexander Frank and Alexander Rheinfeld supported the overpotential analysis. The manuscript was written by Ludwig Kraft and edited by Jan B. Habedank and Andreas Jossen. All authors discussed the data and commented on the results.

Modeling and Simulation of Pore Morphology Modifications using Laser-Structured Graphite Anodes in Lithium-Ion Batteries

Ludwig Kraft, Jan B. Habedank, Alexander Frank, Alexander Rheinfeld, Andreas Jossen

Journal of The Electrochemical Society 167 (1), p. 013506, 2020

Permanent weblink:
http://dx.doi.org/10.1149/2.0062001jes

Journal of The Electrochemical Society, 2020 **167** 013506

Modeling and Simulation of Pore Morphology Modifications using Laser-Structured Graphite Anodes in Lithium-Ion Batteries

Ludwig Kraft, [1,*,z] **Jan B. Habedank,** [2] **Alexander Frank,** [1] **Alexander Rheinfeld,** [1] **and Andreas Jossen** [1]

[1] *Institute for Electrical Energy Storage Technology, Technical University of Munich (TUM), Munich, Germany*
[2] *Institute for Machine Tools and Industrial Management, Technical University of Munich (TUM), Munich, Germany*

The energy density of lithium-ion batteries can be enhanced by using thicker and denser electrodes, which leads to transport limitations in the electrolyte within the porous structures. A pore morphology modification of the electrodes can counteract this limitation mechanism and provide higher rate capabilities of the cells. In this work, graphite anodes are structured with a picosecond laser in order to create transport pathways for the lithium-ions and allow for enhanced penetration of the electrodes. Experimental data from graphite/NMC-111 coin cells with varying areal capacities are used for the development and parameterization of an electrochemical model. The modified pore morphology of the structured electrodes is represented in the model by an adapted tortuosity, which results in lower lithium-ion concentration gradients and reduced diffusion polarization in the electrolyte. The effect of electrode thickness and tortuosity on limiting mechanisms is analyzed via simulation studies in order to derive the impact of structured electrodes. As a result, improved discharge as well as charge rate capability appears beside enhanced safety features such as increased tolerance versus hazardous lithium-plating during fast charging scenarios.
 [DOI: 10.1149/2.0062001JES]

Manuscript submitted June 11, 2019; revised manuscript received August 1, 2019. Published September 23, 2019. *This paper is part of the JES Focus Issue on Mathematical Modeling of Electrochemical Systems at Multiple Scales in Honor of Richard Alkire.*

Lithium-ion batteries are the prevailing energy storage system for electric vehicles, stationary energy devices, mobile applications and power tools.[1] Especially electric vehicles require increasing energy densities to offer a satisfactory driving range for customers.[2,3] While solid state technologies are under ongoing development, they face a lot of challenges and cannot provide the required energy density, current capability and cycling stability.[4] Therefore, lithium-ion batteries comprising porous electrodes filled with liquid electrolyte are still the state-of-the-art technology.

One way to increase the energy density is the use of new active materials,[2,3,5] e.g. combining a nickel-rich lithium nickel manganese cobalt oxide (NMC-811) cathode with a silicon/graphite anode.[6] The performance of an existing active material can also be enhanced by nanostructuring methods[7–10] or by changing the electrode formulation, composed of active material, binder and carbon black.[11–16] Another option lies in an optimized cell design in order to increase the share of active material and reduce the share of passive parts like current collectors, tab connectors or the housing.[17] Thicker and denser electrodes offer an opportunity to increase the required energy density independently of the used active material, but face issues when they are stressed with higher currents.[13,18–21] One major contributor are mass transport limitations in the electrolyte.[21–25]

Electrode pore morphology modifications provide a potential to overcome limitations arising from thicker and denser electrodes.[13,26–28] The path length, the lithium-ions have to travel in the electrolyte through the porous electrode, is defined by the thickness, the porosity and the tortuosity.[17,29] Primarily, high charge/discharge currents lead to a poor battery performance, as the overpotentials increase and the full capacity cannot be utilized.[28] Depending on the application and the desired requirements, current research focuses on improving the properties of anode[30–32] and cathode[33–37] composites by a modification of their structure. Besides an increased battery performance, an introduction of macro channels or pores into the electrode can lead to a reduced wetting time during the cell manufacturing process.[13,38]

The focus in this work lies on modified graphite anodes using a laser-structuring process.[31] It will be demonstrated, that lithium-ion cells comprising structured graphite anodes not only provide a higher discharge rate capability,[39] but also exhibit an opportunity to tackle issues concerning fast charging.[40] While the discharge performance, determined by the maximum discharge current, of state-of-the-art lithium-ion batteries is at a practical level for most applications, fast charging capability of energy storage systems is becoming more and more important. If the energy density of lithium-ion batteries cannot be increased to a satisfactory level, especially electric vehicles rely on fast charging capability to overcome range anxiety of potential customers.

Experimental data gained from measurements on graphite/NMC-111 coin cells comprising unstructured and structured graphite anodes with varying thicknesses are used for the development of an electrochemical pseudo two-dimensional (p2D) model. With the aid of simulation studies, the influence of the electrode pore morphology on the charging and discharging behavior is analyzed and design criteria of electrodes are provided.

Experimental

Electrode fabrication.—A rotation-revolution mixer (Speedmixer DAC 3000, Hauschild Engineering, Germany) was used to mix the components for the electrode inks with N-methyl-2-pyrrolidone (NMP, Sigma-Aldrich, USA) at ambient pressure and temperature. The cathode ink contained 96 wt% $LiNi_{1/3}Co_{1/3}Mn_{1/3}O_2$ (NMC-111) (BASF, Germany), 2 wt% polyvinylidene fluoride (PVDF, Kynar, Arkema, France) and 2 wt% conductive carbon (C65, Timcal, Switzerland). In terms of the anode, 95 wt% graphite (SGL Carbon, Germany) and 5 wt% PVDF were used. Doctor blade coating was performed in an industrial roll-to-roll coating machine (Coatema, Germany) equipped with an infrared dryer at a coating speed of 0.5 m min^{-1}. Four different anode and cathode coating thicknesses were prepared and subsequently calendered in order to achieve a final porosity of approximately 35%. The anode and cathode composition remained constant for each coating. The resulting electrode thicknesses accounted for 71 µm, 79 µm, 90 µm and 116 µm for coatings 1 to 4, respectively.

Laser-structuring of anodes.—For the electrode pore morphology modification, picosecond laser pulses from an Ytterbium fiber laser (YLPP-1-150V-30, IPG Photonics, USA) at infrared wavelengths were locally employed to ablate small fractions of the composite material and induce hole-like structures into the anode coatings. The cathode coatings as well as the current collectors of both electrodes remained pristine. The structuring process parameters were adjusted so that the holes reached down to the copper current collector, which resulted in an ablated fraction of around 5 to 10 wt% of the composite electrode material, depending on the electrode thickness, determined by

*Electrochemical Society Student Member.
[z]E-mail: ludwig.kraft@tum.de

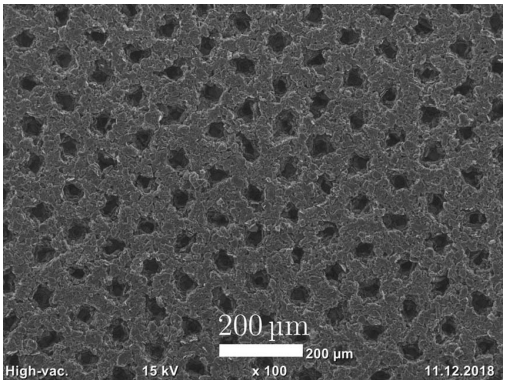

Figure 1. SEM image of a laser-structured graphite anode.

weighing the electrode sheets before and after structuring. The structures were spatially distributed in a hexagonal pattern with a lateral length of 100 µm. As more particles are removed in the structuring process close to the surface of the coating, the structures are not perfectly cylindrical. On the surface, the hole diameter was around 25 to 35 µm, but the structures narrowed toward the deeper parts of the electrode. The structuring process was performed with an average laser power of 10 W, a pulse repetition frequency of 1.2 MHz, a pulse energy of 8.33 µJ and an irradiation time of 0.6 ms per structure. The focal diameter of the laser beam was approximately 25 µm, measured with a high-precision beam diagnostics device (MicroSpotMonitor, PRIMES, Germany). For the deflection of the laser beam, scanning optics (Racoon 21, ARGES, Germany) were used. A scanning electron microscope (SEM) image of a laser-structured graphite anode is displayed in Fig. 1. For a more detailed description of the experimental setup for laser-structuring as well as process analyses, the reader is referred to our previous work.[31,38]

Coin cell assembly.—Coin cells of the type 2032 were assembled in an argon filled glove box (M. Braun Inertgas-Systeme, Germany) at purity (H_2O < 0.1 ppm, O_2 < 0.1 ppm). The cathode coins were punched at a diameter of 14 mm, the anode coins at a diameter of 15 mm. A glass microfiber sheet (Type 691, VWR, USA) with a diameter of 16 mm was used as separator. In its uncompressed state, the separator has a thickness of 260 µm. Due to the compression during cell assembly, the separator thickness is estimated to be around 200 µm.[41] The used glass fiber separator shows a high porosity and low tortuosity, compare Table AI, resulting in a MacMullin number of approximately 1.7. Separators used in commercial lithium-ion cells are thinner (15–30 µm) but exhibit a higher MacMullin number (5–15), which in turn results in a comparable effective path-length for the lithium-ions.[42] Particularly for the assembling of laboratory cells, these glass fiber separators provide a better ease of handling and serve as an electrolyte reservoir that prevents the cell from drying out during cycling.[43,44] Each cell was filled with 100 µl of electrolyte (LP57, BASF, Germany), containing ethylene carbonate (EC) and ethyl-methyl-carbonate (EMC) in a ratio of 3:7 (by weight) with 1 M lithium-hexaflourophosphate ($LiPF_6$). The assembly included two aluminum spacers, each with a thickness of 1 mm in order to fill the housing caps, a wave spring and an insulation ring.

Six coin cells – three cells with unstructured anodes and three with structured anodes – were assembled for each of the four loadings as shown in Table I. The cell capacities used for the formation procedure were calculated by determining the coating mass and assuming mass specific capacities of 150 mAh g^{-1} for NMC-111 and 360 mAh g^{-1} for graphite. The areal capacity of the anode coatings was overbalanced by approximately 20% compared to the capacity of the cathode coatings in order to have a N/P ratio greater than unity and to avoid lithium-plating during charging. The structured anodes still remained overbalanced since the loss of material during the ablation process only accounts for approximately 5–10 wt% of the coating. For a more even balancing, the anodes with more active material due to manufacturing tolerances were used for the structuring process. Additionally, cathodes with less active material, determined by weighing, were paired with anodes with less active material, i.e. the structured ones.

Formation procedure and rate capability test.—After assembly, all cells went through a formation procedure of three charge and discharge cycles at a constant current (CC) of C/10 related to their calculated capacity within a voltage window between 4.2 V and 3.0 V after the first charge. A detailed overview of the measurement procedures is given in Table II. All measurements were performed with a CTS battery test system (BaSyTec, Germany) in a custom-built climate chamber with a controlled ambient temperature of 25°C . The insulated climate chamber uses peltier devices for thermoelectric cooling to control the temperature, similar to the test chamber described by Rheinfeld et al.[45] After formation, a C/20 charge/discharge cycle was used to determine the nominal capacity of each coin cell, listed as average values of a set of three cells in Table I.

In the rate capability test, the cells were charged with a CC phase followed by a constant voltage (CV) phase, which remained unaltered, independent of the applied discharge current. Between each charge and discharge cycle a pause of 1 h was kept to allow for relaxation of the cells. In the discharge procedure, the cells with loading 1 and 2 were discharged with C/5, C/2, 1C, 2C, 3C, 4C, 5C and 10C. To have a better resolution, discharge currents of 1.5C, 2.5C, 3.5C, 4.5C and 6C were added for loading 3 and 4. The results of the rate capability test are shown in Fig. 2. The discharge capacities were referenced to the area of the cathode coins of 1.54 cm^2. Marginal deviations in the final

Table I. Characterization of the four loadings comprising unstructured and structured anodes.

Loading	Anode type	Abbreviation	Measured capacity[I]	Electrode thickness[II]	Modeled areal capacity[III]	Anode tortuosity
1	unstructured	L1U	3.54 mAh	71 µm	2.26 mAh cm^{-2}	5.5
	structured	L1S	3.42 mAh	71 µm	2.26 mAh cm^{-2}	3.5
2	unstructured	L2U	3.90 mAh	79 µm	2.50 mAh cm^{-2}	5.5
	structured	L2S	3.80 mAh	79 µm	2.50 mAh cm^{-2}	3.5
3	unstructured	L3U	4.57 mAh	90 µm	2.90 mAh cm^{-2}	8.5
	structured	L3S	4.33 mAh	90 µm	2.90 mAh cm^{-2}	5.5
4	unstructured	L4U	6.00 mAh	116 µm	3.82 mAh cm^{-2}	8.5
	structured	L4S	5.77 mAh	116 µm	3.82 mAh cm^{-2}	6.5

[I]average cell capacity determined by the C/20 discharge cycle.
[II]accounts for both, anode (l_{neg}) and cathode thickness (l_{pos}).
[III]derived from the averaged measured capacities and normalized to the cathode area of 1.54 cm^2.

Table II. Measurement procedures applied to the coin cells.

Procedure	Charge	Discharge	Cycles
Formation	CC @ C/10 until $U \geq 4.2$ V	CC @ C/10 until $U \leq 3.0$ V	3
Capacity check	CC @ C/20 until $U \geq 4.2$ V CV @ 4.2 V until $I \leq$ C/100	CC @ C/20 until $U \leq 3.0$ V	1
Rate capability test	CC @ C/2 until $U \geq 4.2$ V CV @ 4.2 V until $I \leq$ C/100	CC @ I_L* until $U \leq 2.7$ V	3 (for each I_L)

CC - constant current, CV - constant voltage.
*$I_{L1,L2}$ = C/5, C/2, 1C, 2C, 3C, 4C, 5C, 10C for loading 1 and 2.
$I_{L3,L4}$ = C/5, C/2, 1C, 1.5C, 2C, 2.5C, 3C, 3.5C, 4C, 4.5C, 5C, 6C, 10C for loading 3 and 4.

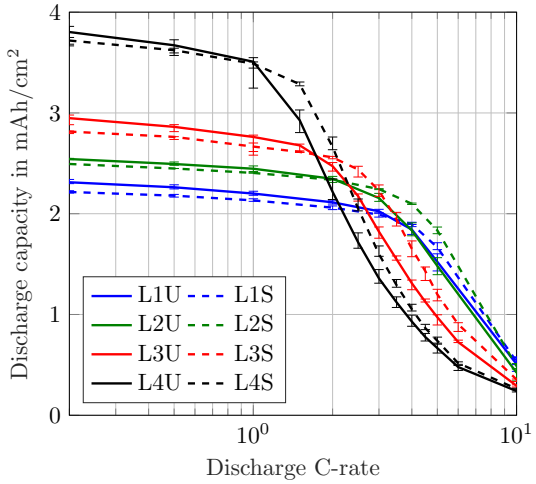

Figure 2. Measured area-specific discharge capacity of coin cells comprising unstructured and structured anodes for C-rates from C/5 to 10C.

coating thicknesses appeared in the range of manufacturing tolerances and led to slight deviances in the measured coin cell capacities.

Modeling

In our previous work, a homogenized 3D model of a representative hole structure was used to describe a structured anode.[39] Simulation results of lithium-ion concentrations in both the electrolyte and the active material helped to understand and clarify occurring inhomogeneities due to the structuring. Among the main findings were the reduced concentration gradients in the liquid electrolyte in the through-plane direction of the cell, which in turn led to the increased discharge rate capability. Moreover, it is difficult to represent the geometric shape of the induced holes in a 3D model. Each hole has a slightly different shape depending on the particles that were removed by the laser ablation process, compare to Fig. 1. In this work, a p2D model according to Doyle, Fuller and Newman[46,47] is used, which consists of the three 1D domains anode, separator and cathode, defined by their thickness l_{neg}, l_{sep} and l_{pos}, respectively. The governing equations are listed in the appendix in Table AII and the parameterization is shown in Table AI. Note, that reducing the spatial dimensions of the electrode to the through-plane dimension holds a simplification of the complex electrode structure. However, the 1D model comes with faster computational speed and is able to adequately describe the processes and limitations in the through-plane direction, which are the main contributors to the determinant cell performance.[39]

In 1D models the geometry does not account for porous structures, as is the case for the electrodes and the separators in a state-of-the-art lithium-ion battery with liquid electrolyte. Hence, an adaption is needed to appropriately represent the prolonged transport pathways in porous structures. This plays an important role, especially when high currents are applied to the cell and the limitation mechanisms in the electrolyte have a major contribution. To account for the morphology of porous structures in 1D models, the electrolyte transport parameters are modified by using a correction term to express the effective diffusivity $D_{l,eff}$ and conductivity κ_{eff} as shown in Eq. 1. An often used term in modeling is the Bruggeman correction,[5,48–52] where the factor α_{Brugg} was calculated to be 1.5 for materials with ideal spherical particles of identical size.[53] Since the electrode particles are not ideally spherical, e.g. natural graphite is platelet-shaped, and are not of the same size, a Bruggeman correction of $\alpha_{Brugg} = 1.5$ just states a lower limit for the correction factor.[17,29,54,55] The MacMullin number N_M, which can be defined as the ratio of the tortuosity τ and the porosity ε_l (Eq. 2) is another possible correction factor.[56]

$$\Psi_{l,eff} = \varepsilon_l^{\alpha_{Brugg}} \Psi_l = \frac{\varepsilon_l}{\tau} \Psi_l = \frac{\Psi_l}{N_M} \quad [1]$$

$$N_M = \frac{\tau}{\varepsilon_l} \quad [2]$$

No matter which correction term is used, a change in the factor will significantly influence the transport properties and thereby the cell behavior. The structuring process modifies the electrode pore morphology and enhances the lithium-ion transport in the electrolyte which has a positive effect on the capacity retention in a certain range of discharge currents.[39] Based on the parameter set of the cells comprising unstructured anodes, a reduction of the MacMullin number is utilized to describe the behavior of the cells comprising structured anodes. Thus, either a reduction in the electrode's tortuosity or an increase in the porosity will improve the local transport properties. However, an increase in the porosity has a higher influence because it directly affects the mass balance

$$\varepsilon_l \frac{\partial c_l}{\partial t} = -\nabla N_l + R_l \quad [3]$$

Regarding the discharge of the cell, i.e. the delithiation of the anode, a higher anode porosity means that there is more space for the lithium-ions in the pore volume and the absolute lithium-ion concentration in the electrolyte c_l is lowered. The lithium-ion concentration in turn has a crucial effect on the electrolyte transport properties, see Table AI.

In this work, the tortuosity was adapted in the model to represent the pore morphology change by the structuring process of the graphite anode. In order to maintain comparability between the different loadings, the sensitivity analysis in this work investigates varying tortuosities only and neglects the alternation of porosity, which may be correlated with a change in tortuosity. The discharge rate behavior of the loadings was adjusted via the electrode thickness and the anode tortuosity, all other modeling parameters remained unaltered. Tortuosity measurements via impedance spectroscopy or 3D tomography offer information about the electrode morphology.[21,29,55,57,58] The tortuosities used in this work are based on values found in the literature, where platelet-shaped natural graphite exhibits comparatively high through-plane values.[29,55] The parameters for the characterization of the different loadings are listed in Table I, whereas the general

model parameters are listed in Table AI. The electrode thickness is the same for the anode (l_{neg}) and the cathode (l_{pos}).

The temperature was set constant to 25°C in the model, owing to the low cell capacities compared to the high heat capacity of the coin cell setup. All measurements were performed at the same ambient temperature, so even for the highest cell capacity of 6 mAh and a discharge current of 10C, no temperature rise was detected. All C-rates used in the simulation studies are referenced to the modeled areal capacities in Table I, which were averaged and remained constant for each loading to allow a better comparison between unstructured and structured anodes.

Overpotential analysis.—The p2D model was implemented in the commercial FEM solver *COMSOL Multiphysics 5.3a*. According to Nyman et al.,[22] the total cell polarization can be ascribed to local potentials and concentrations solved in the p2D model and is composed of the following six sub-processes, the equations are listed in Table AIII:

- Diffusion polarization in the liquid phase
- Diffusion polarization in the solid phase
- Ohmic potential drop in the liquid phase
- Ohmic potential drop in the solid phase
- Activation overpotential
- Contact resistance

The limitation mechanisms in the simulation studies are analyzed via using this implicit characterization method based on the actually solved concentrations and potentials in time and over the electrode thickness. In the separator domain, only diffusion polarization and ohmic potential drop in the electrolyte occur, as there is no active material and no reaction takes place. The contact resistance $R_{contact}$ cannot be ascribed to a single domain and is therefore listed separately in the later analysis. In the model, the cell voltage is corrected by the voltage drop resulting from the contact resistance ($R_{contact} \cdot i_{app}$).

Lithium-plating indication.—Charging a lithium-ion cell can induce lithium-plating on the surface of the graphite anode particles, particularly at low temperatures and high charging currents.[59] Up to a certain extent, this reaction is reversible and the plated metallic lithium gets oxidized either by intercalating into the graphite particles during relaxation or by stripping/dissolution in an subsequent discharge cycle.[60,61] However, part of this reaction remains irreversible and plated lithium tends to form dendrites that can penetrate the separator and cause severe safety problems.[62]

With an equilibrium potential of 0 V vs. Li^0/Li^+, the necessary condition of the lithium-plating reaction is an overpotential of $\eta_{Li} \leq 0\,V$.[52,63–65] The lateral electrode dimensions and the tab positions can cause an inhomogeneous distribution of the current density and therefore result in different local potentials.[6] Besides, both the anode and the cathode properties and the balancing of the two electrodes play an important role for the likelihood of lithium-plating.[64] Regarding the used 1D model, the lithium-plating reaction is presumably most pronounced at the anode/separator interface and the local potential criterion $\Phi_s - \Phi_l \leq 0\,V$ can be interpreted as an indicator for lithium-plating during a charging procedure.[6] Based on this criterion, various fast charging scenarios were evaluated in the later simulations.

Results and Discussion

Model validation and simulation.—For validation of the developed model, the data from Fig. 2 is normalized to the C/5 discharge capacity of each loading and compared to the simulation results, which is shown in Fig. 3a. By normalization of the the discharge capacity, it is more obvious that the lower loadings can withstand higher C-rates. The curves shift from the highest loading L4U to the lowest loading L1U on the very right side. The curves of the cells comprising structured anodes (dashed lines) all bend at higher C-rates so that these lie right of their unstructured counterparts of the same

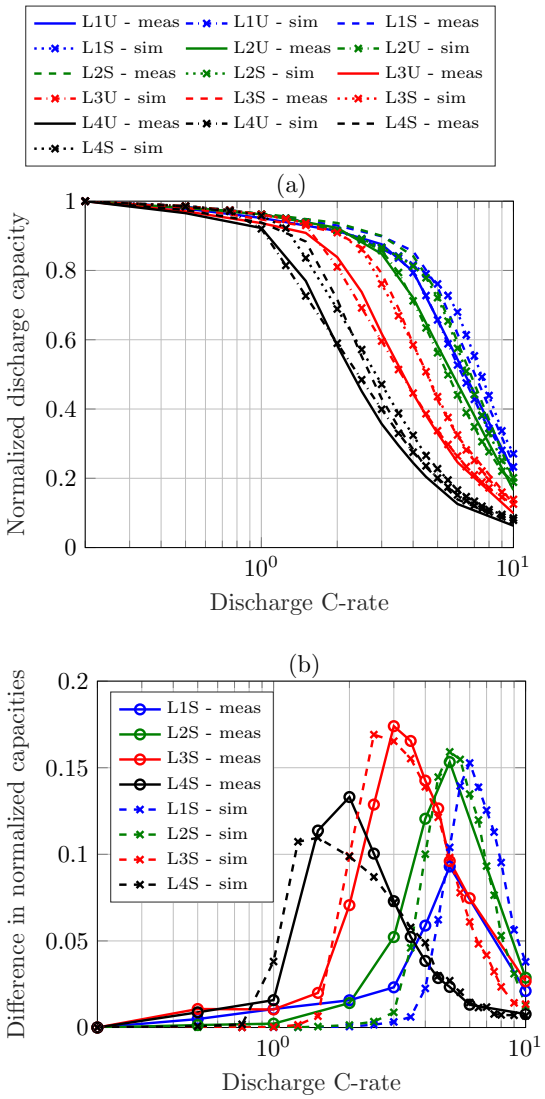

Figure 3. (a) Comparison of measured and simulated C/5-normalized discharge rate capability of coin cells comprising unstructured and structured anodes and (b) observed difference in normalized discharge rate capability.

loading (solid lines). The simulation results represented by the dash-dotted lines for the unstructured electrodes and the dotted lines for the structured electrodes are in good agreement with the measurement data.

The validation of the measured and simulated discharge voltage curves is shown in the appendix in Fig. A1. The gray shaded areas represent the margin of the measured discharge voltages of each set of coin cells for the specified loading. The experimental and simulated rate capability tests covered a wide span of discharge C-rates, for validation of the voltage profiles, the C-rates C/5, 2C, 5C and 10C were selected. In the simulations, only the electrode thickness, the applied current density and the anode tortuosity were adapted to the different loadings and the measurement data is in very good agreement with the simulation results.

The benefit of the structuring process appears in the difference in normalized capacities of the cells comprising structured and unstructured anodes, see Fig. 3b. A categorization in three different stages is visible: for low applied C-rates there is no improvement induced by the

structuring process, for medium C-rates the improvement increases and reaches a maximum and for higher C-rates it diminishes when other limitations become more pronounced. A detailed explanation of the three stages can also be found in our previous work.[39] The location of the maximum determines the range of C-rates where the structuring process has a positive impact. The pore morphology change of the graphite anode leads to an enhanced transport of lithium-ions and a reduction of concentration gradients in the electrolyte. Thereby, the cutoff voltage for the discharge process is reached at a later moment and more capacity can be discharged from the cell. For higher loadings the maximum shifts toward lower C-rates, for lower loadings it shifts toward higher C-rates. Even for the low loading L1 with 2.26 mAh cm^{-2} there is a 15% increase in capacity retention for a discharge rate of 6C. Note, that for loading L1 and L2 the cells were discharged with 5C and then 10C with no further steps in between, so the maximum of L1 was most likely not reached precisely. Modeling and simulation is often used to extend and refine the fundamental data of use case scenarios, such as the variation of discharge C-rates to determine the location of the maximum improvement in capacity retention in this work. The shape of the capacity difference, given by the location and the value of the maximum, will be analyzed with a simulation study next.

The influence of the structuring process as a function of electrode thickness is studied based on the parameter set of loading L1. In this study, an increase in electrode thickness increases the loading, so the discharge current is adapted to the changed loading. Choosing moderate values, the tortuosity of the unstructured anodes is set to 5.5 and the tortuosity of the structured anodes to 3.5. The thickness of the electrodes is increased by 25% in each step ranging from 71 µm to 173 µm. The results are displayed in Fig. 4a. As expected, an increase in the electrode loading causes the maximum to shift toward lower C-rates. The maximum improvement is just slightly affected by the electrode thickness. For thin electrodes with 71 µm thickness there is a 15% capacity enhancement compared to 18% for thick electrodes with 173 µm thickness.

On the other hand, the tortuosity improvement by a pore morphology modification highly affects the maximum enhancement in capacity retention as can be seen in Fig. 4b. This simulation study is based on parameter set L4 that features high tortuosity values. Starting from a tortuosity of 8.5 for the unstructured anode, the tortuosity of the structured anode is reduced by steps of 1 down to 3.5. The electrode thickness and the resulting discharge currents remained constant. The lower the tortuosity of the porous anode, the higher the improvement in capacity retention. The C-rate where the maximum is reached slightly shifts toward higher discharge currents, in this case from around 1.25C up to 2.5C. Note, an electrode porosity of 0.35 results in a tortuosity of 1.7 by using the Bruggeman correlation with $\alpha_{Brugg} = 1.5$. This in turn would lead to an increased discharge capacity of around 45% in this use case scenario. So the morphology of a composite electrode has to be carefully assessed when deriving correction terms for modeling purposes.

Overpotential analysis.—Regarding local polarization within the electrode stack, such as the anode, separator and cathode domain, the overall cell polarization is derived based on the aforementioned implicit overpotential analysis (as described in the modeling section) and outlined in the following to investigate the limiting mechanisms during discharge processes with increasing C-rates.

Based on the parameter set L2U, the initial conditions of the simulation were set to a fully charged state at a cell voltage of 4.2 V. Similar to the rate capability test listed in Table II, the cells were discharged with a CC procedure with C-rates ranging from C/5 to 10C until a cutoff voltage of 2.7 V was reached. The individual overpotentials were temporally averaged over each discharge cycle and then ascribed to one domain based on their occurrence. In Fig. 5a the relative contribution to the cell polarization is shown (they sum up to 1). While the anode contribution is declining for increasing discharge C-rates, it constitutes the major contribution to the total cell polarization up to 7C. This can be explained by the high tortuosity on the one hand and the fact that the

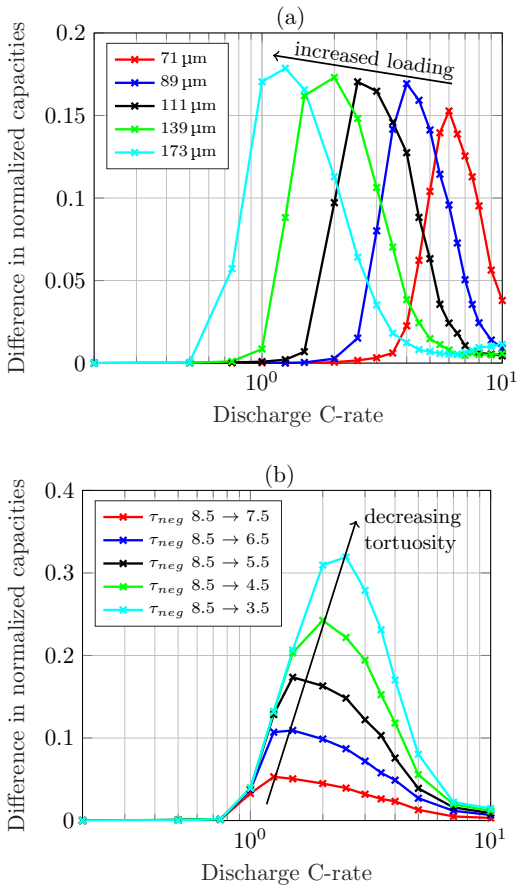

Figure 4. Simulated difference in normalized discharge rate capability of (a) cells with increased loading by increasing the electrode thickness based on parameter set of L1 and (b) cells with decreasing anode tortuosity and constant electrode thickness based on parameter set L4.

anode is the limiting electrode for the discharge process on the other hand. This will be explained in detail in the upcoming part. The cathode and contact contribution overtake the anode at 8C. Since the contact resistance is purely ohmic, the overpotential increases linearly with the applied discharge current. The separator only plays a minor role as only the diffusion polarization and ohmic potential drop in the liquid phase contribute in this domain. To get a better understanding of the impact of the overpotential, the absolute values are plotted in Fig. 5b for selected C-rates. For low discharge currents, e.g. C/5, the absolute cell overpotential is very low, hence its origin is less important. For 1C the total cell overpotential rises to around 100 mV and almost reaches 800 mV for a 10C discharge with the given parameterization set of the p2D model. With medium currents, the dominating anode contribution shows an opportunity to improve the cell design. Therefore, the anode overpotentials are investigated in detail depending on their driving force.

By excluding the contact resistance, the polarization in the anode can be categorized into five groups, namely the diffusion polarization and the ohmic potential drop in the solid and liquid phase and the activation overpotential. In order to investigate the influence of the change in anode pore morphology on the arising overpotentials, the parameter sets L2U and L2S were compared in the simulations. An overview of the absolute anode overpotentials for discharge currents ranging from C/5 to 10C is shown in Fig. 6. For the depicted pair of bars at each simulated discharge C-rate, the left one represents the results for the unstructured and the right one for

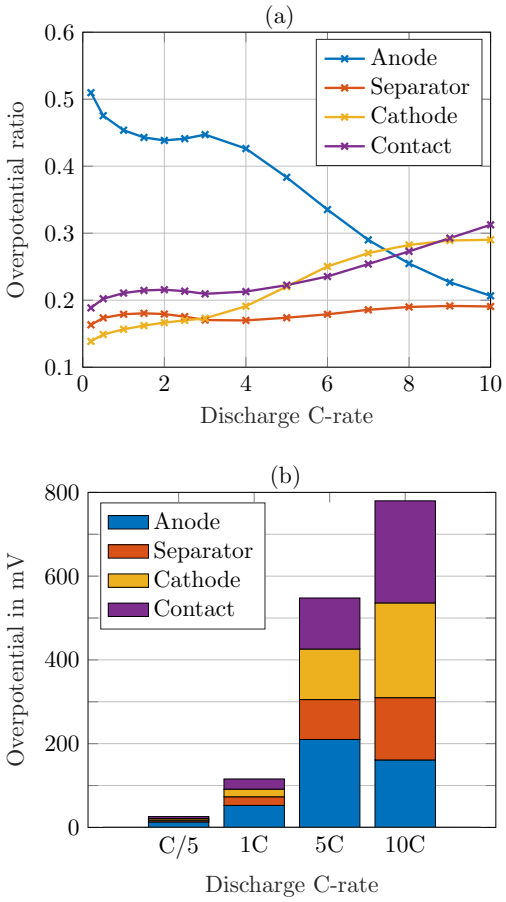

Figure 5. (a) Relative and (b) absolute distribution of cycle-averaged overpotentials of parameter set L2U assigned to the domains anode, separator and cathode and the contact resistance for discharge C-rates from C/5 to 10C.

the structured anode comprising the L2U and L2S parameterization, respectively.

The ohmic potential drop in the solid phase is barely visible which is referred to a high electrical conductivity in natural graphite of around 100 S m^{-1}.[66–70]

The ohmic potential drop in the electrolyte is also very low, with a minor contribution at very high C-rates. With the given parameter set of this work, the electrolyte conductivity κ lies around 1 S m^{-1} for moderate lithium-ion concentrations of 1000 mol m^{-3}, see also electrolyte transport parameters in Table AI. The conductivity of the bulk electrolyte can be measured with a turn-key conductivity sensor[29] and is therefore a well determined electrolyte property. A detailed overview of different electrolyte properties used for modeling purposes, including the conductivity, is given by Rheinfeld et al.[71] In their work the conductivity of five different electrolytes ranges from 0.8 to 1.2 S m^{-1} (at 1000 mol m^{-3} and 25°C). Even with the calculation of the effective conductivity κ_{eff} (see Eq. 1), in our case, the liquid current density i_l is too low to cause a high potential drop in the electrolyte.

The major contributors to the cell overpotential, as can be seen in Fig. 6, are the diffusion polarization in the solid and liquid phase and the activation overpotential. The diffusion polarization in the solid phase is calculated by the difference of the equilibrium potential on the surface of the particles and the average equilibrium potential (equations listed in Table AIII). During the end of discharge, the anode lithiation level x in Li_xC_6 tends toward zero and the corresponding equilibrium voltage $E_{eq,neg}$ reveals increasing potential gradients the more lithium is extracted, which in turn causes the reach of the cell discharge cutoff voltage of 2.7 V. Hence, a low lithium-ion concentration on the particle surface generates a high polarization in the solid phase, especially at the end of discharge.

The activation overpotential is affected by the kinetics as described by the Butler-Volmer equation, e.g. a higher exchange current density i_0 would result in lower overpotentials η (and vice versa) to reach the same surficial molar flux, as defined by the boundary conditions (see electrode kinetics in Table AII). Due to the nonlinear characteristics of the Butler-Volmer equation, a rise in the discharge current does not result in a proportional rise in the activation overpotential. It slightly increases with increasing discharge C-rates. The exchange current density is calculated by the anodic and cathodic reaction rates and the local lithium-ion concentrations. The lithiation process of the

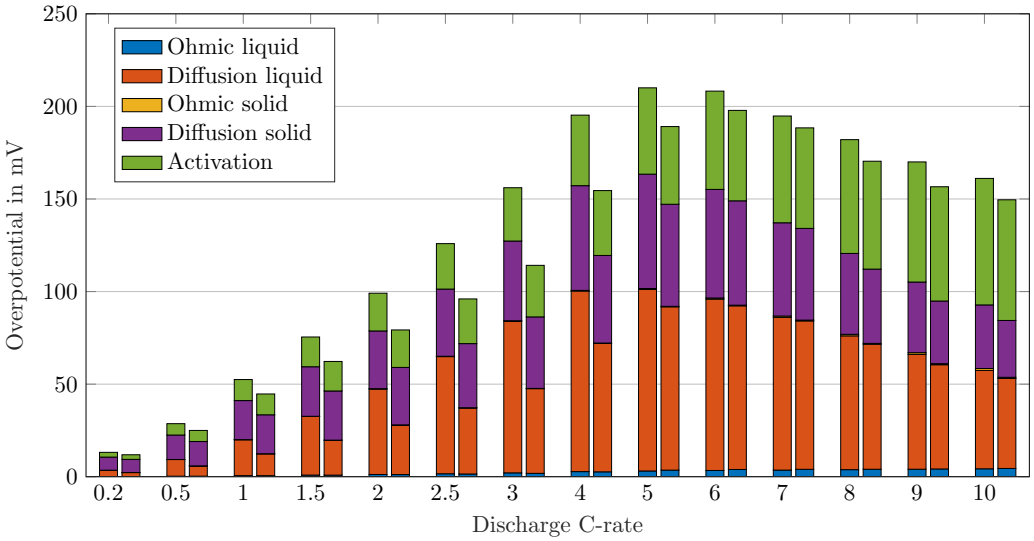

Figure 6. Cycle-averaged anode overpotentials for discharge C-rates from C/5 to 10C. For each pair of bars at a given C-rate the left bar corresponds to the overpotentials of the unstructured anode (L2U) and the right bar of the structured anode (L2S).

active material is either limited by the liquid phase concentration c_l tending toward zero (electrolyte depletion) or the surface concentration of the particles $c_{s,surf}$ reaching the maximum concentration $c_{s,max}$. The delithiation process is limited if the surface concentration of the particles reaches zero. In either case the exchange current density is diminished and the activation overpotential rises. The determination of the kinetic reaction rates is not trivial and not many values can be found in literature. A lot of publications use the reaction rates as fitting parameters[51,72–74] or set the exchange current density to a constant value,[67,68] which makes the reaction rates unnecessary. Generally, high reaction rates result in low activation overpotentials and low reaction rates in high activation overpotentials. Lin et al.[75] list a range of 10^{-12} to 10^{-9}m s^{-1} for the reaction rates of anodes and cathodes. Based on a sensitivity analysis conducted in this work, the reaction rates were estimated to 6×10^{-11} m s^{-1}, which is within the given range by Lin et al.[75]

The diffusion polarization in the liquid phase is the biggest contributor in the anode domain. Its driving force are the lithium-ion concentration gradients in the electrolyte. As explained in the modeling section, the effective electrolyte diffusivity is strongly affected by the porous electrode structure and calculated with the tortuosity and porosity. The high anode tortuosity lowers the effective diffusivity and increases the concentration gradients. Spatially resolved concentration gradients can be found in our previous work.[31] The resulting overpotential of the diffusion in the liquid phase of the unstructured anode reaches a maximum of around 100 mV at 5C and amounts to almost half the overpotential arising in the anode. By structuring the graphite anode, the modeled tortuosity is lowered from 5.5 for loading L2U to 3.5 for L2S. The maximum in capacity retention for this structuring process also occurs at a discharge C-rate of 5C, which corresponds to a peak in the liquid diffusion polarization. The structuring process enhances the transport in the electrolyte and mainly reduces the overpotentials caused by the diffusion polarization. A maximum reduction in anode overpotential of 42 mV is reached at 3C with 36 mV from liquid diffusion polarization.

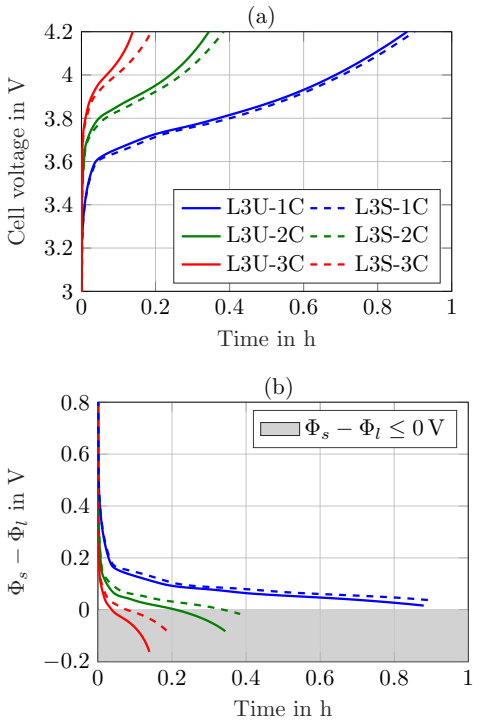

Figure 7. (a) Simulated cell voltage and (b) potential difference $\Phi_s - \Phi_l$ at anode/separator interface for charging currents 1C, 2C and 3C based on parameter set L3.

Fast charging scenario.—In the previous sections, it was demonstrated that lithium-ion cells comprising structured graphite electrodes provide an increased discharge rate capability in a certain range of C-rates by reducing electrolyte concentration gradients and overpotentials. Based on the parameterization that was validated against discharge rate capability tests, a fast charging scenario was simulated.

Therefore, the initial lithium-ion concentrations in both the anode and the cathode were adapted (compare Table AI) in order to represent a fully discharged cell with an initial cell voltage of 2.7 V. The simulations were carried out with a CC charge of 1C, 2C and 3C until a cutoff voltage of 4.2 V was reached, no CV phase was added to the charging procedure. In Fig. 7 the cell voltage and the potential difference at the anode/separator interface are plotted for loading L3. The charged capacities and the lithium-plating indication for all loadings are listed in Table III.

Note, that the gray shaded area for the potential drop in Fig. 7b just gives an indication of possible lithium-plating at the anode. The simulations were carried out under isothermal conditions ($T = 25$°C), which might hold true for a coin cell with low power losses. A heating of the cell would result in enhanced electrolyte transport properties,

Table III. Charged capacity and lithium-plating indication during fast charging scenarios.

	ΔCapacity[I]			ΔSOC[II]			ΔSOC Li-plating[III]			
Loading	1C	2C	3C	1C	2C	3C	1C	2C	3C	Maximum C-rate[IV]
L1U	3.27 mAh	2.97 mAh	2.60 mAh	94.0%	85.2%	74.5%	-	-	59.8%	2.5C
L1S	3.29 mAh	3.02 mAh	2.71 mAh	94.6%	86.7%	78.0%	-	-	-	3.3C
L2U	3.60 mAh	3.21 mAh	2.68 mAh	93.5%	83.4%	69.5%	-	-	44.0%	2.1C
L2S	3.63 mAh	3.29 mAh	2.88 mAh	94.4%	85.6%	74.9%	-	-	74.3%	2.9C
L3U	3.93 mAh	3.07 mAh	1.86 mAh	88.0%	69.0%	41.6%	-	42.2%	11.2%	1.2C
L3S	4.02 mAh	3.43 mAh	2.53 mAh	89.9%	76.9%	56.9%	-	68.0%	23.5%	1.7C
L4U	4.61 mAh	2.46 mAh	1.06 mAh	77.9%	41.7%	18.0%	64.3%	14.7%	6.1%	0.7C
L4S	4.80 mAh	3.03 mAh	1.35 mAh	81.7%	51.5%	23.0%	79.8%	23.8%	7.6%	0.9C

[I]CC charging from 2.7 V to a cutoff voltage of 4.2 V.
[II]referenced to the nominal capacities determined by the corresponding loading in Table I.
[III]ΔSOC when Li-plating is provoked, determined by $\Phi_s - \Phi_l$ at anode/separator interface.
[IV]maximum charging C-rate without Li-plating.

reduced lithium-ion concentration gradients and lower overpotentials that counteract lithium-plating. The simulation study just provides a hint for possible lithium-plating and the effects of the electrode pore morphology modification on charging procedures.

In the simulation in Fig. 7a during the 1C charge of both L3U and L3S, almost 90% of the cell capacity can be charged, the benefit of the structuring is marginal. In the cell voltage there is no option to assess the anode potential and it looks like the structured anodes just give a small benefit in the charged capacity in the end. For a 2C charge however, the reduction in overpotentials can be clearly seen in Fig. 7b, where the potential drop for the structured anodes lies well above the the one for unstructured anodes. After 12 min of charging, the unstructured anode reaches a potential that could invoke lithium-plating, while the structured anode reaches the critical potential only shortly before the end of charge (compare SOC in Table III). This effect is even more pronounced for a 3C charge, where both potential curves lie well below 0 V shortly after applying the charging current. This is a clear indication of possible lithium-plating and the charging current is too high for this cell setup. Regarding the charged capacity for a 3C charging rate, the cells comprising structured anodes reach a 15% higher SOC until the cutoff voltage is exceeded. So not only for discharging, but also for charging procedures the modified electrode pore morphology shows distinct advantages in an overpotential reduction.

An assessment of the other three loadings, as listed in Table III, reveals that for loading L1 with an electrode thickness of 71 μm the structuring shows little benefits regarding the charged capacity. Just at the end of a 3C charge, the potential drop of L1S is a little less and the lithium-plating criterion is not fulfilled. For loading L2 with thicker electrodes, more capacity can be charged and the advantages of structured anodes increase. Especially for a 3C charge, with structured anodes there is almost no lithium-plating provoked compared to the unstructured ones. A comparison of the charged capacities of loading L4 and Fig. 3b reveals, that there is also a range for charging currents with a maximum benefit. The 1C charge adds 3.3% in capacity, the 2C charge 9.8% and the 3C charge 5.0%. At lower charging currents, the concentration gradients are reduced and the pore morphology change has little or no influence. With increasing charging currents, a maximum benefit arises and diminishes again when other limitations come into place. However, for the thick electrodes in the case of L4 (116 μm), all three charging currents would possibly provoke lithium-plating and the current should be reduced for both the cells with unstructured and structured anodes. Just the amount of plated lithium could be less with structured anodes.

In order to assess the maximum charging C-rate for each loading, a simulation study with incremental C-rates with a step size of 0.1C was carried out. The results are listed in the last column in Table III. In each case, the potential difference $\Phi_s - \Phi_l$ at the anode/separator interface would stay slightly above 0 V at the end of charge. The cells comprising structured anodes can withstand higher C-rates for all loadings. With increasing electrode thickness, the maximum charging C-rate has to be reduced. The C-rates are derived from the modeled areal capacities in Table I, a conversion of the C-rates to current densities, due to the changed loading, leads to the same trend. Based on the charged capacities with the maximum C-rate of the cells with unstructured anodes, the C-rates with structured anodes that lead to the same charged capacity can be calculated. The simulated pore morphology modification would allow higher charging currents so that the charged capacity stays the same in the end for the cells comprising unstructured and structured anodes of each loading. This leads to a reduced charging time of around 10% for loadings L1 and L2, 17% for L3 and 13% for L4, respectively. On top of the shorter charging time, the distance to the lithium-plating threshold is higher for the structured anodes and thereby the cell safety enhanced.

Conclusions

An electrochemical model was developed and validated against experimental data gained from lithium-ion cells comprising unstructured and structured graphite anodes. The areal capacities of the cells were varied by changing the electrode thickness, the electrode composition and the porosity remained constant within the manufacturing tolerances. The simulation results are well in line with the discharge rate capability measurements.

The loading of the cell, defined by the electrode thickness, determines the C-rates where the structuring process provides a benefit in capacity retention, which was around 10–18% for the measured cells. The location and shape of this benefit is given by the electrode thickness and the tortuosity reduction. With increasing electrode thickness, the maximum benefit shifts to lower C-rates (and vice versa) and the tortuosity reduction specifies the maximum itself, i.e. a lower tortuosity yields a higher rate capability.

In order to understand the limiting mechanisms, an overpotential analysis was conducted that revealed the anode as a major contributor. Especially the diffusion polarization in the electrolyte limits the performance for medium C-rates. Through modification of the pore morphology, a reduction in the anode tortuosity can be achieved, which results in a reduction of concentration gradients and the accompanying overpotentials and more capacity can be discharged from the cell.

A fast charging scenario for the different loadings revealed that the reduced overpotentials through electrode structuring provide an approach for preventing lithium-plating at the anode. In the fast charging simulation studies, a reduction of the charging time of 10–17% was achieved while keeping the anode potential in a safe area above the lithium-plating threshold.

In this work, laser-structuring was used to modify the electrode pore morphology of graphite anodes and the generated effects were investigated. In conclusion, the tortuosity should be well considered regarding electrode and cell design and simulation studies can support the overall process. Future work will focus on the optimization of the electrode structure, defined by the geometrical dimensions of the induced holes and the amount of structures, i.e. the structure pattern. Tortuosity measurements are necessary in order to identify the change in electrode pore morphology generated by the structuring process. Furthermore, simulations could be used to provide a guideline for an optimal structure for a given set of electrodes, adjusted to the desired performance improvement within the physical bounds of tortuosity reduction.

Acknowledgment

This work was financially supported by the German Federal Ministry of Education and Research (BMBF) under grant number 03XP0081 (ExZellTUM II). The authors thank Johannes Sturm for his critical feedback.

Appendix

The comparison of the measured and simulated discharge voltage curves for all loadings comprising unstructured and structured anodes is displayed in Fig. A1. The representative voltage curves for the discharge C-rates of C/5, 2C, 5C and 10C were selected for validation.

An overview of the most relevant model parameters is shown in Table AI. The electrolyte diffusivity D_l and conductivity κ were taken from Mao et al.[76] However, Mao et al. used a polynomial fitting function for the electrolyte conductivity which is only valid for concentrations below 3000 mol m^{-3}. At higher concentration levels, the conductivity starts to increase, so a correction for extrapolation at highly saturated electrolytes from Rheinfeld et al.[71] was used instead. The electrolyte activity dependence was extracted from Valøen and Reimers.[77] All three functions describing the electrolyte expect the concentration to be in mol m^{-3}.

The differential algebraic equations of the p2D model are listed in Table AII. In order to prevent local lithium-ion concentrations from becoming zero or even negative and thus cause instability, a modification of the Butler-Volmer equation introduced by Mao et al.[76] was implemented.

The equations for calculating the polarization of the different sub-processes are stated in Table AIII. The total current per cross-sectional area i_{tot} is calculated via an integration

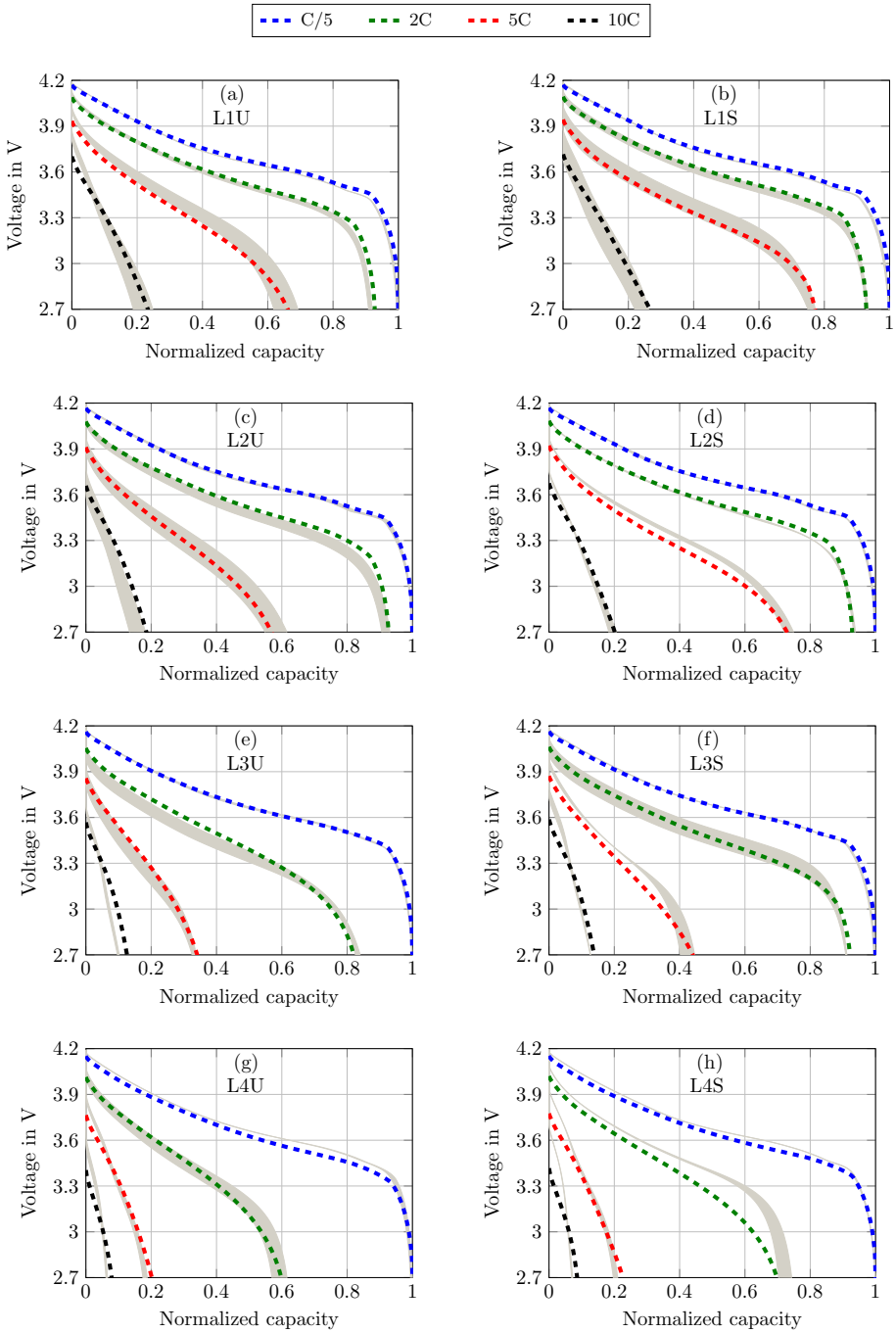

Figure A1. Comparison of measured (gray shaded areas) and simulated discharge voltage curves, normalized to their C/5 capacity for C-rates C/5, 2C, 5C and 10C. The cells comprising unstructured anodes are depicted in (a), (c), (e) and (g) for loadings L1U, L2U, L3U and L4U and the cells comprising structured anodes are depicted in (b), (d), (f) and (h) for loadings L1S, L2S, L3S and L4S, respectively.

of the local current density on the particle surface i_{loc} – as given by the Butler-Volmer equation – multiplied with the specific interfacial area a (ratio of active material surface to volume)

$$i_{tot} = \int_{x_1}^{x_2} a i_{loc} dx \qquad [A1]$$

In order to calculate the average cell polarization, the integration boundaries x_1 and x_2 are chosen to 0 and $L = l_{neg} + l_{sep} + l_{pos}$, respectively. Polarization based on spatial integral values refers to the relevant domains of anode, separator and cathode and the corresponding boundary values in the x-dimension. For a profound explanation of the method and the set of equations, the reader is referred to the original publication of Nyman et al.[22]

Table AI. Model parameters used within this work; numeric values and magnitudes of parameters chosen in this study were referenced to literature where applicable.

Parameter	Anode	Separator	Cathode
Geometry			
Thickness l	Table I	200 µm[41]	Table I
Particle radius r_p	5 µm [I]		5.5 µm [I]
Solid phase fraction ε_s	0.53 [II]		0.5 [II]
Liquid phase fraction ε_l	0.35 [m]	0.7 [e]	0.35 [m]
Tortuosity τ	Table I	1.2 [e]	1.8[55]
Thermodynamics			
Equilibrium voltage E_{eq}	Ref. 31		Ref. 31
Maximum lithium concentration $c_{s,max}$	32000 mol m^{-3}[73]		50000 mol m^{-3}[73]
Lithiation at 100% SOC $\frac{c_{s,100}}{c_{s,max}}$	0.71 [e]		0.43 [e]
Lithiation at 0% SOC $\frac{c_{s,0}}{c_{s,max}}$	0.003 [e]		0.91 [e]
Kinetics			
Anodic reaction rate k_a	6×10^{-11} m s^{-1} [e]		6×10^{-11} m s^{-1} [e]
Cathodic reaction rate k_c	6×10^{-11} m s^{-1} [e]		6×10^{-11} m s^{-1} [e]
Anodic charge-transfer coefficient α_a	0.5[67]		0.5[67]
Cathodic charge-transfer coefficient α_c	0.5[67]		0.5[67]
Transport			
Solid diffusivity D_s	1×10^{-14} m^2 s^{-1}[76]		1.8×10^{-13} m^2 s^{-1}[73]
Solid conductivity σ	100 S m^{-1}[68]		10 S m^{-1}[68]

Parameter	Electrolyte
Electrolyte diffusivity D_l	$5.34 \times 10^{-10} \exp\left(-0.65 \frac{c_l}{1000}\right) \exp\left(2000 \frac{T-298}{298T}\right)$[76] in m^2 s^{-1}
Electrolyte conductivity κ	$729.9912 \exp\left(\frac{-1690}{T}\right) \left(\frac{c_l}{2050}\right)^{0.75} \exp\left(-\left(\frac{cl}{2050}\right)^{1.75}\right)$[71] in S m^{-1}
Activity dependence $\frac{\partial \ln f_\pm}{\partial \ln c_l}$	$\frac{0.601-0.24(c_l/1000)^{0.5}+0.982(c_l/1000)^{1.5}(1-0.0052(T-294))}{1-t_+} - 1$[77]
Transport number t_+	0.38[77]

Parameter	Global
Temperature T	298.15 K [m]
Ohmic contact resistance $R_{contact}$	9.75×10^{-4} Ωm^2 [e]

m measured value, *e* estimated value.
[I] derived from D50 mass-median-diameter from datasheet.
[II] derived from weight ratio of electrode composition.

Table AII. Differential algebraic equations of the p2D model according to Doyle, Fuller and Newman[46] including an adaption for the Butler-Volmer equation from Mao et al.[76]

Type	Equations
Mass balance	$\varepsilon_l \frac{\partial c_l}{\partial t} = \frac{\partial}{\partial x}\left(D_{l,eff} \frac{\partial c_l}{\partial x} + \frac{i_l (1-t_+)}{F}\right)$
	$\varepsilon_s \frac{\partial c_s}{\partial t} = \frac{1}{r^2} \frac{\partial}{\partial r}\left(D_s r^2 \frac{\partial c_s}{\partial r}\right)$
Potentials	$\frac{\partial \Phi_l}{\partial x} = -\frac{i_l}{\kappa_{eff}} + \frac{2RT}{F}(1-t_+)\left(1 + \frac{d\, ln f_\pm}{d\, ln c_l}\right) \frac{\partial\, ln c_l}{\partial x}$
	$\frac{\partial \Phi_s}{\partial x} = -\frac{i_{app}-i_l}{\sigma_s}$ with $i_{app} = i_s + i_l \quad \forall x, t$
Charge balance	$\frac{\partial i_l}{\partial x} + \frac{\partial i_s}{\partial x} = 0$ with $\frac{\partial i_s}{\partial x} = -\frac{3\varepsilon_s}{r_p} F j_n$
Electrode kinetics	$j_n = \frac{i_0}{F} \frac{\exp\left(\frac{\alpha_a F \eta}{RT}\right) - \exp\left(-\frac{\alpha_c F \eta}{RT}\right)}{1 + \frac{1\text{mol m}^{-3}}{c_l} \exp\left(-\frac{\alpha_c F \eta}{RT}\right)}$
	$\eta = \Phi_s - \Phi_l - E_{eq}$
	$i_0 = F\, k_c^{\alpha_a} k_a^{\alpha_c} \left(c_{s,max} - c_{s,surf}\right)^{\alpha_a} \left(c_{s,surf}\right)^{\alpha_c} \left(\frac{c_l}{1\text{mol m}^{-3}}\right)^{\alpha_a}$

Table AIII. Polarization analysis by Nyman et al.[22]

Polarization source	Equation
Diffusion polarization liquid phase	$\frac{1}{i_{tot}} \int_{x_1}^{x_2} \frac{2RT}{c_l F}(1 + \frac{\partial \ln f_\pm}{\partial \ln c_l})(1-t_+) \frac{\partial c_l}{\partial x} i_l dx$
Diffusion polarization solid phase	$\frac{1}{i_{tot}} \int_{x_1}^{x_2} a i_{loc}(E_{eq,surf} - E_{eq,ave}) dx$
Ohmic potential drop liquid phase	$\frac{1}{i_{tot}} \int_{x_1}^{x_2} \frac{i_l^2}{\kappa_{eff}} dx$
Ohmic potential drop solid phase	$\frac{1}{i_{tot}} \int_{x_1}^{x_2} \frac{i_s^2}{\sigma_{eff}} dx$
Activation overpotential	$\frac{1}{i_{tot}} \int_{x_1}^{x_2} a i_{loc}(\Phi_s - \Phi_l - E_{eq,surf}) dx$
Contact resistance	$i_{app} \cdot R_{contact}$

List of symbols

Symbol	Description	Unit
a	Specific interfacial area	m^{-1}
c	Concentration	mol m^{-3}
D	Diffusion coefficient	m^2 s^{-1}
E_{eq}	Equilibrium potential	V
F	Faraday constant	96 485 As mol^{-1}
$f_{\pm}$	Activity coefficient	-
i	Current density	A m^{-2}
j_n	Pore-wall flux	A $m^{-2}s^{-1}$
l	Thickness	m
N_l	Ion flux density	mol $m^{-2}s^{-1}$
N_M	MacMullin number	-
r_p	Particle radius	m
r	r-coordinate in p2D model	m
R	Universal gas constant	8.314 J mol^{-1} K^{-1}
$R_{contact}$	Contact resistance	Ω m^2
R_l	Reaction term	mol $m^{-3}s^{-1}$
t	Time	s
t_+	Transport number	-
T	Temperature	K
x	x-coordinate in p2D model	m
	Greek	
α_{Brugg}	Bruggeman correction term	-
ε	Volume fraction	-
κ	Electrolyte conductivity	S m^{-1}
τ	Tortuosity	-
σ	Solid phase conductivity	S m^{-1}
Φ	Electrical potential	V
Ψ	Transport property in porous media	-
	Subscripts	
a	anodic reaction (oxidation)	
app	applied	
ave	average	
c	cathodic reaction (reduction)	
eff	effective (transport parameter correction)	
l	liquid phase/electrolyte	
loc	local	
max	maximum	
neg	negative electrode/anode	
pos	positive electrode/cathode	
s	solid phase/active material	
sep	separator	
$surf$	surface	
tot	total	

ORCID

Ludwig Kraft https://orcid.org/0000-0003-4324-426X
Jan B. Habedank https://orcid.org/0000-0003-2057-7037
Alexander Frank https://orcid.org/0000-0001-8069-2948
Alexander Rheinfeld https://orcid.org/0000-0003-0995-7266
Andreas Jossen https://orcid.org/0000-0003-0964-1405

References

1. M. A. Hannan, M. M. Hoque, A. Mohamed, and A. Ayob, Review of energy storage systems for electric vehicle applications: Issues and challenges, *Renewable and Sustainable Energy Reviews*, **69**, 771 (2017).
2. O. Gröger, H. A. Gasteiger, and J.-P. Suchsland, Review—Electromobility: Batteries or Fuel Cells? *Journal of the Electrochemical Society*, **162**, A2605 (2015).
3. D. Andre, S.-J. Kim, P. Lamp, S. F. Lux, F. Maglia, O. Paschos, and B. Stiaszny, Future generations of cathode materials: An automotive industry perspective, *Journal of Materials Chemistry A*, **3**, 6709 (2015).
4. K. Kerman, A. Luntz, V. Viswanathan, Y.-M. Chiang, and Z. Chen, Review—Practical Challenges Hindering the Development of Solid State Li Ion Batteries, *Journal of The Electrochemical Society*, **164**, A1731 (2017).
5. Y. Wu, W. Wang, J. Ming, M. Li, L. Xie, X. He, J. Wang, S. Liang, and Y. Wu, An Exploration of New Energy Storage System: High Energy Density, High Safety, and Fast Charging Lithium Ion Battery, *Advanced Functional Materials*, **29**, 1805978 (2019).
6. J. Sturm, A. Rheinfeld, I. Zilberman, F. B. Spingler, S. Kosch, F. Frie, and A. Jossen, Modeling and simulation of inhomogeneities in a 18650 nickel-rich, silicon-graphite lithium-ion cell during fast charging, *Journal of Power Sources*, **412**, 204 (2019).
7. S. Goriparti, E. Miele, F. de Angelis, E. Di Fabrizio, R. Proietti Zaccaria, and C. Capiglia, Review on recent progress of nanostructured anode materials for Li-ion batteries, *Journal of Power Sources*, **257**, 421 (2014).
8. M. Osiak, H. Geaney, E. Armstrong, and C. O'Dwyer, Structuring materials for lithium-ion batteries: Advancements in nanomaterial structure, composition, and defined assembly on cell performance, *Journal of Materials Chemistry A*, **2**, 9433 (2014).
9. A. M. Dreizler, N. Bohn, H. Geßwein, M. Müller, J. R. Binder, N. Wagner, and K. A. Friedrich, Investigation of the Influence of Nanostructured LiNi 0.33 Co 0.33 Mn 0.33 O 2 Lithium-Ion Battery Electrodes on Performance and Aging, *Journal of The Electrochemical Society*, **165**, A273 (2018).
10. R. A. Adams, A. N. Mistry, P. P. Mukherjee, and V. G. Pol, Materials by Design: Tailored Morphology and Structures of Carbon Anodes for Enhanced Battery Safety, *ACS applied materials & interfaces*, **11**, 13334 (2019).
11. G. Liu, H. Zheng, X. Song, and V. S. Battaglia, Particles and Polymer Binder Interaction: A Controlling Factor in Lithium-Ion Electrode Performance, *Journal of The Electrochemical Society*, **159**, A214 (2012).
12. H. Zheng, J. Li, X. Song, G. Liu, and V. S. Battaglia, A comprehensive understanding of electrode thickness effects on the electrochemical performances of Li-ion battery cathodes, *Electrochimica Acta*, **71**, 258 (2012).
13. W. Pfleging, A review of laser electrode processing for development and manufacturing of lithium-ion batteries, *Nanophotonics*, **7**, 549 (2018).
14. R. Morasch, J. Landesfeind, B. Suthar, and H. A. Gasteiger, Detection of Binder Gradients Using Impedance Spectroscopy and Their Influence on the Tortuosity of Li-Ion Battery Graphite Electrodes, *Journal of The Electrochemical Society*, **165**, A3459 (2018).
15. B. L. Trembacki, A. N. Mistry, D. R. Noble, M. E. Ferraro, P. P. Mukherjee, and S. A. Roberts, Editors' Choice—Mesoscale Analysis of Conductive Binder Domain Morphology in Lithium-Ion Battery Electrodes, *Journal of The Electrochemical Society*, **165**, E725 (2018).
16. A. N. Mistry, K. Smith, and P. P. Mukherjee, Secondary-Phase Stochastics in Lithium-Ion Battery Electrodes, *ACS applied materials & interfaces*, **10**, 6317 (2018).
17. S. Malifarge, B. Delobel, and C. Delacourt, Determination of Tortuosity Using Impedance Spectra Analysis of Symmetric Cell, *Journal of The Electrochemical Society*, **164**, E3329 (2017).
18. M. Singh, J. Kaiser, and H. Hahn, Thick Electrodes for High Energy Lithium Ion Batteries, *Journal of the Electrochemical Society*, **162**, A1196 (2015).
19. T. Danner, M. Singh, S. Hein, J. Kaiser, H. Hahn, and A. Latz, Thick electrodes for Li-ion batteries: A model based analysis, *Journal of Power Sources*, **334**, 191 (2016).
20. N. Dufour, M. Chandesris, S. Geniès, M. Cugnet, and Y. Bultel, Lithiation heterogeneities of graphite according to C-rate and mass-loading: A model study, *Electrochimica Acta*, **272**, 97 (2018).
21. S. Malifarge, B. Delobel, and C. Delacourt, Experimental and Modeling Analysis of Graphite Electrodes with Various Thicknesses and Porosities for High-Energy-Density Li-Ion Batteries, *Journal of The Electrochemical Society*, **165**, A1275 (2018).
22. A. Nyman, T. G. Zavalis, R. Elger, M. Behm, and G. Lindbergh, Analysis of the Polarization in a Li-Ion Battery Cell by Numerical Simulations, *Journal of The Electrochemical Society*, **157**, A1236 (2010).
23. K. G. Gallagher, S. E. Trask, C. Bauer, T. Woehrle, S. F. Lux, M. Tschech, P. Lamp, B. J. Polzin, S. Ha, B. Long, Q. Wu, W. Lu, D. W. Dees, and A. N. Jansen, Optimizing Areal Capacities through Understanding the Limitations of Lithium-Ion Electrodes, *Journal of The Electrochemical Society*, **163**, A138 (2015).
24. F. L. E. Usseglio-Viretta, A. Colclasure, A. N. Mistry, K. P. Y. Claver, F. Pouraghajan, D. P. Finegan, T. M. M. Heenan, D. Abraham, P. P. Mukherjee, D. Wheeler, P. Shearing, S. J. Cooper, and K. Smith, Resolving the Discrepancy in Tortuosity Factor Estimation for Li-Ion Battery Electrodes through Micro-Macro Modeling and Experiment, *Journal of The Electrochemical Society*, **165**, A3403 (2018).
25. A. N. Mistry and P. P. Mukherjee, Probing spatial coupling of resistive modes in porous intercalation electrodes through impedance spectroscopy, *Physical chemistry chemical physics : PCCP*, **21**, 3805 (2019).
26. S. Ferrari, M. Loveridge, S. D. Beattie, M. Jahn, R. J. Dashwood, and R. Bhagat, Latest advances in the manufacturing of 3D rechargeable lithium microbatteries, *Journal of Power Sources*, **286**, 25 (2015).
27. E. R. Reale and K. C. Smith, Capacitive Performance and Tortuosity of Activated Carbon Electrodes with Macroscopic Pores, *Journal of The Electrochemical Society*, **165**, A1685 (2018).
28. J. Li, X. Liang, R. Panat, and J. Park, Enhanced Battery Performance through Three-Dimensional Structured Electrodes: Experimental and Modeling Study, *Journal of The Electrochemical Society*, **165**, A3566 (2018).
29. J. Landesfeind, A. Ehrl, M. Graf, W. A. Wall, and H. A. Gasteiger, Direct Electrochemical Determination of Thermodynamic Factors in Aprotic Binary Electrolytes, *Journal of The Electrochemical Society*, **163**, A1254 (2016).
30. V. P. Nemani, S. J. Harris, and K. C. Smith, Design of Bi-Tortuous, Anisotropic Graphite Anodes for Fast Ion-Transport in Li-Ion Batteries, *Journal of The Electrochemical Society*, **162**, A1415 (2015).
31. J. B. Habedank, J. Endres, P. Schmitz, M. F. Zaeh, and H. P. Huber, Femtosecond laser structuring of graphite anodes for improved lithium-ion batteries: Ablation characteristics and process design, *Journal of Laser Applications*, **30**, 032205 (2018).
32. Q. Cheng and Y. Zhang, Multi-Channel Graphite for High-Rate Lithium Ion Battery, *Journal of The Electrochemical Society*, **165**, A1104 (2018).
33. C. L. Cobb and M. Blanco, Modeling mass and density distribution effects on the performance of co-extruded electrodes for high energy density lithium-ion batteries, *Journal of Power Sources*, **249**, 357 (2014).

34. J. Pröll, H. Kim, A. Piqué, H. J. Seifert, and W. Pfleging, Laser-printing and femtosecond-laser structuring of $LiMn_2O_4$ composite cathodes for Li-ion microbatteries, *Journal of Power Sources*, **255**, 116 (2014).
35. C. L. Cobb and S. E. Solberg, Communication—Analysis of Thick Co-Extruded Cathodes for Higher-Energy-and-Power Lithium-Ion Batteries, *Journal of The Electrochemical Society*, **164**, A1339 (2017).
36. B. Delattre, R. Amin, J. Sander, J. de Coninck, A. P. Tomsia, and Y.-M. Chiang, Impact of Pore Tortuosity on Electrode Kinetics in Lithium Battery Electrodes: Study in Directionally Freeze-Cast $LiNi_{0.8}Co_{0.15}A_{l0.05}O_2$ (NCA), *Journal of the Electrochemical Society*, **165**, A388 (2018).
37. T. Tsuda, N. Ando, S. Nakamura, Y. Ishihara, N. Hayashi, N. Soma, T. Gunji, T. Tanabe, T. Ohsaka, and F. Matsumoto, Improvement of high-rate discharging performance of $LiFePO_4$ cathodes by forming micrometer-sized through-holed electrode structures with a pico-second pulsed laser, *Electrochimica Acta*, **296**, 27 (2019).
38. J. B. Habedank, F. J. Günter, N. Billot, R. Gilles, T. Neuwirth, G. Reinhart, and M. F. Zaeh, Rapid electrolyte wetting of lithium-ion batteries containing laser structured electrodes: in situ visualization by neutron radiography, *The International Journal of Advanced Manufacturing Technology*, **102**, 2769 (2019).
39. J. B. Habedank, L. Kraft, A. Rheinfeld, C. Krezdorn, A. Jossen, and M. F. Zaeh, Increasing the Discharge Rate Capability of Lithium-Ion Cells with Laser-Structured Graphite Anodes: Modeling and Simulation, *Journal of The Electrochemical Society*, **165**, A1563 (2018).
40. A. M. Colclasure, A. R. Dunlop, S. E. Trask, B. J. Polzin, A. N. Jansen, and K. Smith, Requirements for Enabling Extreme Fast Charging of High Energy Density Li-Ion Cells while Avoiding Lithium Plating, *Journal of the Electrochemical Society*, **166**, A1412 (2019).
41. J. Landesfeind, D. Pritzl, and H. A. Gasteiger, An Analysis Protocol for Three-Electrode Li-Ion Battery Impedance Spectra: Part I. Analysis of a High-Voltage Positive Electrode, *Journal of the Electrochemical Society*, **164**, A1773 (2017).
42. J. Landesfeind, J. Hattendorff, A. Ehrl, W. A. Wall, and H. A. Gasteiger, Tortuosity Determination of Battery Electrodes and Separators by Impedance Spectroscopy, *Journal of The Electrochemical Society*, **163**, A1373 (2016).
43. F. M. Kindermann, P. J. Osswald, S. Klink, G. Ehlert, J. Schuster, A. Noel, S. V. Erhard, W. Schuhmann, and A. Jossen, Measurements of lithium-ion concentration equilibration processes inside graphite electrodes, *Journal of Power Sources*, **342**, 638 (2017).
44. T. Teufl, D. Pritzl, S. Solchenbach, H. A. Gasteiger, and M. A. Mendez, State of Charge Dependent Resistance Build-Up in Li- and Mn-Rich Layered Oxides during Lithium Extraction and Insertion, *Journal of the Electrochemical Society*, **166**, A1275 (2019).
45. A. Rheinfeld, S. Kosch, S. V. Erhard, P. J. Osswald, B. Rieger, and A. Jossen, Electro-Thermal Modeling of Large Format Lithium-Ion Pouch Cells: A Cell Temperature Dependent Linear Polarization Expression, *Journal of the Electrochemical Society*, **163**, A3046 (2016).
46. M. Doyle, T. F. Fuller, and J. Newman, Modeling of Galvanostatic Charge and Discharge of the Lithium/Polymer/Insertion Cell, *Journal of the Electrochemical Society*, **140**, 1526 (1993).
47. T. F. Fuller, M. Doyle, and J. Newman, Simulation and Optimization of the Dual Lithium Ion Insertion Cell, *Journal of the Electrochemical Society*, **141**, 1 (1994).
48. X. Lin, J. Park, L. Liu, Y. Lee, A. M. Sastry, and W. Lu, A Comprehensive Capacity Fade Model and Analysis for Li-Ion Batteries, *Journal of the Electrochemical Society*, **160**, 1701 (2013).
49. R. Fu, S.-Y. Choe, V. Agubra, and J. Fergus, Development of a physics-based degradation model for lithium ion polymer batteries considering side reactions, *Journal of Power Sources*, **278**, 506 (2015).
50. L. Xia, E. Najafi, Z. Li, H. J. Bergveld, and M. Donkers, A computationally efficient implementation of a full and reduced-order electrochemistry-based model for Li-ion batteries, *Applied Energy*, **208**, 1285 (2017).
51. W. A. Appiah, J. Park, S. Byun, I. Cho, A. Mozer, M.-H. Ryou, and Y. M. Lee, A coupled chemo-mechanical model to study the effects of adhesive strength on the electrochemical performance of silicon electrodes for advanced lithium ion batteries, *Journal of Power Sources*, **407**, 153 (2018).
52. D. Ren, K. Smith, D. Guo, X. Han, X. Feng, L. Lu, M. Ouyang, and J. Li, Investigation of Lithium Plating-Stripping Process in Li-Ion Batteries at Low Temperature Using an Electrochemical Model, *Journal of The Electrochemical Society*, **165**, A2167 (2018).
53. D. A. G. Bruggeman, Berechnung verschiedener physikalischer Konstanten von heterogenen Substanzen. I. Dielektrizitätskonstanten und Leitfähigkeiten der Mischkörper aus isotropen Substanzen, *Annalen der Physik*, **416**, 636 (1935).
54. I. V. Thorat, D. E. Stephenson, N. A. Zacharias, K. Zaghib, J. N. Harb, and D. R. Wheeler, Quantifying tortuosity in porous Li-ion battery materials, *Journal of Power Sources*, **188**, 592 (2009).
55. M. Ebner, D.-W. Chung, R. E. García, and V. Wood, Tortuosity Anisotropy in Lithium-Ion Battery Electrodes, *Advanced Energy Materials*, **4**, 1 (2014).
56. R. B. MacMullin and G. A. Muccini, Characteristics of porous beds and structures, *AIChE Journal*, **2**, 393 (1956).
57. B. Suthar, J. Landesfeind, A. Eldiven, and H. A. Gasteiger, Method to Determine the In-Plane Tortuosity of Porous Electrodes, *Journal of The Electrochemical Society*, **165**, A2008 (2018).
58. J. Landesfeind, M. Ebner, A. Eldiven, V. Wood, and H. A. Gasteiger, Tortuosity of Battery Electrodes: Validation of Impedance-Derived Values and Critical Comparison with 3D Tomography, *Journal of the Electrochemical Society*, **165**, A469 (2018).
59. Z. Li, J. Huang, B. Yann Liaw, V. Metzler, and J. Zhang, A review of lithium deposition in lithium-ion and lithium metal secondary batteries, *Journal of Power Sources*, **254**, 168 (2014).
60. V. Zinth, C. von Lüders, M. Hofmann, J. Hattendorff, I. Buchberger, S. Erhard, J. Rebelo-Kornmeier, A. Jossen, and R. Gilles, Lithium plating in lithium-ion batteries at sub-ambient temperatures investigated by in situ neutron diffraction, *Journal of Power Sources*, **271**, 152 (2014).
61. C. von Lüders, V. Zinth, S. V. Erhard, P. J. Osswald, M. Hofmann, R. Gilles, and A. Jossen, Lithium plating in lithium-ion batteries investigated by voltage relaxation and in situ neutron diffraction, *Journal of Power Sources*, **342**, 17 (2017).
62. R. Zhu, J. Feng, and Z. Guo, In Situ Observation of Dendrite Behavior of Electrode in Half and Full Cells, *Journal of the Electrochemical Society*, **166**, A1107 (2019).
63. S. Hein and A. Latz, Influence of local lithium metal deposition in 3D microstructures on local and global behavior of Lithium-ion batteries, *Electrochimica Acta*, **201**, 354 (2016).
64. A. N. Mistry, K. Smith, and P. P. Mukherjee, Electrochemistry Coupled Mesoscale Complexations in Electrodes Lead to Thermo-Electrochemical Extremes, *ACS applied materials & interfaces*, **10**, 28644 (2018).
65. C. von Lüders, J. Keil, M. Webersberger, and A. Jossen, Modeling of lithium plating and lithium stripping in lithium-ion batteries, *Journal of Power Sources*, **414**, 41 (2019).
66. M. Doyle and J. Newman, Comparison of Modeling Predictions with Experimental Data from Plastic Lithium Ion Cells, *Journal of the Electrochemical Society*, **143**, 1890 (1996).
67. M. Doyle and Y. Fuentes, Computer Simulations of a Lithium-Ion Polymer Battery and Implications for Higher Capacity Next-Generation Battery Designs, *Journal of The Electrochemical Society*, **150**, A706 (2003).
68. K. Smith and C.-Y. Wang, Power and thermal characterization of a lithium-ion battery pack for hybrid-electric vehicles, *Journal of Power Sources*, **160**, 662 (2006).
69. S. G. Stewart, V. Srinivasan, and J. Newman, Modeling the Performance of Lithium-Ion Batteries and Capacitors during Hybrid-Electric-Vehicle Operation, *Journal of the Electrochemical Society*, **155**, A664 (2008).
70. M. Park, X. Zhang, M. Chung, G. B. Less, and A. M. Sastry, A review of conduction phenomena in Li-ion batteries, *Journal of Power Sources*, **195**, 7904 (2010).
71. A. Rheinfeld, J. Sturm, A. Noel, J. Wilhelm, A. Kriston, A. Pfrang, and A. Jossen, Quasi-Isothermal External Short Circuit Tests Applied to Lithium-Ion Cells: Part II. Modeling and Simulation, *Journal of the Electrochemical Society*, **166**, A151 (2019).
72. M. Safari and C. Delacourt, Modeling of a Commercial Graphite/LiFePO4 Cell, *Journal of the Electrochemical Society*, **158**, A562 (2011).
73. S. Tippmann, D. Walper, L. Balboa, B. Spier, and W. G. Bessler, Low-temperature charging of lithium-ion cells part I: Electrochemical modeling and experimental investigation of degradation behavior, *Journal of Power Sources*, **252**, 305 (2014).
74. S. V. Erhard et al., Simulation and Measurement of the Current Density Distribution in Lithium-Ion Batteries by a Multi-Tab Cell Approach, *Journal of The Electrochemical Society*, **164**, A6324 (2017).
75. N. Lin, X. Xie, R. Schenkendorf, and U. Krewer, Efficient Global Sensitivity Analysis of 3D Multiphysics Model for Li-Ion Batteries, *Journal of The Electrochemical Society*, **165**, A1169 (2018).
76. J. Mao, W. Tiedemann, and J. Newman, Simulation of temperature rise in Li-ion cells at very high currents, *Journal of Power Sources*, **271**, 444 (2014).
77. L. O. Valøen and J. N. Reimers, Transport Properties of LiPF6-Based Li-Ion Battery Electrolytes, *Journal of the Electrochemical Society*, **152**, A882 (2005).

5 Conclusion and Outlook

The worldwide demand for applications, especially EVs, that rely on an adequate electrical energy storage system is rapidly growing. Thereby, LIBs with a liquid electrolyte pose the predominant technology for mobile but likewise for stationary energy storage systems today and in the mid-term future. This creates the necessity for further improvements on state-of-the-art LIBs in order to fulfill the demanding requirements with regard to the available energy density and power capability of LIBs. Designing LIBs for EVs is particularly challenging, as a high energy density is needed to reach customer-satisfactory driving ranges, and a high power capability is needed to enable fast charging procedures. This tradeoff between energy and power must be considered in the cell design process, while simultaneously neither the safety nor the lifespan of the battery should be compromised.

Within the scope of this thesis, performance enhancements of LIBs via new active materials as well as an improved electrode and cell design were investigated. The characteristics of a LIB are mainly influenced by the choice of active materials. The capacity of a LIB can be enhanced by anode and cathode active materials with a higher specific capacity. The specific capacities of both active materials, in addition to their corresponding voltage levels, determine the maximum energy density that can be reached. Active material properties such as the electronic conductivity, the ionic diffusivity, and the reaction kinetics for de-/intercalation define the intrinsic power capability. Despite these intrinsic active material properties, the overall cell performance can as well be adjusted via the electrode and cell design. The addition of conductive additives and higher electrode porosities increase the power capability for instance, but concurrently reduce the energy density. The development of specific cell components towards optimized cell characteristics should therefore always be critically assessed.

Prevalent state-of-the-art LIBs are often comprised of a nickel-rich CAM such as NCA or NCM-811 with a specific capacity of about $200\,\mathrm{mAh\,g^{-1}}$. The most common anode active material is graphite with a practical specific capacity of about $360\,\mathrm{mAh\,g^{-1}}$, which can be boosted by the addition of silicon. Such Si-C anodes are already used in commercially available LIBs. A promising not yet commercialized CAM that offers a higher specific capacity of around $250\,\mathrm{mAh\,g^{-1}}$ is lithium- and manganese-rich NCM, also referred to as LMR-NCM. Based on the material stoichiometry, LMR-NCMs are more cost-effective because of their high manganese share in comparison to nickel-rich CAMs, as the price of the commodity manganese is an order of magnitude lower than that of nickel.

In order to thoroughly evaluate the characteristics of cells containing LMR-NCM, the material was employed in multilayer pouch cells together with graphite anodes and compared to similar NCA/graphite pouch cells. Both pouch cell types were designed to reach a capacity of 5.5 Ah at a 1C discharge rate. The energy density and the power capability of the pouch cells were investigated in a discharge rate capability test, and their long-term stability was assessed in an aging study. Distinct differences between the two cell types were the wider voltage window of 2.0–4.6 V of the LMR-NCM/graphite cells as well as the voltage hysteresis between charge and discharge even at low currents, while the NCA/graphite cells were cycled between 3.0–4.3 V and showed almost no voltage hysteresis. In the rate capability test, the specific capacity of the LMR-NCM/graphite pouch cells was about 30% higher

in comparison to the NCA/graphite pouch cells. However, because of the voltage hysteresis and the lower mean discharge voltage of LMR-NCM, the energy density on the cell level was only 11% higher.

In the aging study, the LMR-NCM/graphite pouch cells initially showed a better performance than the NCA/graphite cells. However, due to a faster capacity and voltage fading of the LMR-NCM/graphite cells, their cycling stability was somewhat inferior. While the LMR-NCM/graphite cells already reached the 80% criterion of the remaining energy density after 230 cycles, the NCA/graphite cells lasted for about 710 cycles. The overall cycle life of the LMR-NCM/graphite pouch cells was limited to 250 cycles, as strong gassing, most likely related to electrolyte oxidation, caused a rupture of the pouch foil and the cycling tests were stopped. The 80% criterion of the specific capacity of the LMR-NCM/graphite cells was projected to be reached after 350 cycles, whereas the NCA/graphite cells reached this criterion only after 980 cycles.

During the evaluation of the LMR-NCM/graphite pouch cells, a strong increase in cell temperature especially for higher currents was detected. At the end of a 3C discharge, a maximum temperature of 53 °C was measured on the surface of the LMR-NCM/graphite pouch cells, while the NCA/graphite pouch cells only reached 33 °C. The strong heat generation of cells containing LMR-NCM is caused by an energy inefficiency, which is linked to high overpotentials and the pronounced voltage hysteresis of the material. For a better quantification of the released heat, calorimetric measurements were performed with LMR-NCM/graphite coin cells and NCA/graphite coin cells. The heat generation of the LMR-NCM/graphite cells is particularly high for discharge operations, and was around four times as high as the released heat of the NCA/graphite cells for C/2 and 1C discharges. For an assessment of the implications of this heat generation for larger cell formats, the heat generation was scaled and used as an input parameter for 3D thermal models. Simulations with different cell formats, charge/discharge currents, and cooling conditions revealed, that without any active cooling, discharge rates lower than C/2 are advisable to keep the cell temperature in a safe operational range. For higher loads and larger cell formats, the cooling strategy has to be adapted to the specific application, otherwise critical cell temperatures above 60 °C are easily reached. Generally, the investigations with LMR-NCM demonstrated, that the material is suited for high energy rather than high power applications.

Besides the anode and cathode active material, the electrode and cell design has a major influence on the power capability and energy density of LIBs. In order to enhance the energy density on the cell level, the share of passive components such as current collectors, separator, electrolyte, and the housing can be reduced. Furthermore, the energy density can be increased by a higher share of active materials, i.e., thicker electrodes with a lower porosity. However, such electrodes often have a high tortuosity and face transport limitations caused by lithium-ion concentration gradients in the liquid electrolyte. In order to reduce the electrode tortuosity and overcome these limitations, the electrode morphology can be adapted to facilitate better transport pathways for lithium-ions.

For this purpose, LIBs with an adapted electrode morphology were investigated and laser-structuring was employed to create hole-like structures in graphite anodes. These structured graphite anodes were then assembled together with NCM-111 cathodes in coin cells and compared to NCM-111/graphite coin cells with unstructured anodes. Discharge rate capability tests and accompanying electrochemical simulations identified three different stages. In the first stage, for low C-rates, there is no improvement through electrode structuring, as lithium-ion diffusion is not limiting the discharge processes. In the second stage, when concentration gradients build up, around 15% more capacity could be discharged from the cells with the structured anodes. In the third stage, the benefit in capacity retention declines, as other limitations come into place. Therefore, there is a beneficial C-rate window for the structuring

process that depends mainly on the electrode thickness. For thick electrodes, laser-structuring improves the discharge rate capability at low C-rates, whereas for thin electrodes the improvement is shifted towards higher C-rates as the transport limitations set in later. Moreover, electrochemical simulations suggest, that the fast charging capability of LIBs could also be improved by structured anodes, as the reduced concentration gradients cause lower overpotentials and the lithium-plating onset can be delayed.

Although LMR-NCM cathodes face limitations at higher C-rates, a structuring of these electrodes is not promising, as the rate limitations are rather dominated by poor charge transfer kinetics and/or a slow solid-state diffusion of LMR-NCM and not by transport limitations within the electrolyte. In addition, there are challenges to calender LMR-NCM coatings to porosities lower than 30%. Such electrode porosities together with the spherical shape of the LMR-NCM active material particles result in comparatively low tortuosities of the electrodes and a structuring of LMR-NCM electrodes will most likely not enhance the rate capability.

With the conducted research in this thesis, different possibilities of performance enhancements of LIBs were evaluated. While the capacity and energy of LIBs can be increased by using the high capacitive LMR-NCM, there still remain unsolved challenges with regard to the long-term stability of LMR-NCM. Furthermore, the energy inefficiency and the corresponding heat generation caused by high overpotentials and the pronounced voltage hysteresis of LMR-NCM might pose problems for a commercialization and widespread utilization of the material. In general, the rate capability of LIBs can be boosted by an adapted electrode morphology, e.g., realized via laser-structuring of graphite anodes. However, the suitability of the integration of laser-structuring processes into a large-scale LIB production yet has to be probed and other structuring methods might be easier to implement. Moreover, with new anode active materials like silicon, the benefits of structured anodes must be thoroughly reassessed. In conclusion, there are potentials to optimize the energy density as well as the power capability of state-of-the-art LIBs, though the cell design should always consider a holistic view in order to match the requirements of the final application.

References

[1] Y. Nishi. "Lithium ion secondary batteries; past 10 years and the future". In: *Journal of Power Sources* 100 (1-2) (2001), pp. 101–106. DOI: 10.1016/S0378-7753(01)00887-4.

[2] G. E. Blomgren. "The Development and Future of Lithium Ion Batteries". In: *Journal of The Electrochemical Society* 164 (1) (2017), A5019–A5025. DOI: 10.1149/2.0251701jes.

[3] H. Hesse, M. Schimpe, D. Kucevic, and A. Jossen. "Lithium-Ion Battery Storage for the Grid—A Review of Stationary Battery Storage System Design Tailored for Applications in Modern Power Grids". In: *Energies* 10 (12) (2017), p. 2107. DOI: 10.3390/en10122107.

[4] The Royal Swedish Academy of Sciences. *Press release: The Nobel Prize in Chemistry 2019*. 2019/09/10. URL: https://www.nobelprize.org/prizes/chemistry/2019/press-release/.

[5] K. G. Gallagher and P. A. Nelson. "Manufacturing Costs of Batteries for Electric Vehicles". In: *Lithium-Ion Batteries: Advances and Applications*. Ed. by G. Pistoia. Amsterdam: Elsevier, 2014, pp. 97–126. DOI: 10.1016/B978-0-444-59513-3.00006-6.

[6] D. L. Wood, J. Li, and C. Daniel. "Prospects for reducing the processing cost of lithium ion batteries". In: *Journal of Power Sources* 275 (2015), pp. 234–242. DOI: 10.1016/j.jpowsour.2014.11.019.

[7] H. Popp, N. Zhang, M. Jahn, M. Arrinda, S. Ritz, M. Faber, D. U. Sauer, P. Azais, and I. Cendoya. "Ante-mortem analysis, electrical, thermal, and ageing testing of state-of-the-art cylindrical lithium-ion cells". In: *e & i Elektrotechnik und Informationstechnik* 8 (195) (2020), p. 104. DOI: 10.1007/s00502-020-00814-9.

[8] M. Schindler, J. Sturm, S. Ludwig, J. Schmitt, and A. Jossen. "Evolution of Initial Cell-to-Cell Variations During a Three-Year Production Cycle". In: *eTransportation* 14 (165) (2021), p. 100102. DOI: 10.1016/j.etran.2020.100102.

[9] A. Masias, J. Marcicki, and W. A. Paxton. "Opportunities and Challenges of Lithium Ion Batteries in Automotive Applications". In: *ACS Energy Letters* (2021), pp. 621–630. DOI: 10.1021/acsenergylett.0c02584.

[10] BloombergNEF. *Electric Vehicle Outlook 2020: Executive Summary*. URL: https://about.bnef.com/electric-vehicle-outlook/ (visited on 04/03/2021).

[11] N. Lebedeva, D. Tarvydas, and I. Tsiropoulos. *Li-ion batteries for mobility and stationary storage applications: Scenarios for costs and market growth*. Vol. 29440. EUR, Scientific and technical research series. Luxembourg: Publications Office of the European Union, 2018. DOI: 10.2760/87175.

[12] M. Marinaro et al. "Bringing forward the development of battery cells for automotive applications: Perspective of R&D activities in China, Japan, the EU and the USA". In: *Journal of Power Sources* 459 (2020), p. 228073. DOI: 10.1016/j.jpowsour.2020.228073.

[13] N. Rietmann, B. Hügler, and T. Lieven. "Forecasting the trajectory of electric vehicle sales and the consequences for worldwide CO_2 emissions". In: *Journal of Cleaner Production* 261 (2020), p. 121038. DOI: 10.1016/j.jclepro.2020.121038.

[14] S. M. Aceves, G. Petitpas, F. Espinosa-Loza, M. J. Matthews, and E. Ledesma-Orozco. "Safe, long range, inexpensive and rapidly refuelable hydrogen vehicles with cryogenic pressure vessels". In: *International Journal of Hydrogen Energy* 38 (5) (2013), pp. 2480–2489. DOI: 10.1016/j.ijhydene.2012.11.123.

[15] O. Gröger, H. A. Gasteiger, and J.-P. Suchsland. "Review—Electromobility: Batteries or Fuel Cells?" In: *Journal of The Electrochemical Society* 162 (14) (2015), A2605–A2622. DOI: 10.1149/2.0211514jes.

[16] D. Verstraete. "On the energy efficiency of hydrogen-fuelled transport aircraft". In: *International Journal of Hydrogen Energy* 40 (23) (2015), pp. 7388–7394. DOI: 10.1016/j.ijhydene.2015.04.055.

[17] K. Kerman, A. Luntz, V. Viswanathan, Y.-M. Chiang, and Z. Chen. "Review—Practical Challenges Hindering the Development of Solid State Li Ion Batteries". In: *Journal of The Electrochemical Society* 164 (7) (2017), A1731–A1744. DOI: 10.1149/2.1571707jes.

[18] F. Duffner, N. Kronemeyer, J. Tübke, J. Leker, M. Winter, and R. Schmuch. "Post-lithium-ion battery cell production and its compatibility with lithium-ion cell production infrastructure". In: *Nature Energy* 21 (2021), p. 1939. DOI: 10.1038/s41560-020-00748-8.

[19] Volkswagen AG. *Power Day: Volkswagen presents technology roadmap for batteries and charging up to 2030.* Wolfsburg, 2021. URL: https://www.volkswagenag.com/en/news/2021/03/power-day--volkswagen-presents-technology-roadmap-for-batteries-.html (visited on 03/15/2021).

[20] Visual Capitalist. *What is Lithium Worth?* URL: https://www.visualcapitalist.com/what-is-lithium-worth/ (visited on 04/06/2021).

[21] C. Thiel, W. Nijs, S. Simoes, J. Schmidt, A. van Zyl, and E. Schmid. "The impact of the EU car CO_2 regulation on the energy system and the role of electro-mobility to achieve transport decarbonisation". In: *Energy Policy* 96 (4) (2016), pp. 153–166. DOI: 10.1016/j.enpol.2016.05.043.

[22] European Commission. *Reducing CO_2 emissions from passenger cars - before 2020.* URL: https://ec.europa.eu/clima/policies/transport/vehicles/cars_en (visited on 02/06/2021).

[23] European Commission. *CO_2 emission performance standards for cars and vans (2020 onwards).* URL: https://ec.europa.eu/clima/policies/transport/vehicles/regulation_en (visited on 02/06/2021).

[24] G. Anandarajah, W. McDowall, and P. Ekins. "Decarbonising road transport with hydrogen and electricity: Long term global technology learning scenarios". In: *International Journal of Hydrogen Energy* 38 (8) (2013), pp. 3419–3432. DOI: 10.1016/j.ijhydene.2012.12.110.

[25] P. Mock, Tietge, Wappelhorst, Sandra, G. U. Bieker, and J. Dornoff. *Market Monitor: European Passenger Car Registrations: January-December 2020.* Ed. by International Council on Clean Transportation. 2021. URL: https://theicct.org/publications/market-monitor-eu-jan2021.

[26] D. R. Lide. *CRC Handbook of Chemistry and Physics: Internet Version 2005.* Boca Raton, FL: CRC Press, 2005.

[27] Z. Ogumi and M. Inaba. "Carbon Anodes". In: *Advances in Lithium-Ion Batteries.* Ed. by W. A. van Schalkwijk and B. Scrosati. Boston, MA: Springer US, 2002, pp. 79–101. DOI: 10.1007/0-306-47508-1_3.

[28] J. Xie and Y.-C. Lu. “A retrospective on lithium-ion batteries”. In: *Nature communications* 11 (1) (2020), p. 2499. DOI: 10.1038/s41467-020-16259-9.

[29] D. Lisbona and T. Snee. “A review of hazards associated with primary lithium and lithium-ion batteries”. In: *Process Safety and Environmental Protection* 89 (6) (2011), pp. 434–442. DOI: 10.1016/j.psep.2011.06.022.

[30] P. Barai, K. Higa, and V. Srinivasan. “Impact of External Pressure and Electrolyte Transport Properties on Lithium Dendrite Growth”. In: *Journal of The Electrochemical Society* 165 (11) (2018), A2654–A2666. DOI: 10.1149/2.0651811jes.

[31] M. Armand et al. “Lithium-ion batteries – Current state of the art and anticipated developments”. In: *Journal of Power Sources* 479 (2020), p. 228708. DOI: 10.1016/j.jpowsour.2020.228708.

[32] D. Andre, S.-J. Kim, P. Lamp, S. F. Lux, F. Maglia, O. Paschos, and B. Stiaszny. “Future generations of cathode materials: An automotive industry perspective”. In: *Journal of Materials Chemistry A* 3 (13) (2015), pp. 6709–6732. DOI: 10.1039/C5TA00361J.

[33] N. Nitta, F. Wu, J. T. Lee, and G. Yushin. “Li-ion battery materials: present and future”. In: *Materials Today* 18 (5) (2015), pp. 252–264. DOI: 10.1016/j.mattod.2014.10.040.

[34] C. S. Yoon, K.-J. Park, U.-H. Kim, K. H. Kang, H.-H. Ryu, and Y.-K. Sun. “High-Energy Ni-Rich Li[$Ni_xCo_yMn_{1-x-y}$]O_2 Cathodes via Compositional Partitioning for Next-Generation Electric Vehicles”. In: *Chemistry of Materials* 29 (24) (2017), pp. 10436–10445. DOI: 10.1021/acs.chemmater.7b04047.

[35] F. Wu, J. Maier, and Y. Yu. “Guidelines and trends for next-generation rechargeable lithium and lithium-ion batteries”. In: *Chemical Society reviews* 49 (5) (2020), pp. 1569–1614. DOI: 10.1039/c7cs00863e.

[36] S.-T. Myung, F. Maglia, K.-J. Park, C. S. Yoon, P. Lamp, S.-J. Kim, and Y.-K. Sun. “Nickel-Rich Layered Cathode Materials for Automotive Lithium-Ion Batteries: Achievements and Perspectives”. In: *ACS Energy Letters* 2 (1) (2017), pp. 196–223. DOI: 10.1021/acsenergylett.6b00594.

[37] A. Manthiram. “A reflection on lithium-ion battery cathode chemistry”. In: *Nature communications* 11 (1) (2020), p. 1550. DOI: 10.1038/s41467-020-15355-0.

[38] Y. Ding, Z. P. Cano, A. Yu, J. Lu, and Z. Chen. “Automotive Li-Ion Batteries: Current Status and Future Perspectives”. In: *Electrochemical Energy Reviews* 2 (1) (2019), pp. 1–28. DOI: 10.1007/s41918-018-0022-z.

[39] R. Schmuch, R. Wagner, G. Hörpel, T. Placke, and M. Winter. “Performance and cost of materials for lithium-based rechargeable automotive batteries”. In: *Nature Energy* 3 (4) (2018), pp. 267–278. DOI: 10.1038/s41560-018-0107-2.

[40] J. R. Croy, M. Balasubramanian, K. G. Gallagher, and A. K. Burrell. “Review of the U.S. Department of Energy’s ”deep dive” effort to understand voltage fade in Li- and Mn-rich cathodes”. In: *Accounts of chemical research* 48 (11) (2015), pp. 2813–2821. DOI: 10.1021/acs.accounts.5b00277.

[41] T. Teufl, D. Pritzl, S. Solchenbach, H. A. Gasteiger, and M. A. Mendez. “State of Charge Dependent Resistance Build-Up in Li- and Mn-Rich Layered Oxides during Lithium Extraction and Insertion”. In: *Journal of The Electrochemical Society* 166 (6) (2019), A1275–A1284. DOI: 10.1149/2.1131906jes.

[42] D. Becker, M. Börner, A. Friesen, S. Klein, U. Rodehorst, M. Diehl, M. Winter, T. Placke, and R. Schmuch. "Towards High-Performance Li-rich NCM|Graphite Cells by Germanium-Polymer Coating of the Positive Electrode Material". In: *Journal of The Electrochemical Society* 167 (6) (2020), p. 060524. DOI: 10.1149/1945-7111/ab8401.

[43] J. Helbig, T. Beuse, V. Siozios, T. Placke, M. Winter, and R. Schmuch. "Li|Mn-Rich Cathode Materials with Low-Cobalt Content and Core-Shell Particle Design for High-Energy Lithium Ion Batteries". In: *Journal of The Electrochemical Society* 167 (6) (2020), p. 060519. DOI: 10.1149/1945-7111/ab8405.

[44] L. Kraft, T. Zünd, D. Schreiner, R. Wilhelm, F. J. Günter, G. Reinhart, H. A. Gasteiger, and A. Jossen. "Comparative Evaluation of LMR-NCM and NCA Cathode Active Materials in Multilayer Lithium-Ion Pouch Cells: Part II. Rate Capability, Long-Term Stability, and Thermal Behavior". In: *Journal of The Electrochemical Society* 168 (2) (2021), p. 020537. DOI: 10.1149/1945-7111/abe5e6.

[45] G. Assat, S. L. Glazier, C. Delacourt, and J.-M. Tarascon. "Probing the thermal effects of voltage hysteresis in anionic redox-based lithium-rich cathodes using isothermal calorimetry". In: *Nature Energy* 4 (8) (2019), pp. 647–656. DOI: 10.1038/s41560-019-0410-6.

[46] N. Leifer, T. Penki, R. Nanda, J. Grinblat, S. Luski, D. Aurbach, and G. Goobes. "Linking structure to performance of $Li_{1.2}Mn_{0.54}Ni_{0.13}Co_{0.13}O_2$ (Li and Mn rich NMC) cathode materials synthesized by different methods". In: *Physical chemistry chemical physics : PCCP* 22 (16) (2020), pp. 9098–9109. DOI: 10.1039/d0cp00400f.

[47] D. Schreiner et al. "Comparative Evaluation of LMR-NCM and NCA Cathode Active Materials in Multilayer Lithium-Ion Pouch Cells: Part I. Production, Electrode Characterization, and Formation". In: *Journal of The Electrochemical Society* 168 (3) (2021), p. 030507. DOI: 10.1149/1945-7111/abe50c.

[48] L. Kraft, A. Hoefling, T. Zünd, A. Kunz, M. Steinhardt, J. Tübke, and A. Jossen. "Implications of the Heat Generation of LMR-NCM on the Thermal Behavior of Large-Format Lithium-Ion Batteries". In: *Journal of The Electrochemical Society* 168 (5) (2021), p. 053505. DOI: 10.1149/1945-7111/ac0069.

[49] Y.-K. Sun, D.-J. Lee, Y. J. Lee, Z. Chen, and S.-T. Myung. "Cobalt-free nickel rich layered oxide cathodes for lithium-ion batteries". In: *ACS applied materials & interfaces* 5 (21) (2013), pp. 11434–11440. DOI: 10.1021/am403684z.

[50] N. Zhang et al. "Cobalt-Free Nickel-Rich Positive Electrode Materials with a Core-Shell Structure". In: *Chemistry of Materials* 31 (24) (2019), pp. 10150–10160. DOI: 10.1021/acs.chemmater.9b03515.

[51] H. Li, M. Cormier, N. Zhang, J. Inglis, J. Li, and J. R. Dahn. "Is Cobalt Needed in Ni-Rich Positive Electrode Materials for Lithium Ion Batteries?" In: *Journal of The Electrochemical Society* 166 (4) (2019), A429–A439. DOI: 10.1149/2.1381902jes.

[52] N. Muralidharan, R. Essehli, R. P. Hermann, A. Parejiya, R. Amin, Y. Bai, Z. Du, and I. Belharouak. "$LiNi_xFe_yAl_zO_2$, a new cobalt-free layered cathode material for advanced Li-ion batteries". In: *Journal of Power Sources* 471 (2020), p. 228389. DOI: 10.1016/j.jpowsour.2020.228389.

[53] N. Muralidharan et al. “Lithium Iron Aluminum Nickelate, $LiNi_xFe_yAl_zO_2$ -New Sustainable Cathodes for Next-Generation Cobalt-Free Li-Ion Batteries”. In: *Advanced materials (Deerfield Beach, Fla.)* 32 (34) (2020), p. 2002960. DOI: 10.1002/adma.202002960.

[54] W.-C. Chen, Y.-F. Song, C.-C. Wang, Y. Liu, D. T. Morris, P. A. Pianetta, J. C. Andrews, H.-C. Wu, and N.-L. Wu. “Study on the synthesis–microstructure-performance relationship of layered Li-excess nickel–manganese oxide as a Li-ion battery cathode prepared by high-temperature calcination”. In: *Journal of Materials Chemistry A* 1 (36) (2013), pp. 10847–10856. DOI: 10.1039/c3ta11716b.

[55] M. Naumann, M. Schimpe, P. Keil, H. C. Hesse, and A. Jossen. “Analysis and modeling of calendar aging of a commercial $LiFePO_4$/graphite cell”. In: *Journal of Energy Storage* 17 (12) (2018), pp. 153–169. DOI: 10.1016/j.est.2018.01.019.

[56] M. Naumann, F. B. Spingler, and A. Jossen. “Analysis and modeling of cycle aging of a commercial $LiFePO_4$/graphite cell”. In: *Journal of Power Sources* 451 (14) (2020), p. 227666. DOI: 10.1016/j.jpowsour.2019.227666.

[57] M. Winter, J. O. Besenhard, M. E. Spahr, and P. Novák. “Insertion Electrode Materials for Rechargeable Lithium Batteries”. In: *Advanced materials* 10 (10) (1998), pp. 725–763. DOI: 10.1002/(SICI)1521-4095(199807)10:10{\textless}725::AID-ADMA725{\textgreater}3.0.CO;2-Z.

[58] J. Asenbauer, T. Eisenmann, M. Kuenzel, A. Kazzazi, Z. Chen, and D. Bresser. “The success story of graphite as a lithium-ion anode material – fundamentals, remaining challenges, and recent developments including silicon (oxide) composites”. In: *Sustainable Energy & Fuels* 4 (11) (2020), pp. 5387–5416. DOI: 10.1039/D0SE00175A.

[59] F. B. Spingler, S. Kücher, R. Phillips, E. Moyassari, and A. Jossen. “Electrochemically Stable In Situ Dilatometry of NMC, NCA and Graphite Electrodes for Lithium-Ion Cells Compared to XRD Measurements”. In: *Journal of The Electrochemical Society* 168 (4) (2021), p. 040515. DOI: 10.1149/1945-7111/abf262.

[60] D. Jantke, R. Bernhard, E. Hanelt, T. Buhrmester, J. Pfeiffer, and S. Haufe. “Silicon-Dominant Anodes Based on Microscale Silicon Particles under Partial Lithiation with High Capacity and Cycle Stability”. In: *Journal of The Electrochemical Society* 166 (16) (2019), A3881–A3885. DOI: 10.1149/2.1311915jes.

[61] Z. Luo, D. Fan, X. Liu, H. Mao, C. Yao, and Z. Deng. “High performance silicon carbon composite anode materials for lithium ion batteries”. In: *Journal of Power Sources* 189 (1) (2009), pp. 16–21. DOI: 10.1016/j.jpowsour.2008.12.068.

[62] E. Moyassari et al. “Impact of Silicon Content within Silicon-Graphite Anodes on Performance and Li Concentration Profiles of Li-Ion Cells using Neutron Depth Profiling”. In: *Journal of The Electrochemical Society* 168 (2) (2021), p. 020519. DOI: 10.1149/1945-7111/abe1db.

[63] J. Sturm, A. Rheinfeld, I. Zilberman, F. B. Spingler, S. Kosch, F. Frie, and A. Jossen. “Modeling and simulation of inhomogeneities in a 18650 nickel-rich, silicon-graphite lithium-ion cell during fast charging”. In: *Journal of Power Sources* 412 (2019), pp. 204–223. DOI: 10.1016/j.jpowsour.2018.11.043.

[64] M. J. Lain, J. Brandon, and E. Kendrick. “Design Strategies for High Power vs. High Energy Lithium Ion Cells”. In: *Batteries* 5 (4) (2019), p. 64. DOI: 10.3390/batteries5040064.

[65] J. Qian, W. A. Henderson, W. Xu, P. Bhattacharya, M. Engelhard, O. Borodin, and J.-G. Zhang. "High rate and stable cycling of lithium metal anode". In: *Nature communications* 6 (2015), p. 6362. DOI: 10.1038/ncomms7362.

[66] D. Lin, Y. Liu, and Y. Cui. "Reviving the lithium metal anode for high-energy batteries". In: *Nature nanotechnology* 12 (3) (2017), pp. 194–206. DOI: 10.1038/nnano.2017.16.

[67] X.-B. Cheng, R. Zhang, C.-Z. Zhao, and Q. Zhang. "Toward Safe Lithium Metal Anode in Rechargeable Batteries: A Review". In: *Chemical reviews* 117 (15) (2017), pp. 10403–10473. DOI: 10.1021/acs.chemrev.7b00115.

[68] M. Genovese, A. J. Louli, R. Weber, S. Hames, and J. R. Dahn. "Measuring the Coulombic Efficiency of Lithium Metal Cycling in Anode-Free Lithium Metal Batteries". In: *Journal of The Electrochemical Society* 165 (14) (2018), A3321–A3325. DOI: 10.1149/2.0641814jes.

[69] A. J. Louli, M. Genovese, R. Weber, S. G. Hames, E. R. Logan, and J. R. Dahn. "Exploring the Impact of Mechanical Pressure on the Performance of Anode-Free Lithium Metal Cells". In: *Journal of The Electrochemical Society* 166 (8) (2019), A1291–A1299. DOI: 10.1149/2.0091908jes.

[70] R. Weber, M. Genovese, A. J. Louli, S. Hames, C. Martin, I. G. Hill, and J. R. Dahn. "Long cycle life and dendrite-free lithium morphology in anode-free lithium pouch cells enabled by a dual-salt liquid electrolyte". In: *Nature Energy* 4 (8) (2019), pp. 683–689. DOI: 10.1038/s41560-019-0428-9.

[71] S.-T. Myung, Y. Sasaki, S. Sakurada, Y.-K. Sun, and H. Yashiro. "Electrochemical behavior of current collectors for lithium batteries in non-aqueous alkyl carbonate solution and surface analysis by ToF-SIMS". In: *Electrochimica Acta* 55 (1) (2009), pp. 288–297. DOI: 10.1016/j.electacta.2009.08.051.

[72] M. Yamada, T. Watanabe, T. Gunji, J. Wu, and F. Matsumoto. "Review of the Design of Current Collectors for Improving the Battery Performance in Lithium-Ion and Post-Lithium-Ion Batteries". In: *Electrochem* 1 (2) (2020), pp. 124–159. DOI: 10.3390/electrochem1020011.

[73] J. W. Braithwaite, A. Gonzales, G. Nagasubramanian, S. J. Lucero, D. E. Peebles, J. A. Ohlhausen, and W. R. Cieslak. "Corrosion of Lithium-Ion Battery Current Collectors". In: *Journal of The Electrochemical Society* 146 (2) (1999), pp. 448–456. DOI: 10.1149/1.1391627.

[74] S.-T. Myung, Y. Hitoshi, and Y.-K. Sun. "Electrochemical behavior and passivation of current collectors in lithium-ion batteries". In: *Journal of Materials Chemistry* 21 (27) (2011), pp. 9891–9911. DOI: 10.1039/c0jm04353b.

[75] S. Hildebrand, C. Vollmer, M. Winter, and F. M. Schappacher. "Al_2O_3 , SiO_2 and TiO_2 as Coatings for Safer $LiNi_{0.8}Co_{0.15}Al_{0.05}O_2$ Cathodes: Electrochemical Performance and Thermal Analysis by Accelerating Rate Calorimetry". In: *Journal of The Electrochemical Society* 164 (9) (2017), A2190–A2198. DOI: 10.1149/2.0071712jes.

[76] J. B. Habedank, L. Kraft, A. Rheinfeld, C. Krezdorn, A. Jossen, and M. F. Zaeh. "Increasing the Discharge Rate Capability of Lithium-Ion Cells with Laser-Structured Graphite Anodes: Modeling and Simulation". In: *Journal of The Electrochemical Society* 165 (7) (2018), A1563–A1573. DOI: 10.1149/2.1181807jes.

[77] R. Morasch, J. Landesfeind, B. Suthar, and H. A. Gasteiger. "Detection of Binder Gradients Using Impedance Spectroscopy and Their Influence on the Tortuosity of Li-Ion Battery Graphite Electrodes". In: *Journal of The Electrochemical Society* 165 (14) (2018), A3459–A3467. DOI: 10.1149/2.1021814jes.

[78] F. Friedrich, B. Strehle, A. T. S. Freiberg, K. Kleiner, S. J. Day, C. Erk, M. Piana, and H. A. Gasteiger. "Editors' Choice—Capacity Fading Mechanisms of NCM-811 Cathodes in Lithium-Ion Batteries Studied by X-ray Diffraction and Other Diagnostics". In: *Journal of The Electrochemical Society* 166 (15) (2019), A3760–A3774. DOI: 10.1149/2.0821915jes.

[79] V. Müller, R.-G. Scurtu, K. Richter, T. Waldmann, M. Memm, M. A. Danzer, and M. Wohlfahrt-Mehrens. "Effects of Mechanical Compression on the Aging and the Expansion Behavior of Si/C-Composite|NMC811 in Different Lithium-Ion Battery Cell Formats". In: *Journal of The Electrochemical Society* 166 (15) (2019), A3796–A3805. DOI: 10.1149/2.1121915jes.

[80] L. Kraft, J. B. Habedank, A. Frank, A. Rheinfeld, and A. Jossen. "Modeling and Simulation of Pore Morphology Modifications using Laser-Structured Graphite Anodes in Lithium-Ion Batteries". In: *Journal of The Electrochemical Society* 167 (1) (2020), p. 013506. DOI: 10.1149/2.0062001JES.

[81] V. Müller, R.-G. Scurtu, M. Memm, M. A. Danzer, and M. Wohlfahrt-Mehrens. "Study of the influence of mechanical pressure on the performance and aging of Lithium-ion battery cells". In: *Journal of Power Sources* 440 (2019), p. 227148. DOI: 10.1016/j.jpowsour.2019.227148.

[82] D.-H. Yoon, M. Marinaro, P. Axmann, and M. Wohlfahrt-Mehrens. "Study of the Binder Influence on Expansion/Contraction Behavior of Silicon Alloy Negative Electrodes for Lithium-Ion Batteries". In: *Journal of The Electrochemical Society* 167 (16) (2020), p. 160537. DOI: 10.1149/1945-7111/abcf4f.

[83] M. Park, X. Zhang, M. Chung, G. B. Less, and A. M. Sastry. "A review of conduction phenomena in Li-ion batteries". In: *Journal of Power Sources* 195 (24) (2010), pp. 7904–7929. DOI: 10.1016/j.jpowsour.2010.06.060.

[84] H. Zheng, R. Yang, G. Liu, X. Song, and V. S. Battaglia. "Cooperation between Active Material, Polymeric Binder and Conductive Carbon Additive in Lithium Ion Battery Cathode". In: *The Journal of Physical Chemistry C* 116 (7) (2012), pp. 4875–4882. DOI: 10.1021/jp208428w.

[85] G. E. Blomgren. "Electrolytes for advanced batteries". In: *Journal of Power Sources* 81-82 (1999), pp. 112–118. DOI: 10.1016/S0378-7753(99)00188-3.

[86] A. M. Haregewoin, A. S. Wotango, and B.-J. Hwang. "Electrolyte additives for lithium ion battery electrodes: progress and perspectives". In: *Energy Environ. Sci.* 9 (6) (2016), pp. 1955–1988. DOI: 10.1039/C6EE00123H.

[87] K. Xu. "Nonaqueous liquid electrolytes for lithium-based rechargeable batteries". In: *Chemical reviews* 104 (10) (2004), pp. 4303–4417. DOI: 10.1021/cr030203g.

[88] Q. Li, J. Chen, L. Fan, X. Kong, and Y. Lu. "Progress in electrolytes for rechargeable Li-based batteries and beyond". In: *Green Energy & Environment* 1 (1) (2016), pp. 18–42. DOI: 10.1016/j.gee.2016.04.006.

[89] P. Verma, P. Maire, and P. Novák. "A review of the features and analyses of the solid electrolyte interphase in Li-ion batteries". In: *Electrochimica Acta* 55 (22) (2010), pp. 6332–6341. DOI: 10.1016/j.electacta.2010.05.072.

[90] E. Peled and S. Menkin. “Review—SEI: Past, Present and Future”. In: *Journal of The Electrochemical Society* 164 (7) (2017), A1703–A1719. DOI: 10.1149/2.1441707jes.

[91] A. Barré, B. Deguilhem, S. Grolleau, M. Gérard, F. Suard, and D. Riu. “A review on lithium-ion battery ageing mechanisms and estimations for automotive applications”. In: *Journal of Power Sources* 241 (2013), pp. 680–689. DOI: 10.1016/j.jpowsour.2013.05.040.

[92] C. R. Birkl, M. R. Roberts, E. McTurk, P. G. Bruce, and D. A. Howey. “Degradation diagnostics for lithium ion cells”. In: *Journal of Power Sources* 341 (2017), pp. 373–386. DOI: 10.1016/j.jpowsour.2016.12.011.

[93] G. E. Blomgren. “Liquid electrolytes for lithium and lithium-ion batteries”. In: *Journal of Power Sources* 119-121 (2003), pp. 326–329. DOI: 10.1016/S0378-7753(03)00147-2.

[94] A. Manuel Stephan. “Review on gel polymer electrolytes for lithium batteries”. In: *European Polymer Journal* 42 (1) (2006), pp. 21–42. DOI: 10.1016/j.eurpolymj.2005.09.017.

[95] S.-J. Tan, X.-X. Zeng, Q. Ma, X.-W. Wu, and Y.-G. Guo. “Recent Advancements in Polymer-Based Composite Electrolytes for Rechargeable Lithium Batteries”. In: *Electrochemical Energy Reviews* 1 (2) (2018), pp. 113–138. DOI: 10.1007/s41918-018-0011-2.

[96] M. Galiński, A. Lewandowski, and I. Stępniak. “Ionic liquids as electrolytes”. In: *Electrochimica Acta* 51 (26) (2006), pp. 5567–5580. DOI: 10.1016/j.electacta.2006.03.016.

[97] A. Lewandowski and A. Świderska-Mocek. “Ionic liquids as electrolytes for Li-ion batteries—An overview of electrochemical studies”. In: *Journal of Power Sources* 194 (2) (2009), pp. 601–609. DOI: 10.1016/j.jpowsour.2009.06.089.

[98] A. Balducci. “Ionic Liquids in Lithium-Ion Batteries”. In: *Topics in current chemistry (Cham)* 375 (2) (2017), pp. 1–27. DOI: 10.1007/s41061-017-0109-8.

[99] A. Manthiram, X. Yu, and S. Wang. “Lithium battery chemistries enabled by solid-state electrolytes”. In: *Nature Reviews Materials* 2 (4) (2017), p. 16103. DOI: 10.1038/natrevmats.2016.103.

[100] L. Fan, S. Wei, S. Li, Q. Li, and Y. Lu. “Recent Progress of the Solid-State Electrolytes for High-Energy Metal-Based Batteries”. In: *Advanced Energy Materials* 8 (11) (2018), p. 1702657. DOI: 10.1002/aenm.201702657.

[101] Z. Gao, H. Sun, L. Fu, F. Ye, Y. Zhang, W. Luo, and Y. Huang. “Promises, Challenges, and Recent Progress of Inorganic Solid-State Electrolytes for All-Solid-State Lithium Batteries”. In: *Advanced materials* 30 (17) (2018), p. 1705702. DOI: 10.1002/adma.201705702.

[102] T. Famprikis, P. Canepa, J. A. Dawson, M. S. Islam, and C. Masquelier. “Fundamentals of inorganic solid-state electrolytes for batteries”. In: *Nature materials* 18 (12) (2019), pp. 1278–1291. DOI: 10.1038/s41563-019-0431-3.

[103] X. Huang. “Separator technologies for lithium-ion batteries”. In: *Journal of Solid State Electrochemistry* 15 (4) (2011), pp. 649–662. DOI: 10.1007/s10008-010-1264-9.

[104] H. Lee, M. Yanilmaz, O. Toprakci, K. Fu, and X. Zhang. “A review of recent developments in membrane separators for rechargeable lithium-ion batteries”. In: *Energy Environ. Sci.* 7 (12) (2014), pp. 3857–3886. DOI: 10.1039/C4EE01432D.

[105] G. Venugopal, J. Moore, J. Howard, and S. Pendalwar. “Characterization of microporous separators for lithium-ion batteries”. In: *Journal of Power Sources* 77 (1) (1999), pp. 34–41. DOI: 10.1016/S0378-7753(98)00168-2.

[106] J. Landesfeind, J. Hattendorff, A. Ehrl, W. A. Wall, and H. A. Gasteiger. "Tortuosity Determination of Battery Electrodes and Separators by Impedance Spectroscopy". In: *Journal of The Electrochemical Society* 163 (7) (2016), A1373–A1387. DOI: 10.1149/2.1141607jes.

[107] J.-A. Choi, S. H. Kim, and D.-W. Kim. "Enhancement of thermal stability and cycling performance in lithium-ion cells through the use of ceramic-coated separators". In: *Journal of Power Sources* 195 (18) (2010), pp. 6192–6196. DOI: 10.1016/j.jpowsour.2009.11.020.

[108] A. Rheinfeld, J. Sturm, A. Frank, S. Kosch, S. V. Erhard, and A. Jossen. "Impact of Cell Size and Format on External Short Circuit Behavior of Lithium-Ion Cells at Varying Cooling Conditions: Modeling and Simulation". In: *Journal of The Electrochemical Society* 167 (1) (2020), p. 013511. DOI: 10.1149/2.0112001JES.

[109] J. Sturm, A. Frank, A. Rheinfeld, S. V. Erhard, and A. Jossen. "Impact of Electrode and Cell Design on Fast Charging Capabilities of Cylindrical Lithium-Ion Batteries". In: *Journal of The Electrochemical Society* 167 (13) (2020), p. 130505. DOI: 10.1149/1945-7111/abb40c.

[110] G. Reinhart et al. "Research and Demonstration Center for the Production of Large-Area Lithium-Ion Cells". In: *Future Trends in Production Engineering*. Ed. by G. Schuh, R. Neugebauer, and E. Uhlmann. Vol. 12. Berlin, Heidelberg: Springer Berlin Heidelberg, 2013, pp. 3–12. DOI: 10.1007/978-3-642-24491-9_1.

[111] R. Schröder, M. Aydemir, and G. Seliger. "Comparatively Assessing different Shapes of Lithium-ion Battery Cells". In: *Procedia Manufacturing* 8 (2017), pp. 104–111. DOI: 10.1016/j.promfg.2017.02.013.

[112] A. Kwade, W. Haselrieder, R. Leithoff, A. Modlinger, F. Dietrich, and K. Droeder. "Current status and challenges for automotive battery production technologies". In: *Nature Energy* 3 (4) (2018), pp. 290–300. DOI: 10.1038/s41560-018-0130-3.

[113] T. Bandhauer, S. Garimella, and T. F. Fuller. "Electrochemical-Thermal Modeling to Evaluate Battery Thermal Management Strategies: I. Side Cooling". In: *Journal of The Electrochemical Society* 162 (1) (2015), A125–A136. DOI: 10.1149/2.0571501jes.

[114] H. Lundgren, P. Svens, H. Ekström, C. Tengstedt, J. Lindström, M. Behm, and G. Lindbergh. "Thermal Management of Large-Format Prismatic Lithium-Ion Battery in PHEV Application". In: *Journal of The Electrochemical Society* 163 (2) (2016), A309–A317. DOI: 10.1149/2.09411602jes.

[115] DIN Deutsches Institut für Normung e. V. *Electrically propelled road vehicles - Battery systems - Design specifications for Lithium-Ion battery cells*. 2016/01/11.

[116] P. G. Balakrishnan, R. Ramesh, and T. Prem Kumar. "Safety mechanisms in lithium-ion batteries". In: *Journal of Power Sources* 155 (2) (2006), pp. 401–414. DOI: 10.1016/j.jpowsour.2005.12.002.

[117] J. Schmitt, B. Kraft, J. P. Schmidt, B. Meir, K. Elian, D. Ensling, G. Keser, and A. Jossen. "Measurement of gas pressure inside large-format prismatic lithium-ion cells during operation and cycle aging". In: *Journal of Power Sources* 478 (14) (2020), p. 228661. DOI: 10.1016/j.jpowsour.2020.228661.

[118] P. Svens, M. Kjell, C. Tengstedt, G. Flodberg, and G. Lindbergh. "Li-Ion Pouch Cells for Vehicle Applications — Studies of Water Transmission and Packing Materials". In: *Energies* 6 (1) (2013), pp. 400–410. DOI: 10.3390/en6010400.

[119] X. Zhang and T. Wierzbicki. "Characterization of plasticity and fracture of shell casing of lithium-ion cylindrical battery". In: *Journal of Power Sources* 280 (2015), pp. 47–56. DOI: 10.1016/j.jpowsour.2015.01.077.

[120] J. Zhu, X. Zhang, E. Sahraei, and T. Wierzbicki. "Deformation and failure mechanisms of 18650 battery cells under axial compression". In: *Journal of Power Sources* 336 (2016), pp. 332–340. DOI: 10.1016/j.jpowsour.2016.10.064.

[121] L. Sheng, Z. Zhang, L. Su, H. Zhang, H. Zhang, Y. Fang, K. Li, and W. Ye. "Quasi steady state method to measure thermophysical parameters of cylindrical lithium ion batteries". In: *Journal of Power Sources* 485 (1) (2021), p. 229342. DOI: 10.1016/j.jpowsour.2020.229342.

[122] T. Placke, R. Kloepsch, S. Dühnen, and M. Winter. "Lithium ion, lithium metal, and alternative rechargeable battery technologies: the odyssey for high energy density". In: *Journal of Solid State Electrochemistry* 21 (7) (2017), pp. 1939–1964. DOI: 10.1007/s10008-017-3610-7.

[123] J. B. Quinn, T. Waldmann, K. Richter, M. Kasper, and M. Wohlfahrt-Mehrens. "Energy Density of Cylindrical Li-Ion Cells: A Comparison of Commercial 18650 to the 21700 Cells". In: *Journal of The Electrochemical Society* 165 (14) (2018), A3284–A3291. DOI: 10.1149/2.0281814jes.

[124] T. G. Tranter, R. Timms, P. R. Shearing, and D. J. L. Brett. "Communication—Prediction of Thermal Issues for Larger Format 4680 Cylindrical Cells and Their Mitigation with Enhanced Current Collection". In: *Journal of The Electrochemical Society* 167 (16) (2020), p. 160544. DOI: 10.1149/1945-7111/abd44f.

[125] H. Zheng, J. Li, X. Song, G. Liu, and V. S. Battaglia. "A comprehensive understanding of electrode thickness effects on the electrochemical performances of Li-ion battery cathodes". In: *Electrochimica Acta* 71 (2012), pp. 258–265. DOI: 10.1016/j.electacta.2012.03.161.

[126] M. Singh, J. Kaiser, and H. Hahn. "Thick Electrodes for High Energy Lithium Ion Batteries". In: *Journal of The Electrochemical Society* 162 (7) (2015), A1196–A1201. DOI: 10.1149/2.0401507jes.

[127] K. G. Gallagher et al. "Optimizing Areal Capacities through Understanding the Limitations of Lithium-Ion Electrodes". In: *Journal of The Electrochemical Society* 163 (2) (2015), A138–A149. DOI: 10.1149/2.0321602jes.

[128] C. Heubner, M. Schneider, and A. Michaelis. "Diffusion–Limited C–Rate: A Fundamental Principle Quantifying the Intrinsic Limits of Li–Ion Batteries". In: *Advanced Energy Materials* 10 (2) (2020), p. 1902523. DOI: 10.1002/aenm.201902523.

[129] J. Landesfeind, A. Eldiven, and H. A. Gasteiger. "Influence of the Binder on Lithium Ion Battery Electrode Tortuosity and Performance". In: *Journal of The Electrochemical Society* 165 (5) (2018), A1122–A1128. DOI: 10.1149/2.0971805jes.

[130] B. L. Trembacki, A. N. Mistry, D. R. Noble, M. E. Ferraro, P. P. Mukherjee, and S. A. Roberts. "Editors' Choice—Mesoscale Analysis of Conductive Binder Domain Morphology in Lithium-Ion Battery Electrodes". In: *Journal of The Electrochemical Society* 165 (13) (2018), E725–E736. DOI: 10.1149/2.0981813jes.

[131] M. Keyser et al. "Enabling fast charging – Battery thermal considerations". In: *Journal of Power Sources* 367 (2017), pp. 228–236. DOI: 10.1016/j.jpowsour.2017.07.009.

[132] T. M. Bandhauer, S. Garimella, and T. F. Fuller. "A Critical Review of Thermal Issues in Lithium-Ion Batteries". In: *Journal of The Electrochemical Society* 158 (3) (2011), R1–R25. DOI: 10.1149/1.3515880.

[133] M. Steinhardt, E. I. Gillich, M. Stiegler, and A. Jossen. “Thermal conductivity inside prismatic lithium-ion cells with dependencies on temperature and external compression pressure”. In: *Journal of Energy Storage* 32 (2020), p. 101680. DOI: 10.1016/j.est.2020.101680.

[134] Y. Liu, Y. Zhu, and Y. Cui. “Challenges and opportunities towards fast-charging battery materials”. In: *Nature Energy* 4 (7) (2019), pp. 540–550. DOI: 10.1038/s41560-019-0405-3.

[135] A. Hales, R. Prosser, L. Bravo Diaz, G. White, Y. Patel, and G. Offer. “The Cell Cooling Coefficient as a design tool to optimise thermal management of lithium-ion cells in battery packs”. In: *eTransportation* 6 (2020), p. 100089. DOI: 10.1016/j.etran.2020.100089.

[136] P. J. Osswald, S. V. Erhard, J. Wilhelm, H. E. Hoster, and A. Jossen. “Simulation and Measurement of Local Potentials of Modified Commercial Cylindrical Cells”. In: *Journal of The Electrochemical Society* 162 (10) (2015), A2099–A2105. DOI: 10.1149/2.0561510jes.

[137] S. V. Erhard, P. J. Osswald, J. Wilhelm, H. E. Hoster, and A. Jossen. “Simulation and Measurement of Local Potentials of Modified Commercial Cylindrical Cells: II: Multi-Dimensional Modeling and Validation”. In: *Journal of The Electrochemical Society* 162 (14) (2015), A2707–A2719. DOI: 10.1149/2.0561510jes.

[138] P. J. Osswald, S. V. Erhard, A. Noel, P. Keil, F. M. Kindermann, H. Hoster, and A. Jossen. “Current density distribution in cylindrical Li-Ion cells during impedance measurements”. In: *Journal of Power Sources* 314 (2016), pp. 93–101. DOI: 10.1016/j.jpowsour.2016.02.070.

[139] S. V. Erhard et al. “Simulation and Measurement of the Current Density Distribution in Lithium-Ion Batteries by a Multi-Tab Cell Approach”. In: *Journal of The Electrochemical Society* 164 (1) (2017), A6324–A6333. DOI: 10.1149/2.0551701jes.

[140] V. P. Nemani, S. J. Harris, and K. C. Smith. “Design of Bi-Tortuous, Anisotropic Graphite Anodes for Fast Ion-Transport in Li-Ion Batteries”. In: *Journal of The Electrochemical Society* 162 (8) (2015), A1415–A1423. DOI: 10.1149/2.0151508jes.

[141] J. B. Habedank, J. Endres, P. Schmitz, M. F. Zaeh, and H. P. Huber. “Femtosecond laser structuring of graphite anodes for improved lithium-ion batteries: Ablation characteristics and process design”. In: *Journal of Laser Applications* 30 (3) (2018), p. 032205. DOI: 10.2351/1.5040611.

[142] Q. Cheng and Y. Zhang. “Multi-Channel Graphite for High-Rate Lithium Ion Battery”. In: *Journal of The Electrochemical Society* 165 (5) (2018), A1104–A1109. DOI: 10.1149/2.1171805jes.

[143] K.-H. Chen et al. “Efficient fast-charging of lithium-ion batteries enabled by laser-patterned three-dimensional graphite anode architectures”. In: *Journal of Power Sources* 471 (2020), p. 228475. DOI: 10.1016/j.jpowsour.2020.228475.

[144] C.-J. Bae, C. K. Erdonmez, J. W. Halloran, and Y.-M. Chiang. “Design of battery electrodes with dual-scale porosity to minimize tortuosity and maximize performance”. In: *Advanced materials* 25 (9) (2013), pp. 1254–1258. DOI: 10.1002/adma.201204055.

[145] C. L. Cobb and M. Blanco. “Modeling mass and density distribution effects on the performance of co-extruded electrodes for high energy density lithium-ion batteries”. In: *Journal of Power Sources* 249 (2014), pp. 357–366. DOI: 10.1016/j.jpowsour.2013.10.084.

[146] J. Pröll, H. Kim, A. Piqué, H. J. Seifert, and W. Pfleging. “Laser-printing and femtosecond-laser structuring of $LiMn_2O_4$ composite cathodes for Li-ion microbatteries”. In: *Journal of Power Sources* 255 (2014), pp. 116–124. DOI: 10.1016/j.jpowsour.2013.12.132.

[147] C. L. Cobb and S. E. Solberg. “Communication—Analysis of Thick Co-Extruded Cathodes for Higher-Energy-and-Power Lithium-Ion Batteries”. In: *Journal of The Electrochemical Society* 164 (7) (2017), A1339–A1341. DOI: 10.1149/2.0101707jes.

[148] B. Delattre, R. Amin, J. Sander, J. de Coninck, A. P. Tomsia, and Y.-M. Chiang. “Impact of Pore Tortuosity on Electrode Kinetics in Lithium Battery Electrodes: Study in Directionally Freeze-Cast $LiNi_{0.8}Co_{0.15}Al_{0.05}O_2$ (NCA)”. In: *Journal of The Electrochemical Society* 165 (2) (2018), A388–A395. DOI: 10.1149/2.1321802jes.

[149] T. Tsuda et al. “Improvement of high-rate discharging performance of $LiFePO_4$ cathodes by forming micrometer-sized through-holed electrode structures with a pico-second pulsed laser”. In: *Electrochimica Acta* 296 (2019), pp. 27–38. DOI: 10.1016/j.electacta.2018.11.014.

[150] J. Billaud, F. Bouville, T. Magrini, C. Villevieille, and A. R. Studart. “Magnetically aligned graphite electrodes for high-rate performance Li-ion batteries”. In: *Nature Energy* 1 (8) (2016), p. 1. DOI: 10.1038/nenergy.2016.97.

[151] M. Ebner, D.-W. Chung, R. E. García, and V. Wood. “Tortuosity Anisotropy in Lithium-Ion Battery Electrodes”. In: *Advanced Energy Materials* 4 (5) (2014), pp. 1–6. DOI: 10.1002/aenm.201301278.

[152] S. Malifarge, B. Delobel, and C. Delacourt. “Quantification of preferred orientation in graphite electrodes for Li-ion batteries with a novel X-ray-diffraction-based method”. In: *Journal of Power Sources* 343 (2017), pp. 338–344. DOI: 10.1016/j.jpowsour.2017.01.065.

[153] S. Malifarge, B. Delobel, and C. Delacourt. “Experimental and Modeling Analysis of Graphite Electrodes with Various Thicknesses and Porosities for High-Energy-Density Li-Ion Batteries”. In: *Journal of The Electrochemical Society* 165 (7) (2018), A1275–A1287. DOI: 10.1149/2.0301807jes.

[154] W. Pfleging. “Recent progress in laser texturing of battery materials: a review of tuning electrochemical performances, related material development, and prospects for large-scale manufacturing”. In: *International Journal of Extreme Manufacturing* 3 (1) (2021), p. 012002. DOI: 10.1088/2631-7990/abca84.

[155] M. Kerler, P. Burda, M. Baumann, and M. Lienkamp. “A concept of a high-energy, low-voltage EV battery pack”. In: *2014 IEEE International Electric Vehicle Conference (IEVC), Florence, Italy* (2014), pp. 1–8. DOI: 10.1109/IEVC.2014.7056185.

[156] C. Suarez and W. Martinez. “Fast and Ultra-Fast Charging for Battery Electric Vehicles – A Review”. In: *2019 IEEE Energy Conversion Congress and Exposition (ECCE), Baltimore, MD, USA* (2019), pp. 569–575. DOI: 10.1109/ECCE.2019.8912594.

[157] I. Aghabali, J. Bauman, P. Kollmeyer, Y. Wang, B. Bilgin, and A. Emadi. “800V Electric Vehicle Powertrains: Review and Analysis of Benefits, Challenges, and Future Trends”. In: *IEEE Transactions on Transportation Electrification* (2020), pp. 1–22. DOI: 10.1109/TTE.2020.3044938.

[158] newsroom - The Media Portal by Porsche. *The battery: Sophisticated thermal management, 800-volt system voltage*. URL: https://newsroom.porsche.com/en/products/taycan/battery-18557.html (visited on 03/10/2021).

[159] S. Yang. “A Review of Lithium-Ion Battery Thermal Management System Strategies and the Evaluate Criteria”. In: *International Journal of Electrochemical Science* (2019), pp. 6077–6107. DOI: 10.20964/2019.07.06.

[160] Q. Wang, P. Ping, X. Zhao, G. Chu, J. Sun, and C. Chen. “Thermal runaway caused fire and explosion of lithium ion battery”. In: *Journal of Power Sources* 208 (2012), pp. 210–224. DOI: 10.1016/j.jpowsour.2012.02.038.

[161] M. Ikezoe, N. Hirata, C. AMEMIYA, T. Miyamoto, Y. Watanabe, T. Hirai, and T. Sasaki. “Development of High Capacity Lithium- Ion Battery for NISSAN LEAF”. In: *SAE International* 2012-01-0664 (2012). DOI: 10.4271/2012-01-0664.

[162] J. Kim, J. Oh, and H. Lee. “Review on battery thermal management system for electric vehicles”. In: *Applied Thermal Engineering* 149 (2019), pp. 192–212. DOI: 10.1016/j.applthermaleng.2018.12.020.

[163] S. S. Zhang, K. Xu, and T. R. Jow. “Charge and discharge characteristics of a commercial $LiCoO_2$-based 18650 Li-ion battery”. In: *Journal of Power Sources* 160 (2) (2006), pp. 1403–1409. DOI: 10.1016/j.jpowsour.2006.03.037.

[164] K. Kumaresan, G. Sikha, and R. E. White. “Thermal Model for a Li-Ion Cell”. In: *Journal of The Electrochemical Society* 155 (2) (2008), A164–A171. DOI: 10.1149/1.2817888.

[165] Y. Ji, Y. Zhang, and C.-Y. Wang. “Li-Ion Cell Operation at Low Temperatures”. In: *Journal of The Electrochemical Society* 160 (4) (2013), A636–A649. DOI: 10.1149/2.047304jes.

[166] J. Landesfeind and H. A. Gasteiger. “Temperature and Concentration Dependence of the Ionic Transport Properties of Lithium-Ion Battery Electrolytes”. In: *Journal of The Electrochemical Society* 166 (14) (2019), A3079–A3097. DOI: 10.1149/2.0571912jes.

[167] V. Zinth, C. von Lüders, M. Hofmann, J. Hattendorff, I. Buchberger, S. Erhard, J. Rebelo-Kornmeier, A. Jossen, and R. Gilles. “Lithium plating in lithium-ion batteries at sub-ambient temperatures investigated by in situ neutron diffraction”. In: *Journal of Power Sources* 271 (2014), pp. 152–159. DOI: 10.1016/j.jpowsour.2014.07.168.

[168] Z. Li, J. Huang, B. Yann Liaw, V. Metzler, and J. Zhang. “A review of lithium deposition in lithium-ion and lithium metal secondary batteries”. In: *Journal of Power Sources* 254 (2014), pp. 168–182. DOI: 10.1016/j.jpowsour.2013.12.099.

[169] C. von Lüders, V. Zinth, S. V. Erhard, P. J. Osswald, M. Hofmann, R. Gilles, and A. Jossen. “Lithium plating in lithium-ion batteries investigated by voltage relaxation and in situ neutron diffraction”. In: *Journal of Power Sources* 342 (2017), pp. 17–23. DOI: 10.1016/j.jpowsour.2016.12.032.

[170] X.-G. Yang and C.-Y. Wang. “Understanding the trilemma of fast charging, energy density and cycle life of lithium-ion batteries”. In: *Journal of Power Sources* 402 (2018), pp. 489–498. DOI: 10.1016/j.jpowsour.2018.09.069.

[171] S.-B. Son, D. Robertson, Z. Yang, Y. Tsai, S. Lopykinski, and I. Bloom. “Fast Charge-Driven Li Plating on Anode and Structural Degradation of Cathode”. In: *Journal of The Electrochemical Society* 167 (14) (2020), p. 140506. DOI: 10.1149/1945-7111/abc031.

[172] Y. Ji and C. Y. Wang. “Heating strategies for Li-ion batteries operated from subzero temperatures”. In: *Electrochimica Acta* 107 (2013), pp. 664–674. DOI: 10.1016/j.electacta.2013.03.147.

[173] X.-G. Yang, T. Liu, Y. Gao, S. Ge, Y. Leng, D. Wang, and C.-Y. Wang. “Asymmetric Temperature Modulation for Extreme Fast Charging of Lithium-Ion Batteries”. In: *Joule* (2019). DOI: 10.1016/j.joule.2019.09.021.

[174] S. F. Schuster, T. Bach, E. Fleder, J. Müller, M. Brand, G. Sextl, and A. Jossen. "Nonlinear aging characteristics of lithium-ion cells under different operational conditions". In: *Journal of Energy Storage* 1 (2015), pp. 44–53. DOI: 10.1016/j.est.2015.05.003.

[175] P. Keil and A. Jossen. "Impact of Dynamic Driving Loads and Regenerative Braking on the Aging of Lithium-Ion Batteries in Electric Vehicles". In: *Journal of The Electrochemical Society* 164 (13) (2017), A3081–A3092. DOI: 10.1149/2.0801713jes.

[176] P. Keil, S. F. Schuster, J. Wilhelm, J. Travi, A. Hauser, R. C. Karl, and A. Jossen. "Calendar Aging of Lithium-Ion Batteries: I. Impact of the Graphite Anode on Capacity Fade". In: *Journal of The Electrochemical Society* 163 (9) (2016), A1872–A1880. DOI: 10.1149/2.0411609jes.

[177] P. Keil and A. Jossen. "Calendar Aging of NCA Lithium-Ion Batteries Investigated by Differential Voltage Analysis and Coulomb Tracking". In: *Journal of The Electrochemical Society* 164 (1) (2017), A6066–A6074. DOI: 10.1149/2.0091701jes.

[178] L. Lander, E. Kallitsis, A. Hales, J. S. Edge, A. Korre, and G. Offer. "Cost and carbon footprint reduction of electric vehicle lithium-ion batteries through efficient thermal management". In: *Applied Energy* 289 (2021), p. 116737. DOI: 10.1016/j.apenergy.2021.116737.

[179] H. Park. "A design of air flow configuration for cooling lithium ion battery in hybrid electric vehicles". In: *Journal of Power Sources* 239 (2013), pp. 30–36. DOI: 10.1016/j.jpowsour.2013.03.102.

[180] Y. Deng, C. Feng, J. E, H. Zhu, J. Chen, M. Wen, and H. Yin. "Effects of different coolants and cooling strategies on the cooling performance of the power lithium ion battery system: A review". In: *Applied Thermal Engineering* 142 (2018), pp. 10–29. DOI: 10.1016/j.applthermaleng.2018.06.043.

[181] X. Feng, X. He, M. Ouyang, L. Lu, P. Wu, C. Kulp, and S. Prasser. "Thermal runaway propagation model for designing a safer battery pack with 25 Ah $LiNi_xCo_yMn_zO_2$ large format lithium ion battery". In: *Applied Energy* 154 (2015), pp. 74–91. DOI: 10.1016/j.apenergy.2015.04.118.

[182] A. de Vita, A. Maheshwari, M. Destro, M. Santarelli, and M. Carello. "Transient thermal analysis of a lithium-ion battery pack comparing different cooling solutions for automotive applications". In: *Applied Energy* 206 (2017), pp. 101–112. DOI: 10.1016/j.apenergy.2017.08.184.

[183] M. Henke and G. Hailu. "Thermal Management of Stationary Battery Systems: A Literature Review". In: *Energies* 13 (16) (2020), p. 4194. DOI: 10.3390/en13164194.

[184] R. Sabbah, R. Kizilel, J. R. Selman, and S. Al-Hallaj. "Active (air-cooled) vs. passive (phase change material) thermal management of high power lithium-ion packs: Limitation of temperature rise and uniformity of temperature distribution". In: *Journal of Power Sources* 182 (2) (2008), pp. 630–638. DOI: 10.1016/j.jpowsour.2008.03.082.

[185] I. A. Hunt, Y. Zhao, Y. Patel, and J. Offer. "Surface Cooling Causes Accelerated Degradation Compared to Tab Cooling for Lithium-Ion Pouch Cells". In: *Journal of The Electrochemical Society* 163 (9) (2016), A1846–A1852. DOI: 10.1149/2.0361609jes.

[186] Y. Zhao, Y. Patel, T. Zhang, and G. J. Offer. "Modeling the Effects of Thermal Gradients Induced by Tab and Surface Cooling on Lithium Ion Cell Performance". In: *Journal of The Electrochemical Society* 165 (13) (2018), A3169–A3178. DOI: 10.1149/2.0901813jes.

[187] O. Dondelewski, T. Szemberg O'Connor, Y. Zhao, I. A. Hunt, A. Holland, A. Hales, G. J. Offer, and Y. Patel. "The role of cell geometry when selecting tab or surface cooling to minimise cell degradation". In: *eTransportation* 5 (1–2) (2020), p. 100073. DOI: 10.1016/j.etran.2020.100073.

[188] A. Adam, J. Wandt, E. Knobbe, G. Bauer, and A. Kwade. "Fast-Charging of Automotive Lithium-Ion Cells: In-Situ Lithium-Plating Detection and Comparison of Different Cell Designs". In: *Journal of The Electrochemical Society* 167 (13) (2020), p. 130503. DOI: 10.1149/1945-7111/abb564.

[189] S. Chen, N. Bao, X. Peng, A. Garg, and Z. Chen. "A Thermal Design and Experimental Investigation for the Fast Charging Process of a Lithium-Ion Battery Module With Liquid Cooling". In: *Journal of Electrochemical Energy Conversion and Storage* 17 (2) (2020), p. 021109. DOI: 10.1115/1.4045324.

[190] S. Panchal, R. Khasow, I. Dincer, M. Agelin-Chaab, R. Fraser, and M. Fowler. "Thermal design and simulation of mini-channel cold plate for water cooled large sized prismatic lithium-ion battery". In: *Applied Thermal Engineering* 122 (93) (2017), pp. 80–90. DOI: 10.1016/j.applthermaleng.2017.05.010.

[191] A. H. Mohammed, M. Alhadri, W. Zakri, H. Aliniagerdroudbari, R. Esmaeeli, S. R. Hashemi, G. Nadkarni, and S. Farhad. "Design and Comparison of Cooling Plates for a Prismatic Lithium-ion Battery for Electrified Vehicles". In: *SAE Technical Paper* (2018), pp. 2018-01–1188. DOI: 10.4271/2018-01-1188.

[192] S. Chen, X. Peng, N. Bao, and A. Garg. "A comprehensive analysis and optimization process for an integrated liquid cooling plate for a prismatic lithium-ion battery module". In: *Applied Thermal Engineering* 156 (2) (2019), pp. 324–339. DOI: 10.1016/j.applthermaleng.2019.04.089.

[193] J. Zhao, Z. Rao, and Y. Li. "Thermal performance of mini-channel liquid cooled cylinder based battery thermal management for cylindrical lithium-ion power battery". In: *Energy Conversion and Management* 103 (2015), pp. 157–165. DOI: 10.1016/j.enconman.2015.06.056.

[194] Z. Rao, Z. Qian, Y. Kuang, and Y. Li. "Thermal performance of liquid cooling based thermal management system for cylindrical lithium-ion battery module with variable contact surface". In: *Applied Thermal Engineering* 123 (2017), pp. 1514–1522. DOI: 10.1016/j.applthermaleng.2017.06.059.

[195] D. T. Adams et al. "Battery Pack Thermal Management System: Patent Application Publication". US 2009/0023056A1. 2009.

[196] R. Kizilel, R. Sabbah, J. R. Selman, and S. Al-Hallaj. "An alternative cooling system to enhance the safety of Li-ion battery packs". In: *Journal of Power Sources* 194 (2) (2009), pp. 1105–1112. DOI: 10.1016/j.jpowsour.2009.06.074.

[197] Z. Rao, S. Wang, and G. Zhang. "Simulation and experiment of thermal energy management with phase change material for ageing $LiFePO_4$ power battery". In: *Energy Conversion and Management* 52 (12) (2011), pp. 3408–3414. DOI: 10.1016/j.enconman.2011.07.009.

[198] F. Chen, R. Huang, C. Wang, X. Yu, H. Liu, Q. Wu, K. Qian, and R. Bhagat. "Air and PCM cooling for battery thermal management considering battery cycle life". In: *Applied Thermal Engineering* 173 (2020), p. 115154. DOI: 10.1016/j.applthermaleng.2020.115154.

[199] F. Bai, M. Chen, W. Song, Z. Feng, Y. Li, and Y. Ding. “Thermal management performances of PCM/water cooling-plate using for lithium-ion battery module based on non-uniform internal heat source”. In: *Applied Thermal Engineering* 126 (2017), pp. 17–27. DOI: 10.1016/j.applthermaleng.2017.07.141.

[200] D. Kong, R. Peng, P. Ping, J. Du, G. Chen, and J. Wen. “A novel battery thermal management system coupling with PCM and optimized controllable liquid cooling for different ambient temperatures”. In: *Energy Conversion and Management* 204 (2020), p. 112280. DOI: 10.1016/j.enconman.2019.112280.

[201] D. A. Howey, S. A. Roberts, V. Viswanathan, A. Mistry, M. Beuse, E. Khoo, and S. C. DeCaluwe. “Free Radicals: Making a Case for Battery Modeling”. In: *Electrochemical Society Interface* 29 (4) (2020), pp. 30–34. DOI: 10.1149/2.F03204IF.

[202] K. E. Thomas, J. Newman, and R. M. Darling. “Mathematical Modeling of Lithium Batteries”. In: *Advances in Lithium-Ion Batteries*. Ed. by W. A. van Schalkwijk and B. Scrosati. Boston, MA: Springer US, 2002, pp. 345–392. DOI: 10.1007/0-306-47508-1_13.

[203] A. Jokar, B. Rajabloo, M. Désilets, and M. Lacroix. “Review of simplified Pseudo-two-Dimensional models of lithium-ion batteries”. In: *Journal of Power Sources* 327 (2016), pp. 44–55. DOI: 10.1016/j.jpowsour.2016.07.036.

[204] K. Shah et al. “State of the Art and Future Research Needs for Multiscale Analysis of Li-Ion Cells”. In: *Journal of Electrochemical Energy Conversion and Storage* 14 (2) (2017), pp. 1–17. DOI: 10.1115/1.4036456.

[205] S. G. Marquis, R. Timms, V. Sulzer, C. P. Please, and S. J. Chapman. “A Suite of Reduced-Order Models of a Single-Layer Lithium-Ion Pouch Cell”. In: *Journal of The Electrochemical Society* 167 (14) (2020), p. 140513. DOI: 10.1149/1945-7111/abbce4.

[206] G. M. Goldin, A. M. Colclasure, A. H. Wiedemann, and R. J. Kee. “Three-dimensional particle-resolved models of Li-ion batteries to assist the evaluation of empirical parameters in one-dimensional models”. In: *Electrochimica Acta* 64 (2012), pp. 118–129. DOI: 10.1016/j.electacta.2011.12.119.

[207] T. Hutzenlaub, S. Thiele, N. Paust, R. Spotnitz, R. Zengerle, and C. Walchshofer. “Three-dimensional electrochemical Li-ion battery modelling featuring a focused ion-beam/scanning electron microscopy based three-phase reconstruction of a LiCoO2 cathode”. In: *Electrochimica Acta* 115 (2014), pp. 131–139. DOI: 10.1016/j.electacta.2013.10.103.

[208] S. Hein and A. Latz. “Influence of local lithium metal deposition in 3D microstructures on local and global behavior of Lithium-ion batteries”. In: *Electrochimica Acta* 201 (2016), pp. 354–365. DOI: 10.1016/j.electacta.2016.01.220.

[209] H. Mendoza, S. A. Roberts, V. E. Brunini, and A. M. Grillet. “Mechanical and Electrochemical Response of a $LiCoO_2$ Cathode using Reconstructed Microstructures”. In: *Electrochimica Acta* 190 (2016), pp. 1–15. DOI: 10.1016/j.electacta.2015.12.224.

[210] P. R. Shearing, L. E. Howard, P. S. Jørgensen, N. P. Brandon, and S. J. Harris. “Characterization of the 3-dimensional microstructure of a graphite negative electrode from a Li-ion battery”. In: *Electrochemistry Communications* 12 (3) (2010), pp. 374–377. DOI: 10.1016/j.elecom.2009.12.038.

[211] M. Ebner, F. Geldmacher, F. Marone, M. Stampanoni, and V. Wood. “X-Ray Tomography of Porous, Transition Metal Oxide Based Lithium Ion Battery Electrodes”. In: *Advanced Energy Materials* 3 (7) (2013), pp. 845–850. DOI: 10.1002/aenm.201200932.

[212] A. P. Cocco, G. J. Nelson, W. M. Harris, A. Nakajo, T. D. Myles, A. M. Kiss, J. J. Lombardo, and W. K. S. Chiu. “Three-dimensional microstructural imaging methods for energy materials”. In: *Physical chemistry chemical physics : PCCP* 15 (39) (2013), pp. 16377–16407. DOI: 10.1039/c3cp52356j.

[213] M. Ender, J. Joos, A. Weber, and E. Ivers-Tiffée. “Anode microstructures from high-energy and high-power lithium-ion cylindrical cells obtained by X-ray nano-tomography”. In: *Journal of Power Sources* 269 (2014), pp. 912–919. DOI: 10.1016/j.jpowsour.2014.07.070.

[214] J. Joos, T. Carraro, A. Weber, and E. Ivers-Tiffée. “Reconstruction of porous electrodes by FIB/SEM for detailed microstructure modeling”. In: *Journal of Power Sources* 196 (17) (2011), pp. 7302–7307. DOI: 10.1016/j.jpowsour.2010.10.006.

[215] T. Hutzenlaub, S. Thiele, R. Zengerle, and C. Ziegler. “Three-Dimensional Reconstruction of a $LiCoO_2$ Li-Ion Battery Cathode”. In: *Electrochemical and Solid-State Letters* 15 (3) (2012), A33–A36. DOI: 10.1149/2.002203esl.

[216] M. Kroll, D. Hlushkou, S. Schlabach, A. Höltzel, B. Roling, and U. Tallarek. “Reconstruction–Simulation Approach Verifies Impedance-Derived Ion Transport Tortuosity of a Graphite Battery Electrode”. In: *Journal of The Electrochemical Society* 165 (13) (2018), A3156–A3163. DOI: 10.1149/2.0711813jes.

[217] M. Doyle, T. F. Fuller, and J. Newman. “Modeling of Galvanostatic Charge and Discharge of the Lithium/Polymer/Insertion Cell”. In: *Journal of The Electrochemical Society* 140 (6) (1993), pp. 1526–1533. DOI: 10.1149/1.2221597.

[218] T. F. Fuller, M. Doyle, and J. Newman. “Simulation and Optimization of the Dual Lithium Ion Insertion Cell”. In: *Journal of The Electrochemical Society* 141 (1) (1994), pp. 1–10. DOI: 10.1149/1.2054684.

[219] J. S. Newman and N. P. Balsara. *Electrochemical systems*. Fourth edition. The Electrochemical Society series. Hoboken, NJ: John Wiley & Sons Inc, 2021.

[220] J. S. Newman and C. W. Tobias. “Theoretical Analysis of Current Distribution in Porous Electrodes”. In: *Journal of The Electrochemical Society* 109 (12) (1962), pp. 1183–1191. DOI: 10.1149/1.2425269.

[221] A. Rheinfeld, S. Kosch, S. V. Erhard, P. J. Osswald, B. Rieger, and A. Jossen. “Electro-Thermal Modeling of Large Format Lithium-Ion Pouch Cells: A Cell Temperature Dependent Linear Polarization Expression”. In: *Journal of The Electrochemical Society* 163 (14) (2016), A3046–A3062. DOI: 10.1149/2.0701614jes.

[222] B. Rieger, S. V. Erhard, S. Kosch, M. Venator, A. Rheinfeld, and A. Jossen. “Multi-Dimensional Modeling of the Influence of Cell Design on Temperature, Displacement and Stress Inhomogeneity in Large-Format Lithium-Ion Cells”. In: *Journal of The Electrochemical Society* 163 (14) (2016), A3099–A3110. DOI: 10.1149/2.1051614jes.

[223] S. Kosch, Y. Zhao, J. Sturm, J. Schuster, G. Mulder, E. Ayerbe, and A. Jossen. “A Computationally Efficient Multi-Scale Model for Lithium-Ion Cells”. In: *Journal of The Electrochemical Society* 165 (10) (2018), A2374–A2388. DOI: 10.1149/2.1241810jes.

[224] G. Ning and B. N. Popov. “Cycle Life Modeling of Lithium-Ion Batteries”. In: *Journal of The Electrochemical Society* 151 (10) (2004), pp. 1584–1591. DOI: 10.1149/1.1787631.

[225] S. Santhanagopalan, Q. Guo, P. Ramadass, and R. E. White. “Review of models for predicting the cycling performance of lithium ion batteries”. In: *Journal of Power Sources* 156 (2) (2006), pp. 620–628. DOI: 10.1016/j.jpowsour.2005.05.070.

[226] M. Guo, G. Sikha, and R. E. White. “Single-Particle Model for a Lithium-Ion Cell: Thermal Behavior”. In: *Journal of The Electrochemical Society* 158 (2) (2011), A122–A132. DOI: 10.1149/1.3521314.

[227] S. Khaleghi Rahimian, S. Rayman, and R. E. White. “Extension of physics-based single particle model for higher charge–discharge rates”. In: *Journal of Power Sources* 224 (2013), pp. 180–194. DOI: 10.1016/j.jpowsour.2012.09.084.

[228] J. Li, N. Lotfi, R. G. Landers, and J. Park. “A Single Particle Model for Lithium-Ion Batteries with Electrolyte and Stress-Enhanced Diffusion Physics”. In: *Journal of The Electrochemical Society* 164 (4) (2017), A874–A883. DOI: 10.1149/2.1541704jes.

[229] J. Newman and W. Tiedemann. “Potential and Current Distribution in Electrochemical Cells: Interpretation of the Half–Cell Voltage Measurements as a Function of Reference–Electrode Location”. In: *Journal of The Electrochemical Society* 140 (7) (1993), pp. 1961–1968. DOI: 10.1149/1.2220746.

[230] S. Kosch, A. Rheinfeld, S. V. Erhard, and A. Jossen. “An extended polarization model to study the influence of current collector geometry of large-format lithium-ion pouch cells”. In: *Journal of Power Sources* 342 (2017), pp. 666–676. DOI: 10.1016/j.jpowsour.2016.12.110.

[231] B. Y. Liaw, G. Nagasubramanian, R. G. Jungst, and D. H. Doughty. “Modeling of lithium ion cells - A simple equivalent-circuit model approach”. In: *Solid State Ionics* 175 (1-4) (2004), pp. 835–839. DOI: 10.1016/j.ssi.2004.09.049.

[232] H. He, R. Xiong, and J. Fan. “Evaluation of Lithium-Ion Battery Equivalent Circuit Models for State of Charge Estimation by an Experimental Approach”. In: *Energies* 4 (4) (2011), pp. 582–598. DOI: 10.3390/en4040582.

[233] J. Gomez, R. Nelson, E. E. Kalu, M. H. Weatherspoon, and J. P. Zheng. “Equivalent circuit model parameters of a high-power Li-ion battery: Thermal and state of charge effects”. In: *Journal of Power Sources* 196 (10) (2011), pp. 4826–4831. DOI: 10.1016/j.jpowsour.2010.12.107.

[234] T. Feng, L. Yang, X. Zhao, H. Zhang, and J. Qiang. “Online identification of lithium-ion battery parameters based on an improved equivalent-circuit model and its implementation on battery state-of-power prediction”. In: *Journal of Power Sources* 281 (2015), pp. 192–203. DOI: 10.1016/j.jpowsour.2015.01.154.

[235] C. Campestrini, T. Heil, S. Kosch, and A. Jossen. “A comparative study and review of different Kalman filters by applying an enhanced validation method”. In: *Journal of Energy Storage* 8 (2016), pp. 142–159. DOI: 10.1016/j.est.2016.10.004.

[236] X. Hu, S. Li, and H. Peng. “A comparative study of equivalent circuit models for Li-ion batteries”. In: *Journal of Power Sources* 198 (2012), pp. 359–367. DOI: 10.1016/j.jpowsour.2011.10.013.

[237] X. Lin, J. Park, L. Liu, Y. Lee, A. M. Sastry, and W. Lu. “A Comprehensive Capacity Fade Model and Analysis for Li-Ion Batteries”. In: *Journal of The Electrochemical Society* 160 (10) (2013), pp. 1701–1710. DOI: 10.1149/2.040310jes.

[238] R. Fu, S.-Y. Choe, V. Agubra, and J. Fergus. “Development of a physics-based degradation model for lithium ion polymer batteries considering side reactions”. In: *Journal of Power Sources* 278 (2015), pp. 506–521. DOI: 10.1016/j.jpowsour.2014.12.059.

[239] L. Xia, E. Najafi, Z. Li, H. J. Bergveld, and M. Donkers. “A computationally efficient implementation of a full and reduced-order electrochemistry-based model for Li-ion batteries”. In: *Applied Energy* 208 (2017), pp. 1285–1296. DOI: 10.1016/j.apenergy.2017.09.025.

[240] W. A. Appiah, J. Park, S. Byun, I. Cho, A. Mozer, M.-H. Ryou, and Y. M. Lee. “A coupled chemo-mechanical model to study the effects of adhesive strength on the electrochemical performance of silicon electrodes for advanced lithium ion batteries”. In: *Journal of Power Sources* 407 (2018), pp. 153–161. DOI: 10.1016/j.jpowsour.2018.06.079.

[241] D. A. G. Bruggeman. “Berechnung verschiedener physikalischer Konstanten von heterogenen Substanzen. I. Dielektrizitätskonstanten und Leitfähigkeiten der Mischkörper aus isotropen Substanzen”. In: *Annalen der Physik* 416 (7) (1935), pp. 636–664. DOI: 10.1002/andp.19354160705.

[242] D.-W. Chung, P. R. Shearing, N. P. Brandon, S. J. Harris, and R. E. García. “Particle Size Polydispersity in Li-Ion Batteries”. In: *Journal of The Electrochemical Society* 161 (3) (2014), A422–A430. DOI: 10.1149/2.097403jes.

[243] M. Ender. “An extended homogenized porous electrode model for lithium-ion cell electrodes”. In: *Journal of Power Sources* 282 (2015), pp. 572–580. DOI: 10.1016/j.jpowsour.2015.02.098.

[244] S. T. Taleghani, B. Marcos, K. Zaghib, and G. Lantagne. “A Study on the Effect of Porosity and Particles Size Distribution on Li-Ion Battery Performance”. In: *Journal of The Electrochemical Society* 164 (11) (2017), E3179–E3189. DOI: 10.1149/2.0211711jes.

[245] S. Müller, J. Eller, M. Ebner, C. Burns, J. Dahn, and V. Wood. “Quantifying Inhomogeneity of Lithium Ion Battery Electrodes and Its Influence on Electrochemical Performance”. In: *Journal of The Electrochemical Society* 165 (2) (2018), A339–A344. DOI: 10.1149/2.0311802jes.

[246] L. Bläubaum, F. Röder, C. Nowak, H. S. Chan, A. Kwade, and U. Krewer. “Impact of Particle Size Distribution on Performance of Lithium–Ion Batteries”. In: *ChemElectroChem* 7 (23) (2020), pp. 4755–4766. DOI: 10.1002/celc.202001249.

[247] I. V. Thorat, D. E. Stephenson, N. A. Zacharias, K. Zaghib, J. N. Harb, and D. R. Wheeler. “Quantifying tortuosity in porous Li-ion battery materials”. In: *Journal of Power Sources* 188 (2) (2009), pp. 592–600. DOI: 10.1016/j.jpowsour.2008.12.032.

[248] R. B. MacMullin and G. A. Muccini. “Characteristics of porous beds and structures”. In: *AIChE Journal* 2 (3) (1956), pp. 393–403. DOI: 10.1002/aic.690020320.

[249] S. C. Chen, C. C. Wan, and Y. Y. Wang. “Thermal analysis of lithium-ion batteries”. In: *Journal of Power Sources* 140 (1) (2005), pp. 111–124. DOI: 10.1016/j.jpowsour.2004.05.064.

[250] G.-H. Kim, K. Smith, K.-J. Lee, S. Santhanagopalan, and A. Pesaran. “Multi-Domain Modeling of Lithium-Ion Batteries Encompassing Multi-Physics in Varied Length Scales”. In: *Journal of The Electrochemical Society* 158 (8) (2011), A955–A969. DOI: 10.1149/1.3597614.

[251] D. Chen, J. Jiang, G.-H. Kim, C. Yang, and A. Pesaran. “Comparison of different cooling methods for lithium ion battery cells”. In: *Applied Thermal Engineering* 94 (2) (2016), pp. 846–854. DOI: 10.1016/j.applthermaleng.2015.10.015.

[252] R. Kantharaj and A. M. Marconnet. “Heat Generation and Thermal Transport in Lithium-Ion Batteries: A Scale-Bridging Perspective”. In: *Nanoscale and Microscale Thermophysical Engineering* 23 (2) (2019), pp. 128–156. DOI: 10.1080/15567265.2019.1572679.

[253] W. Polifke and J. Kopitz. *Wärmeübertragung: Grundlagen, analytische und numerische Methoden*. 2nd ed. Munich: Pearson Studium, 2009.

[254] D. Bernardi, E. Pawlikowski, and J. Newman. “A General Energy Balance for Battery Systems”. In: *Journal of The Electrochemical Society* 132 (1) (1985), pp. 5–12. DOI: 10.1149/1.2113792.

[255] J. B. Habedank, J. Kriegler, and M. F. Zaeh. “Enhanced Fast Charging and Reduced Lithium-Plating by Laser-Structured Anodes for Lithium-Ion Batteries”. In: *Journal of The Electrochemical Society* 166 (16) (2019), A3940–A3949. DOI: 10.1149/2.1241915jes.

[256] J. B. Habedank, D. Schwab, B. Kiesbauer, and M. F. Zaeh. “Paving the way for industrial ultrafast laser structuring of lithium-ion battery electrodes by increasing the scanning accuracy”. In: *Journal of Laser Applications* 32 (2) (2020), p. 022053. DOI: 10.2351/7.0000078.

List of Publications

IX J. Kriegler, L. Hille, S. Stock, **L. Kraft**, J. Hagemeister, J. B. Habedank, A. Jossen, M. F. Zaeh. "Enhanced Performance and Lifetime of Lithium-Ion Batteries by Laser Structuring of Graphite Anodes". In: *Applied Energy* 303, p. 117693, 2021. DOI: 10.1016/j.apenergy.2021.117693.

VIII M. Steinhardt, E. I. Gillich, A. Rheinfeld, **L. Kraft**, M. Spielbauer, O. Bohlen, A. Jossen. "Low-effort determination of heat capacity and thermal conductivity for cylindrical 18650 and 21700 lithium-ion cells". In: *Journal of Energy Storage* 42, p. 103065, 2021. DOI: 10.1016/j.est.2021.103065.

VII **L. Kraft**, A. Hoefling, T. Zünd, A. Kunz, M. Steinhardt, J. Tübke, A. Jossen. "Implications of the Heat Generation of LMR-NCM on the Thermal Behavior of Large-Format Lithium-Ion Batteries". In: *Journal of The Electrochemical Society* 168 (5), p. 053505, 2021. DOI: 10.1149/1945-7111/ac0069.

VI D. Schreiner, T. Zünd, F. J. Günter, **L. Kraft**, B. Stumper, F. Linsenmann, M. Schüßler, R. Wilhelm, A. Jossen, G. Reinhart, H. A. Gasteiger. "Comparative Evaluation of LMR-NCM and NCA Cathode Active Materials in Multilayer Lithium-Ion Pouch Cells: Part I. Production, Electrode Characterization, and Formation". In: *Journal of The Electrochemical Society* 168 (3), p. 030507, 2021. DOI: 10.1149/1945-7111/abe50c.

V **L. Kraft**, T. Zünd, D. Schreiner, R. Wilhelm, F. J. Günter, G. Reinhart, H. A. Gasteiger, A. Jossen. "Comparative Evaluation of LMR-NCM and NCA Cathode Active Materials in Multilayer Lithium-Ion Pouch Cells: Part II. Rate Capability, Long-Term Stability, and Thermal Behavior". In: *Journal of The Electrochemical Society* 168 (2), p. 020537, 2021. DOI: 10.1149/1945-7111/abe5e6.

IV W. Ai, **L. Kraft**, J. Sturm, A. Jossen, B. Wu. "Electrochemical Thermal-Mechanical Modelling of Stress Inhomogeneity in Lithium-Ion Pouch Cells". In: *Journal of The Electrochemical Society* 167 (1), p. 013512, 2020. DOI: 10.1149/2.0122001jes.

III **L. Kraft**, J. B. Habedank, A. Frank, A. Rheinfeld, A. Jossen. "Modeling and Simulation of Pore Morphology Modifications using Laser-Structured Graphite Anodes in Lithium-Ion Batteries". In: *Journal of The Electrochemical Society* 167 (1), p. 013506, 2020. DOI: 10.1149/2.0062001jes.

II J. B. Habedank, **L. Kraft**, A. Rheinfeld, C. Krezdorn, A. Jossen, M. F. Zaeh. "Increasing the Discharge Rate Capability of Lithium-Ion Cells with Laser-Structured Graphite Anodes: Modeling and Simulation". In: *Journal of The Electrochemical Society* 165 (7), pp. A1563–A1573, 2018. DOI: 10.1149/2.1181807jes.

I N. Paul, J. Keil, F. M. Kindermann, S. Schebesta, O. Dolotko, M. J. Mühlbauer, **L. Kraft**, S. V. Erhard, A. Jossen, R. Gilles. "Aging in 18650-type Li-ion cells examined with neutron diffraction, electrochemical analysis and physico-chemical modeling". In: *Journal of Energy Storage* 17, pp. 383–394, 2018. DOI: 10.1016/j.est.2018.03.016.

Acknowledgment

First of all, I want to thank my supervisor Prof. Andreas Jossen for giving me the opportunity to do my PhD in the field of lithium-ion batteries at the Institute for Electrical Energy Storage Technology (EES) at the Technical University of Munich (TUM). I really enjoyed the time I spent at the EES together with all my colleagues, who supported my personal and professional development. It was mostly the teamwork that motivated me to reach my goals.

Special thanks go to my colleague and EES roommate Johannes Sturm for his personal encouragement and all the fruitful scientific discussions. He always helped me to stay focused and to push my work towards publication. Many thanks likewise go to my colleague and namesake Sebastian Ludwig (the shared part of the name caused quite some confusion during our time at the EES), who was always available for a drink whenever necessary. I thank all the remaining colleagues and friends as well who supported my work even though I cannot name all of them.

I also want to acknowledge my ExZellTUM project colleagues, in particular Tanja Zünd and Fabian Linsenmann from the Chair of Technical Electrochemistry (TEC) and their supervisor Prof. Hubert A. Gasteiger as well as David Schreiner, Jan B. Habedank, and Johannes Kriegler from the Institute of Machine Tools and Industrial Management (*iwb*) for our joint work and scientific discussions, resulting in multiple shared publications in the end. Our interdisciplinary work helped me to expand my horizons in the big wide world of lithium-ion batteries.

Finally, I want to thank my family and friends for the time spent together, which allowed me to keep my work-life-balance and thereby supporting me along the way through my studies at university.